SOUND WAVES EXCITATION BY FLOW IN A PIPE HOUSING A SHALLOW CAVITY

SOUND WAVES EXCITATION BY FLOW IN A PIPE HOUSING A SHALLOW CAVITY

BY

SABER MOHAMED, M.Sc., B.Eng. (Honors)

A Thesis
Submitted to the School of Graduate Studies
in Partial Fulfillment of the Requirements
for the Degree
Doctor of Philosophy
McMaster University

Doctor of Philosophy (2015) McMaster University
(Mechanical Engineering) Hamilton, Ontario, Canada

TITLE: Sound Waves Excitation by Flow in a Pipe Housing a shallow Cavity

AUTHOR: Saber Mohamed
M.Sc., B.Eng. (Honors), Mechanical Engineering
Cairo University, Cairo, Egypt

SUPERVISOR: Dr. Samir Ziada

NUMBER OF PAGES: xxiv; 204

ABSTRACT

This research introduces a new application of the three microphones method, which was originally developed to analyse standing waves, to measure the aeroacoustic power of a duct housing a shallow cavity coupled with a longitudinal acoustic mode. In addition, this work provides, for the first time, the spatial distribution of the aeroacoustic sound sources over the cavity region for this type of flow-sound-structure interaction pattern. Furthermore, this research includes a comprehensive study of the effect of cavity geometrical parameters on the characteristics of the cavity aeroacoustic source.

An experimental investigation of the aeroacoustic source of an axisymetric cavity in a pipeline is presented. This aeroacoustic source is generated due to the interaction of the cavity shear layer oscillation with the resonant acoustic field in the pipe. The source is determined under high Reynolds number, fully developed turbulent pipe flow. The experimental technique (Sound Wave Method, SWM) employs six microphones distributed upstream and downstream of the cavity to evaluate the fluctuating pressure difference generated by the oscillating cavity shear layer in the presence of externally imposed sound waves. The results of the dimensionless aeroacoustic sources are in good agreement with the concepts of free shear layer instability and the fluid resonant oscillation behavior.

A validation study is performed in order to validate the measurement technique and the measured source term from the SWM. The validation methodology consisted of comparing the self-excited resonance response obtained from self-excitation measurements with that estimated from an acoustic model supplemented with the

measured source term using the SWM. The comparison depicts a very good agreement for the resonance frequency, lock-in ranges, and the resonance amplitude.

Extensive PIV flow measurements are performed to clarify the non-linear behavior of the aeroacoustic source at high levels of the acoustic particle velocity, and to understand the dependence of the flow-sound interaction patterns on the main system parameters such as the Strouhal number and excitation level. The results of a finite element analysis of the resonant sound field are combined with those of the PIV flow measurements into Howe's aeroacoustic integrand to compute the spatial and temporal distributions of the aeroacoustic sources. The results are also compared with the measured aeroacoustic source strength obtained by means of the SWM. This comparison highlights the superior efficiency of the SWM technique. Identification of the aeroacoustic source distributions as function of the acoustic excitation level showed that the non-linear behaviour of the source strength, which occurs at moderate sound levels, is caused by a gradual transition in the vorticity field oscillation pattern; from a distributed vorticity cloud over the whole cavity length at small excitation amplitudes to a pattern involving rapid formation of (discrete) vortices at the leading edge which becomes dominant at large excitation levels.

The spatial distribution of the acoustic power over the cavity length at resonance condition shows sources of sound generation at the first and last thirds of the cavity mouth and an absorption sink in the middle third. This distribution is different from that observed for deep cavities and trapped modes of shallow cavities. Due to these differences in the aeroacoustic source distributions, the effects of cavity geometrical parameters for the present shallow cavity are not necessarily similar to those reported in the literature for deep cavities and trapped mode resonance cases.

A comprehensive study of the effect of cavity geometrical parameters (including rounding-off the cavity edges) on the aeroacoustic sound sources is also included. Nine cavity sizes are studied in three different groups of length to depth ratios (L/H) with three different cavity volumes for each group of L/H. The aeroacoustic source strength and the Strouhal number corresponding to its maximum value are found to increase in a systematic manner as the cavity volume is increased for the same L/H ratio. These results indicate that the aeroacoustic sources of shallow cavities are affected not only by the ratio L/H, but also by the cavity volume.

The effect of cavity edge curvatures on the resonance response is experimentally investigated by testing different sizes of curvatures at different locations (upstream, downstream or both edges). The results show that rounding-off the cavity edges causes a reduction in the vertical component of the acoustic particle velocity but also an increase in the cavity length. These two consequences have opposite effects on acoustic power generation and therefore, rounding-off the edges has no significant effect on the resonance amplitude in the present case, except for relatively large radius.

To my wife; Fatma Abdalla

Who has given me the love, the happiness, and the meaning of my life

ACKNOWLEDGEMENTS

In the name of God “Allah”, most gracious, most merciful. The Lord, who taught the use of the pen and taught human that which he did not know.

I would like to express my great appreciation to my supervisor, Professor S. Ziada, for his support throughout the thesis, for his concern about his graduate students’ life, for his insight and inspiration, for his guidance and encouragement. I feel very fortunate to have worked under his supervision. Professor Ziada set for me the perfect model of a great scientist and a great educator who I wish to be in the future.

I would also like to thank my supervisory committee members, Professors J. Cotton and S. Tullis, for their time and interest, and for their great suggestions through the course of this work. I would like to extend special thanks to Dr. H.R. Graf for his great help at the beginning of this work. In addition, I would like to extend thanks to all the members of the Aeroacoustic group for their support and for raising important and inspirational questions whenever I presented my work at our weekly group meetings. Also, I would like to express special thanks to the staff of the mechanical engineering department machine shop for their great and invaluable help.

Last but not least, I would like to thank my parents, my wife’s parents for their unconditional love and support from afar, which helped me to overcome all the difficulties and to progress in my work. I would also like to extend special thanks to my wife and my children who shared me the hard times during this work.

NOMENCLATURE

A	Cross-sectional area at the cavity (m^2)
C_o	Wave propagation speed or speed of sound, (m/s)
D	Main pipe diameter (m)
D_c	Cavity diameter (m)
dP	Pitot tube dynamic pressure (Pa)
e^{ikx}	Complex representation of the simple harmonic motion with respect to location x
$e^{i\omega t}$	Complex representation of the simple harmonic motion with respect to time t
f	Resonance frequency of the acoustic wave (Hz)
F	Froude's friction factor
H	Cavity depth (m)
k	Wave number ($k = 2\pi / \lambda$) (m^{-1})
k_r	Reflected wave number (m^{-1}), $k_r = \omega / (C_o - U) = k / (1 - M)$
k_f	Forward wave number (m^{-1}), $k_f = \omega / (C_o + U) = k / (1+ M)$
$k. D/2$	Helmholtz number
L	Cavity length in the flow direction (m)
L/H	Cavity length to depth ratio
L/U_c	Travel time of the vortex along the cavity mouth (s)
L_{up} & L_{dn}	Upstream and downstream pipe lengths (m)
M	Mach number, U/C_o
m	Diametral nodal lines
M_{up} & M_{dn}	Upstream and downstream transfer matrices (Munjal, 1987)

n	Nodal circles
P	Instantaneous aeroacoustic power in (Watts)
p_o	mean fluid pressure (Pa)
$\mathbf{p}(x, y, t)$	Acoustic (fluctuating) pressure (Pa)
$p(t)$	Acoustic pressure time variation component (Pa)
$\mathbf{p}^-(x)$	Complex amplitude of the reflected wave (Pa)
$\mathbf{p}(x, y)$	Acoustic pressure spatial variation component (Pa)
$p/\rho C_o U$	Normalized amplitude ratio
p^+	Constant amplitudes of the incident wave between the sound source and a discontinuity
$\mathbf{p}^+(x)$	Complex amplitude of the incident wave (Pa)
$\mathbf{p}^+_d$ & $\mathbf{p}^-_d$	Downstream piping section forward and backward waves
$\mathbf{p}^+_u$ & $\mathbf{p}^-_u$	Upstream piping section forward and backward waves
p_{max}	Maximum acoustic pressure amplitude (Pa)
p_{mi}	Pressure signal measured by microphone number i
P_r	Prandtl number
$\mathbf{q}_c$	Acoustic volume velocity at the cavity centre ($\mathbf{q}_c = \upsilon \cdot A$),
$\mathbf{R}$	Molecular gas constant (J/kg.K)
Real ($\mathbf{S}$)	Real component of normalized source term
r_{dn}	Downstream cavity edge curvature (m)
r_{up}	Upstream cavity edge curvature (m)
$\mathbf{R}_x$	Standing wave reflection coefficient
$\mathbf{S}$	Normalized source term ($\mathbf{S} = \frac{\Delta \mathbf{p} / \frac{1}{2} \rho U^2}{\upsilon / U}$)

$\mathbf{s}(x,t)$	Fluctuating component of the entropy (J/K)
St	Strouhal number (f L/U)
St_{pw1}	Strouhal number at peak whistling condition
t	Time (seconds)
T_o	Mean ambient temperature (K)
U	Mean flow velocity (m/s)
U_c	Convection (phase) speed of a traveling vortex over the cavity mouth. (m/s)
U_{peak}	Flow velocity at the peak-whistling resonance condition (m/s)
U_{peak1}	Flow velocity at the first hydrodynamic resonance condition
U_{peak2}	Flow velocity at the second hydrodynamic resonance condition (m/s)
V	Cavity region volume (m^3)
x	Distance from the cavity leading edge with the flow (m)
x_{FD}	Developing entrance length for the turbulent pipe flow (m)
x_P	Pitot tube location distance from the pipe entrance (m)
y	cross-stream distance from pipe centerline (m)
$\mathbf{Y}$	Characteristic impedance, $Y = \rho_o C_o \left(1 - \frac{\alpha}{k} + i\frac{\alpha}{k}\right)$
Y_o	Ideal acoustic impedance ($Y_o = \rho_o C_o$). ($kg.m^{-2}.s^{-1}$)
$\mathbf{Z}_x$	Acoustic impedance (the ratio of fluctuating pressure to particle velocity at the same location, x) ($kg.m^{-2}.s^{-1}$)
α	Total aeroacoustic attenuation coefficient in a moving medium (m^{-1}) ($\alpha = \alpha_o + \zeta M$)
$-\alpha_i$	Spatial amplification rate of the initial disturbance
α_o	Viscothermal attenuation coefficient (m^{-1}) (Eqn. 2.11)

$\boldsymbol{\beta}$	Complex wave number ($\boldsymbol{\beta} = \omega / C_o + \alpha\,(1- i) \approx k - i\,\alpha$) ($m^{-1}$)
γ	Specific heat ratio
Δ	velocity factor, $\Delta = \frac{U_1 - U_2}{U_1 + U_2}$
$\Delta \mathbf{p}$	Induced acoustic pressure difference at the cavity (Pa)
$\Delta \mathbf{p}_{load}$	Load impedance at the cavity ($kg.m^{-2}.s^{-1}$)
μ	Local dynamic viscosity (Pa. s)
ε	Complex wave number including the effect of flow ($\varepsilon = \frac{i\,\beta}{1- M^2}$)
ζ	Turbulent flow friction coefficient ($\zeta = F / 2\,D$) (m^{-1})
θ	Angle (rad.)
θ_m	Momentum thickness (m)
λ	Acoustic wavelength (m)
ρ_o	Mean fluid density (kg/m^3)
$\rho\,(x,t)$	Fluid density fluctuations (kg/m^3)
υ	Acoustic particle velocity (m/s)
υ/U	Acoustic oscillation amplitude ratio
υ_y	Cross stream component of the acoustic particle velocity (m/s)
χ	Disturbance dimensionless frequencies
χ_1	Disturbance fundamental frequency; frequency at which the disturbance growth rate is maximum
ω	Angular velocity ($\omega = 2\pi f$) (rad/s)
ω	Vorticity (s^{-1})
Γ	Vortex circulation (m/s)

Abbreviations

2-D	Two dimensional
3-D	Three dimensional
BWR	Boiling water reactor
CFD	Computational fluid dynamics
FD	Fully developed
MSLs	Main steam lines
NRC	Nuclear Regularity Commission
NSE	Navier-Stokes equation
Mic.	Microphone
PIV	Particle image velocimetry
PVC	Poly vinyl chloride
SRVs	Safety relief valves
SWM	Sound wave method

TABLE OF CONTENTS

TABLE OF FIGURES

Chapter 1

Introduction

Flow-Sound-Structure interaction is a branch of fluid mechanics that is concerned with the study of generation or absorption of sound occurring when unsteady flow interacts with solid bodies (Howe, 1998). This phenomenon is encountered in many industrial applications such as gas transportation in piping systems, steam flow in turbines, and compressor pipe connections. Moreover, acoustic-fluid-structure interaction is also a common problem in automotive applications as in the pressure-induced structure-borne sound of intake and exhaust systems. It can be noted that the main common feature between these applications is the presence of a piping system with fittings. Such fittings include valves, side-branches, area changes…etc.

Flow-excited acoustic resonances can cause acute noise levels, and, in some cases, can result in catastrophic failure due to acoustic fatigue of the associated structure. A recent example of the damaging effects of this phenomenon is the acoustic fatigue damage of the steam dryer of a boiling water reactor (BWR) at the Quad Cities nuclear power plant in 2002 (NRC information notice, 2002-26; Ziada, 2010). According to NRC information notice (2002), during the operation of the BWR-3 steam dryer in the Quad Cities Unit 2 Nuclear Power, the damage was occurred due to a high cycle fatigue in the stub pipes of the safety relief valves (SRVs) in the main steam lines (MSLs). The flow-induced acoustic resonance in these stub pipes was considered the cause of the dryer failure. The acoustic resonance was generated by the interaction between the sound field and an unstable shear layer across the opening of the SRV stub pipes. This acoustic resonance caused cracks in the steam dryer and resulted in an unscheduled plant shut-down to repair the steam dryer for almost a month. (Note that the plant total electric capacity is approximately 1,800 MW).

Flow-structure interaction in a piping system housing a cavity or corrugations is usually associated with sound generation. In this phenomenon, the presence of the cavity disturbs the boundary layer flow in the pipe and produces an unstable free shear layer at the cavity opening, while the sound field in the pipe (i.e. the acoustic particle velocity at the cavity region) provides the feedback disturbance in a closed loop excitation mechanism. This feedback disturbance may magnify or reduce the shear layer disturbance, which either leads to acoustic resonance oscillations or dampens the free shear layer oscillations, respectively. The degree of magnification of the original disturbance depends on several parameters such as the original disturbance convection velocity and the timing of the sound feedback oscillation. These parameters are influenced by the sound wave frequency f, the cavity length in the flow direction L, and the sound intensity as expressed by the acoustic particle velocity **υ** along the cavity. These relevant parameters are normalized in two dimensionless groups; the Strouhal number (f L/U) and the amplitude ratio (υ/U), where U is the mean velocity of the flow grazing the cavity.

The interaction mechanism between the flow field and the sound field that magnifies the original disturbance and sustains an acoustic resonance is called fluid-resonant mechanism by Rockwell and Naudascher (1978) and is associated with strong pressure oscillations and high noise levels. These strong oscillations can cause fatigue failure of the piping structure. Moreover, these pulsations increase the dynamic energy loss from the main flow by consuming part of the flow energy to feed the acoustic resonance of the system.

Design considerations for flow-excited acoustic resonances must include the flow velocity at the onset of resonance (which can be derived from the Strouhal number at which resonance starts) and the amplitude of resonance (driven from the aeroacoustic source strength). From the literature, the onset of resonance is well defined for different applications like flow over cavities and side-branches (Geveci et al., 2003; Graf & Ziada, 1992; Graf & Ziada, 2010; Hourigan et al., 1990; Martínez et al., 2009; Rockwell et al., 2003; Ziada & Blake, 2003; Ziada & Shine, 1999). However, previous investigations of the second design criteria; the amplitude of resonance or the aeroacoustic power source; are insufficient to provide reasonable predictions for various industrial applications.

It is generally recognized that the aeroacoustic sound sources depend very strongly on the local details of the sound and vorticity fields. These details include; the local magnitude and direction of the flow velocity, U, and vorticity, ω; the local amplitude, phase and direction of the acoustic particle velocity, υ; the acoustic wavelength, λ, relative to the length scale, L; and the acoustic mode shape (e.g. in the flow or the cross direction). In most of the previous studies (experimental and numerical), the unsteady details of the flow field at the object are required to estimate the aeroacoustic source, which necessitates a lot of simplifications of the flow field and the geometries of the structural boundaries (Hourigan et al., 1990; Howe, 1975; Mohany & Ziada, 2009; Nakiboğlu et al., 2010; Nakiboğlu et al., 2011; Oshkai & Yan, 2008).

1.1 Scope of the Work

This research experimentally investigates the aeroacoustic excitation source for an axisymmetric shallow cavity coupled with acoustic longitudinal modes in a duct conveying a high Reynolds number and fully developed turbulent air flows. The measuring technique developed by Graf and Ziada (2010) for closed side-branches, the Sound Wave Method (SWM), has been further developed here to measure the aeroacoustic power without the need to resolve the details of the flow field inside the cavity. The SWM can be used for complex geometries and three-dimensional turbulent flows.

The research is divided into four modules. The first module is an experimental characterization of the flow-induced acoustic source of an axisymmetric shallow cavity, coupled to longitudinal acoustic modes in a circular pipeline conveying fully developed turbulent flow. This aeroacoustic source is generated due to the interaction of the cavity shear layer oscillation with the resonant acoustic field in the pipe. The distributed aeroacoustic source is modeled by a lumped acoustic dipole source which is dependent on the Strouhal number and the acoustic particle velocity at the cavity. The amplitude and phase of this source are determined experimentally and presented in the form of a dimensionless complex source term. The second module deals with the validation of the measured source, where tests generating self-excited acoustic resonances are performed, and the source measured in the first module is used to predict the amplitude of resonance. The third module investigates the effect of different parameters on both the aeroacoustic source power and the resonance fluctuation amplitude of the shallow cavity. Here, the effect of the cavity geometry (length and depth) and rounding-off the cavity edge are investigated. In the fourth module, the flow-sound interaction mechanism is studied by means of Particle Image Velocimetry (PIV) to better understand the non-linear nature of the interaction mechanism at large amplitude pulsations. Also, the PIV flow field measurements are coupled with finite element simulation of the acoustic field in order to predict the aeroacoustic source using Howe's integrand. The aeroacoustic source power determined from this elaborate methodology is then compared with that obtained by the much more efficient approach (SWM) which is developed in the first module.

1.2 Thesis Outline

This thesis consists of seven chapters. In Chapter 2, the basic phenomenon of flow-structure-sound interaction is reviewed for the configurations of flow over cavities. Subsequently, previous methods of characterizing the aeroacoustic source strength are summarized. In Chapter 3, the experimental setup and the measurement techniques used in different sections of this thesis are described. The results of the Sound Wave Method for the flow-induced acoustic source of an axisymmetric shallow cavity coupled to longitudinal acoustic modes in a pipeline are presented in Chapter 4. The final section of Chapter 4 provides the validation of the measurement technique. In Chapter 5, an investigation of the flow-structure-sound interaction mechanism using the PIV technique is presented. Thereafter, the effects of the cavity geometrical parameters and edges on the aeroacoustic source are addressed in Chapter 6. The summary and the conclusions of this work, as well as some recommendations for future work, are provided in Chapter 7.

Chapter 2

Basic Phenomenon and Literature Review

The subject of flow over a cavity received early attention from researches since the middle of the twentieth century when Karamcheti (1955) investigated the generation of noise and oscillations in naval and aeronautical industries. This early attention suggests this flow geometry to be a strong source of flow oscillation and noise generation. More recently, extensive investigations of flow over cavities have been conducted because of its wide scale presence in many applications such as pipeline corrugations (Belfroid et al., 2007, Debut et al., 2007, Nakiboglu et al., 2011 , Goyder, 2013), as well as side-branches and valves (Graf & Ziada, 2010, and Ziada et al., 1989). Two recent reviews of cavity aeroacoustics have been published by Tonon et al. (2011) and Ziada & Lafon (2014).

In this chapter, the first section presents a background about duct acoustics, sound wave propagations, reflection, and attenuations. The second section reviews the physical phenomenon of oscillations due to flow over a cavity, including the free shear layer instability, the flow patterns of flow over cavities, and the classifications of the feedback mechanism causing cavity oscillations. The last section provides a critical review of the previous work on the determinations of aeroacoustic sources generated from flow-sound interaction.

2.1 Duct Acoustics

Flow duct systems are essential components of power generation plants, petrochemical stations, and pipelines for liquid and gas distribution systems. In real applications, the duct geometrical configurations are complicated and convoluted, including fittings and discontinuities that often generate noise and vibrations in the piping system. In the cases when sound sources exists in the system, design concerns regarding the transmission of the acoustic energy and the distribution of fluctuating pressure throughout the system become significant.

Sound, by definition, is a pressure wave transmitted through a medium, composed of frequencies within the range of hearing and of a level sufficiently strong to be heard. When the oscillations caused by the displacement of the fluid particle are in the same direction of the wave propagation, the sound wave mode is called a longitudinal (or plane) mode (similar to axial vibration of bars). However, if the displacement of the medium is perpendicular to the direction of wave propagation, the acoustic wave mode is called a transverse (or cross) mode (similar to the vibration of a string), see figure 2.1.

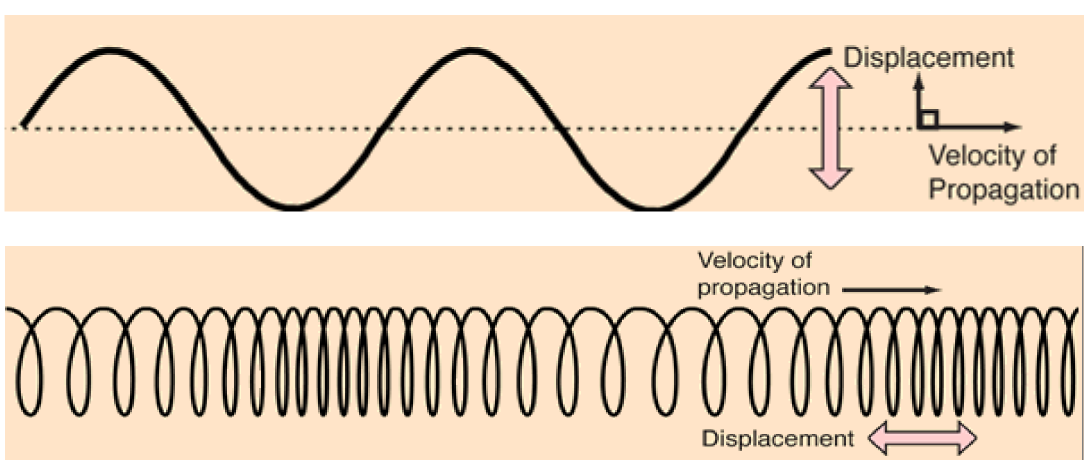

Figure 2.1: Transverse and longitudinal waves.
(http://www.electrical-knowhow.com/2012/01/fundamentals-of-acoustics-and-audio.html)

In this research, the main focus is on the plane acoustic wave and the application of the plane wave acoustic theory to pressure wave propagation in flow ducts, which include area changes and other discontinuities. There are many industrial applications that experience plane sound wave propagation such as noise emission in living and working environments, sound signals transmission for testing and communication and the most relevant application to this research which is the wave propagation from a specific source in a flow duct.

2.1.1 Limitations of the Plane Wave Acoustic Theory in Flow Ducts

Plane wave properties allow useful simplifications of the governing equations and better explanation of the physical factors influence on the wave propagation. Moreover, because the acoustic pressure and particle velocity distributions in the plane wave are uniform over any cross-section of the duct, they can be defined by measurements on the surface of the flow ducts without disturbing the fluid flow. In order to consider the sound wave in a duct as plane wave propagation, some conditions must be satisfied.

An acoustic wave in a duct is considered a plane wave if its wavelength λ exceeds the major dimension of the duct cross-section. For circular cross-sectional ducts with diameter D and no flow, the first transverse acoustic mode with wave number k ($k = 2\pi / \lambda$) occurs once the value of the Helmholtz number (k. D/2) exceeds 1.84. The second such mode will propagate when (k.D/2) exceeds a value just over 3, and for propagation of the first circular mode, the value must exceed 3.8 as shown in figure 2.2. According to Munjal (1987) and Davies (1988), the mean flow at a Mach number M reduces the limiting values of Helmholtz number approximately by the factor of ($1- M^2$). Therefore, the limiting value of the Helmholtz number for a plane wave is 1.84, or a little less, which covers many flow duct noise problems.

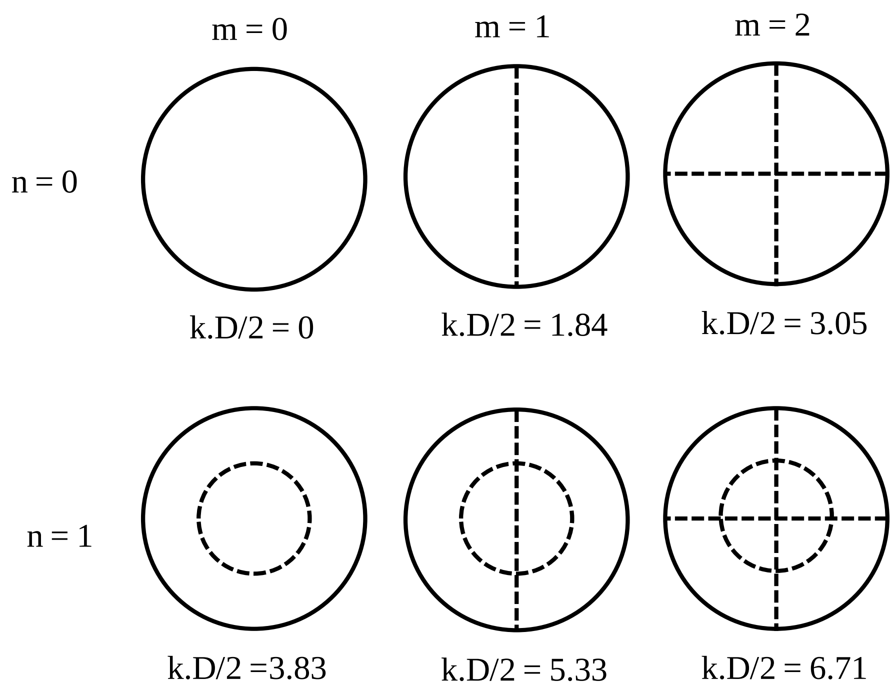

Figure 2.2: Nodal lines for transverse modes in circular pipe. m is the diametral nodal lines and n is the nodal circles; m = 0 and n = 0 is the plane wave mode.

The second limitation of considering the duct acoustic wave as a plane wave is the amplitude of the pressure fluctuations. According to Davies (1987), as long as this amplitude is very small the plane wave acoustic theory is applicable. These pressure fluctuation amplitudes range from 0.01 to 0.001 bar, and the upper limit decreases as the frequency increases (Davies, 1987).

Another limitation of applying the plane acoustic wave theory to flow ducts is the duct wall stiffness. As long as the duct walls are acoustically hard, not absorbent, this facilitates a rapid decay of any excited transverse (or cross) mode inside the pipe. In other words, the higher modes will be trapped at their excitation locations.

2.1.2 Propagation of Plane Waves in Ducts

The propagation of the plane sound wave in a pipe section between some discontinuities usually takes the form of standing waves along the duct. Such standing waves are formed as a result of interference between the forward wave traveling from the sound source and the backward reflected wave from each discontinuity. Therefore, it is realistic to present the standing wave as well as the acoustic parameters at any instant t and any point x as follows:

$$\mathbf{p}(x,t) = \mathbf{p}^{+}(x,t) + \mathbf{p}^{-}(x,t) \qquad (2.1)$$

where $\mathbf{p}(x,t)$ is the acoustic pressure at any location x and time instant t, and $\mathbf{p}^{+}(x,t)$ and $\mathbf{p}^{-}(x,t)$ are the complex amplitude of the incident and reflected waves respectively. Although $\mathbf{p}(x, t)$ is a standing wave, its magnitude $\mathbf{p}(x)$ varies consistently with the location along the pipe length, the magnitudes of the incident and reflected waves $\mathbf{p}^{+}(x)$ and $\mathbf{p}^{-}(x)$ remain constant between interruptions, whereas the relative phase of each wave varies in an orderly manner.

Along a straight uniform duct section, the plane acoustic wave takes, theoretically, the form of isentropic elastic compressions and rarefactions with associated pressure, $\mathbf{p}(x,t)$, and density, $\boldsymbol{\rho}(x,t)$, fluctuations and corresponding fluctuating fluid particle velocity, $\boldsymbol{\upsilon}(x,t)$. All these isentropic disturbances travel through the fluid at the wave propagation speed C_o relative to the fluid, given by

$$C_o^2 = (p/\rho)_s = \gamma RT_o \qquad (2.2)$$

where **s**(x,t) is the fluctuating component of the entropy, T_o is the mean ambient temperature, γ is the specific heat ratio, and R is the molecular gas constant. For the case of a moving fluid with mean velocity U , the wave propagating with the flow direction has a propagating speed (C_o + U) or C_o(1+M), while the wave propagated against the flow direction has the speed of C_o(1-M), where M is the Mach number, U/C_o .

In reality, the propagation of waves includes some losses which are produced from the viscothermal processes at the walls due to friction and heat transfer, and their local effects are confined to this region. The viscothermal losses cause an exponential decay of wave amplitude as the wave propagates along the straight duct section. Other sources of losses are the viscous dissipation and heat conduction in the free shear layers that develop due to the turbulent mixing region downstream of any discontinuity. With these losses, the isentropic condition can no longer be valid.

In the following sections, the plane wave propagation governing equations are solved for the simplest case which assumes an absence of flow and isentropic conditions, then the effects of flow and losses are discussed.

2.1.2.1 Isentropic Propagation of Plane Waves in Ducts without Flow

In the case of no flow (U = 0) and no variation of the mean pressure (p_o), the conservation equations will depend on the fluctuating components such as the fluctuating pressure **p**(x, t) and the fluctuating particle velocity $\boldsymbol{\upsilon}$(x, t) associated with compressions and rarefactions generated by the wave propagation. These equations are the conservation of mass for isentropic conditions and Newton's second law of motion (Euler equation). These equations are expressed respectively as follows:

$$\rho_o \frac{\partial \upsilon}{\partial x} = -\frac{\partial \rho}{\partial t} = -\frac{1}{C_o^2}\frac{\partial p}{\partial t} \tag{2.3}$$

$$\rho_o \frac{\partial \upsilon}{\partial t} = -\frac{\partial p}{\partial x} \tag{2.4}$$

by differentiating equation (2.3) with respect to time and equation (2.4) with respect to x, the difference between the two resulting equations eliminates the acoustic velocity variable and produces the one-dimensional wave equation describing the propagation of the acoustic pressure by plane waves as follows:

$$\frac{\partial^2 p}{\partial x^2} = \frac{1}{C_o^2}\frac{\partial^2 p}{\partial t^2} \tag{2.5}$$

Similarly, the one-dimensional wave equation of the acoustic particle velocity of plane waves can be expressed as:

$$\frac{\partial^2 \upsilon}{\partial x^2} = \frac{1}{C_o^2}\frac{\partial^2 \upsilon}{\partial t^2} \tag{2.6}$$

Normal1y, the resulting acoustic fluctuations in space and time are simple harmonic functions. They also take the form of standing waves as shown in equation 2.1. A suitable representation of the fluctuating pressure in a duct section between discontinuities is:

$$\mathbf{p}_{(x,t)} = \left(p^+ e^{-ik\,x} + p^- e^{ik\,x}\right) e^{i\omega t} \tag{2.7}$$

The terms p^+ and p^- are the constant amplitudes of the incident and reflected waves between the sound source and a discontinuity. $e^{ik\,x}$ is the complex representation of the simple harmonic motion with respect to location x and $e^{i\omega t}$ is the complex representation of the simple harmonic motion with respect to time t. The variable ω is the angular velocity ω = 2πf, where f is wave frequency in Hz, k is the wave number ($k = \omega / C_o = 2\pi / \lambda$), λ is the wavelength, and i is the square root of -1.

Similarly, the acoustic particle velocity distribution in the case of no flow with isentropic condition can be expressed by:

$$\boldsymbol{\upsilon}_{(x,t)} = \frac{1}{Y_o}\left(p^+ \, e^{-ik\,x} - p^- \, e^{ik\,x}\right) e^{i\omega t} \qquad (2.8)$$

Where Y_o is the ideal specific acoustic impedance ($Y_o = \rho_o C_o$).

1.2.2.2 Effect of Flow and Viscothermal Attenuation on the Propagation of Plane Waves in Uniform Duct Section

The propagation speed of the plane acoustic wave is affected by the mean flow speed as mentioned before, so the wave propagating with the flow direction will have a propagating speed (C_o + U) or C_o(1+M) while the wave propagating against the flow direction will have a speed C_o(1-M). Therefore, the wave number will be different for the case of forward wave, k_f, than the reflected wave, k_r, as follow:

$$k_f = \omega / (C_o + U) = k / (1+ M)$$

$$k_r = \omega / (C_o - U) = k / (1 - M)$$

Thus, equation 2.7 is modified according to the effect of the flow as follows:

$$\mathbf{p}_{(x,t)} = \left(p^+ \, e^{-\frac{ik\,x}{(1+M)}} + p^- \, e^{\frac{ik\,x}{(1-M)}}\right) e^{i\omega t} \qquad (2.9)$$

According to Munjal (1987), and Davies (1981), the viscothermal losses at the pipe walls affecting the wave number k will be replaced by a complex wave number **β** as follows:

$$\boldsymbol{\beta} = \omega / C_o + \alpha\,(1- i) \approx k - i\,\alpha \qquad (2.10)$$

where α is the total aeroacoustic attenuation in a moving medium, which is the sum of the contributions from the viscothermal attenuation coefficient α_o and the turbulent flow friction ζM. The value of α for plane wave propagation in a circular pipe of diameter D can be expressed as:

$$\alpha = \alpha_o + \zeta\, M$$

where ζ = F / 2 D , F is Froude's friction factor and

$$\alpha_o = \frac{2}{DC_o}\sqrt{\frac{\mu\omega}{2\rho_o}}\left(1+\left(\sqrt{\gamma}-\frac{1}{\sqrt{\gamma}}\right)\sqrt{\frac{1}{P_r}}\right) \qquad (2.11)$$

where μ is the local dynamic viscosity and P_r is the Prandtl number for the gas in the pipe (Davies et al., 1980).

By combining both the effects of flow and viscothermal attenuation losses, the acoustic pressure and the acoustic particle velocity can be expressed by

$$\mathbf{p}_{(x,t)} = \left(p^{+}\, e^{-\frac{i\boldsymbol{\beta}\, x}{(1+M)}} + p^{-}\, e^{\frac{i\boldsymbol{\beta}\, x}{(1-M)}}\right) e^{i\omega t} = (\mathbf{p}_{\mathbf{x}}^{+} + \mathbf{p}_{\mathbf{x}}^{-})\, e^{i\omega t} \qquad (2.12)$$

$$\boldsymbol{\upsilon}_{(x,t)} = \frac{1}{Y}\left(p^{+}\, e^{-\frac{i\boldsymbol{\beta}\, x}{(1+M)}} - p^{-}\, e^{\frac{i\boldsymbol{\beta}\, x}{(1-M)}}\right) e^{i\omega t} \qquad (2.13)$$

Where **Y** is the characteristic impedance that is equal to

$$\mathbf{Y} = \rho_o C_o \left(1 - \frac{\alpha}{k} + i\frac{\alpha}{k}\right) \tag{2.14}$$

$\mathbf{p}_\mathbf{x}^+$ and $\mathbf{p}_\mathbf{x}^-$ can be experimentally measured using two dynamic pressure sensors (microphones) that are flush mounted on the duct wall inner surface with a separated known distance. This technique is called the 2-microphones method which was originally introduced by Davies et al. (1980).

One of the basic characteristics of the standing wave is the reflection coefficient $\mathbf{R}_x$, that is defined as the ratio between the complex amplitude of the reflected wave to the complex amplitude of the incident wave. Thus, $\mathbf{R}_x$ is normally a complex quantity. An infinitely hard reflecting surface is considered an exception case for which the reflection coefficient is unity.

$$\mathbf{R}_X = \frac{\mathbf{p}_X^-}{\mathbf{p}_X^+} = |R|\, e^{-i\theta} \tag{2.15}$$

The acoustic impedance $\mathbf{Z}_x$ is an alternative description of the wave reflection and it is one of the main properties in acoustic waves. The acoustic impedance is defined as the ratio of fluctuating pressure to particle velocity at the same location, x. It can be expressed by dividing equation 2.12 by equation 2.13 as follow:

$$\mathbf{Z}_X = \frac{\mathbf{p}_X}{\boldsymbol{\upsilon}_X} = \mathbf{Y}\,\frac{(\mathbf{p}_X^+ + \mathbf{p}_X^-)}{(\mathbf{p}_X^+ - \mathbf{p}_X^-)} = \mathbf{Y}\,\frac{(1+\mathbf{R}_X)}{(1-\mathbf{R}_X)} \tag{2.16}$$

The pressure reflection coefficient for several types of pipe terminations and discontinuities has been extensively studied both theoretically and experimentally. For more details, see the work by Davies (1988), Munjal (1987), and Munjal and Doige (1990).

In summary, the main characteristics of acoustic plane wave propagation in ducts were discussed including the limitation of the application of the linear plane wave acoustic theory; the wave equation and its solution; and the effects of flow and viscothermal and turbulent friction losses on the acoustic wave propagation. The questions remain as to how the acoustic wave is generated by the flow and how it is coupled with the flow field to sustain the acoustic resonance. To address these issues, the basic phenomenon governing the flow over a cavity is discussed in the next section.

2.2 Instability of Free Shear Layer Flows

Flow is considered unstable if it has the ability to magnify small disturbances into large disturbances. Conversely, the stable flow is one that resists the amplification of small disturbances whether these disturbances are self-induced or externally imposed. Flow instability is a common phenomenon in many flow applications; such as flow of unstable free shear layers over cavities and side-branches; likewise, jet flows and flows in orifices and valves are considered examples of unstable flows. The common flow feature exhibited by the above examples of unstable flows is the mixing between flow streams that have different flow velocities. For example, in pipe flow over a cavity, there are two flow regions; one is the almost stagnant fluid inside the cavity and the other is the main pipe flow stream that flows with the mean velocity in the pipe, where a mixing layer region forms at the cavity mouth as shown in figure 2.3. The velocity profile in the mixing region usually includes an inflection point that is considered a sufficient condition of instability.

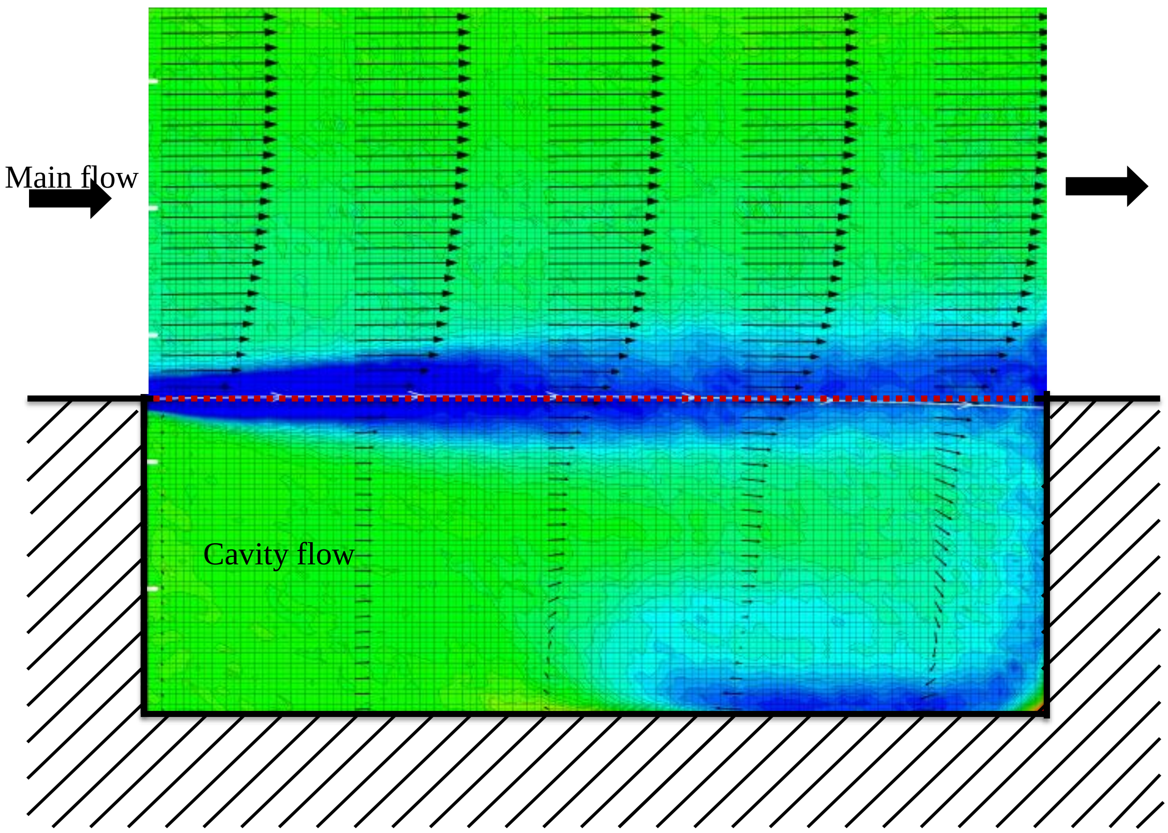

Figure 2.3: The free mixing layer at the cavity mouth (PIV measurements)

A shear layer in a flow is a region where there is a velocity gradient perpendicular to the streamlines. The shear layer is characterized by its velocity profile. Rayleigh's inflection point theorem (1880), on the stability of velocity profiles, states that "the existence of a point of inflection is a sufficient and necessary condition for the shear layer to become unstable". Thus, if there is a point of inflection in the velocity profile, there must be some form of disturbance which will be amplified in this shear layer. But the inviscid theory by Rayleigh did not mention the reason for the instability of some flows without the presence of an inflection point (e.g. the instability in straight pipe flow that causes the transition from laminar to turbulent flow without any inflection point in the velocity profile). The viscous theory however shows that there is a critical Reynolds number below which all disturbances are stable, and above which some disturbances are unstable (Schlichting, 2000).

In the following sections, the hydrodynamic stability theory of shear flows will be discussed. This theory examines the flow instability in the presence of small perturbations and shows the main features of the unstable flows such as the amplification rates of the small disturbance. In addition to the stability theory, the different feedback mechanisms that magnify or dampen the oscillations of the unstable free shear layer flows are discussed. Feedback disturbances such as pressure fluctuations due to flow impingement, fluid particle fluctuations due to the presence of sound wave and fluid fluctuations due to vibrations in the system structure will be illustrated.

2.2.1 Hydrodynamic Stability Theory of Shear Flows

Hydrodynamic Stability Theory was developed by Lord Rayleigh (1880). He used the perturbation form of the Navier-Stokes equation (NSE) to examine the flow instability by calculating the amplification factor (whether temporal or spatial). The amplification factor determines the rate at which an infinitesimal disturbance in the shear layer will amplify or decay, once it introduced, (with time or space). The theory considers that the decay of the small disturbances is the necessary condition for stability. Thus, it aimed to determine the flow response to small disturbances, which is representative of the initial phase of instability. Since a linearized form of the perturbed NSE was used, the theory was called the linear stability theory. Other simplifications that used in the linear stability theory are the assumption of two-dimensional flow, and neglecting the viscous effects for high Reynolds number flows. Later studies showed that the critical Reynolds number for unstable flow is lower and the amplification rate is larger for 2-D flows than those for 3-D flows. Thus, the 2-D analysis is conservative for 3-D flows (Kim and Choi, 2005). Further, because of neglecting the viscous effects at high Reynolds number flows, the stability theory is sometimes called the inviscid linear stability theory.

The important results of the linear stability theory are the prediction of the frequency range at which the flow is unstable and the most unstable frequency of the disturbance (i.e. the frequency which has the largest amplification factor). The theory identifies the amplification factor, the phase speed and the wave number as functions of the disturbance frequency. Lucas et al. (1997) summarized some applications of the inviscid stability theory to analyze flows with different velocity profiles. Such profiles as discontinuous profile, piecewise linear profile, hyperbolic-tangent velocity profile, planner jet mixing layer profile, axisymmetric jet and wake velocity profiles were presented. The analysis of the hyperbolic-tangent velocity profiles that is produced by two parallel streams of unequal velocities will be presented in this section since it is similar to flow over a cavity. Michalke (1964, 1965) determined numerically the stability characteristics of both temporal and spatial waves for hyperbolic-tangent velocity profiles of velocity factor Δ =1, that means a stream has zero velocity. In 1982, Monewitz and Huerre completed the analysis for different ratios of the velocity factor from 0 to 1. Where

$$\Delta = \frac{U_1 - U_2}{U_1 + U_2}; \qquad U(y, \Delta) = 1 + \Delta \tanh(y/2) \qquad (2.17)$$

Figure 2.4 by Lucas et al. (1997) shows a thin mixing shear layer that is produced by two parallel streams of unequal velocities U_1 and U_2 resulting in hyperbolic-tangent velocity profiles. As shown in the figure, the initial shear layer fundamental disturbance is spatially amplified in x-direction by an exponential amplification rate $e^{-\alpha i}$. This spatial amplification rate, $-\alpha_i$, is shown as a straight line on a semi-log coordinate graph between the amplitude of the fundamental mode disturbance verses the x-axis (bottom of figure 2.4). As the disturbance continues to amplify in the streamwise direction, the amplitude increases until there is a departure from the linear growth region to non-linear growth and transition to turbulent flow. The inviscid linear stability theory identifies the growth rate of the initial disturbances in the linear growth region either in space or time at different disturbance dimensionless frequencies χ. Figure 2.5 (Monewitz & Huerre, 1982) highlights that there is a specified dimensionless frequency χ_1 at which the disturbance growth rate is maximum. This frequency is called the fundamental frequency. Also, the figure shows that there is a frequency band for unstable initial disturbances (χ = 0 to 0.5).

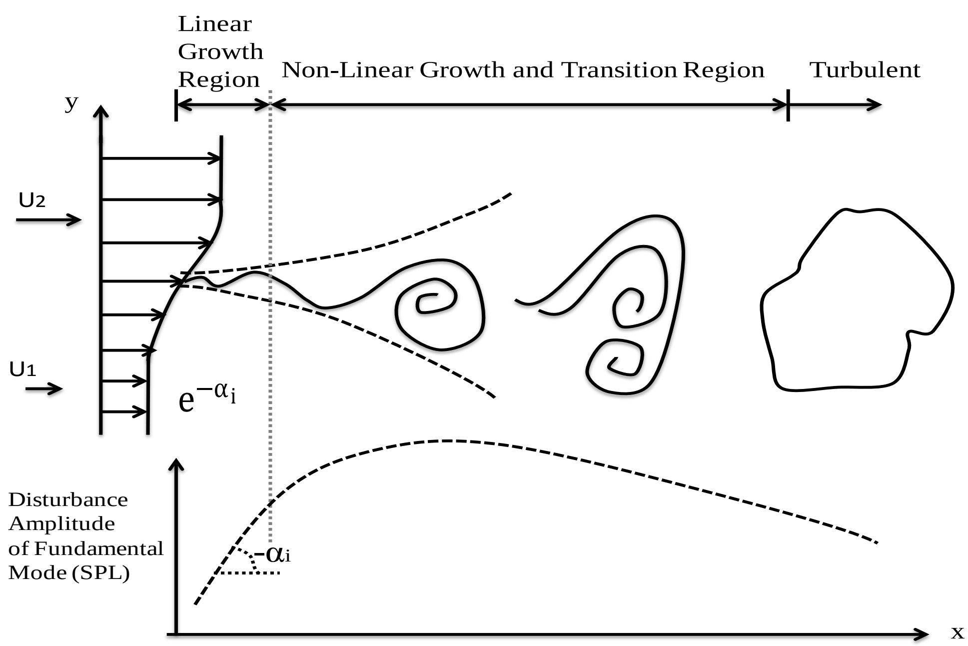

Figure 2.4: Features of disturbance growth in a thin mixing shear layer. (Lucas et al., 1997).

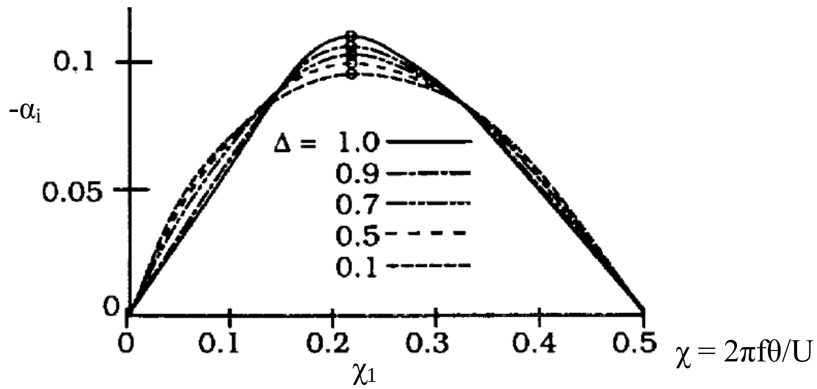

Figure 2.5: Disturbance growth rate ($-\alpha_i$) in a thin mixing shear layer with a hyperbolic tangent velocity profile at different velocity factors Δ with the disturbance dimensionless frequency $\chi = 2\pi f\theta/U$, where θ is the momentum thickness and f is the periodic disturbance frequency. Application of the invicid linear stability theory by Monewitz and Huerre (1982).

The experiments done by Freymuth (1966) on axisymmetric jets showed that the results of the linear stability theory were in good agreement with the experimental results in the initial region of transition, where the disturbances still have small amplitudes. Figure 2.6 shows good agreement between the experimental and the theoretical results of the spatial growth rate for St < 0.012, where St is the Strouhal number based on the momentum thickness of the boundary layer at the nozzle edge and the jet velocity ($St = f\theta_m/U$). For higher Strouhal numbers, the agreement with the disturbance temporal growth rate is better. The nonlinear growth of a mixing layer was studied by Miksad (1972). He found that the nonlinear effects become important when the ratio of the amplitude of the disturbance fluctuation velocity to the mean flow velocity reaches 3.5%.

From the above discussion of the characteristics of the free shear layers stability, it is clear that these characteristics support disturbances amplification and propagation in the flow for a wide frequency range. The next section will demonstrate the behaviour of the unstable free shear layers when it is subjected to a forced perturbation at specified conditions which is provided by a feedback disturbance. Possible feedback disturbances are: pressure fluctuations that are produced from an impinging flow; fluid particle fluctuations that are generated by the associated sound field; and fluid fluctuations that are caused by vibrations of the system structure.

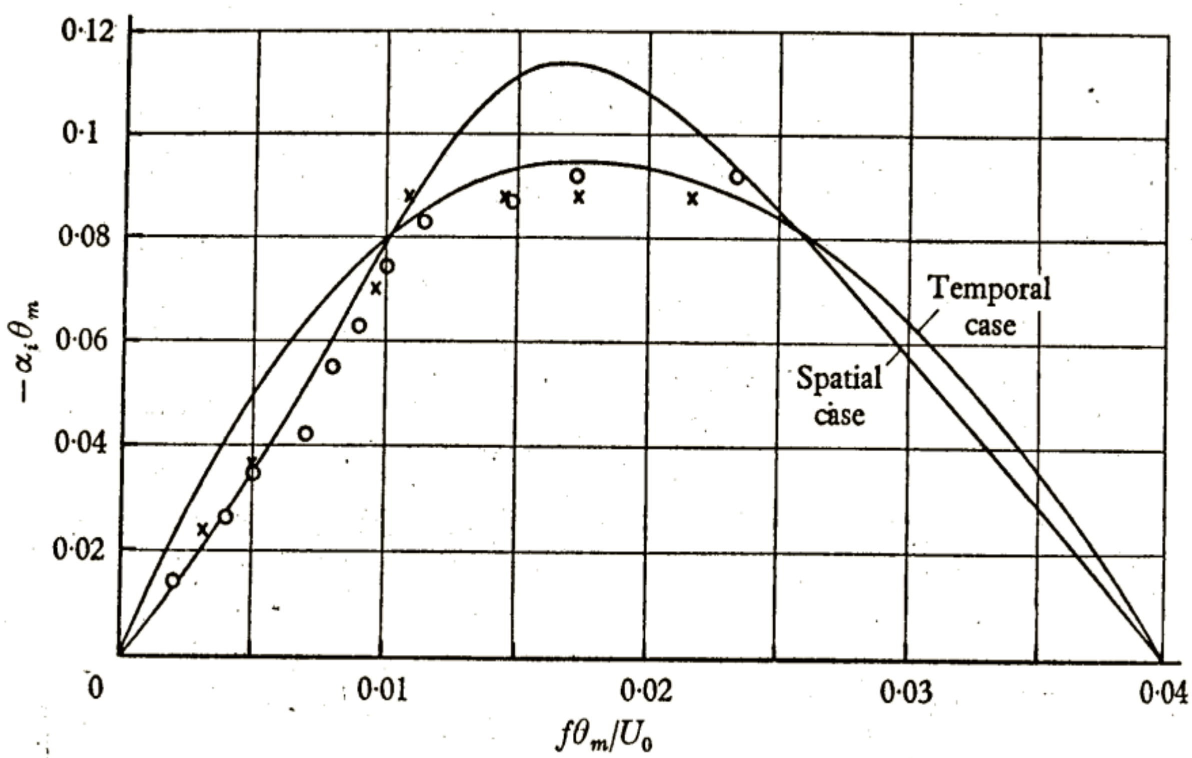

Figure 2.6: The variation of the growth rate ($-\alpha_i$) with Strouhal number (St = $f\theta_m/U_o$). o, axisymmetric nozzle; x, plane nozzle. θ_m is the momentum thickness (Freymuth, 1966).

2.2.2 Forced Perturbation of Free Shear Layers and Feedback Mechanisms

Forced external excitation of free shear layers was used in the literature to understand the shear layer response to specific disturbances and the effect of the self-generated feedback disturbances on the generation of self-sustaining oscillations. Blevins (1985) noticed that the excitation of the free shear layer at a single frequency restrains the broadband fluctuations and leads to a very structured train of vortical structures. One of the mechanisms which generates upstream perturbations that control the shear layer oscillations is the impingement on an object such as a wedge, a surface, etc. Rockwell and Naudascher (1979), Rockwell and Knisely (1979), and Ziada and Rockwell (1982) experimentally investigated the effect of impingement on the velocity fluctuations along impinging mixing layers as shown in figures 2.7 and 2.8. The comparison between shear flow oscillations in both impinging and non-impinging conditions shows the ability of the impinging free shear layer to sustain a noticeable level of organized oscillations as well as the suppression of the broadband velocity fluctuations. The effect of the geometrical and hydrodynamic parameters on these kinds of flows had been investigated in many previous works. A brief review of the general characteristics of impinging shear flows is presented here.

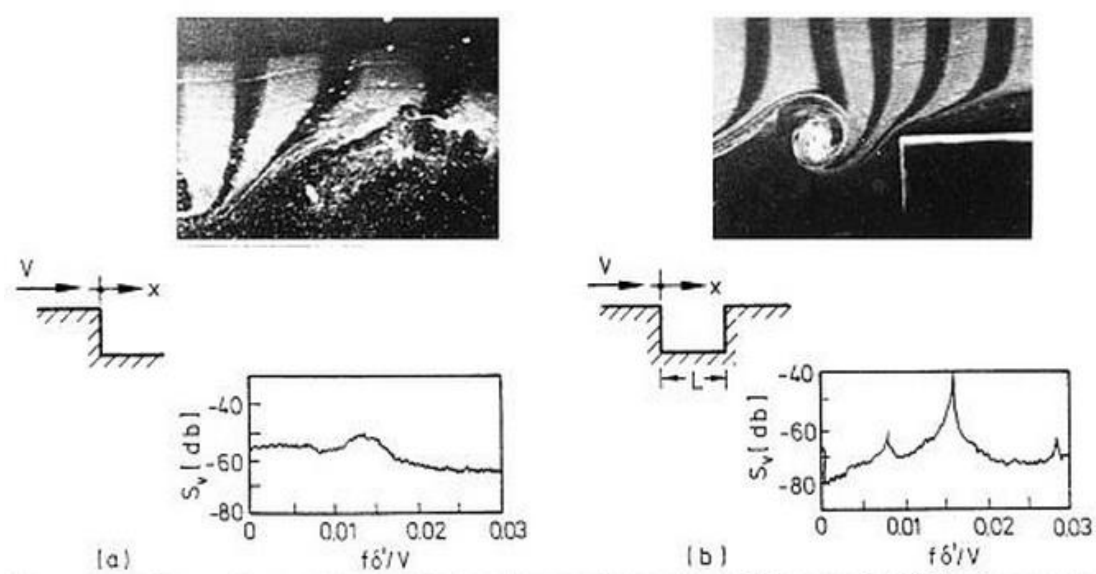

Figure 2.7: Effect of impingement on the flow field and velocity fluctuations (Rockwell & Knisely, 1979).

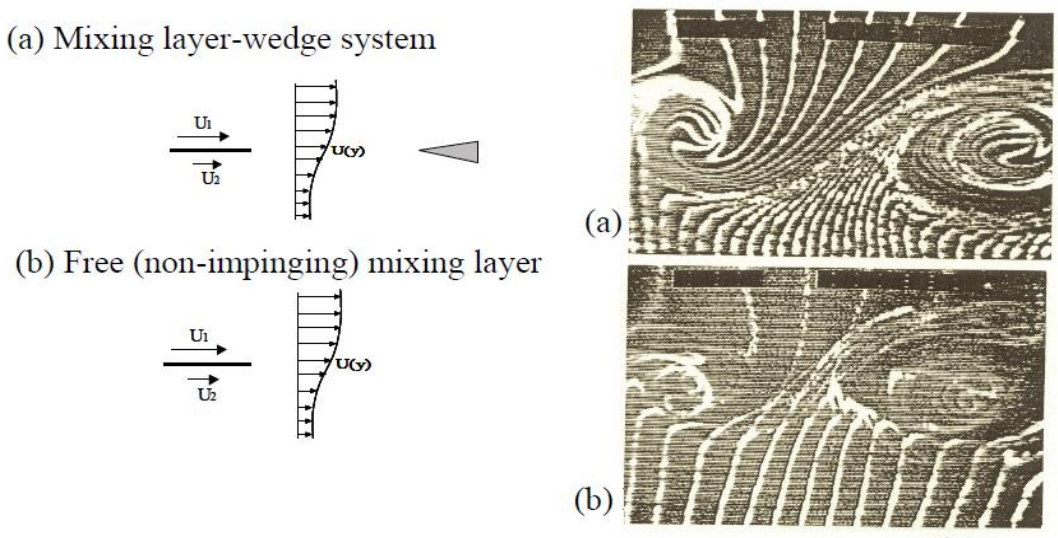

Figure 2.8: Effect of impingement on the flow field along the mixing layer in a mixing layer-wedge system. (Ziada and Rockwell, 1982)

Rockwell (1983) investigated the ability of an impinging free shear flow system to generate a self-sustained oscillation. He formulated a number of events that have to occur to sustain the oscillations as shown in figure 2.9. First, the flow impingement on the downstream edge generates a pressure pulse that travels upstream. Then, this pressure pulse provides an upstream feedback that perturbs the free shear layer at the separation upstream edge, causing it to oscillate. Finally, the initial perturbation grows and forms a new vortex, while the free shear layer progresses downstream. The self-excitation mechanism which generates and sustains the shear layer oscillations according to the above events is referred to as the Fluid Dynamic Oscillations Mechanism by Rockwell and Naudascher (1978). The self-sustained oscillation frequency depends on the length and the velocity scales of the impinging free shear layer. In this case, the length scale is usually considered to be the distance between the separation and the impingement edges, and the convection velocity of the disturbance is considered as the velocity scale.

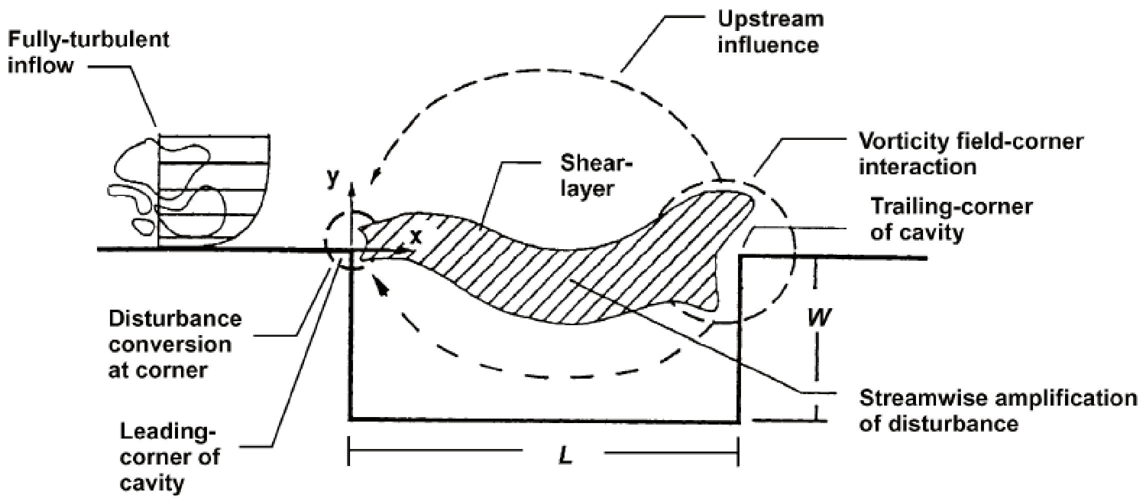

Figure 2.9: General features of a self-sustained oscillation in a cavity "Fluid dynamic mechanism" (Rockwell et al., 2003)

Rockwell and Naudascher (1978) classified the excitation mechanism of the cavity oscillations into three categories according to the source of the feedback mechanism that triggers the self-sustained oscillation as follows. First, in the ***fluid-dynamic oscillation*** mechanism, the interaction between the free-shear layer and the downstream cavity edge (impinging) generates the upstream feedback perturbation in the form of pressure fluctuations propagating upstream (Sarohia, 1977; Tam & Block, 1978). The second oscillation mechanism is the ***fluid-elastic oscillation*** in which the feedback perturbations are generated by the vibration of the cavity flexible structure if it is large enough to control the excitation mechanism (Ziada & Bühlmann, 1991; Ziada, 2002). These vibrations are produced from the flow-structure interaction with low stiffness structure walls. This mechanism may occur only if the cavity structural resonance frequency is close to the most amplified frequencies of the free-shear layer. When the feedback perturbations to the free shear layer oscillation are produced by a resonant acoustic field, the oscillation mechanism is called the ***fluid-resonant oscillation.*** This mechanism produces strong highly coherent oscillations (Ziada, 1994; Ziada, 1995; Ziada, 2001).

Naudascher and Rockwell (1994) summarized the free jet flow oscillations according to the three different categories of oscillation mechanisms as shown in figure 2.10. In the case of a solid impinging edge and unconfined jet flow, the mechanism of oscillation is the fluid-dynamic mechanism as shown in case (a). However, the flexible impinging edge leads to a fluid-elastic oscillation mechanism as shown in case (b), but the confined jet flow with impingement leads to the generation of an acoustic field and oscillations according to the case of fluid-resonant mechanism.

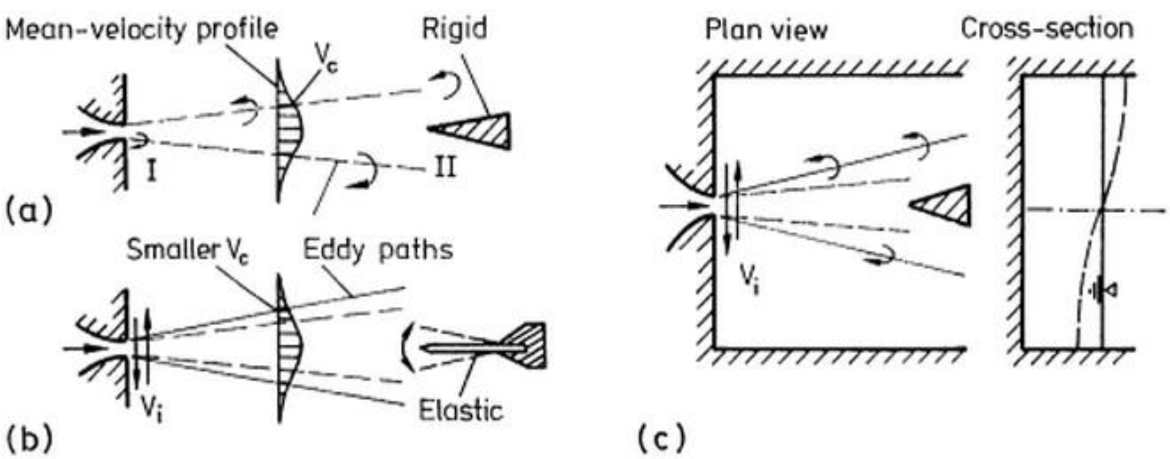

Figure 2.10: Jet flow oscillation mechanisms; a) Fluid-dynamic, b) Fluid-elastic, and c) Fluid-resonant. (Naudascher & Rockwell, 1994)

As the upstream feedback is considered the most important event of the excitation mechanism, Ziada (1995) developed an active control technique to eliminate this feedback in order to break the cycle of events of the excitation mechanism and thereby suppresses the self-sustained oscillations. Figure 2.11 presents the basic idea of the active control block diagram and an application example of controlling an impinging jet flow oscillation (Ziada, 1995). Oscillation control can be achieved according to the following events. First, the jet oscillations is sensed by a transducer such as a microphone. Second, the signal from the sensed oscillations must be phase shifted and amplified optimally before it is sent to loudspeakers which are focused on the jet exit only. as shown in figure 2.11.

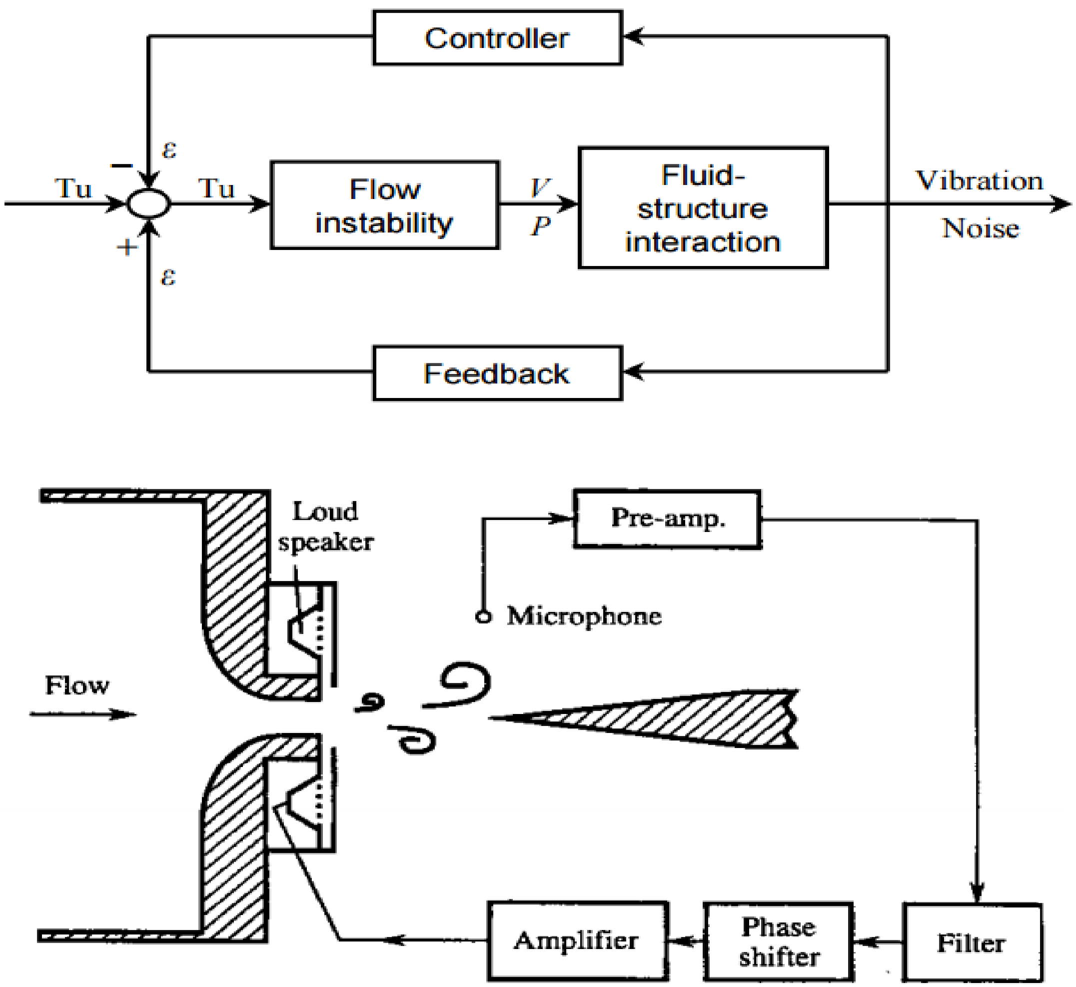

Figure 2.11: Flow diagram of the active control circuit of impinging jet flow oscillations (Ziada, 1995)

In this present research, the fluid-resonant cavity oscillation type is the main focus of investigation. From the literature, the acoustic resonance of the cavity volume has been reported for deep cavities (Ziada, 1994; Ziada & Shine, 1999; Graf & Ziada, 2010), and also for shallow cavities subjected to high flow velocities (Aly, 2008). At low Mach number, the coupling between the shallow cavity oscillations and the longitudinal resonance modes of the attached pipes was investigated by many researchers in the literature (Huang & Weaver, 1994; Davies, 1981; Rockwell & Schachenmann, 1982 and 1983; Rockwell et al., 2003; Geveci et al., 2003). Other researchers (such as Keller & Escudier, 1983; Ziada et al., 2003; Aly & Ziada, 2010 and 2012) focused on the shear layer interaction with the transverse acoustic modes which propagate normal to the flow direction. These investigations illustrated the importance of the local interaction patterns between the flow and the acoustic fields. These various interaction patterns are reviewed in the next section.

2.3. Flow-Sound Interaction Patterns

The nature of the flow-sound interaction mechanism and the resulting aeroacoustic sound sources depend very strongly on the local details of the sound and vorticity fields. These details include the local magnitude and direction of the flow velocity and vorticity and the local amplitude, phase and direction of the acoustic particle velocity. Howe (1975 and 1980) showed that the instantaneous acoustic power P in a non-vanishing vorticity field within a volume V is proportional to the triple product of the vorticity, flow velocity and acoustic particle velocity as follows:

$$P = - \rho_o \int \omega \cdot (U \times \upsilon)\, dV \qquad (2.18)$$

ω is the vorticity vector and ρ_o is the mean fluid density. Figure 2.12 shows a summary of different patterns of flow-sound interaction mechanisms, where υ is the acoustic particle velocity, U is the mean flow velocity and λ is the sound wavelength.

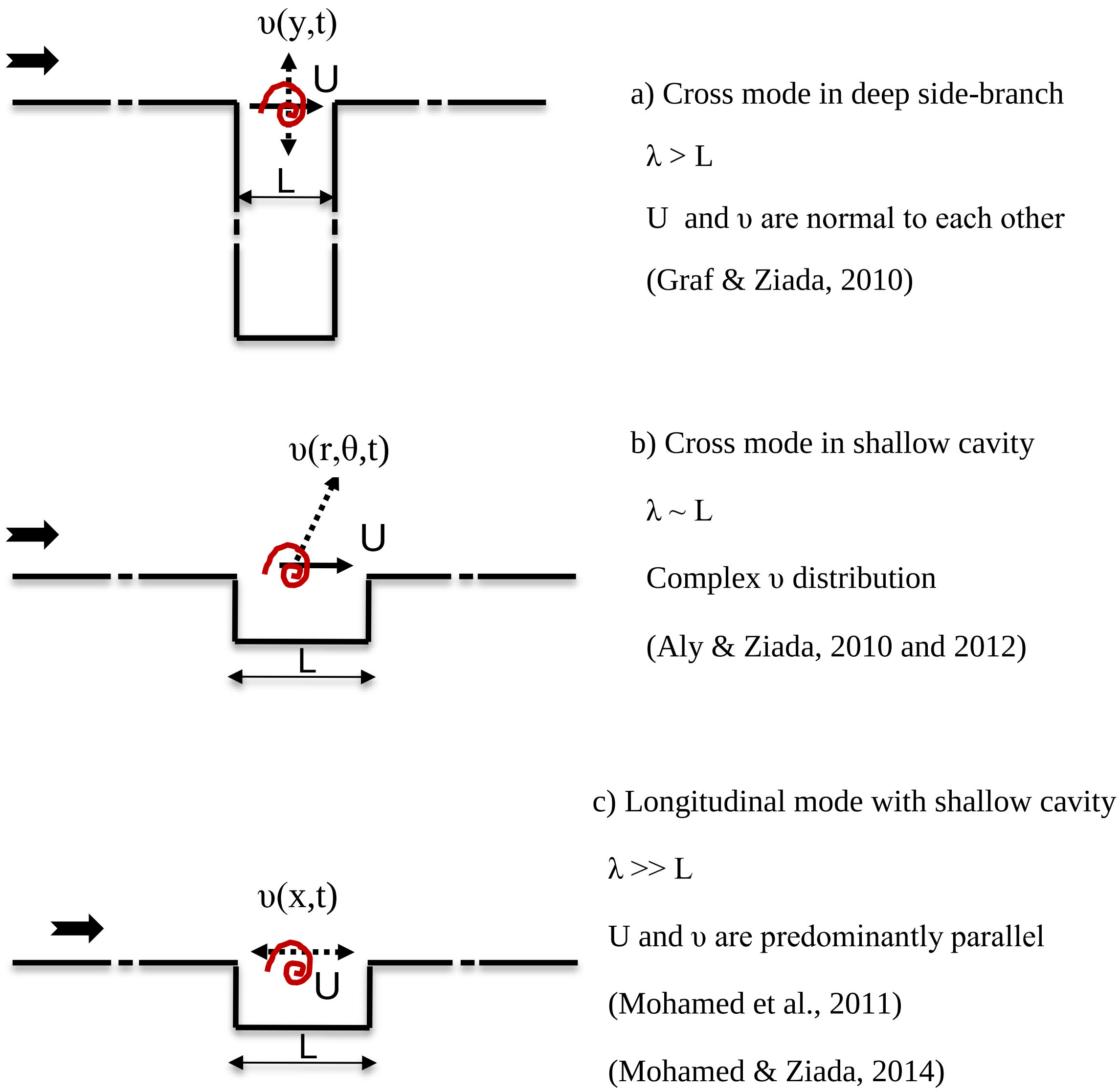

Figure 2.12: Summary of flow-sound interaction patterns

In the case of side-branches, figure 2.12-a, the presence of the deep branches guides the acoustic wave between the branches in y- direction as illustrated in figure 2.13. So, the acoustic particle velocity (υ) is predominantly orthogonal to the vortices convection velocity. This orthogonal case leads to very strong sound generation based on Howe's integrand. The geometry of the deep side-branches is associated with a large sound wavelength, λ, compared with the side-branch width or diameter (L). Graf and Ziada (2010) measured the sound source from circular side-branches with different arrangements. In summary, the side-branches case is characterized by a cross mode acoustic wave, orthogonality between U and υ directions, and large wavelength compared with the branch (or cavity) length scale. This flow situation is associated with the strongest sound generation level.

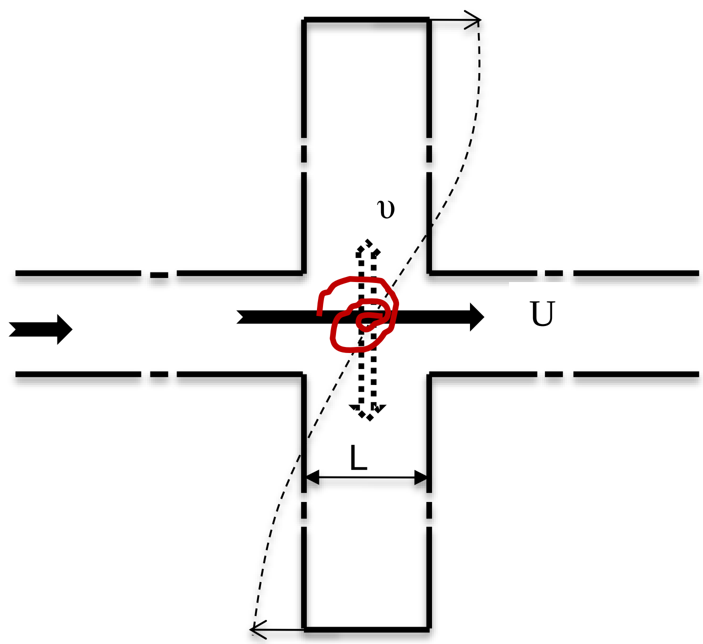

Figure 2.13: Side-branches showing the flow and acoustic parameters of the strongest sound generation mechanism

Figure 2.12-b presents the case of cross-mode excitation for a shallow cavity in a duct. In this case, the sound field is very complex, where the acoustic particle velocity varies in the radial and the azimuthal directions $\upsilon(r,\theta,t)$, as illustrated in figure 2.14. The cross mode acoustic wavelength, λ, is of the same order of magnitude as the cavity length, L. For this case, it is still difficult to measure the acoustic power due to the complexity of the sound and flow fields. Aly and Ziada (2010 and 2012) investigated the self-excitation mechanism of this flow geometry.

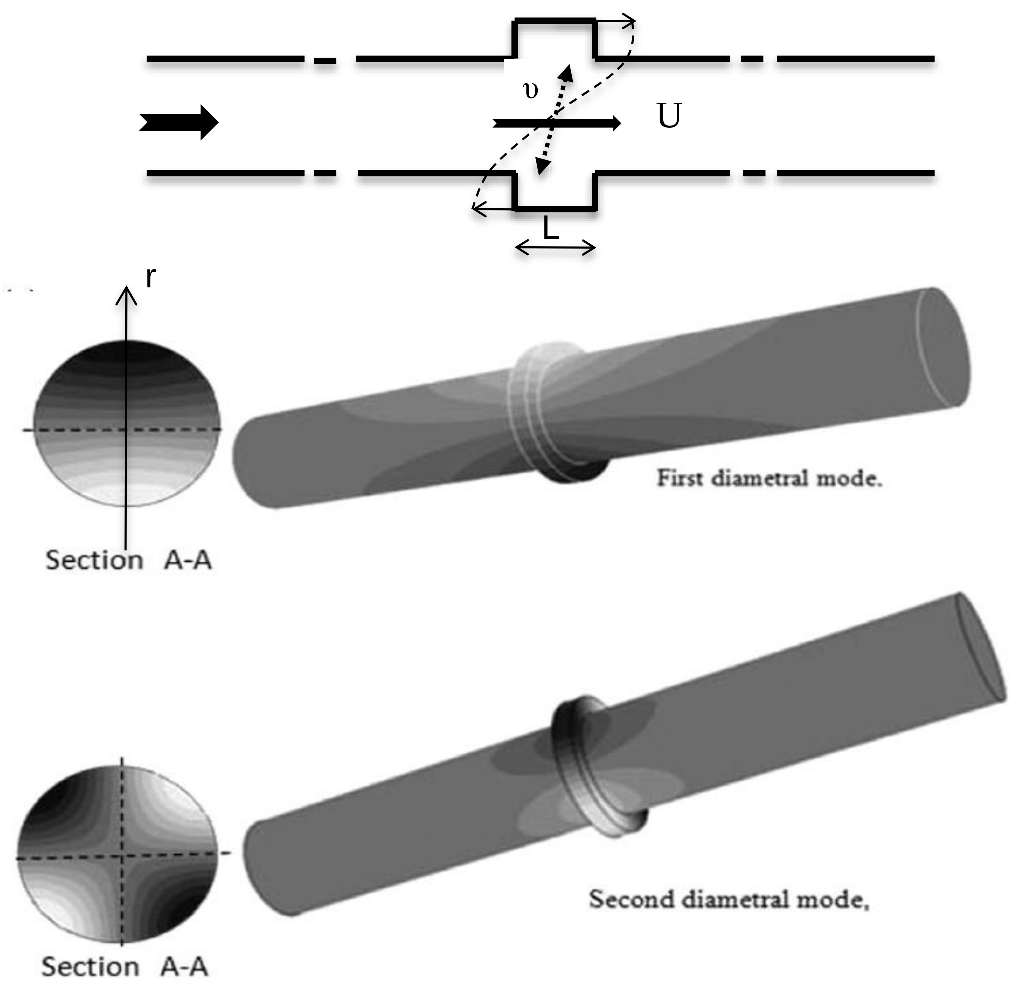

Figure 2.14: Acoustic cross mode of shallow cavity in a duct (Aly & Ziada, 2010)

Figure 2.12-c presents the case of the shallow cavity in a pipe with a longitudinal acoustic mode. In this case, acoustic plane waves propagate in the longitudinal direction, and the wavelength, λ, is very long compared with the cavity length, L. As shown in figure 2.15, the acoustic particle velocity is predominantly parallel to the flow velocity except near the cavity corners. The aeroacoustic source generated by turbulent flow over a shallow cavity in the presence of a longitudinal acoustic wave is the subject of this research.

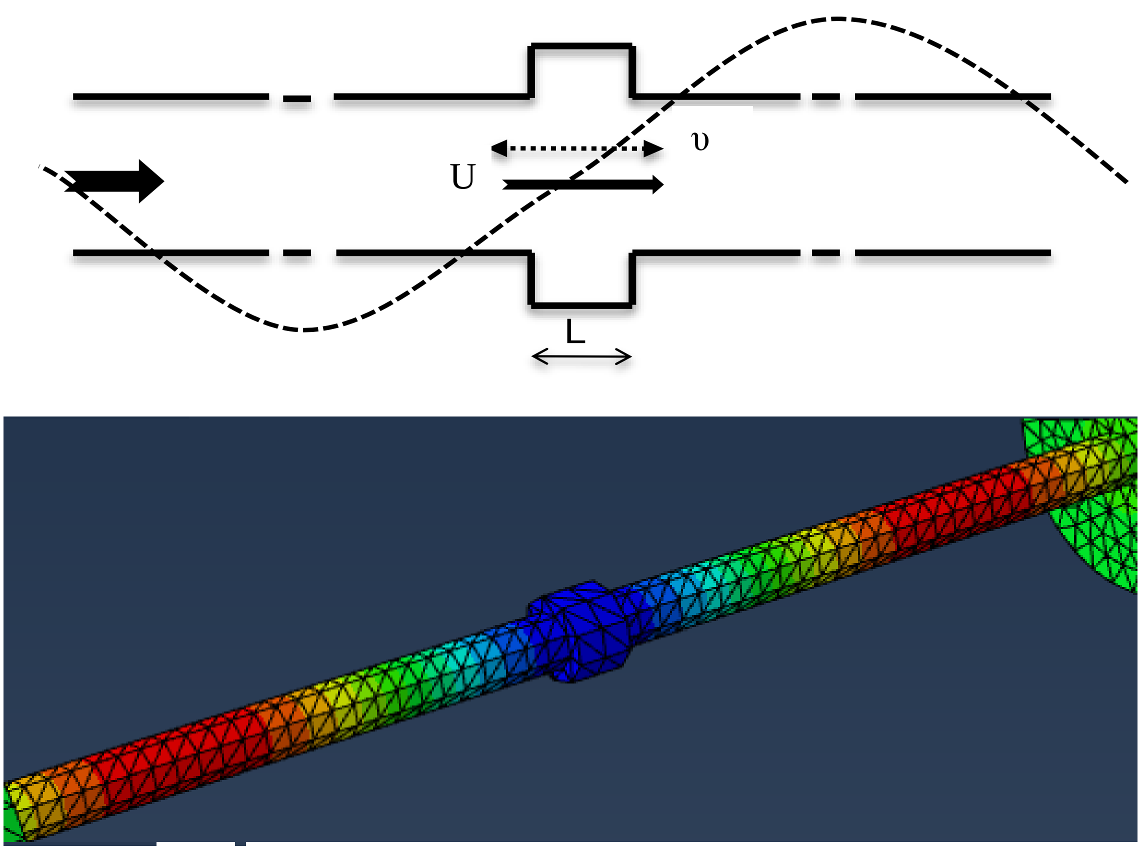

Figure 2.15: Longitudinal acoustic mode of a shallow cavity in a pipe

Design considerations for flow-excited acoustic resonances must include the flow velocity at the onset of resonance (or the Strouhal number at which resonance starts) and the amplitude of resonance (or the aeroacoustic source strength). From the literature, the onset of resonance is well defined for different applications like flow over cavities and side-branches (Geveci et al., 2003; Graf & Ziada, 2010; Hourigan et al., 1990; Martínez et al., 2009; Rockwell et al., 2003; Ziada et al., 2003; Ziada & Shine, 1999). For the amplitude of resonance, or the aeroacoustic power source, the following section presents the concept of aeroacoustic energy generation and a review of the previous attempts to evaluate this energy.

2.4 Aeroacoustic Energy Exchange

Energy exchange between the acoustic field and the flow field at any location along the cavity opening is directly dependent, among other things, on the phase difference between the acoustic particle velocity oscillations and the fluctuations of the free shear layer at this location. In other words, when the disturbance caused by the unstable shear layer and the feedback of the acoustic standing wave at a certain position have a favorable phase difference, energy will be transferred from the flow field to the acoustic field, thus amplifying the resonant sound field and thereby producing an aeroacoustic source (sound generation). On the other hand, when the shear layer disturbance and the acoustic feedback are not phase matched, the opposite occurs (aeroacoustic sink). The summation of the aeroacoustic energy (sources and sinks) over the flow field yields the instantaneous aeroacoustic energy from the flow over the cavity. Moreover, integrating this instantaneous aeroacoustic energy over a complete acoustic cycle yields the time average acoustic energy which is generated by the flow-sound interaction.

The present research will be mainly concerned with measurements of the aeroacoustic power resulting from the coupling between the acoustic field and the flow field in a pipe flow system. Hence, the literature discussing the evaluation of the aeroacoustic power will be further discussed in the following sections.

2.4.1 Experimental Determination of the Aeroacoustic Power

An early attempt of measuring the generated sound power was done by Coltman (1968). He measured the sound resulting from the instability of the free shear layer of air flow over the mouth of a flute. His methodology depended on the balance between the measured sound generation, in the form of source impedance, and the linear acoustic system impedance difference calculated around the flute mouth. In his experimental work, he externally excited the system using a loudspeaker with a harmonic excitation at a specified frequency and amplitude then he evaluated the source impedance as the induced pressure across the mouth of the flute divided by the acoustic volume flux through the mouth.

A different experimental technique using the energy balance between sound production and acoustic dissipation (radiation losses and viscothermal losses) was developed by Bruggeman (1987) and Bruggeman et al. (1991). In this technique, the acoustic source power was determined by measuring the acoustic radiation using the two microphones method and estimating the viscothermal power losses by means of Kirchhoff's theory (1868). The results suggested a linear dependence between the acoustic power and acoustic amplitude υ.

The aeroacoustic source in double side-branch piping systems was experimentally determined by Graf and Ziada (2010). They evaluated the aeroacoustic source resulting from the interaction between the sound and vorticity fields. In their work, a very strong cross-mode sound wave guided by the side-branches was produced. This strong sound generation was caused by the orthogonal orientation between the acoustic particle velocity and the flow velocity. The methodology of Graf and Ziada was developed to measure the source impedance, which is defined as the acoustic pressure difference across the shear layer at the side-branch divided by the acoustic volume velocity at the mouth of the side-branch, is illustrated in figure 2.16. An external excitation by a loudspeaker was used at the branches' resonance frequency. The source impedance from these experiments (**S**) is a function of Strouhal number (St) and the normalized acoustic particle velocity by the flow velocity (υ/U).

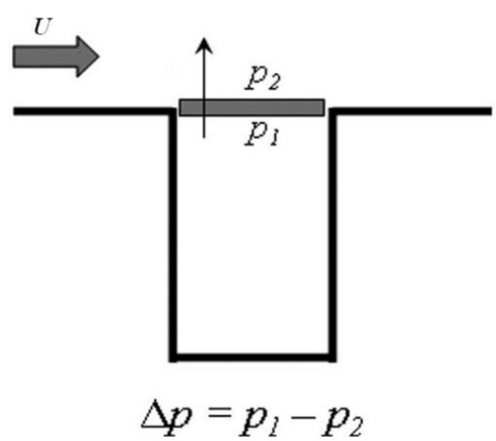

Figure 2.16: The acoustic impedance model at the side-branch opening (Graf & Ziada, 2010)

Graf and Ziada have shown that the measured source is proportional to the square root of the acoustic pulsation amplitude, instead of the linear dependence proposed by Bruggeman (1987). They also evaluated the non-linear saturation behaviour of the shear layer disturbances at high amplitude pulsations.

Another experimental method used by many researchers to evaluate the aeroacoustic source power is Howe's integral, in which the acoustic energy source is modeled using Howe's theory for inviscid, isotropic and rotational flow (Howe, 1975 and 1980). The input data to this integral is experimentally determined using particle image velocimetry, to quantify the flow field structure, and using dynamic pressure sensors (microphones) to construct the acoustic field (such as Finnegan et al., 2009 and 2010; Oshkai & Yan, 2008).

Howe states that the instantaneous acoustic power in a non-vanishing vorticity field is proportional to the triple product of the vorticity, flow velocity and acoustic particle velocity as described by equation 2.18. Durgin and Graf (1992) demonstrated that, as the flow velocity changes, the convection and location of the vortices relative to the phase of the acoustic cycle is the key feature to determine the acoustic power (be it a source or sink). Therefore, acoustic power is generated at certain locations along the cavity span and is absorbed at other locations. Equation (2.18) gives the integral of this power over a specified control volume V, and its integration over a complete acoustic cycle yields the net energy generated (or absorbed) per cycle. For an acoustic resonance to be self-excited, this double integration over volume and time must be positive.

Howe's integral requires a great deal of input data such as the flow field data (unsteady velocity and vorticity fields) as well as the acoustic field data (acoustic particle velocity field), The work by Oshkai and Yan (2008) and Finnegan et al. (2010) are recent examples using Howe's integral with input data from experiments using PIV and microphones. The authors investigated acoustically-coupled flow past a coaxial deep cavity (side-branch) resonator mounted in a duct as shown in figure 2.17. They calculated the aeroacoustic power using the following steps; first, measuring the velocity field by PIV then calculating the vorticity field from the velocity gradients. Second, they used microphones to measure the pressure fluctuations **p**(x,t) and computed the acoustic particle velocity υ from the pressure measurements. Finally, all these data were inputted into Howe's integral to evaluate the instantaneous power as shown in figure 2.18. Figure 2.19 shows the spatial distribution of the aeroacoustic power, for this pattern of flow-sound interaction in deep side-branch with cross acoustic mode. From these results, the aeroacoustic sink or acoustic energy absorption occurs along the first half of the-side-branch opening (blue contours in figure 2.19), and the generation of the aeroacoustic energy occurs along the whole side-branch mouth (the green regions in figure 2.19). The limitation of this work is that it can be used for 2-Dimensional geometries only but not for complex geometries.

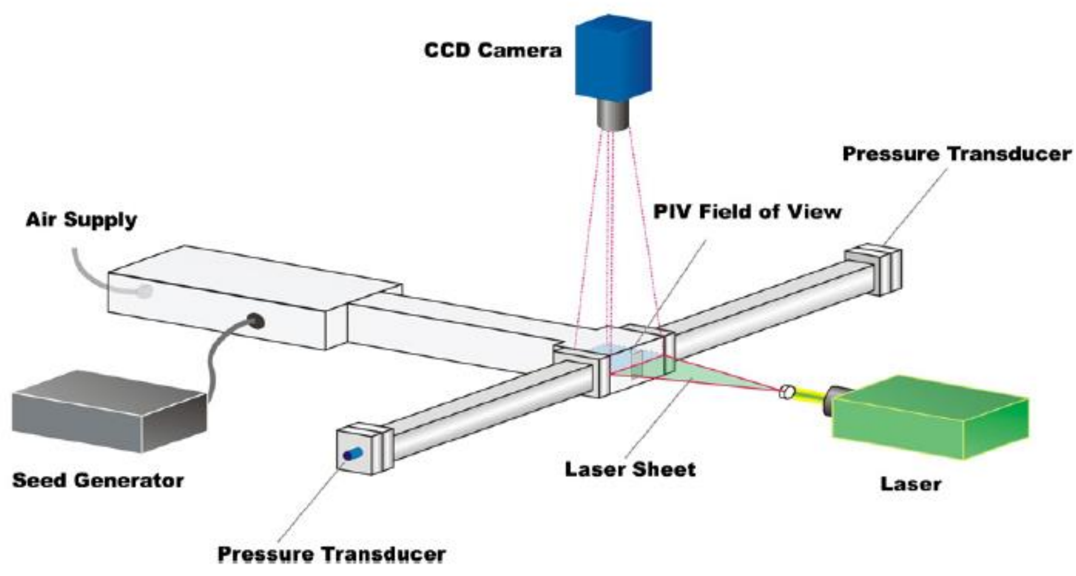

Figure 2.17: Test section and experimental setup of Oshkai and Yan (2008)

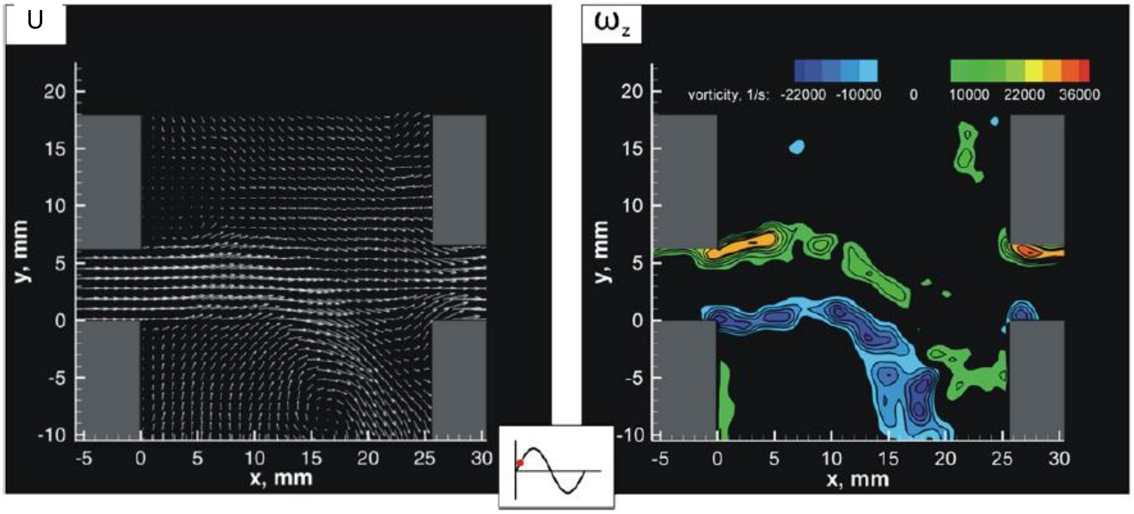

Figure 2.18: Input data to Howe's integrand; the flow velocity (left); the vorticity (right) and the acoustic particle velocity (bottom middle) (Oshkai & Yan, 2008).

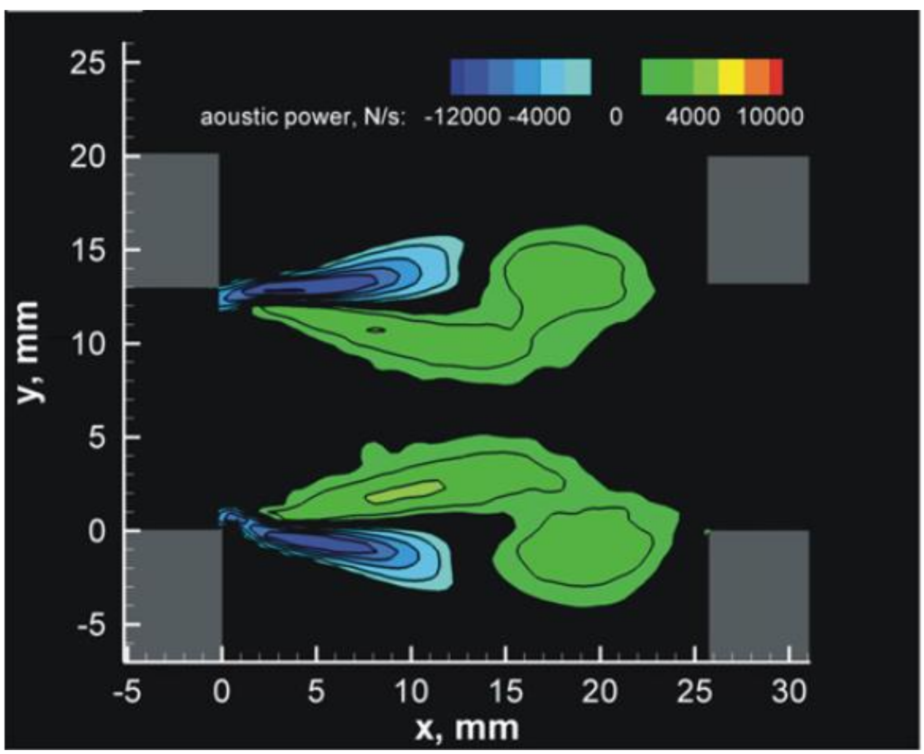

Figure 2.19: The spatial distribution of the aeroacoustic power along the opening of a deep side-branch coupled with a cross acoustic mode (Oshkai & Yan, 2008).

2.4.2. Analytical and Numerical Investigation of the Aeroacoustic Power

There have been many attempts to evaluate the aeroacoustic source both analytically and numerically. Starting from 1965 till now, many analytical and numerical models were developed. A summary is presented in table 2.1.

Table 2.1: Summary of the analytical and numerical attempts of aeroacoustic sources' evaluation.

Model Name and idea	Done and/or improved by
Linear Models: In these models; • Kutta-like condition was used to estimate the perturbation of the shear layer. • The spatial amplification of the perturbation was calculated by means of the linear stability theory • The source of sound was assumed to be a dipole resulting from the "impact" of the shear layer disturbances on the downstream edge.	(Elder, 1978 and 1980; Ronneberger, 1972 and 1980; Rockwell, 1977; Abom et al., 2009; Karlsson & Abom, 2010)
Single Vortex Models: These models; • **Started with calculated vortex path and circulation** 1- Assuming that the vorticity is concentrated into a single line vortex. 2- The circulation of the vortex was determined by a Kutta condition. 3- This method failed to provide a correct source when compared with experimental work.	(Howe, 1975; Peters, 1993)
• **Modified to imposed vortex path and calculated circulation** 1- Based on detailed flow measurements a line vortex was assumed to be formed at the upstream edge with each time the acoustic flow turned into the cavity.	(Nelson et al., 1981 and 1983; Hirschberg & Rienstra, 1994)

2- The circulation of this vortex is the integral of the vorticity shed at the upstream edge and the vortex was assumed to be convected downstream at a constant speed along a straight line. 3- The vortex path was assumed to be independent of the oscillation amplitude. 4- Subsequent modification to use a uniform acoustic flow normal to the vortex path. 5- Provided good insight in the aeroacoustic behavior but failed to give accurate quantitative predictions. • **Modified to imposed path and distributed vorticity** 1- Assumption of a distributed vorticity along a line segment. 2- Taking into account the diffusivity of the vortices travelling downstream, a vortex concentration parameter was empirically estimated.	(Bruggeman, 1987; Dequand et al., 2003; Kook & Mongeau, 2002)
Models based on the numerical solution of the flow field: These models include; • Vortex Blob Simulations • CFD of laminar incompressible flow in conjunction with Howe's theory • CFD of unsteady turbulent compressible in conjunction with Howe's theory • LES of the unsteady turbulent flow in a cavity These models include over- simplifying assumptions and use simple geometries which are not similar to actual industrial applications.	(Thompson et al., 1988 and 1992; Stoneman et al., 1988; Hourigan et al., 1990; Kriesels et al., 1995; Hofmans, 1998; Radavich et al., 2001; Martínez-Lera et al., 2009; Mohany & Ziada, 2009; Nakiboglu & Hirschberg, 2010; Nakiboglu et al., 2011; Föller et al., 2010); Akula et al., 2015; Luo et al., 2015

Recent studies by Nakiboglu et al. (2011 and 2012) are very relevant as are other recent works that used Howe's integrand with semi-numerical input tools. In these studies, incompressible 2-D computational fluid dynamic simulations on a cylindrical symmetric shallow cavity domain associated with longitudinal acoustic mode using Fluent 6.3 were performed. As shown in figure 2.20, the imposed inlet velocity profile in the numerical simulation is composed of a mean velocity profile u(r) that takes the shape of the fully developed turbulent velocity profile with zero turbulence intensity (laminar flow) in addition to a uniform acoustic oscillating velocity u'(t) in the axial direction with a frequency, f, and an amplitude, |u'| /U . Where:

$$U = u(r) + u'(t) \; ; \qquad u'(t) = (|u'| /U)\sin(2\pi f\, t) \qquad (2.19)$$

The amplitude |u'| /U is the maximum fluctuation amplitude in the piping section which is **measured experimentally** by self-excited system measurements, where $|u'| /U = p'_{max} / \rho_o C_o U$. The details of the simulation parameters are provided in Nakiboglu et al. (2011).

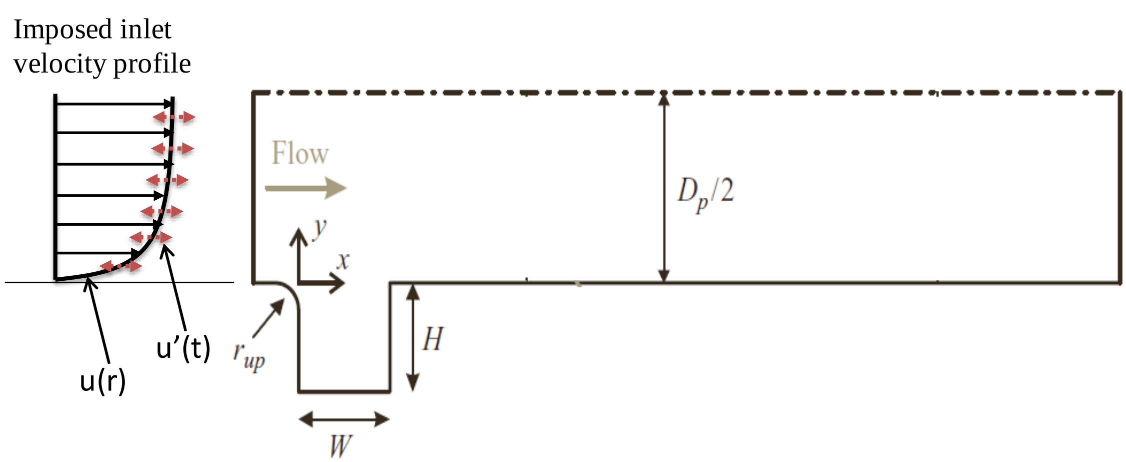

Figure 2.20: CFD simulation domain and the input velocity profile. (Nakiboglu et al., 2011)

The results from the laminar simulations as well as the self-excitation measurement results are used as input data to Howe's integrand while ignoring the viscous effects and the rotational component of the particle velocity. The results from this study reveal the relationship between the aeroacoustic power and the flow and acoustic parameters. However, the effects of ignored terms and simplifications in the flow and geometry are not examined. In addition, the self-excited amplitude was substantially underestimated when the computed aeroacoustic source was used in an energy balance model between the generated source energy and the system losses (Nakiboglu et al., 2011 and 2012), as shown in figures 2.21 and 2.22.

In summary, the interaction mechanism between the flow field and the sound field that magnifies the original disturbance and sustains an acoustic resonance is called the fluid-resonance mechanism (Rockwell and Naudascher, 1978). This mechanism is characterized by strong pressure oscillations and high noise levels. These strong oscillations can cause fatigue failure of the associated piping components. Moreover, these pulsations increase the dynamic energy loss from the main flow by consuming part of the flow energy to resonate the system. Design considerations for flow-excited acoustic resonances must include the flow velocity at the onset of resonance and the amplitude of resonance (or the aeroacoustic source strength). In the literature, the onset of resonance is well defined for different applications like flow over cavities and side-branches, but for the amplitude of resonance, or the aeroacoustic power source, *more work is required in order to cover different flow types, complex geometries and different acoustic modes*.

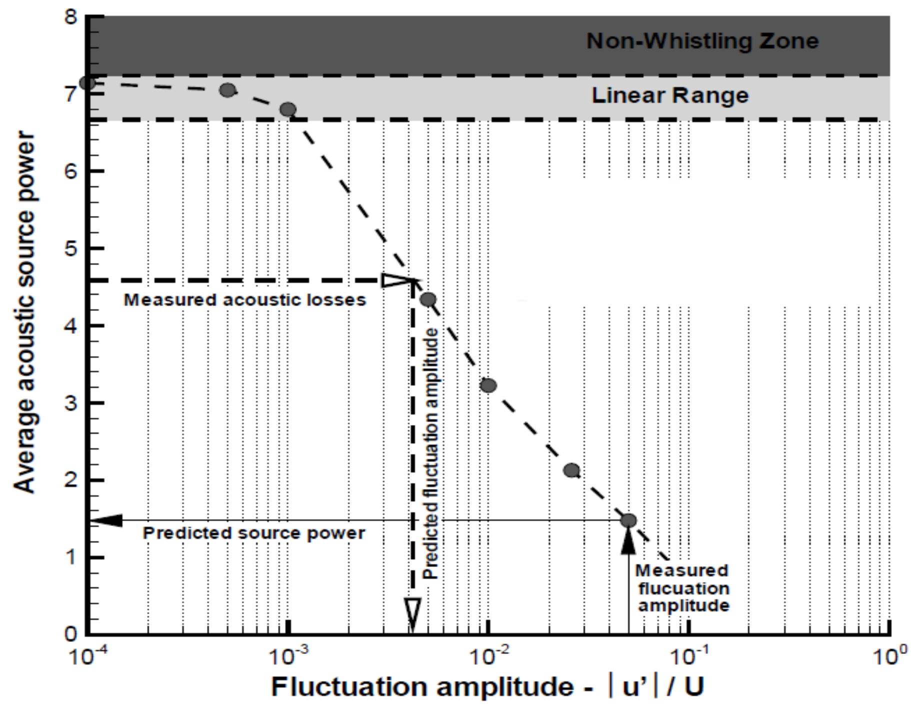

Figure 2.21: The difference in the fluctuation amplitudes based on the measured acoustic losses and the predicted source power (Nakiboglu et al., 2012).

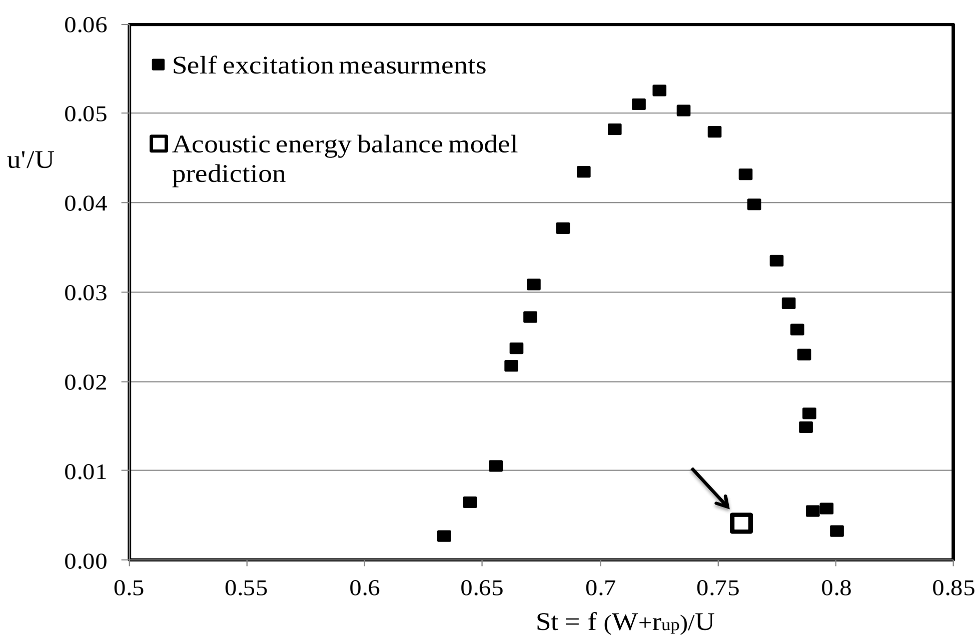

Figure 2.22: The difference between the measured self-excited fluctuation amplitude and that predicted by the developed source power (Nakiboglu et al., 2012).

It is generally recognized that the aeroacoustic sound sources depend very strongly on the local details of the sound and vorticity fields. Therefore, in most of the previous work (experimentally and numerically), the unsteady details of the flow field at the object are required to estimate the aeroacoustic source, which required a lot of simplifications of the flow and geometries (Hourigan et al., 1990; Howe, 1975; Mohany & Ziada, 2009; Nakiboğlu et al., 2010; Nakiboğlu et al., 2011; Oshkai & Yan, 2008).

Graf and Ziada (2010) introduced a methodology that avoids these simplifications both in geometry and flow and they used it to measure the aeroacoustic source for the case of flow-sound interaction pattern of deep side-branches with cross acoustic mode (pattern a in figure 2.12-a).

In this research, the methodology of Graf and Ziada is further developed and adapted to characterize the aeroacoustic power source of an isolated shallow cavity in a pipeline in the presence of a longitudinal acoustic resonance (pattern c in figure 2.12-c). The experiments are performed at high Reynolds number, and three-dimensional fully developed turbulent pipe flow. The developed research methodology neither deals with the details of the unsteady flow field nor the flow-sound interaction mechanism. Therefore, it is very efficient for complex geometries and flows which make it superior to other methods and models.

It is also observed from the literature that the effect of cavity size on the self-excited resonant oscillations was always presented as an effect of the length to depth ratio (L/H). Some examples of these studies are the work done by Rockwell et al. (2003) and Nakiboglu at al. (2012). In these studies, the ratio L/H was controlled by changing the cavity depth while the cavity length was kept constant. Open issues still has not been investigated such as the effect of cavity size for the same L/H ratio and the effect of changing the cavity length for the same cavity depth. Hence, *there is a need for a comprehensive study of the effect of cavity geometry on the aeroacoustic source*. *This comprehensive study is one of the current research objectives.*

Observations from the literature on the effect of rounding-off the cavity edges show inconsistencies. In the case of a deep side-branch associated with trapped acoustic mode, such rounding dampens the oscillations (Knotts et al., 2003). Conversely, such rounding enhances the oscillations in the case of a shallow cavity with trapped acoustic mode (Bolduc et al., 2014). Also, there is no comprehensive study in the literature covering the effect of edge rounding-off on the aeroacoustic source for the case of shallow cavities coupled with longitudinal acoustic modes. Therefore, *the effect of rounding-off the edges on the flow-sound interaction mechanism is also studied in the present work.*

Another main objective of the present research is to experimentally investigate the spatial and temporal distribution of the aeroacoustic power along the cavity mouth for this type of flow-sound interaction pattern (shallow cavity flow coupled with longitudinal acoustic mode). Knowledge from this investigation can be used to understand the nonlinear behaviour of the aeroacoustic source at large amplitudes of acoustic pulsations.

Chapter 3

Experimental Set-up

Various sets of experiments were performed on different shallow cavities in pipe flow. The cavities have different sizes with sharp and rounded edges. The main objective of these experiments is to investigate the characteristics of the aeroacoustic source generated by the flow-structure interaction in the cavity coupled with the longitudinal sound standing wave in the piping system. The used methodology does not deal with the details of the unsteady flow field or the complexity of the flow or the geometry. This method is called the Sound Wave Method and uses three microphones upstream the cavity and another three microphones set downstream the cavity to measure the acoustic pressure wave and extracts the aeroacoustic source from these measurements. The test set-up and the measuring technique of this method will be described in the first section of this chapter. In order to validate the measured aeroacoustic source, self-excitation measurements are required. Therefore, a smaller piping system was designed and built for this purpose. Finally, in order to better understand the flow-sound interaction in the cavity and the behavior of the aeroacoustic source at different sound levels in the piping system, Particle Image Velocimetry (PIV) measurements for a single shallow cavity at different flow conditions and acoustic resonance amplitudes were performed. The third section of this chapter will give the details of the test set-up and the procedure of these measurements.

3.1 Sound Wave Method

3.1.1 Test Set-up

Experiments are conducted in an open circuit PVC piping system (4 inches nominal diameter) located at the suction side of a variable speed pressure blower in order to control the flow velocity. A bell mouth is fitted at the entrance of the piping system followed by a honeycomb to produce a uniform flow and minimize velocity fluctuations. At entrance, a pitot tube is used to measure the mean flow velocity at the test section entrance downstream of the honeycomb. The cavity leading edge is 46 pipe diameters downstream of the entrance in order to ensure that the incoming flow is a fully developed turbulent flow. A side-branch is attached to the flow pipe at a specified distance downstream of the cavity to guide the standing acoustic wave where the cavity is located between the pipe inlet and the side-branch. A flexible hose connects the pipeline to the suction side of the pressure blower in order to isolate the piping system from the vibrations of the blower as shown in figure 3-1. The blower was equipped with a 15 HP motor and a variable speed controller to change the flow velocity during the test.

The distance from the entrance to the cavity mid plane is designed to be 4.4 meter, which constitutes one wavelength λ, for the acoustic mode with a frequency of 78 Hz, 2 wavelengths for that with a frequency of 156 Hz or 3λ for a frequency of 234 Hz. The mode at 78 Hz with $\lambda \approx 4.4$ m will be referred to hereafter as the first harmonic acoustic mode and the others at 156 Hz and 234 Hz as the second and third harmonic acoustic modes. The distance from the cavity mid plane to the side-branch center location is 2.2 m or $\lambda/2$ for first mode, λ for the second mode or $3\lambda/2$ for third mode. While the side-branch length and the pipe section from the side-branch center to the flexible hose entrance are selected to be 1.1 m each, this is equal to $\lambda/4$ for the first mode or $3\lambda/4$ for the third mode. These lengths should be modified to $\lambda/4 = 0.55$ m when using the second harmonic mode. A loudspeaker mounted at the end of the side-branch is used to excite the system at the desired frequency. This well-tuned design of the piping system dimensions facilitates the following features during the tests: first, the cavity location is in the fully developed turbulent flow region which is similar to the flow conditions in most of the industrial applications. Second, it is possible to operate the system at different acoustic modes while the cavity is located at an acoustic pressure node (acoustic particle velocity anti-node). This cavity location maximizes the aeroacoustic source generated which increases the measurement accuracy. Third, the length of the side-branch and the pipe part from the side-branch center to the flexible hose entrance are selected to have an acoustic pressure anti-node at the hose entrance. This arrangement de-couples the exit pipe form the rest of the test arrangement and thereby reduces sound radiation into the hose. The standing wave will therefore be confined between the loudspeaker and the pipe entrance. This arrangement gives the ability to excite the system at very high levels of acoustic fluctuations.

The test object is an axisymmetric shallow cavity, which is designed such that the ratio of L/H can be changed, where L is the cavity length in the flow direction and H is the cavity depth. In addition, the cavity edges can be changed from sharp edges to curved edges as shown in figure 3-2. The experimental test setup is designed with the ability to control the mean flow velocity, U, the excitation frequency, f (or the wavelength λ), the acoustic oscillations velocity amplitude, υ, and the cavity geometry parameters. Therefore, the aeroacoustic source power can be evaluated as a function of these variables or dimensionless groups including them.

With a loudspeaker mounted at the side-branch end, the acoustic waves in the piping system can be excited at various frequencies and any desired level of acoustic oscillation amplitude within a wide range, thus, overriding self-excitation based on the specified wavelength and pipe geometry. The measurements of the resonance frequencies of the piping system for the first, second, and third harmonic modes were performed using random noise excitation by a loudspeaker without flow.

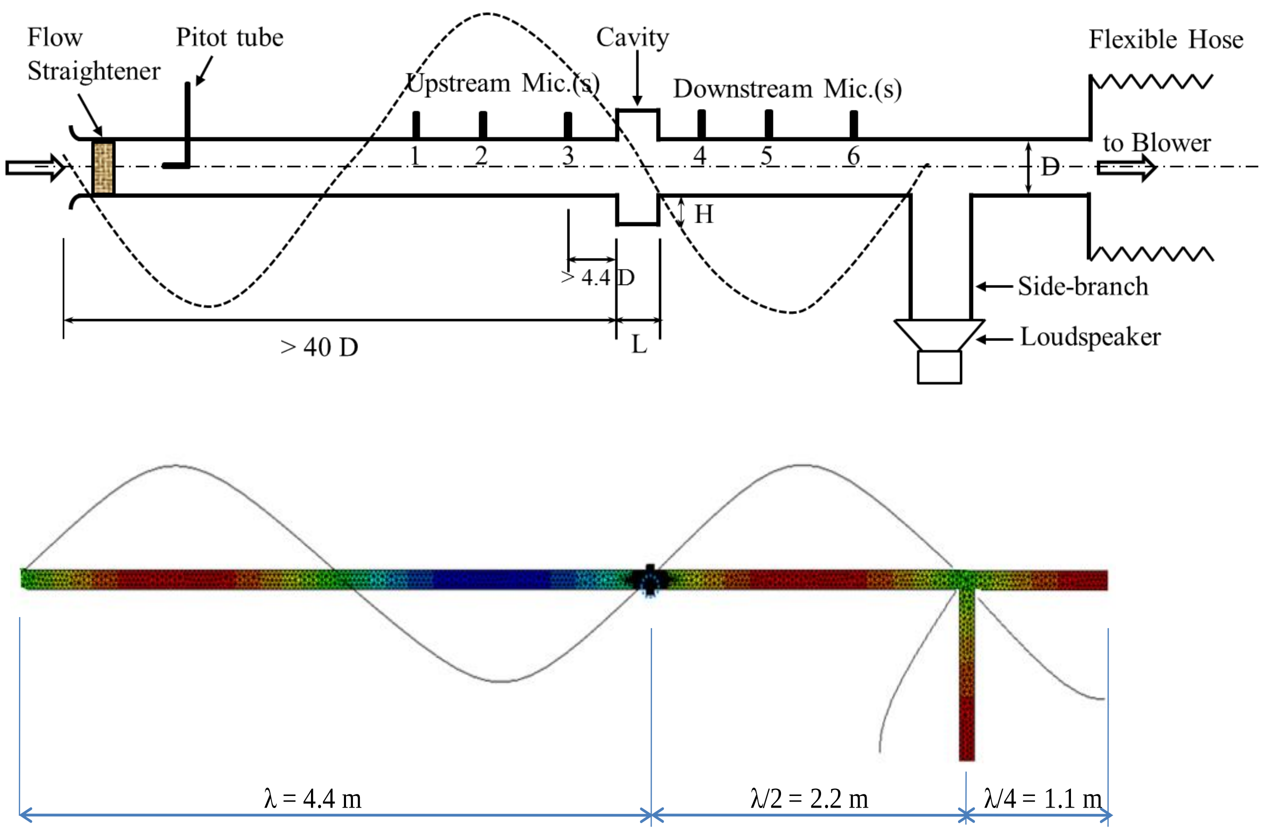

Figure 3.1: Sound Wave Method test setup

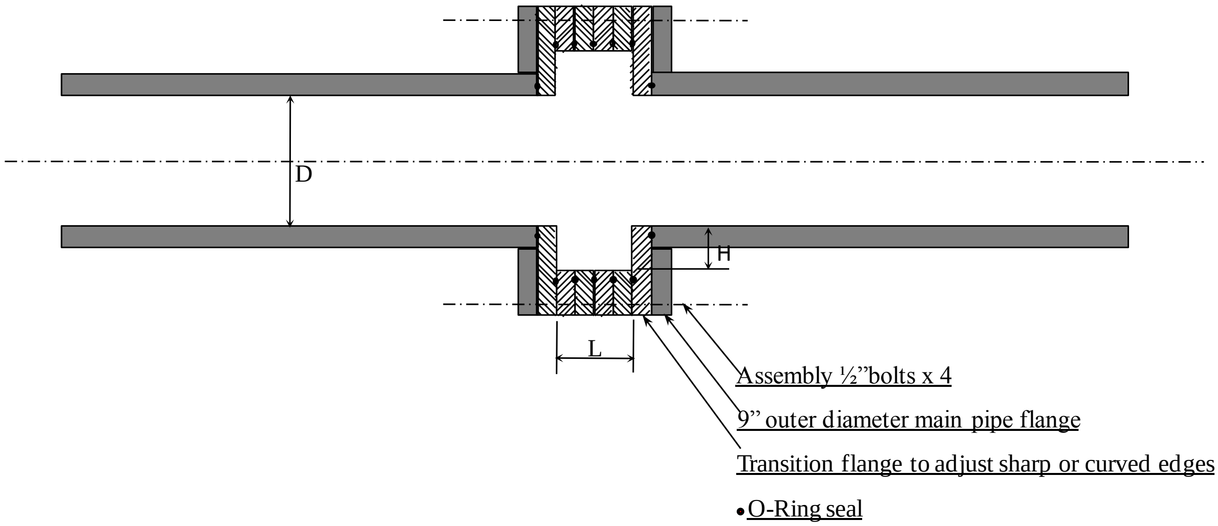

Figure 3.2: Cavity design and assembly

3.1.2 Measurement Technique

3.1.2.1 Mean Flow Velocity

The flow velocity at the centerline of the pipe was measured by means of a pitot tube which was connected to a Validyne differential pressure transducer of model number DP15-42 which has an accuracy of ± 0.25% of the full scale. Different pressure diaphragm sizes were used according to the measured velocity ranges. The analog signal from the transducer is connected to the first channel of 8-channels National Instruments data acquisition card. The pitot tube was centered along the pipe axis and was located at a distance, x_P, of 10 times the pipe diameter, D, from the pipe entrance to avoid any effects from the entrance on the measured velocity.

According to White and Corfield (1991), the developing entrance length for turbulent pipe flow is approximately 40 D. So, the pitot tube is located in the developing region core which has a uniform flow velocity as shown in figure 3-3. This uniform velocity profiles in the core increase the accuracy of the measured velocity, and the measurement becomes independent of small offsets between the pitot tube and the pipe centerline. Doherty (2007) measured the variation of the centerline flow velocity in the developing turbulent flow region. According to Doherty (2007), $U_{centerline}$ at $x_P/D = 10$ is equal to 0.87 $U_{centerline})_{FD}$ at the fully developed turbulent flow. White and Corfield (1991) stated that the mean flow velocity in the fully developed turbulent flow, U, is equal to 0.84 $U_{centerline})_{FD}$. The following relations are showing the procedure of measuring the mean flow velocity, U

$$U = 0.84\ U_{centerline})_{FD}$$

But $$U_{centerline})_{FD} = [\text{measured velocity, } U_{centerline)x/D=10}\ ] / 0.87$$

So,

$$U = \text{Measured velocity} * 0.84/ 0.87$$

Validation of the measured mean flow velocity, U, was carried out by measuring the velocity profile at the cavity entrance using the Particle Image Velocimetry technique. A comparison between the mean flow velocities measured by the pitot tube and by the PIV system showed a maximum difference of about 0.5%. Figure 3.4 shows the measured velocity profiles at the cavity entrance using the PIV system for different flow conditions in comparison to the Power law and the experimental fully developed turbulent velocity profile measured by Laufer (1954). From this comparison, the entrance velocity profile of the cavity region can be considered to represent a fully developed turbulence flow which is representative of flow conditions in industrial applications.

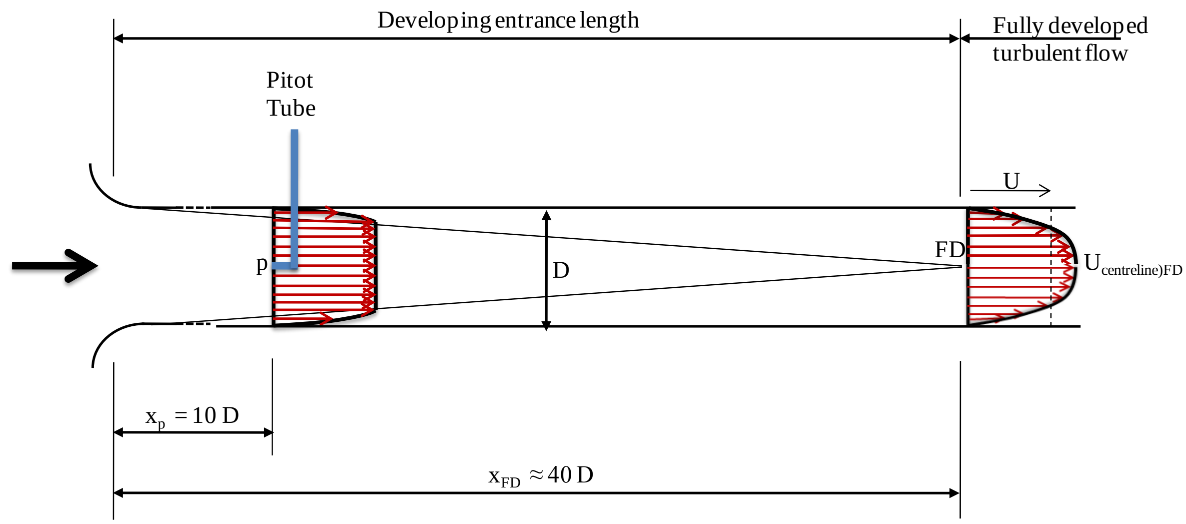

Figure 3.3: Flow velocity measurement

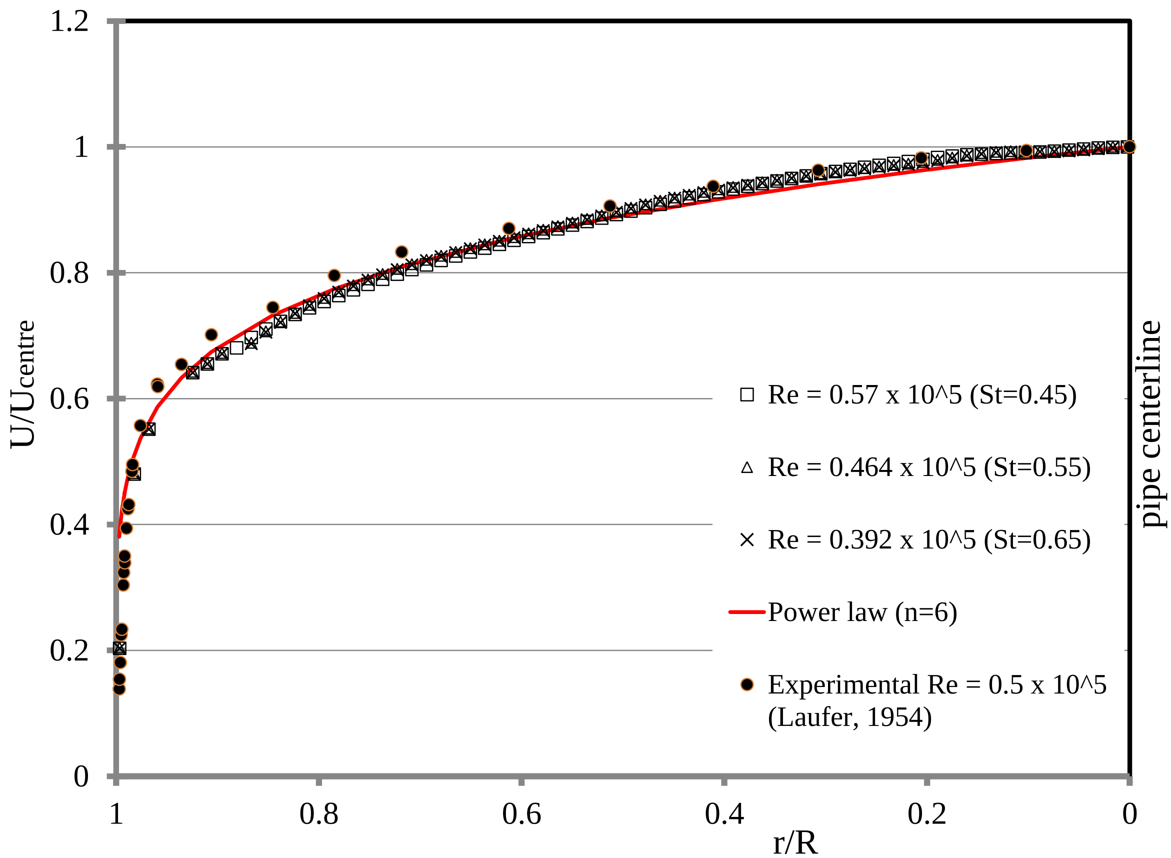

Figure 3.4: Cavity inlet velocity profile at different flow conditions compared to the Power law and experimental turbulent fully developed profile. All measurements were taken at υ/U= 5%

3.1.2.2 Acoustic Pressure Measurements

The acoustic (fluctuating) pressure inside the pipeline is measured by means of 1/4" GRAS 40BP condenser microphones with a sensitivity of 1.6 mV/Pa and a resonance frequency of 50 kHz. For the longitudinal (plane) standing sound wave inside the pipe, the acoustic pressure is uniform over any cross-sectional plane of the pipe but only changes along the pipe axis. Therefore, the microphones were flush mounted at specified locations along the pipe top wall. Figure 3.5 shows the attachment method of the microphone in the pipe top wall where a ¼" tapered threaded hole in the pipe wall was drilled and a Swagelok fitting with specified dimensions was used to hold the microphone and its preamplifier in the pipe hole and to ensure that the microphone tip is flush with the inner pipe surface.

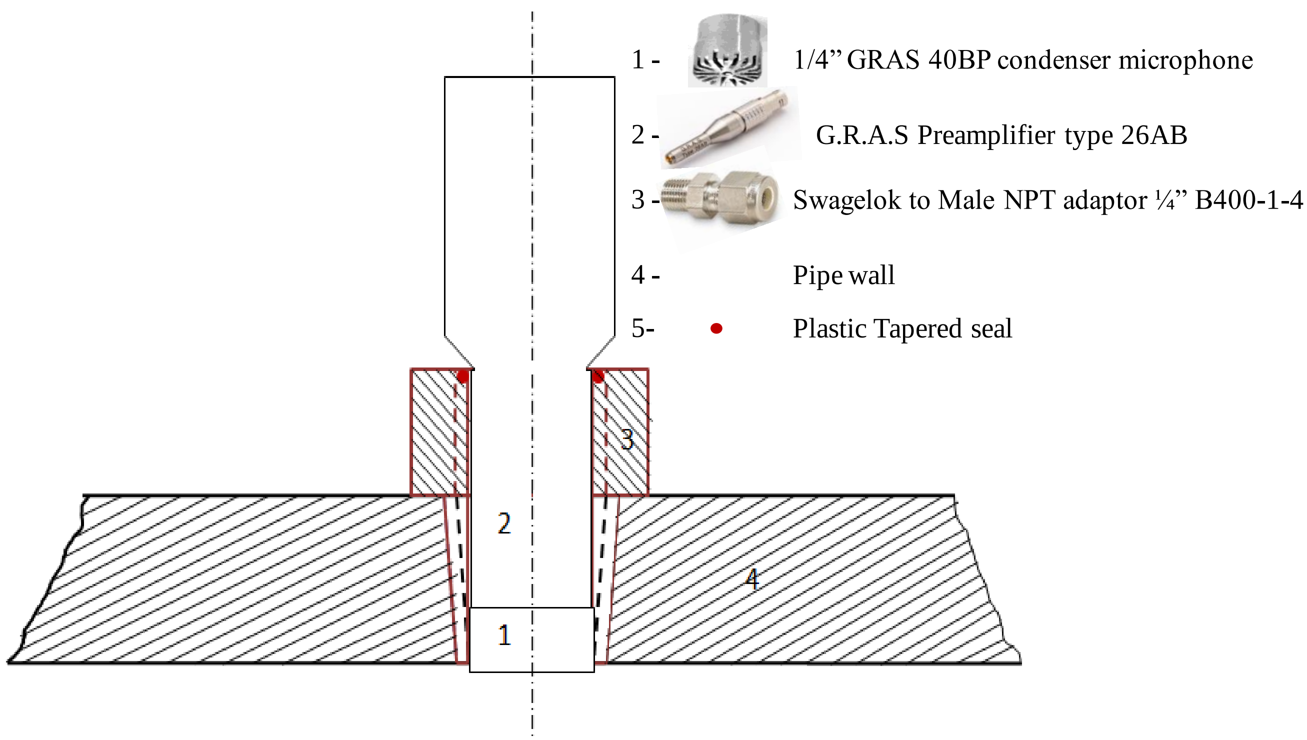

Figure 3.5: Installation method of the microphone

The Sound Wave Method requires measuring the sound pressure waves in both the upstream and downstream piping sections of the cavity. Therefore, a set of three microphones was used in the upstream piping section, and another set was used in the downstream part as shown in figure 3.1. Selection of microphones locations takes into consideration the following requirements:

- No redundancy: to avoid measuring the same signal from different microphones at different locations. In order to avoid that, each three microphones set should have the following arrangement; the middle microphone should be located very close to a pressure anti-node and the distances between the middle microphone and both neighbours should be different.
- High signal to noise ratio can be accomplished by putting the nearest microphone to a pressure node at a minimum distance of $\lambda/8$. This distance was established from accumulated experience with signal measurements during this research.
- The assumption of plane wave propagation can be accomplished by selecting low frequencies of operation (in this research, all measurements are at Helmholtz number < 0.2). This assumption is adequate and the higher order transversal modes which are generated in the vicinity of the cavity decay very rapidly after a short distance. According to Munjal (1987), the first transverse mode decays at a rate of -66.5 dB/diameter and higher transverse modes decay at steeper rates than the first. The closest microphone to the cavity is located at 4.4 D from the cavity nearest edge, where even the first transverse mode is attenuated to a negligible level.

- Interference from other sound sources must be avoided to ensure that the measured aeroacoustic source is due to the cavity only. This can be achieved if the pipe section from the first upstream microphone to the last downstream one does not include any pipe fitting that can cause sound generation except from the cavity. This condition not only removes the interference of other sources but also eliminates the effect of the piping system boundary conditions.

3.1.3 Calibration of Measuring Devices

3.1.3.1 Pressure Transducer Calibration

For each pressure diaphragm size used in the DP15-42 Validyne differential pressure transducer to measure a specified velocity range, calibration is required. This calibration was done by using a differential pressure calibrator that pumps the diaphragm with known pressures and recording the readings of the transducer output voltage. Therefore a linear calibration equation was produced as follows:

The dynamic pressure (dP) in Pascal = A * Reading output Voltage + B

Where, A and B are constants that refer to the calibration line slope and the zero error, respectively. Therefore, the Mean flow velocity of the fully developed turbulent flow, U is calculated from the following equation:

$$U = \sqrt{\frac{2\ dP}{\rho_o}} * 0.84/0.87 \qquad (m/s) \qquad (3.1)$$

3.1.3.2 Microphones Calibration

The relative sensitivity and phase responses of the six microphones are critical for accurate results. In order to calibrate the microphones, they were mounted in a test-chamber as shown in Figure 3.6. This test chamber was made of a wood plate with 6 equally spaced centered holes of ¼” diameter. The 6 microphones are mounted in these 6 holes and leveled on the top side of the plate while the microphones’ preamplifiers and cables connections are on the bottom side of the wood plate. A PVC pipe flange is centered on the top side of the plate with a loudspeaker above it. The test chamber was driven by the loudspeaker with a white noise of a fixed amplitude of 0.1 Volt peak to peak and a frequency range of 0 - 2 kHz. Then, the relative amplitude and phase of the microphone signals were measured and recorded simultaneously. The test is repeated with different amplitudes of the white noise excitation (1 and 3 Voltage peak to peak) and the same frequency range to ensure the independency of the microphones' relative signals from the excitation amplitude.

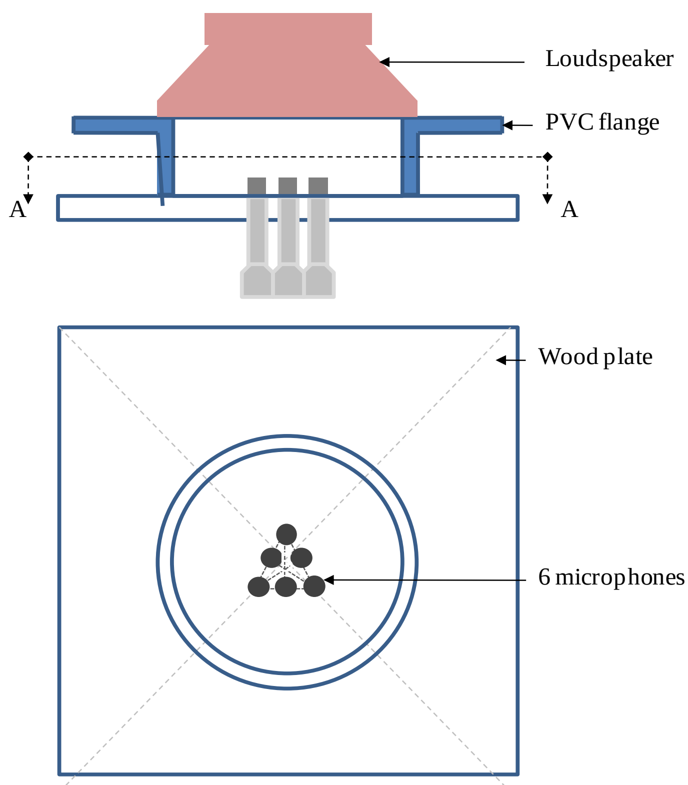

Figure 3.6: Relative calibration setup of Microphones

Figure 3.7 shows the relative calibration results for both the amplitude and phase. In this figure, all signals of microphones are relative to one microphone (the reference microphone), for which its relative amplitude is unity and its phase difference is zero, while the other microphones' relative amplitude ratios and phase differences differ slightly from the reference microphone.

The absolute sensitivity of the reference microphone was calibrated with a microphone calibrator (pistonphone). This pistonphone generates a tone of 114 dB (10 Pa) at 1000 Hz. The reference microphone measured response was 16.725 mV at 1000 Hz, which means the reference microphone sensitivity is 1.6725 mV/Pa. The measurements in the piping system were then corrected according to this calibration.

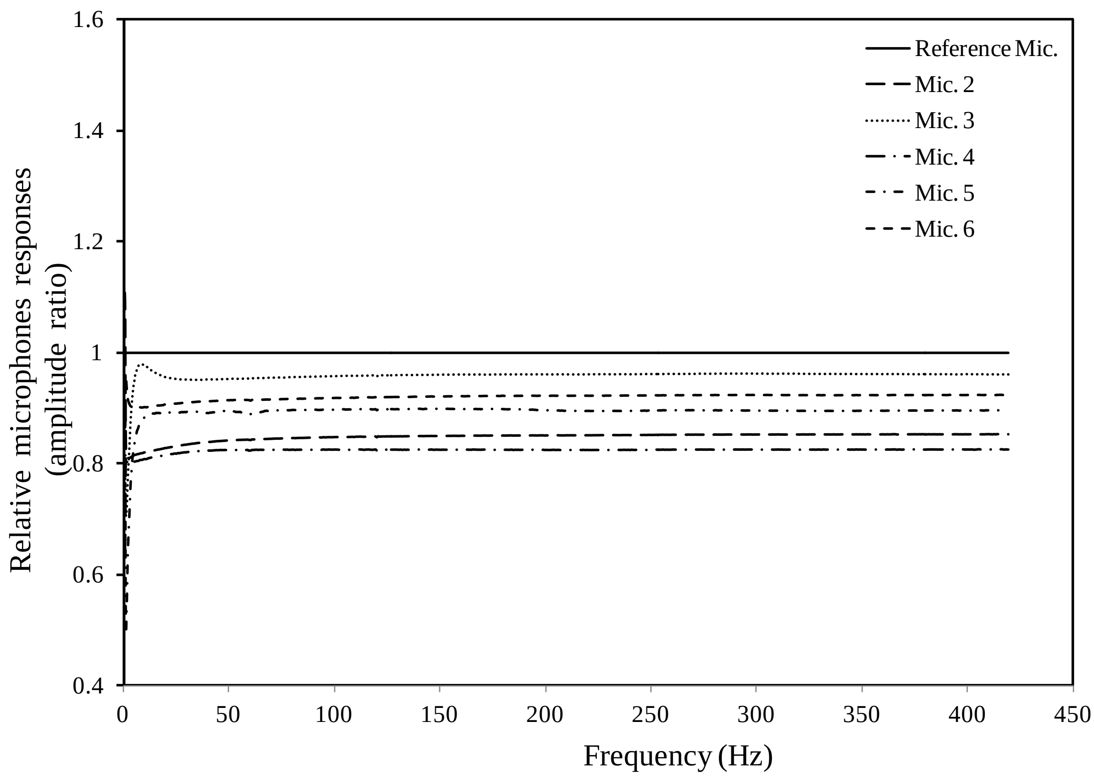

Figure 3.7-a: Microphones relative calibration response (amplitude ratio)

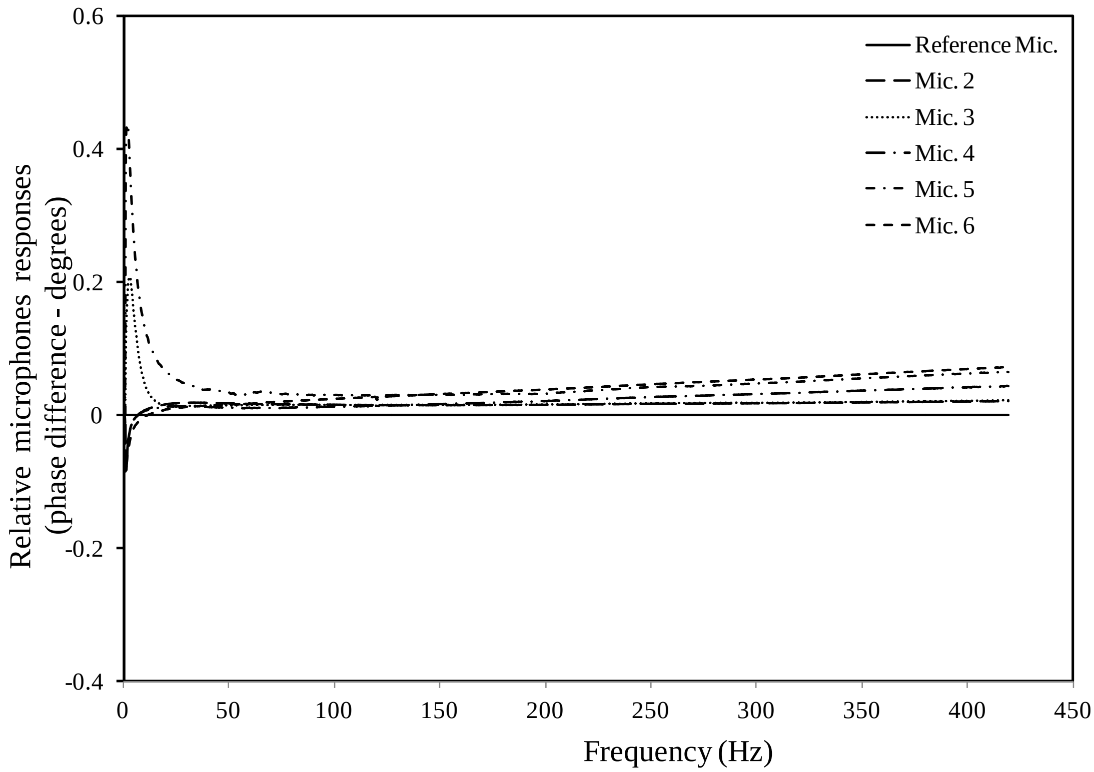

Figure 3.7-b: Microphones relative calibration response (phase difference)

3.1.4 Methodology and Experimental Procedure

The Sound Wave Method considers the acoustic power generated by the unsteady flow to be equal to the induced pressure difference across the object (cavity) multiplied by the local acoustic particle velocity. This method was established by Graf and Ziada (2010) for side-branches experiencing transverse acoustic mode resonance, and it is further developed in this research work in order to use it for the application of shallow cavities exposed to a flow and plane sound waves. In this method, the pressure difference across the cavity induced by the unsteady vortical flow in the cavity cannot be measured directly due to the complex structure of the flow and acoustic fields in the region of the cavity (note: the cavity is located at a pressure node as mentioned before). Instead, the pressure difference is computed based on the acoustic pressure which is measured with flush mounted 1/4" microphones at 6 different positions along the length of the main pipe (with 3 positions upstream and 3 positions downstream of the cavity). The acoustic waves in the upstream and the downstream sections of the main pipe can be computed from the pressure signals measured by the three microphones separated by an axial distance. The computational procedure is based on the theory by Munjal (1987), describing plane acoustic waves in pipes. For sufficient accuracy, the effects of flow and attenuation are taken into account. Figure 3.8 is a typical example of the complex domain presentation of the measured sound pressures. It presents the measured sound pressure by each microphone in the form of real and imaginary parts instead of amplitude and phase relative to the acoustic particle velocity at the cavity. In this figure, points 1, 2 and 3 give the sound pressure signals of the three upstream microphones while points 4, 5 and 6 are for the downstream microphones. More details about the procedure of extracting the pressure difference Δp across the cavity are presented in section 4.2.2 and figure 4.3

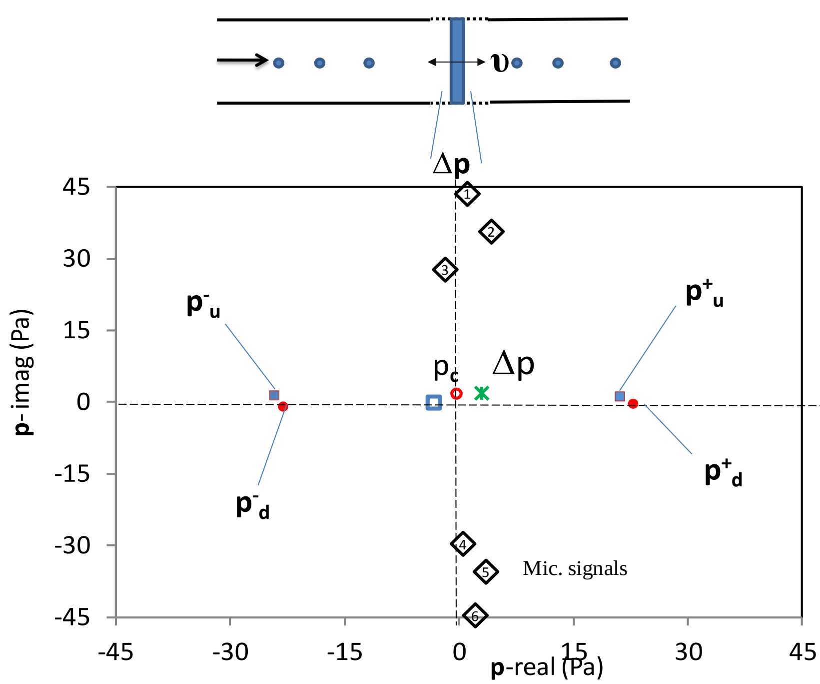

Figure 3.8: Measurement technique

The sound standing wave in a pipeline can be presented as a summation of two waves; a forward wave propagating in the flow direction ($\mathbf{p}^{+}$) and a backward wave propagating opposite to the flow direction ($\mathbf{p}^{-}$). As shown in figure 3.8, $\mathbf{p}^{+}_{u}$ and $\mathbf{p}^{-}_{u}$ represent the forward and backward waves of the upstream piping section standing wave. Similarly, $\mathbf{p}^{+}_{d}$ and $\mathbf{p}^{-}_{d}$ represent the downstream piping section standing wave. From the known standing waves in both piping sections, the sound pressure at the mid plane of the cavity can be calculated from both sides (the empty square and the empty circle in figure 3.8). The difference in the acoustic pressures at the middle of the cavity calculated from the upstream and the downstream pipe sections is the lumped pressure difference $\Delta\mathbf{p}$. This pressure difference is normalized to represent the source term **S** using the mean flow velocity U and the acoustic particle velocity υ as follows:

$$\mathbf{S} = \frac{\Delta\mathbf{p} / \frac{1}{2}\rho_o \mathrm{U}^2}{\upsilon/\mathrm{U}} \qquad (3.2)$$

In order to measure the aeroacoustic source as a function of Strouhal number St and excitation level υ/U, the loudspeaker controller and the blower speed controller are used to adjust the test parameters. First, an excitation frequency of 78Hz is selected to perform the tests at the first acoustic mode. This frequency is based on an experimental determination of the resonance frequency. Secondly, the excitation amplitude (υ/U) is adjusted to a certain value by means of the loudspeaker, and the blower speed controller is used to adjust the flow velocity to a selected Strouhal number. At these conditions, the microphone signals are recorded simultaneously using a PC-based data acquisition card with 8 channels. In addition to the 6 microphone signals, the excitation signal of the loudspeaker and the signal of the pressure difference of the pitot-tube are recorded. The 8 signals are recorded simultaneously for duration of 60 seconds. The measured data are then analysed by a MATLAB code to evaluate the aeroacoustic source at the specified Strouhal number and (υ/U) ratio. By repeating the same procedure for different combinations of Strouhal number and (υ/U) ratio, the aeroacoustic source is determined as a function of those two dimensionless variables.

3.2 Self-Excited Measurements

In order to validate the measured aeroacoustic source by the Sound Wave Method, self-excitation measurements are required. Therefore, a smaller piping system was designed and built for this objective.

3.2.1 Test Set-up

A short piping system is carefully designed in order to generate self-excited resonances within a suitable velocity range and to reduce the viscous losses to easily sustain acoustic resonances. In other words, if we use the original long piping system, the wavelength of the acoustic standing wave would be too long, and therefore the resonance frequency would be rather small. Since the resonance Strouhal number for a shallow cavity is around 0.6, the smallness of the resonance frequency would lead to a low flow velocity at resonance and therefore the acoustic resonance, if it materializes at all, would be very weak. In addition to the small flow velocity, the long pipe increases viscous losses that lead to additional difficulties in sustaining a well-defined acoustic resonance.

As shown in Figure 3.9, the cavity in this alternative design is centered between two equally long pipe sections of 0.65 m each. Two microphones are used in specified locations of the downstream pipe section. The first microphone is located at the peak location of the sound pressure standing wave of the first harmonic mode (middle of the downstream pipe section) and the second microphone is located at the peak of the second harmonic mode (quarter of the downstream pipe length from the outlet section). The flow velocity at the centerline of the pipe was measured by means of a pitot tube as described before in section 3.1.2.1

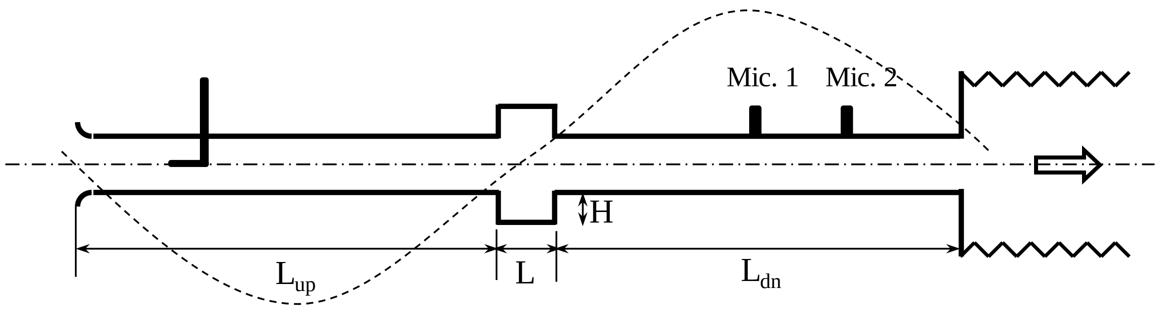

$L_{up} = L_{dn} = 0.65$ m

.

Figure 3.9: Test setup for the self-excited measurements

3.2.2 Measurement Procedure

The blower speed controller was used to operate the system at different values of the flow velocity U while the two microphone signals are recorded for 60 seconds and then averaged to get the frequency spectrum at each flow velocity using MATLAB code. From the spectrum, the resonance lock-in velocity ranges, the peak amplitude of different harmonic modes were investigated. The two microphone simultaneous signals were used in the prediction of the outlet plane acoustic impedance which is required in the process of model validation. This part is described in details in section 4.3.

3.3 Particle Image Velocimetry Measurements

The main objective of this part is to perform flow visualization measurements using the PIV system in order to better understand the flow-sound interaction patterns and the behavior of the aeroacoustic source with the variation of the Strouhal number and the excitation level (υ/U). The test setup and procedure for this objective is described in the following sections.

3.3.1 Test Set-up

The test setup for the flow visualization is the same piping system used in the aeroacoustic source measurements using the Sound Wave Method that was described in details in section 3.1.1 and illustrated in figure 3.1. Some modifications in the cavity were made in order to facilitate an optical access without distortion. The cavities that were used in this PIV part were made of a clear acrylic plate, and they are two-dimensional (i.e. has a square cross-section). However, the square cavity side dimensions are equal to the axisymmetric cavity diameter used in the Sound Wave Method, and the inlet and outlet pipes connected to the 2-D cavity are maintained circular as shown in figure 3.10. Two cavity sizes were tested in the PIV study. The first cavity dimensions are 52 mm in length and 26 mm in depth and the second cavity dimensions are 104 mm long and 52 mm deep. Thus, both cavities have the same L/H ratio of 2 but differ in volume.

The PIV system includes a single Power View 4MP 12 bit CCD camera with Nikon AF 50mm lens, a 532nm New Wave Solo 120XT pulsed Nd:YAG laser which is capable of generating an output power of 120 mJ per pulse, and a TSI Laser Pulse synchronizer Model 610035 in combination with Insight 3G software to synchronize the camera capture and laser pulse timing.

The flow was seeded with bis (2ethylhexyl) sebacate via a Laskin aerosol generator, which creates a dispersion of particles with a mean diameter of 1 µm. Seeding of the flow for PIV imaging was performed outside the pipe and close to its entrance The quantity of seeding material, the camera focal position and zooming are adjusted and tested such that each image contains vector validation rates (ratio of number of good vectors to the total number of vectors) in excess of 99%. The Stokes number of seeding particles, which indicates how seeding particles follow the fluid flow particles, for all PIV cases based on the seed droplet properties and the maximum test flow velocity, is much smaller than 0.1 which results in tracking error of less than 1%. (Tropea, et al., 2007). The laser sheet and the camera location are aligned to be perpendicular while the capture region is selected to be from the cavity wall to the main flow center line (figure 3.10).

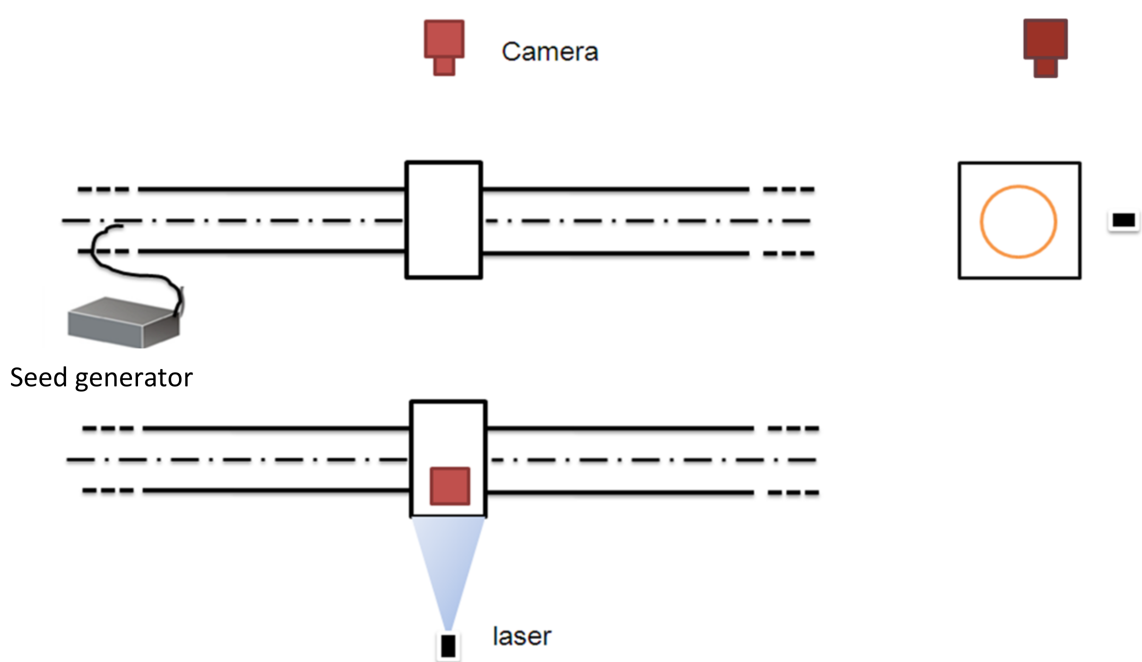

Figure 3.10: PIV measurement technique

3.3.2 Measurement Technique and Procedure

The loudspeaker is used to control the excitation frequency and the acoustic oscillation amplitude while the blower speed controller is used to adjust the flow velocity. Therefore, a wide range of Strouhal number and excitation level (υ/U) combinations can be tested. Multiple microphones are used to quantify the acoustic field (the acoustic particle velocity at the cavity).

At each specified Strouhal number and fluctuation amplitude ratio, the acoustic cycle is divided into eight time instants, uniformly spaced 45° apart, and 200 image pairs were used to compute the flow field which were then averaged to determine eight instantaneous flow fields. An external trigger synchronized with the loudspeaker signal provides a mean of phase-locking or flow freezing, over the 200 images with a known phase in the acoustic cycle. Time delay available in the Insight 3G software gives the ability to trigger the laser and the camera at the required phase instant in the acoustic cycle.

Insight 3G software is used to process each image pair separately using a classic PIV analysis algorithm in two steps from 32 pixel coarse square grid to 16 pixel square deformation grid which is computationally expensive but provides the most accurate analysis of the flow field. The average vector field for each set of the 200 images was computed using Tecplot, and then a special MATLAB code is used for further analysis.

3.3.3 Measurement Conditions

As the measured whistling Strouhal number for the smaller cavity (52 x 26 mm) is equal to 0.65 for the first hydrodynamic mode, the PIV measurements are taken at this Strouhal number with four values of the fluctuation amplitude ratio (υ/U = 1%, 5%, 10% and 20%) in order to understand the nonlinear behaviour of the aeroacoustic source and its saturation at high amplitude ratio.

In addition to understanding the nonlinear behaviour of the aeroacoustic source with the amplitude ratio, the effect of Strouhal number at the same amplitude ratio is investigated by measuring the flow field at υ/U = 5% for several values of Strouhal numbers (St = 0.55, 0.6, 0.65, 0.75 and 0.8), which is the range of Strouhal numbers at which the aeroacoustic power is generated at the first hydrodynamic mode of the shear layer oscillation.

PIV measurements for a larger cavity were performed to understand the change in whistling Strouhal number and the aeroacoustic source strength with the cavity volume. This larger cavity has a whistling Strouhal number of 0.75 for the first hydrodynamic mode and 1.3 for the second hydrodynamic mode. Therefore, the PIV measurements are taken at these Strouhal numbers with four values of the fluctuation amplitude ratio (υ/U= 1%, 5%, 10% and 20%). Also the effect of Strouhal number at the same amplitude ratio is investigated by measuring the flow field at υ/U = 5% for several values of Strouhal number (St = 0.6, 0.7, 0.75, 0.82, 0.9, 1.0, 1.1, 1.2, 1.3, 1.4 and 1.5).

3.4 Summary

In this chapter, the test set-up, measurement techniques and conditions are described for the Sound Wave Method, the self-excitation measurements and the PIV flow visualization measurements, respectively. The next few chapters will present the detailed results and conclusions.

Chapter 4

Sound Wave Method: Results and Validation

4.1 Introduction

In this chapter, the flow-induced acoustic source of an axisymmetric shallow cavity, coupled with longitudinal acoustic waves in a pipeline is characterized experimentally for circular pipes conveying fully developed turbulent flow using the Sound Wave Method (SWM). This aeroacoustic source is generated due to the interaction of the cavity shear layer oscillation with the acoustic field in the pipe. Because of the small size of cavity compared to the acoustic wavelength, the aeroacoustic source is modeled by a lumped acoustic dipole source which is dependent on the Strouhal number and the acoustic particle velocity at the cavity. The amplitude and phase of this source are determined experimentally and presented in the form of a dimensionless complex source term. In addition to the source measurements, a validation of the measurement technique and the measured source is presented. The validation technique depends on comparing the self-excited resonance response (resonance amplitude and frequency) obtained from self-excitation measurements with that estimated from an acoustic model supplemented with the measured source term using the SWM. The present results were obtained for an axisymmetric shallow cavity with sharp corners and length L = 9 cm, depth H = 2.65 cm, in a pipe diameter D = 9.5 cm, and cavity diameter D_c = 14.8 cm as shown in figure 4.1.

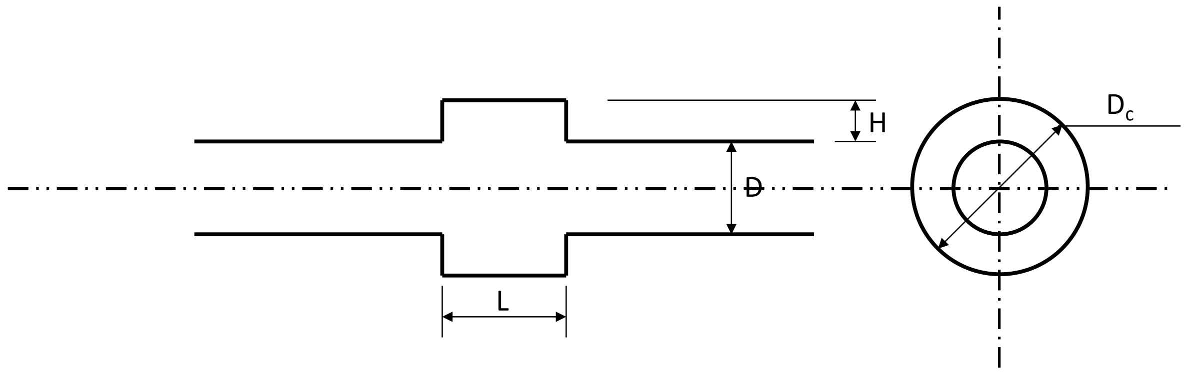

Figure 4-1: Cavity dimensions

4.2 Experimental Investigation of the Aeroacoustic Source

4.2.1 Identification of the Resonance Frequency

Experiments are conducted in an open circuit PVC piping system that was described in section 3.1.1. With the loudspeaker, the acoustic waves in the piping system can be excited at various frequencies and levels within a wide range. The frequency is typically selected in order that a pressure node is near the middle of the cavity. The flow velocity is then adjusted by the blower speed controller to operate at the desired Strouhal number.

The frequency at which a pressure node is near the middle of the cavity (resonance frequency) can be determined by the excitation of the piping system with a random noise signal with a frequency band (75-85 Hz) that has a center frequency near the expected resonance frequency. This is typically done without flow. The analysis for a series of frequencies around this center frequency indicates the resonance frequency at which the dynamic pressure at the middle of the cavity is purely real. These tests are repeated at three levels of excitations (low, moderate and high amplitude) to ensure the independence of the resonance frequency from the strength of the sound wave. Figure 4.2 shows the imaginary component of the acoustic pressure at the cavity center as a function of the frequency of the random external excitation. From this figure, the frequency of 77.8 Hz is the first harmonic acoustic resonance frequency of the system. By using the same methodology, the second acoustic resonance frequency is 155.8 Hz, and the third acoustic mode occurs at 236 Hz.

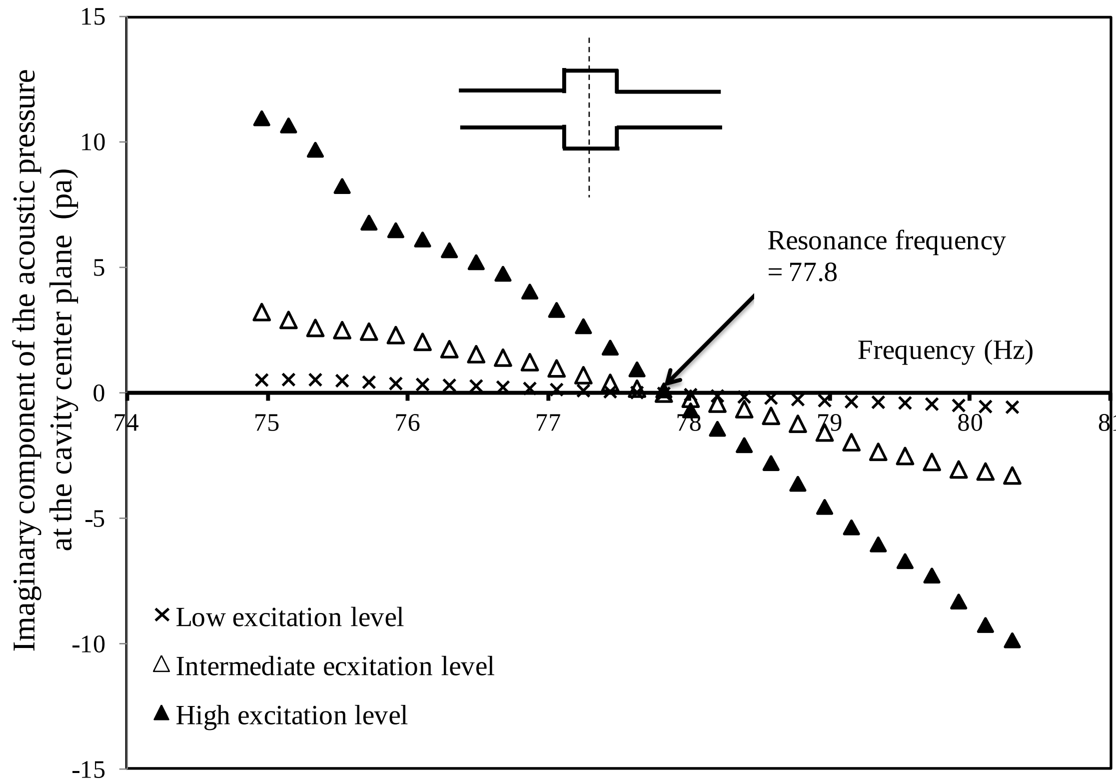

Figure 4.2: Pipeline system response to forced random acoustic excitations; the imaginary components of the acoustic pressure at the cavity center verses the excitation frequency. Note: the resonance frequency occurs at a pure real acoustic pressure (zero imaginary components).

4.2.2 Methodology and Test Conditions

The Sound Wave Method considers the acoustic power generated by the unsteady flow to be equal to the induced pressure difference across the cavity, $\Delta \mathbf{p}$, multiplied by the local acoustic particle velocity υ. The pressure difference induced by the unsteady vortical flow in the cavity cannot be measured directly due to the complex structure of the flow and acoustic fields in the region of the cavity. Therefore, the pressure difference was computed based on the acoustic pressure which was measured with flush-mounted microphones at 6 different positions in the main pipe. Using a pure tone (sine wave) excitation signal to operate the loudspeaker, complex values of the acoustic pressures p_{m1} …p_{m6} at the excitation frequency are measured for each microphone. The preprocessed data was then saved for further analysis. The relative amplitude sensitivity and phase difference of the microphones are critical for accurate results. The fluctuating pressure difference $\Delta\mathbf{p}$ induced by the unsteady flow in the cavity is rather small; it is generally smaller than 10% of the maximum acoustic pressure in the main pipe. In order to calibrate the microphones, they were mounted in a test-chamber as described in sub-section 3.1.3.2.

The acoustic waves in the upstream and the downstream sections of the main pipe can be computed from the pressure signals measured by the three microphones. For sufficient accuracy, the effects of flow and attenuation are taken into account. At these low frequencies, the assumption of plane wave propagation is adequate and the higher order transverse modes, which are generated in the vicinity of the cavity, decay very rapidly after a short distance (Graf & Ziada, 2010). Actually, the first transverse mode decays proportional to $e^{-3.83x/(D/2)}$ or -66.5 dB/diameter and higher transverse modes decay even steeper than the first. The closest microphone is 4.4 D upstream of the cavity, where the first transverse mode has already decayed by 292.6 dB.

The acoustic waves in a section of straight pipe, **p**(x), can be modeled as the superposition of forward, $\mathbf{p_x^+}$ and backward, $\mathbf{p_x^-}$, propagating waves which can be expressed using equation (2.12) with some modifications as:

$$\mathbf{p}(x) = e^{\boldsymbol{\varepsilon} Mx} \left(p^+ e^{-\boldsymbol{\varepsilon} x} + p^- e^{\boldsymbol{\varepsilon} x} \right) \qquad (4.1)$$

This equation must be satisfied at all three microphone positions x_i in the respective pipe section, yielding 3 linear equations in two unknowns p^+ and p^-. The complex value of the attenuation coefficient **ε** that includes the effect of flow can be expressed as:

$$\boldsymbol{\varepsilon} = \frac{\alpha + i\,(k_o + \alpha)}{1-M^2} = \frac{i\,\boldsymbol{\beta}}{1-M^2} \qquad (4.2)$$

where **β** is defined in equation (2.10) and the Mach number, M, is computed with the speed of sound, C_o, which is a function of air temperature and relative humidity (Cramer, 1993). The speed of sound computed with 25% typical relative humidity increases by 0.4 m/s compared to dry air, which is taken into account for an accurate identification of the acoustic waves. The absorption coefficient α is the sum of a thermo-viscous term (Davies, l988) and a turbulent friction term (Munjal, 1987). The Mach number M is computed based on the measured mean flow velocity. The resulting over-determined system of linear equations is solved by means of least squares algorithm using MATLAB. The residuals of the three equations are used to assess the accuracy of the methodology. From the identified complex amplitudes p^+ and p^-, the acoustic pressure and volume velocity at the edge of the cavity can be computed using the following equations:

$$\mathbf{p}(x_{edge}) = e^{\boldsymbol{\varepsilon} Mx_{edge}} \left(\mathbf{p}^+ e^{-\boldsymbol{\varepsilon} x_{edge}} + \mathbf{p}^- e^{\boldsymbol{\varepsilon} x_{edge}} \right) \qquad (4.3)$$

$$\mathbf{q}(x_{edge}) = \frac{e^{\varepsilon M x_{edge}}}{\mathbf{Y}} \left(\mathbf{p}^{+} e^{-\varepsilon x_{edge}} - \mathbf{p}^{-} e^{\varepsilon x_{edge}}\right) \tag{4.4}$$

The induced pressure difference is modeled as a lumped pressure difference $\Delta\mathbf{p}$ at the middle of the cavity. The acoustic pressure is extrapolated from the upstream and downstream edges to the center of the cavity using the transfer matrix method described by Munjal (1987). According to the theory by Karal (1953) and Kergomard and Garcia (1987), the transition inductance between the main pipe diameter and the larger cavity diameter was also considered and the extrapolation was computed using a pipe section of length equal to half the cavity length (L/2) and ignoring flow and damping in this short section of the pipe. The difference in the extrapolated acoustic pressures at the cavity center from the upstream ($\mathbf{p}_{c,up}$) and downstream ($\mathbf{p}_{c,dn}$) edges is the lumped pressure difference $\Delta\mathbf{p}$. Note that $\Delta\mathbf{p}$ is a complex value, and its phase reference is the acoustic volume velocity at the middle of the cavity. This pressure difference is then normalized according to the definition of the source term **S** as follows:

$$\mathbf{S} = \frac{2\,\Delta\mathbf{p}}{\mathbf{q}_c\, M\, Y_o} \tag{4.5}$$

where $\mathbf{q}_c$ is the acoustic volume velocity at the center of the cavity ($\mathbf{q}_c = \boldsymbol{\upsilon}\ .\ A$), Y_o is the specific acoustic impedance, $\rho_o C_o$, and M is the Mach number, U/C_o. Based on the conservation of mass principle, the acoustic volume velocity at the center of the cavity should be identical for extrapolations from both sides; the difference is computed and assessed as a measure of the accuracy of the methodology.

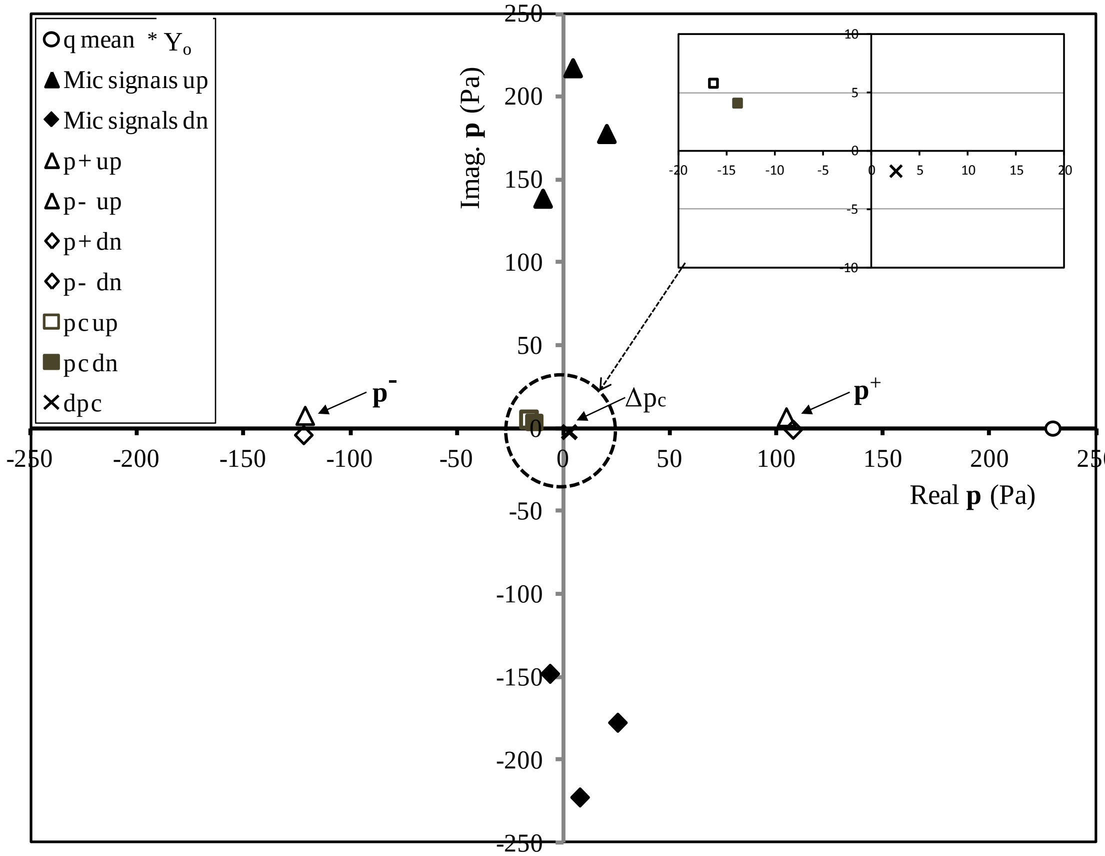

Figure 4.3: An example of the analysis of one measurement showing all the measured and computed acoustic pressures and volume velocities at the cavity center.

The loudspeaker mounted at the side-branch end is used to excite the acoustic waves in the piping system at the desired frequency (78 Hz). This excitation overrides the self-excitation of the first harmonic mode. The source term was measured by the procedure mentioned above for different combinations of St and υ/U, the St is varied from 0.3 to 1.2 by controlling the flow velocity in the range from 25 m/s to 5 m/s (Reynolds number 1.4 x 10^5 to 0.3 x 10^5), and the ratio of the acoustic particle velocity to mean flow velocity is changed from 0.2% to 25%. The following section shows the results at these measurement conditions.

4.2.3 Accuracy and Uncertainty

The pressure difference $\Delta\mathbf{p}$ induced by the unsteady flow in the cavity is rather small; depending on the flow conditions, it ranges from 0 to approximately 10% of the maximum acoustic pressure in the main pipe. The value of $\Delta\mathbf{p}$ is determined as the difference between two fluctuating pressure amplitudes, which are both affected by several sources of inaccuracy. It is, therefore, difficult to evaluate $\Delta\mathbf{p}$ accurately because small relative inaccuracies in the microphone signals or the wave number (frequency) can lead to substantial relative inaccuracies in the source term **S**. Therefore, many accuracy checks were performed as described in the following sections.

The accuracy was first evaluated by calculating the residuals of the microphones, which are obtained from the difference between the measured acoustic pressure at the location of each individual microphone and that obtained at the same location from the superposition of the computed upstream and downstream travelling waves, which are determined by the least squares algorithm using all 3 microphone signals. These residuals of the microphone signals were less than 0.25% of the sound pressure at the microphones as shown in figure 4.4.

The second methodology of accuracy evaluation was performed by calculating the residuals-2 of the microphones, which are obtained from the difference between the measured acoustic pressure at the location of each individual microphone and that obtained at the same location from the superposition of the upstream and downstream travelling waves, which are computed using the other 2 microphone signals. These residuals of the microphone signals were less than 0.35% of the sound pressure at the microphones as shown in figure 4.5. The difference in acoustic volume velocity at the cavity mid-span, calculated from both sides of the cavity, is the third accuracy check that showed an offset of approximately 1 % of the volume velocity at this velocity anti-node location as shown in figure 4.6.

Additional tests were performed to further evaluate the ***overall accuracy*** of the method. These included measurements with a section of straight pipe instead of the cavity. Also, measurements with a cavity without flow were taken and analyzed using the same procedure. For these configurations, the induced pressure difference Δp and therefore also the source term **S** are expected to vanish. In the first case, which involves a piece of straight pipe instead of the cavity, unsteady flow structures are not expected to form, and if they form anywhere within the measurement section, their propagation would be axial, and thus parallel to the acoustic particle velocity, and, therefore, no acoustic power would be generated (Howe, 1975). Figure 4.7 presents the real part of the measured source of a straight pipe section in comparison with that measured for the cavity. It is clear that the source term for the no cavity case is negligibly small over the test range.

In the second case, aeroacoustic sources would also vanish in the absence of flow. Measurements were taken at several frequencies near 78 Hz, which is the pipe resonance frequency, and for a wide range of flow velocities and acoustic pulsation amplitudes. Note that the source term is not defined for the no-flow condition and, therefore, the results are given in term of $\Delta \mathbf{p}$. Typical results of the measured $\Delta \mathbf{p}$ with and without flow are given in figure 4.8. The no-flow results correspond to two excitation levels, $\upsilon = 0.02$ and 0.05 m/s. the results taken with flow correspond to a mean flow velocity range of 5-23 m/s and excitation level $\upsilon/U = 0.2$ to 25%. The results show that the measured pressure difference $\Delta \mathbf{p}$ without flow is less than 0.14 Pa, which is less than 3% of the maximum pressure difference measured with flow.

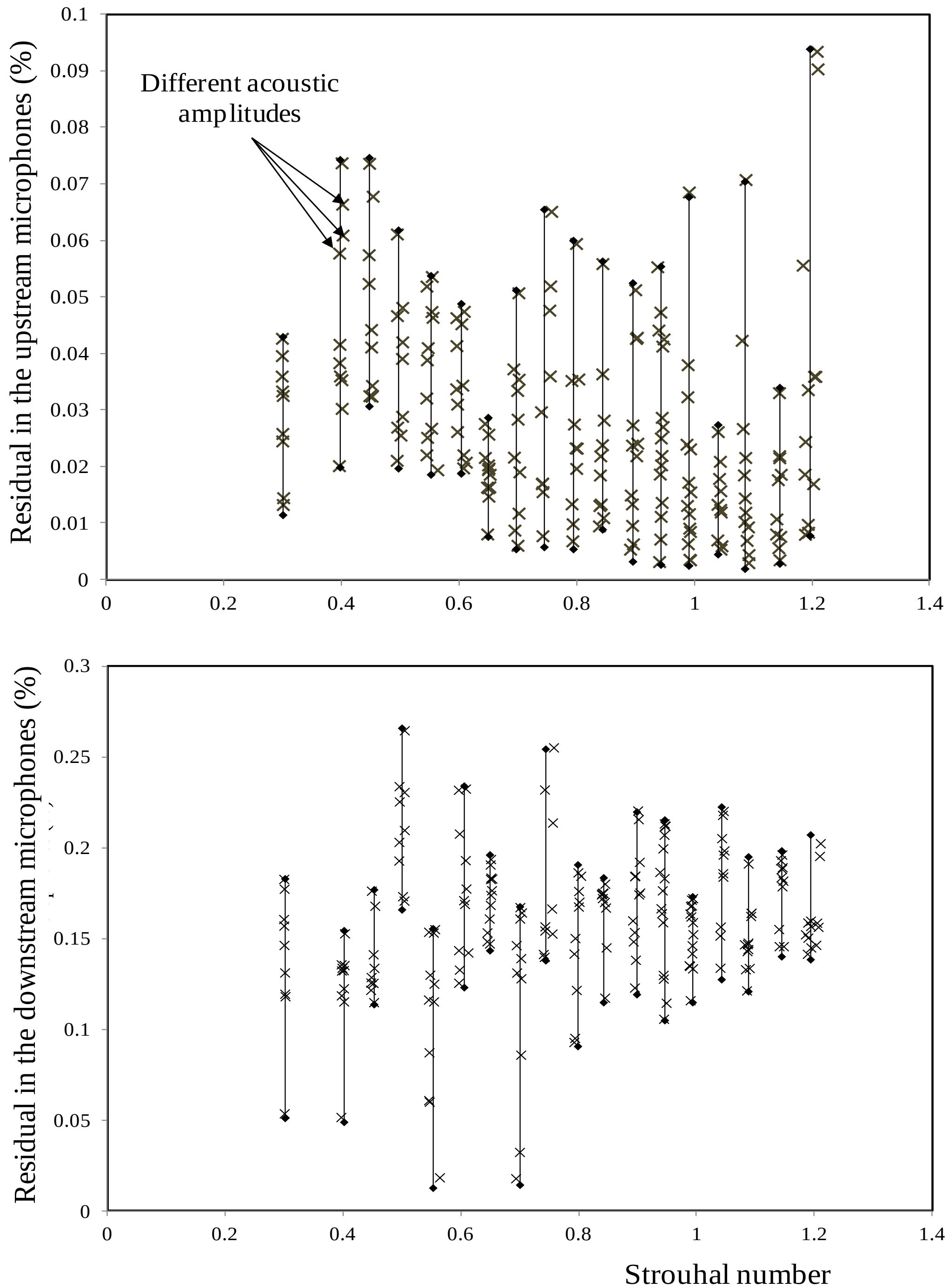

Figure 4.4: Microphones residuals calculated as the difference between the measured acoustic pressure at the location of each individual microphone and that obtained at the same location from the superposition of the computed upstream and downstream traveling waves.

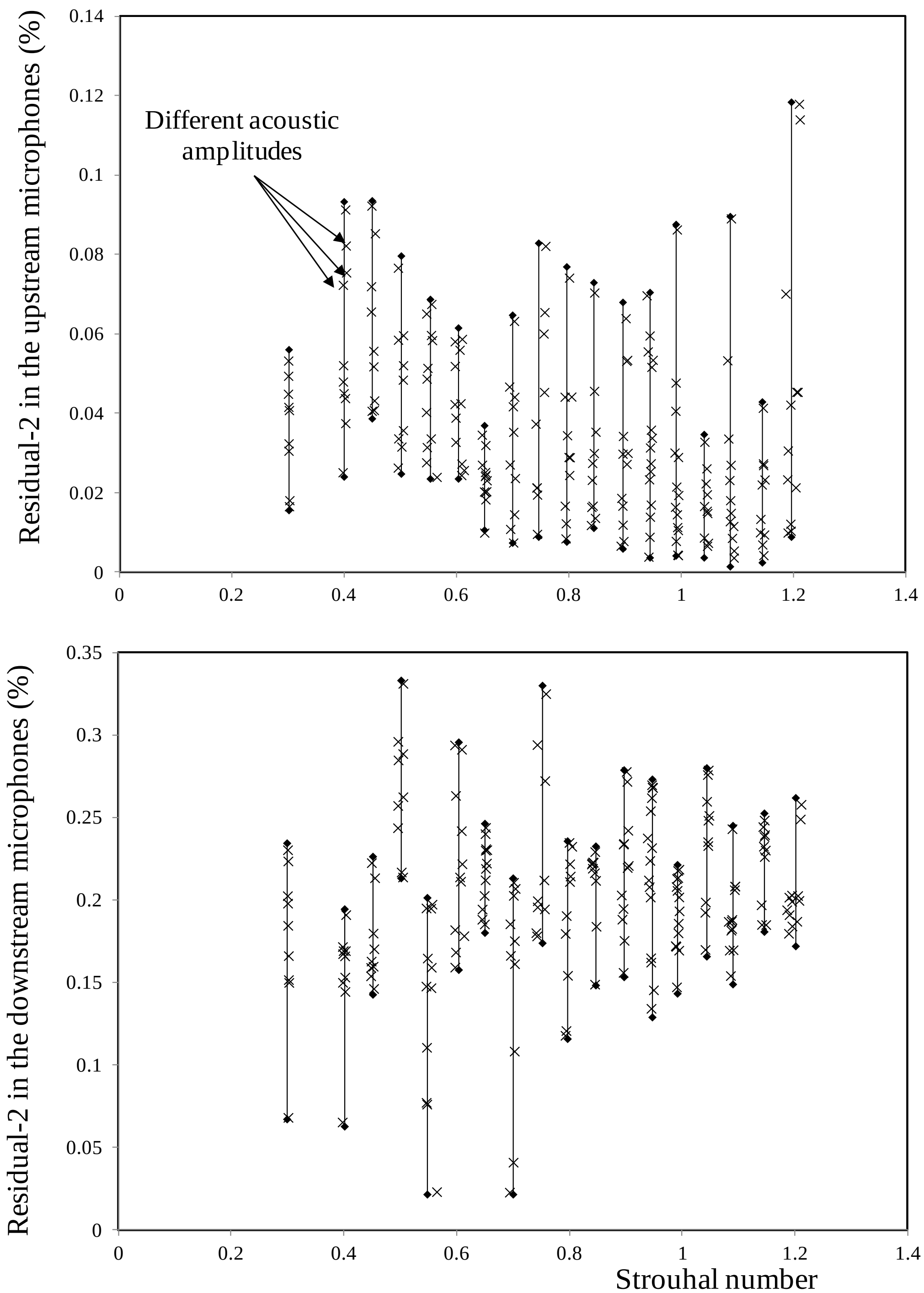

Figure 4.5: Microphones residual-2 which was obtained from the difference between the measured acoustic pressure at the location of each individual microphone and that obtained at the same location from the superposition of the computed upstream and downstream travelling waves, which were identified using the other 2 microphone signals.

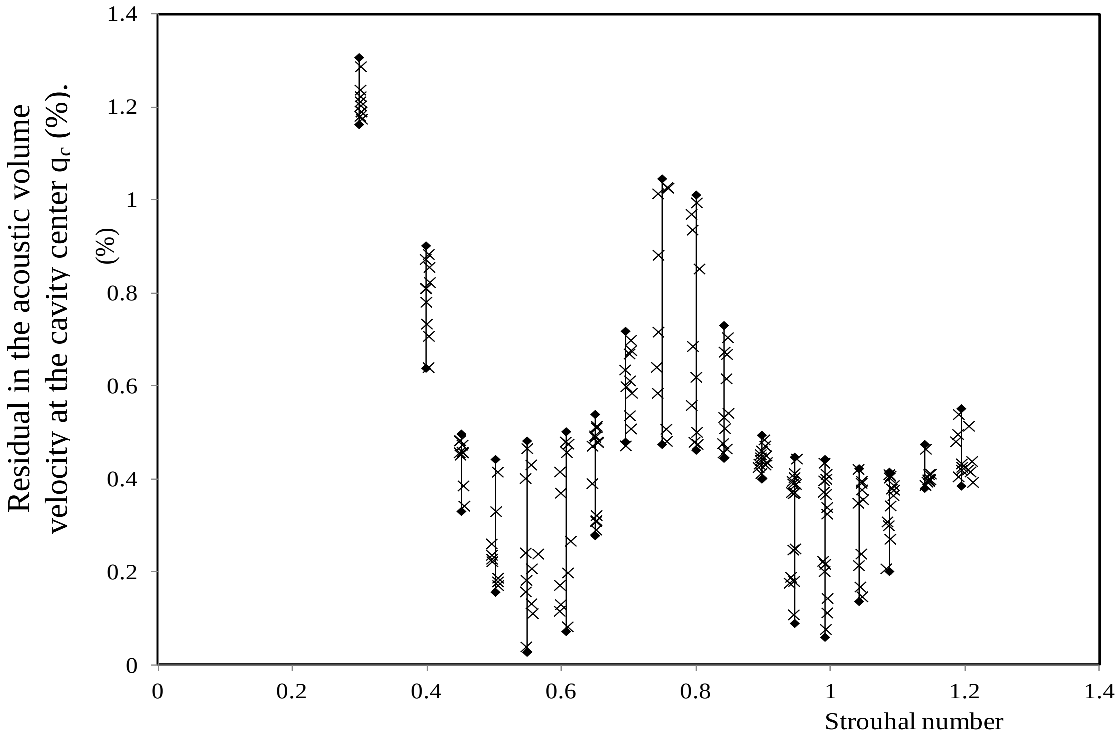

Figure 4.6: Residual in the acoustic volume velocity at the cavity mid span which describes the ratio of the difference in acoustic volume velocity at the cavity mid-span, calculated from both sides of the cavity, to the mean value of the acoustic volume velocity at this location

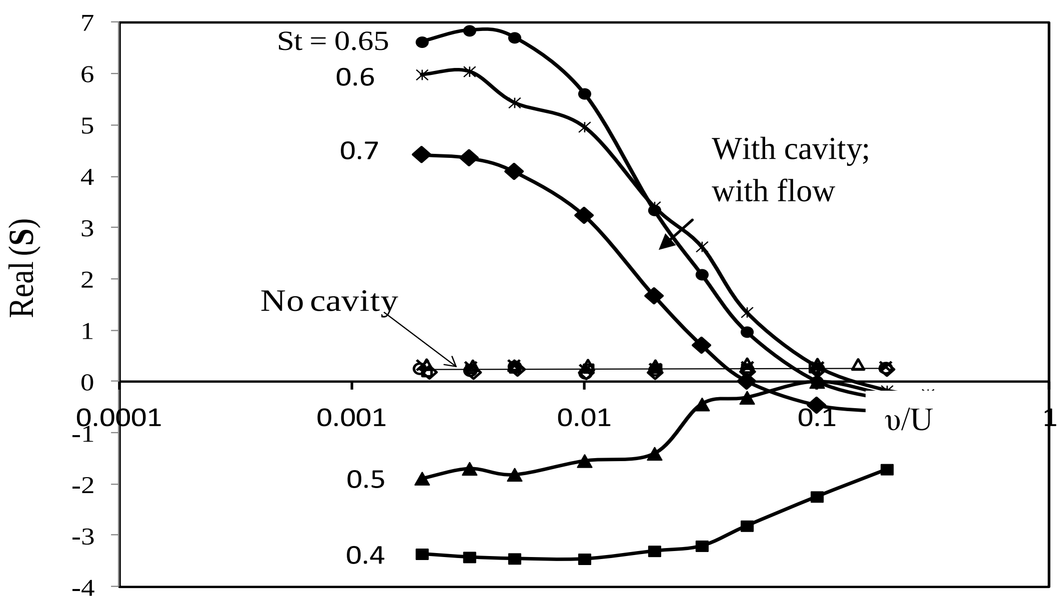

Figure 4.7: Results of overall accuracy check tests showing the variation of real source term with the amplitude ratio υ/U for both cases with and without cavity for different values of Strouhal number.

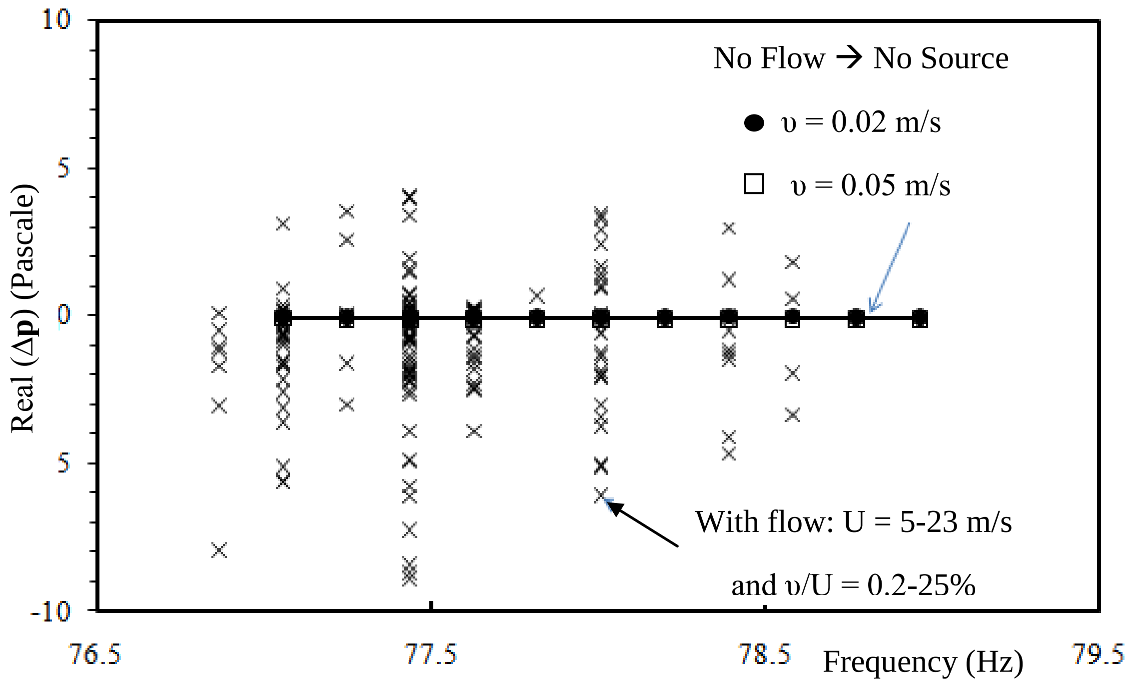

Figure 4.8: Results of overall accuracy check tests showing the variation of real $\Delta\mathbf{p}$ with the frequency for both cases; with and without flow.

4.2.4 Characteristics of the Aeroacoustic Source

The lumped complex pressure difference $\Delta\mathbf{p}$ at the center of the cavity and the complex source term **S** were determined experimentally as a function of the Strouhal number, St, and the ratio between the acoustic particle velocity at the cavity center and the mean flow velocity in the main pipe, υ/U. Figure 4.9 shows the dependence of the complex pressure difference $\Delta\mathbf{p}$ on the Strouhal number St and the oscillation amplitude υ /U. Each data point indicates one value of $\Delta\mathbf{p}$ based on a steady state measurement at given Strouhal number and excitation amplitude. From this figure, as the St Number decreases, the pressure difference $\Delta\mathbf{p}$ increases. At St around 0.6, the pressure difference is nearly positive real, which means the acoustic disturbance is completely in-phase with the acoustic particle velocity at the cavity, and this should result in a very strong aeroacoustic source. While at St between 0.3-0.4 and around 0.9, the pressure difference is approximately negative real, which means the acoustic disturbance is completely out of phase with the acoustic particle velocity at the cavity, resulting in an aeroacoustic sink and flow absorption of energy from the acoustic field. The positive imaginary component of the pressure difference acts like an additional stiffness which slightly increases the frequency of self-excited oscillations. The negative imaginary component acts as an added mass, thus reducing the self-excited frequency.

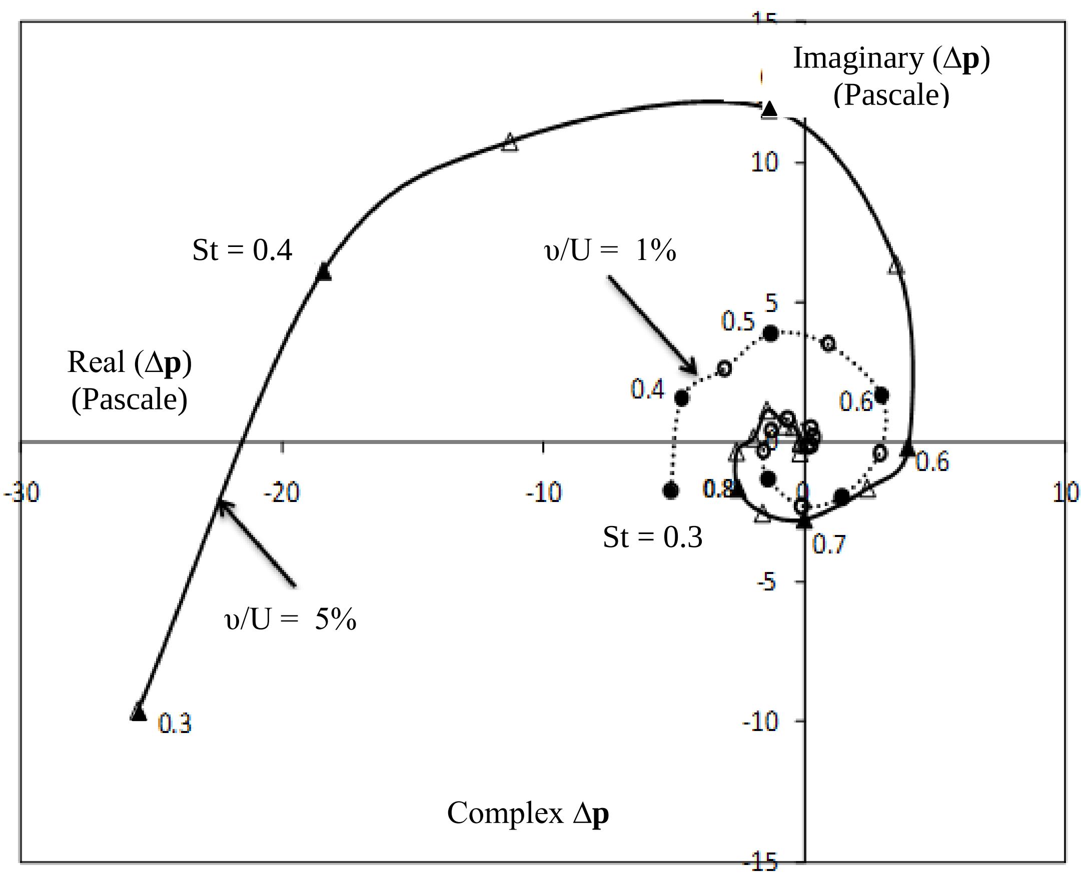

Figure 4.9: The complex pressure difference Δ**p** at υ/U= 5% (——) and υ/U = 1% (·····). The filled data points represent the indicated values of St number.

Figure 4.10 shows the same data of figure 4.9 but in the form of the normalized source term S. The data shows the dependence of this complex source term on the Strouhal number and the oscillation amplitude. The Strouhal number, St, has primarily an effect on the argument, i.e. the phase of **S**, and therefore it controls the phasing between the acoustic field and the vortex propagation in the shear layer. On the other hand, the oscillation amplitude, υ/U, influences mainly the modulus, or the absolute value of **S**. The complex-valued nature of the source term is a key feature of the concept presented in this research; the real part represents the generation or absorption of acoustic power, whereas the imaginary part is associated with reactive power which has the effect of additional mass or stiffness. Since only the real part is responsible for the exchange of active acoustic power, let's have a closer look at this component, although the imaginary component is equally important in the overall context.

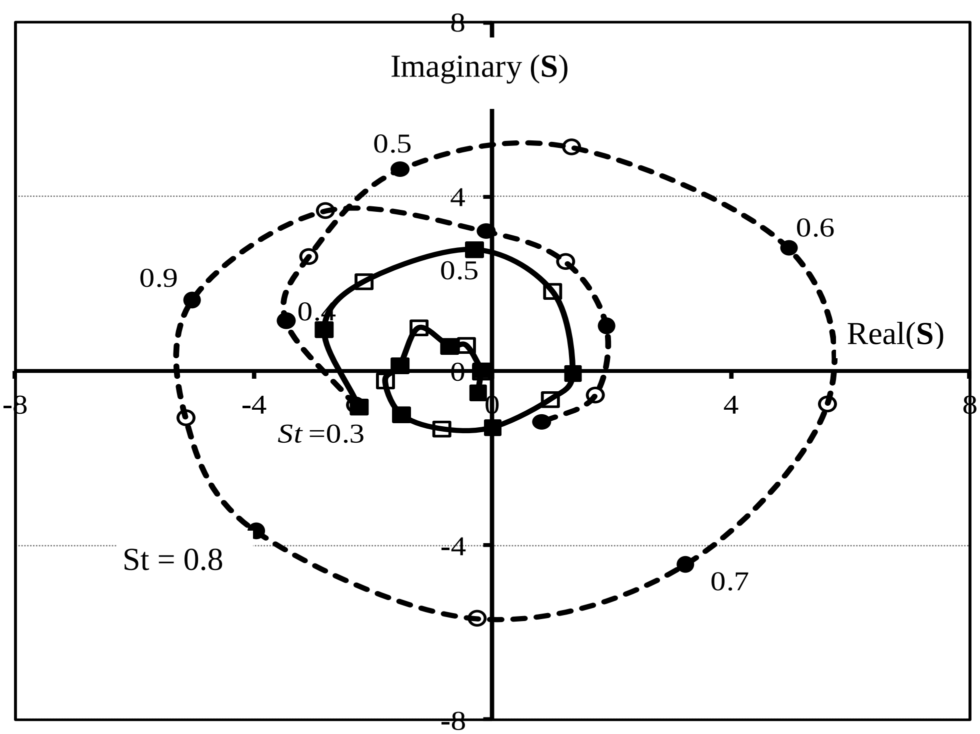

Figure 4.10: The complex source term, **S**, at υ/U= 5% (——) and υ/U = 1% (•••••). The filled data points represent the indicated values of St number with a step 0.1

Figure 4.11 shows the real part of the source term as a function of the oscillation level for different Strouhal numbers as parameters. The figure reveals that acoustic power is generated by the shear layer for Strouhal numbers around St ≈ 0.65 and oscillation levels υ/U < 0.1. At very low oscillation levels, υ/U < 0.005, the source term is approximately independent of oscillation level; this is considered the linear range where the induced pressure difference is proportional to the excitation level υ/U (and consequently their ratio is constant). In this range, the initial shear layer disturbances are very small, and the wavelike pattern of the shear layer grows exponentially for the most part as it travels downstream and does hardly roll up into vortices-like structures.

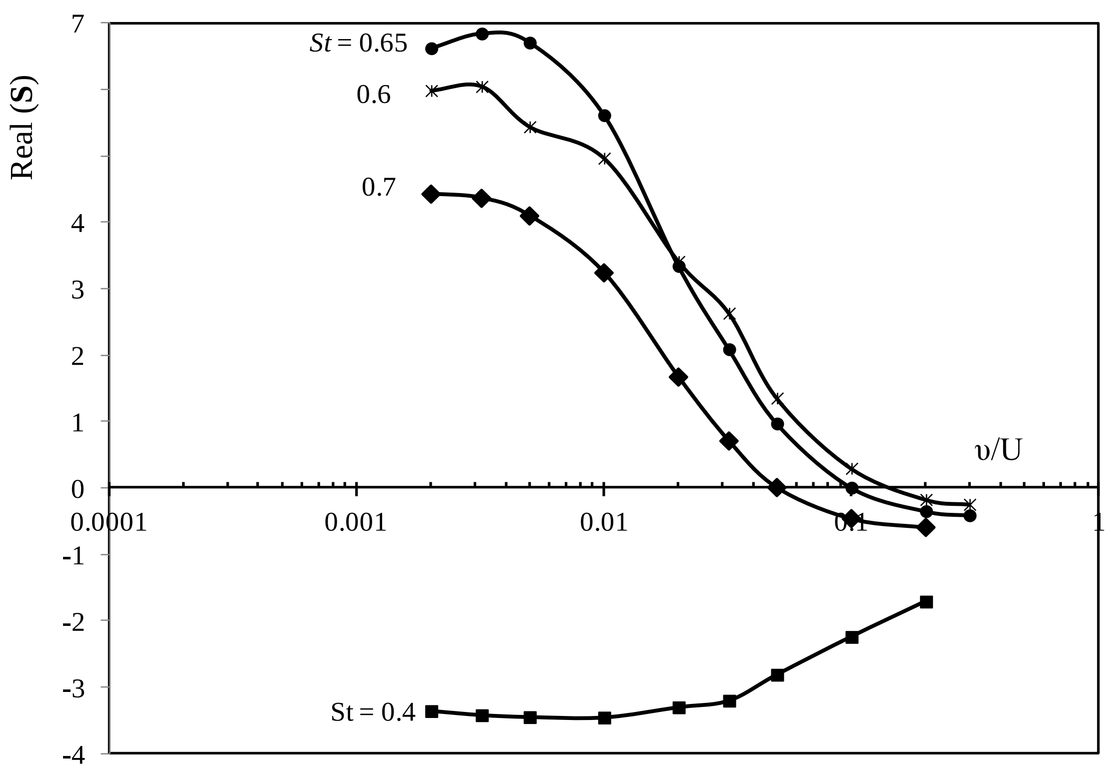

Figure 4.11: Real part of the aeroacoustic source as a function of acoustic particle velocity, υ/U, at the cavity center for different values of St number.

For the range $0.005 < \upsilon/U < 0.1$, the real part of the source term drops considerably, indicating that the induced pressure difference increases substantially less than proportional to the excitation level. This is indicative of nonlinear effects due to amplitude saturation of the shear layer oscillation. As illustrated in the flow visualization by Ziada (1994), most of the vorticity in the shear layer rolls up into vortices and the roll up starts earlier, i.e. closer and closer to the upstream edge, as the oscillation amplitude increases. For $\upsilon/U > 0.1$, the real part of the source term remains negative for all Strouhal numbers. In this range, the mechanism is dominated by absorption of acoustic power due to vortex damping (Ziada, 1994). The source behaviour in this non-linear range will be discussed in detail with the aid of the PIV measurements in Chapter 5.

Figure 4.12 presents the real component of the source term as a function of Strouhal number with the oscillation level as a parameter. Two ranges of Strouhal number with the generation of acoustic power are apparent: St ≈ 0.5 to 0.75 and St ≈ 1.0 to 1.25. Based on previous investigations, the lower range of Strouhal number resulting in generation of acoustic power can be attributed to the "Single Vortex Mode", where only one discrete vortex is formed over the cavity length, and the higher range of St ≈ 1.0 to 1.25 is likely resulting from the "Double Vortex Mode", where two vortices are formed over the cavity length at any instant in the acoustic cycle. In fact, the data trend in Figure 4.12 suggests a nearly periodic system of Strouhal number ranges with alternating generation and absorption of acoustic power.

The effect of the excitation level υ/U on the source term shown in figure 4.12 indicates a slight decrease of St for the condition of maximum power generation as the oscillation level increases, e.g. at $\upsilon/U = 0.005$, the peak of power generation is at St ≈ 0.65, whereas for υ/U = 0.1, the peak of power generation is at St ≈ 0.55. Based on the flow visualization study by Ziada (1994), this is because the level of oscillation influences the timing and the location of the formation of the shear layer vortices and thereby their propagation within the acoustic cycle. At very high oscillation levels, the discrete vortices form earlier, closer to the upstream edge and deeper inside the cavity, where the convection velocity is lower therefore their propagation across the cavity span is delayed in comparison to the case of lower υ/U. Consequently, the timing for the optimal generation of acoustic power requires higher U at a given frequency and cavity span L, and, therefore, the corresponding St is somewhat lower.

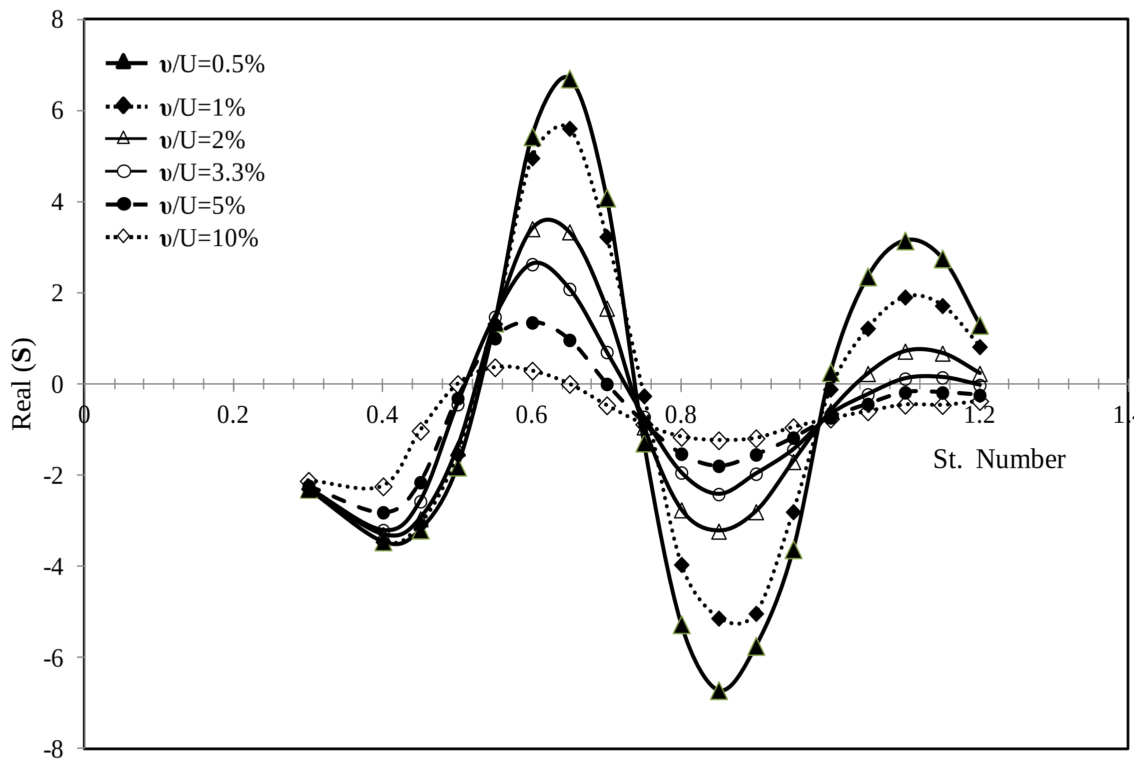

Figure 4.12: Real part of the aeroacoustic source as a function of St number for different values of acoustic particle velocity, υ/U, at the cavity center.

In summary, an experimental characterization of the aeroacoustic source of an axisymmetric cavity in a pipeline is presented. The source is determined for high Reynolds number, fully developed turbulent pipe flow. The experimental technique employs six microphones distributed upstream and downstream of the cavity to evaluate the fluctuating pressure difference generated by the oscillating cavity shear layer in the presence of externally imposed sound waves. The amplitude and phase of this pressure difference are used to determine the dimensionless aeroacoustic source of the cavity shear layer. The accuracy of the method is discussed in some detail. The results are in good agreement with the concepts of free shear layer instability and the fluid-resonant oscillations behavior. The dependence of the source term on the Strouhal number and acoustic velocity at the cavity is presented for one shallow cavity geometry. The next section will discuss the validation of the SWM results.

4.3 Validation of the Measurement Technique and the Measured Source

The main objective of this section of the research is to validate the measurement technique and the measured source term from the Sound Wave Method. The validation methodology depends on comparing the self-excited resonance response (resonance amplitude and frequency) obtained from self-excitation measurements of the same axisymmetric cavity with that estimated from an acoustic model supplemented with the measured source term using the SWM. This validation process is addressed in the following subsections.

4.3.1 Experimental Investigation of the Self-Excited Resonance Oscillations

In the experimental work of the SWM, the resonance in the pipe system is driven externally by the loudspeaker in order to be able to control the pulsation amplitude and frequency. In industrial applications, the acoustic resonance is self-excited by the aeroacoustic source in the cavity. Therefore, an additional piping system was designed which includes the same cavity that was used in section 4.2.1, but without the loudspeaker. By changing the flow velocity, the frequency and amplitude of the self-excited pressure fluctuations can be measured by means of two microphones. The test setup for the self-excited measurements was described in detail in section 3.2 and figure 3.8. At different values of the flow velocity U, the two microphone signals were recorded for 60 seconds and then averaged to get the frequency spectrum using MATLAB code. The results from the self-excited system are presented in figures 4.13 and 4.14.

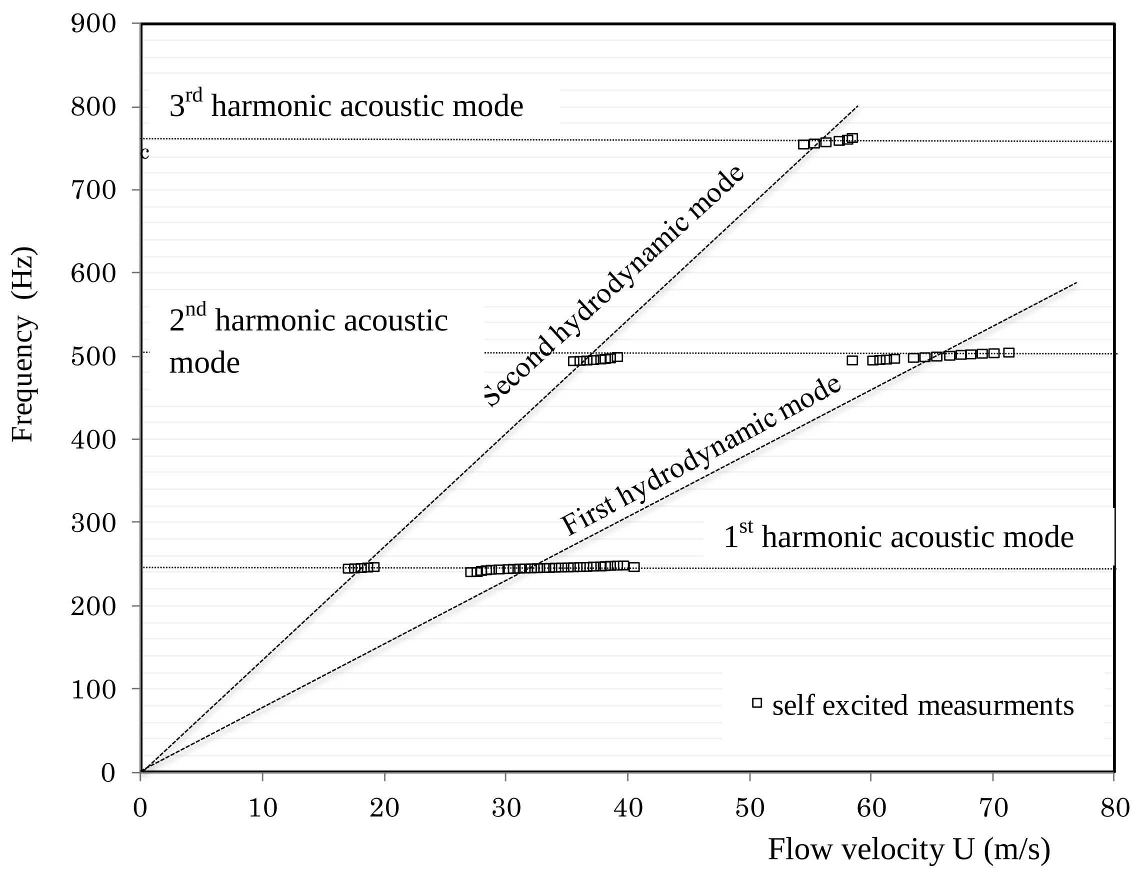

Figure 4.13: Self-excited results; resonance frequencies verses the flow velocity

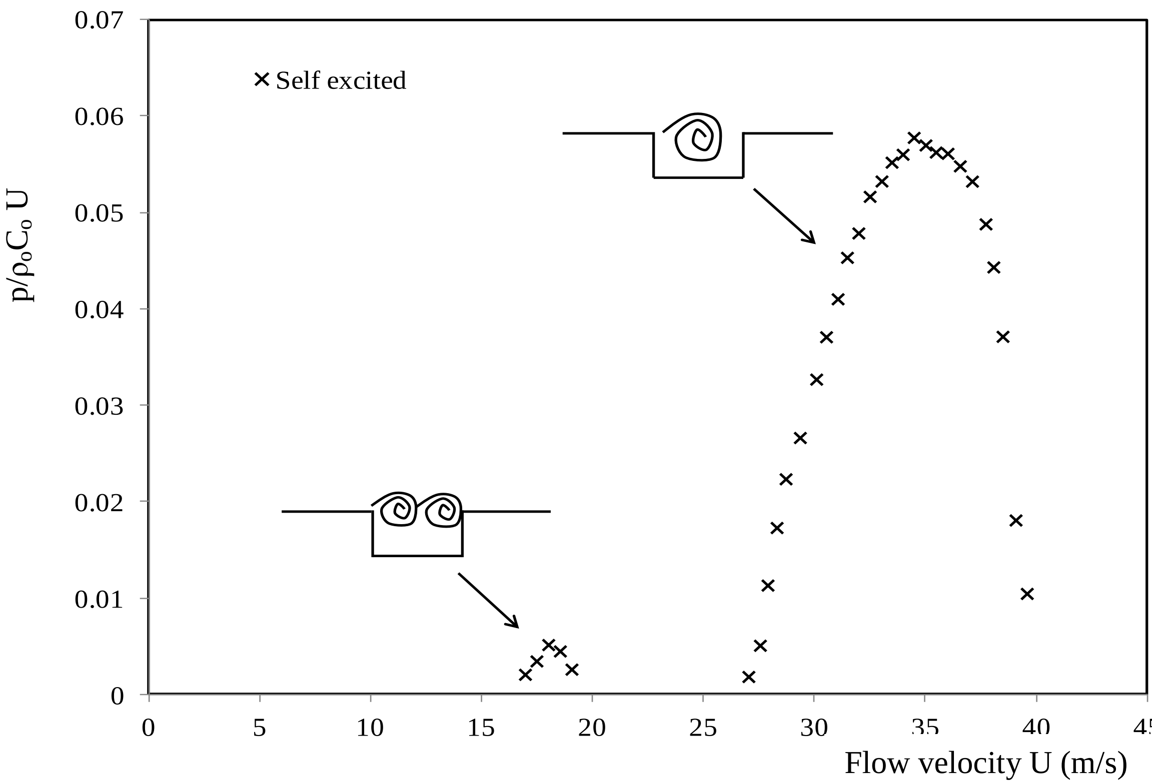

Figure 4.14: Self-excited results; normalized acoustic amplitude verses the flow velocity

Figure 4.13 shows that three acoustic modes are self-excited within the tested flow range. It also shows the lock-in velocity ranges for the first and the second hydrodynamic modes (i.e. the shear layer oscillation modes). Figure 4.14 shows the resonance intensity verses the flow velocity for the first harmonic acoustic mode. The resonance intensity is presented by the normalized amplitude ratio ($p/\rho_o C_o U$), which is equivalent to υ/U, where C_o is the speed of sound. From this figure, resonance by the first hydrodynamic mode, i.e. the first mode of the shear layer oscillations, occurs over the velocity range from 27 m/s to 40 m/s with a maximum amplitude ratio of 5.8%. However, the second hydrodynamic mode resonance occurs in the velocity range of 17 to 19 m/s with a relatively small peak amplitude ratio of 0.5%.

4.3.2 Modeling of Flow-Excited Resonance

The aim of this task is to use the measured source from the SWM as a function of Strouhal number and oscillation amplitude ratio to predict the self-excited oscillation amplitude and frequency for a given acoustic system and flow conditions. This model consists of a linear acoustic model of the piping system supplemented by the source strength for the same cavity measured from SWM in section 4.2. Note that although the piping model is linear, the source strength is highly non-linear, in both the Strouhal number and acoustic amplitude ratio and, therefore, an iterative method will be used to obtain the self-excited oscillations characteristics.

In order to predict the amplitude and frequency of the flow-excited oscillation, the acoustic pressure difference $\Delta\mathbf{p}$ required to drive the acoustic oscillation at a given volume velocity was computed. The acoustic input impedances for the upstream and the downstream pipes at the middle of the cavity were computed. The difference between these acoustic impedances represents the load impedance ($\Delta\mathbf{p}_{load}/\ \boldsymbol{\upsilon}$). Steady state oscillations will occur when the aeroacoustic source term, **S**, is equal to the normalized load impedance:

$$\frac{(\Delta\mathbf{p}_{load} / \ \frac{1}{2}\rho_o U^2\ )}{\upsilon/U} - \mathbf{S}\left(St\ ,\ \frac{\upsilon}{U}\right) = 0 \qquad (4.6)$$

The real part of this equation implies that the acoustic absorption in the piping system is balanced by the acoustic energy generation by the aeroacoustic source. The imaginary part of this equation implies that the reactive load of the piping system is balanced by the reactive component of the source term. Both, the real and imaginary parts of the equation must be satisfied for steady state oscillations. From the above equation, the measured source as a function of Strouhal number and oscillation amplitude ratio can be used to predict the oscillation amplitude and frequency of a given acoustic system and flow condition.

4.3.2.1 Calculation of the Load Impedance (Δp_{load})

In the schematic of figure 4.15, the procedure of calculating the load impedance at the cavity center is described. In this figure, the acoustic impedance at point 1 is $\mathbf{Z}_1 = \mathbf{p}_1 / \boldsymbol{\upsilon}_1$, and at point 2 is $\mathbf{Z}_2 = \mathbf{p}_2 / \boldsymbol{\upsilon}_2$.

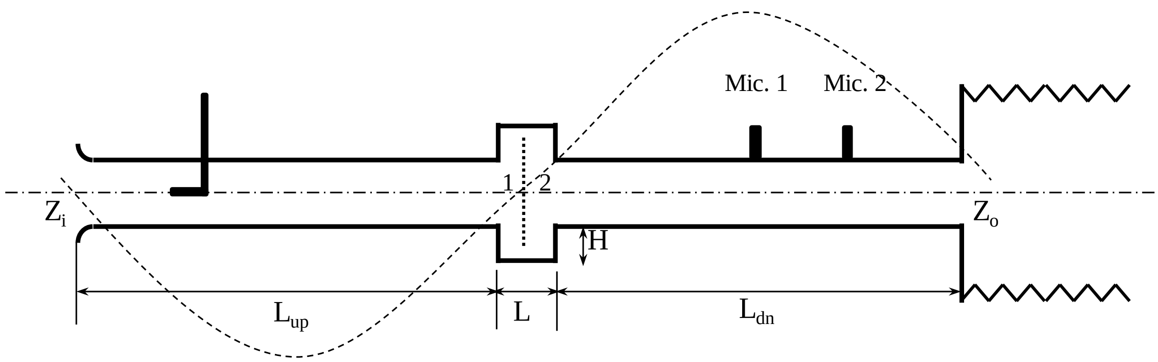

Figure 4.15: Schematic of the aeroacoustic model for the calculation of the load impedance difference at the cavity mid-span

Since from continuity, $\boldsymbol{\upsilon}_1 = \boldsymbol{\upsilon}_2 = \boldsymbol{\upsilon}$ (4.7)

$\Delta\mathbf{Z}_{load} = (\mathbf{p}_1 - \mathbf{p}_2) / \boldsymbol{\upsilon} = \Delta\, \mathbf{p}_{load} / \boldsymbol{\upsilon}$ (4.8)

And the normalized $\Delta\mathbf{Z}_{load}$ is:

$\Delta\mathbf{Z}_{loadN} = (\Delta\, \mathbf{p}_{load} / ½\, \rho_o U^2) / (\upsilon / U) = (\mathbf{Z}_1 - \mathbf{Z}_2) / ½\, \rho_o U$, (4.9)

Where

$\mathbf{Z}_1 = \mathbf{Z}_i * [\, M_{up}]$ & $\mathbf{Z}_2 = \mathbf{Z}_o * [\, M_{dn}]$ (4.10)

Here $\mathbf{Z}_i$ is the open pipe radiation impedance at the pipe entrance (Munjal, 1987). This radiation impedance is a function of the pipe diameter and the frequency (wave number) and the specific acoustic impedance ($Y_o = \rho_o C_o$). M_{up} and M_{dn} are the upstream and downstream transfer matrices respectively, which are multiplier factors that include the effects of the straight pipes L_{up} and L_{dn}, area changes from pipe to cavity diameters, and half of the cavity length from each side. They also include the thermo-viscous attenuation factor and the turbulent viscous losses and, therefore, these matrices are functions of geometry, flow conditions, and frequency of the acoustic standing wave (Munjal, 1987).

Referring to figure 4.15 again, $\mathbf{Z}_o$ is the radiation acoustic impedance from the pipe to the hose and it would be overestimated by considering it similar to radiation acoustic impedance from an open pipe to atmosphere, or underestimated by considering it similar to radiation acoustic impedance at area enlargement from a solid pipe to a solid larger diameter pipe instead of a flexible hose. Figure 4.16 shows a schematic of the different reflection coefficient **R** at the pipe outlet using the different evaluation methods, where the acoustic impedance $\mathbf{Z}_o = (1/(1+\mathbf{R}))$. For an accurate evaluation of this acoustic impedance, experimental measurements of the acoustic impedance at the hose using the two–microphone method were performed. Two methods were used in these measurements, first, by using external excitation with the aid of a loudspeaker without flow, and secondly, during broad band pipe response which was self-excited by flow.

The Steady state oscillations will occur when the aeroacoustic source term is equal to the normalized load impedance as shown in equation (4.6). This nonlinear complex equation is solved for two unknowns, the frequency and the amplitude ratio, using a MATLAB code with a nonlinear complex equations solver toolbox.

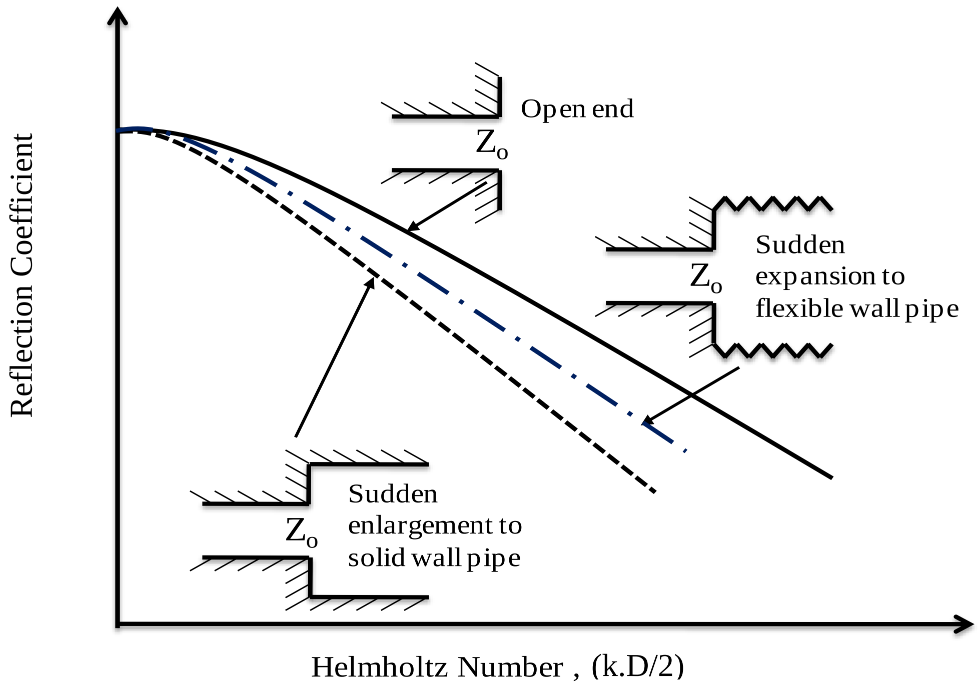

Figure 4.16: Schematic of different reflection coefficients, $|R|$ at the pipe outlet using three different evaluation methods

A comparison is then performed between the resonance oscillation amplitude and frequency as obtained from the self-excitation measurements and from applying the model of flow-excited resonance and the measured aeroacoustic source. This comparison is presented in figures 4.17 and 4.18 in order to validate the measured aeroacoustic source using SWM in section 4.2

A comparison of the resonance frequency verses the flow velocity between the self-excited resonance measurements and the acoustic model using the measured source from SWM is shown in figure 4.17. This comparison depicts a very good agreement for the resonance frequency and lock-in ranges. Therefore, it can be concluded that the measured source term can accurately predict the onset and frequency of resonance.

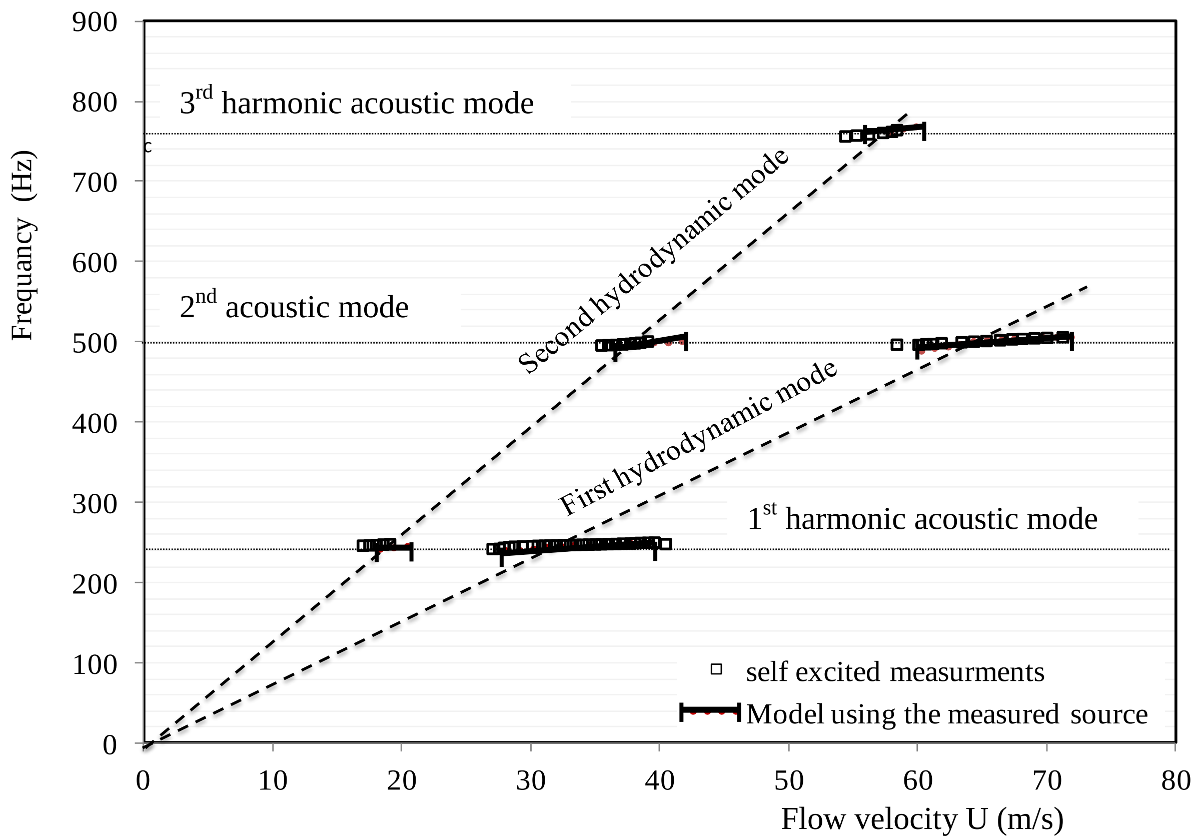

Figure 4.17: Validation of the measured source term by comparing the measured self-excited frequencies and lock-in range with those predicted by the source term.

Figure 4.18 compares the results of the resonance amplitude for both the self-excitation measurements and the acoustic model using the measured source term. From this comparison, there is an excellent prediction of the amplitude of resonance using the acoustic model with the measured source. Therefore, these results validate the aeroacoustic source measured by the SWM. Figure 4.18 also shows the acoustic model results using different evaluation methods of the acoustic impedance $\mathbf{Z}_o$ at the connection between the pipe and the hose. The method of measuring $\mathbf{Z}_o$ with self-excitation by the flow gives the best agreement with the self-excited results, because the effect of flow was taken into consideration when measuring the exit impedance $\mathbf{Z}_o$.

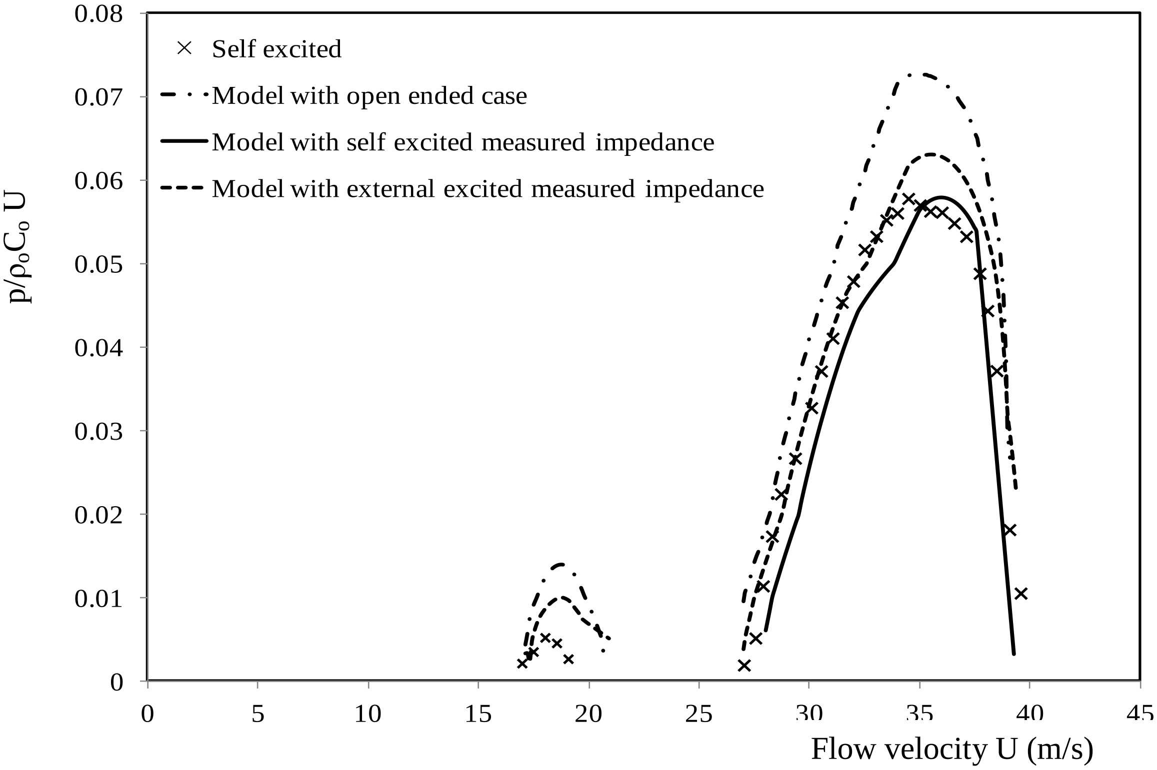

Figure 4.18: Validation of the measured source term by comparing the measured self-excited amplitude of the first acoustic mode and the model results

In summary, the results of this section validate the measured source term by the SWM. It can also be noted that the prediction of the resonance amplitude and frequency by means of the acoustic model and the measured source term is truly superior to all models existing in the literature to date. In the next chapter, an investigation of the flow-structure-sound interaction mechanism using the PIV measurement technique is presented.

Chapter 5

Flow-Structure-Sound Interaction Mechanism: Spatial Distribution of Aeroacoustic Sources

In this chapter, an investigation of the flow-structure-sound interaction mechanism using the PIV technique is performed in the first part. The characteristics of this interaction mechanism are explored for different combinations of Strouhal number and acoustic resonance amplitude as well as for different cavity sizes and hydrodynamic modes. In the second section of this chapter, the results of the PIV flow measurements and finite element simulations of the acoustic mode are combined into Howe's aeroacoustic integrand to compute the spatial and temporal distributions of the aeroacoustic sources resulting from the cavity shear layer interaction with the sound field. The spatially and temporally averaged aeroacoustic source is then compared with that obtained by means of the Sound Wave Method (SWM) to highlight the advantages and disadvantages of each methodology. The PIV measurements test setup was discussed in detail in section 3.3.

5.1 Flow-Structure-Sound Interaction Mechanism

There are three main objectives of performing flow visualization measurements of the flow-structure-sound interaction mechanism using the PIV system. The first objective is to understand the behavior of the aeroacoustic source with the variation of the Strouhal number and the excitation level (υ/U) and to provide a physical explanation of the non-linear variations of the aeroacoustic power at large amplitude acoustic oscillations. The second objective is to clarify the effect of the cavity volume on the flow characteristics in the cavity region such as the convection speed and the mixing mechanism. This may lead to a better understanding of the effect of the cavity volume on the onset of resonance and on the aeroacoustic source amplitude. The third objective is to quantify the unsteady velocity and vorticity fields in order to use them as input data to Howe's integrand to identify the instantaneous and time averaged spatial distribution of the aeroacoustic sources.

5.1.1 Tested Cavities and Measuring Conditions

Two cavity sizes were used in this flow visualization study with dimensions of 52 mm in length by 26 mm in depth (L x H = 52 x 26 mm), and 104 mm by 52 mm. So, both cavities have the same L/H ratio of 2 but are different in volumes. The loudspeaker is used to control the excitation frequency and the acoustic oscillation amplitude while the blower speed controller is used to adjust the flow velocity. Therefore, a wide range of Strouhal number and excitation level (υ/U) combinations can be tested. Multiple microphones are used to quantify the acoustic field (the acoustic particle velocity at the cavity). At each specified Strouhal number and fluctuation amplitude ratio, the acoustic cycle is divided into eight time instants, uniformly spaced at 45° apart, as shown in figure 5.1. At each time instant, 200 image pairs were captured which were then averaged to determine eight instantaneous flow fields from a total of 1600 image pairs.

For the smaller cavity used, the whistling Strouhal number is 0.65 for the first hydrodynamic mode. Therefore, the PIV measurements are taken at this Strouhal number for five values of the fluctuation amplitude ratio (υ/U =0.2%, 1%, 5%, 10%, and 20%) in order to understand the nonlinear behaviour of the aeroacoustic source and its saturation at high amplitude ratio. In addition, the effect of Strouhal number at the same amplitude ratio is investigated by measuring the flow field at υ/U = 5% for several values of Strouhal numbers (St = 0.55, 0.6, 0.65, 0.75, and 0.8), which is the range of Strouhal numbers at which positive aeroacoustic power is generated at the first hydrodynamic mode.

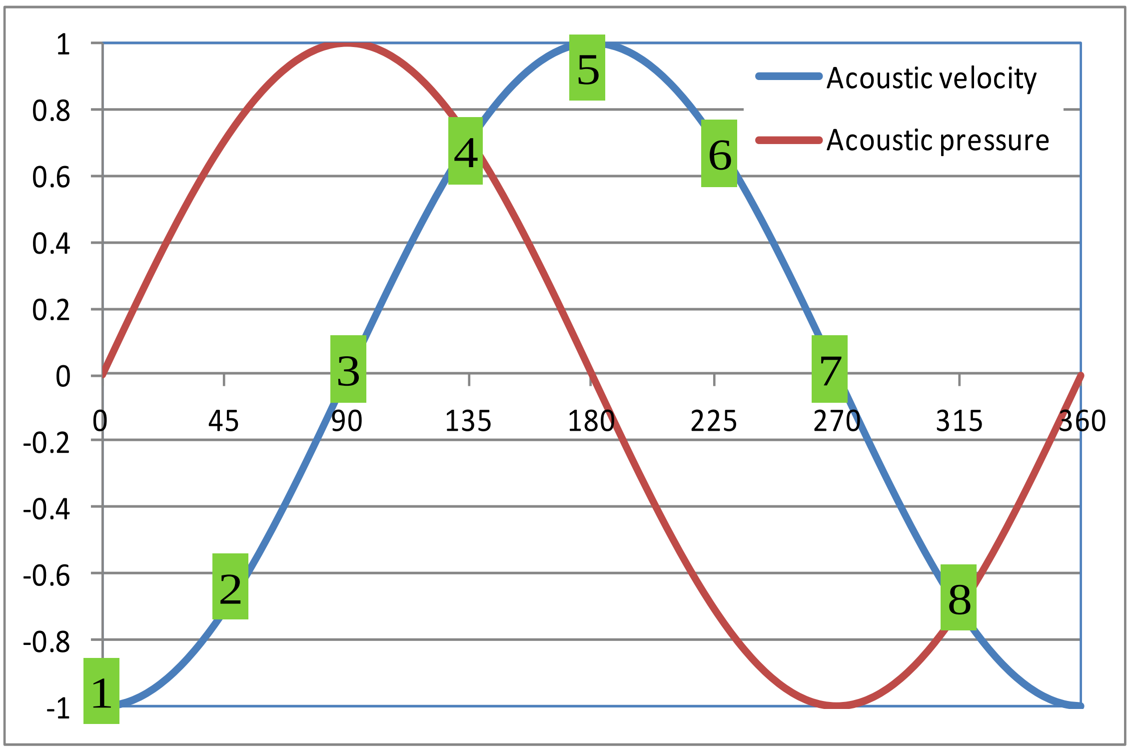

Figure 5.1: The eight time instants (phase locked) during the acoustic cycle

For the larger size cavity, the flow visualization was performed to understand the effect of the cavity volume on the whistling Strouhal number and the aeroacoustic source strength. First, the effect of Strouhal number at the same amplitude ratio is investigated by measuring the flow field at υ/U = 5% for several values of Strouhal number (St = 0.6

to 1.5). This large size cavity has a whistling Strouhal number of 0.8 for the first hydrodynamic mode and 1.3 for the second hydrodynamic mode. Therefore, the PIV measurements are taken at these Strouhal numbers with five values of the fluctuation amplitude ratio (υ/U = 0.2%, 1%, 5%, 10% and 20%). The flow visualization domain is selected to be from the cavity centerline to the cavity walls as shown in figure 5.2.

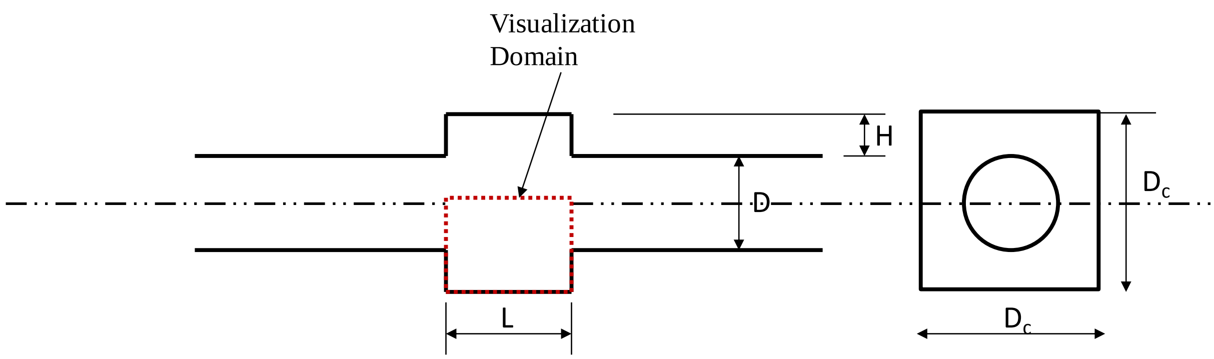

Figure 5.2: Visualization domain and geometrical parameters

Sample results of the flow visualization for the small cavity (52 x 26 mm) are shown in figure 5.3. In this figure, the flow velocity and vorticity magnitudes at different phase instants in the acoustic cycle are presented. These sample results are taken at a Strouhal number of 0.65 and an amplitude ratio of υ/U = 5%. The dark contours in the velocity fields identify the location of the vortical structures over the cavity opening. These vortex contours and the weighted center location of the vortex are calculated using the velocity discriminate parameter proposed by Vollmers [16]. The ratio between the differences in vortical structure center locations in two consecutive phase instants to the time interval between these two phase instants is the convection speed of the structure.

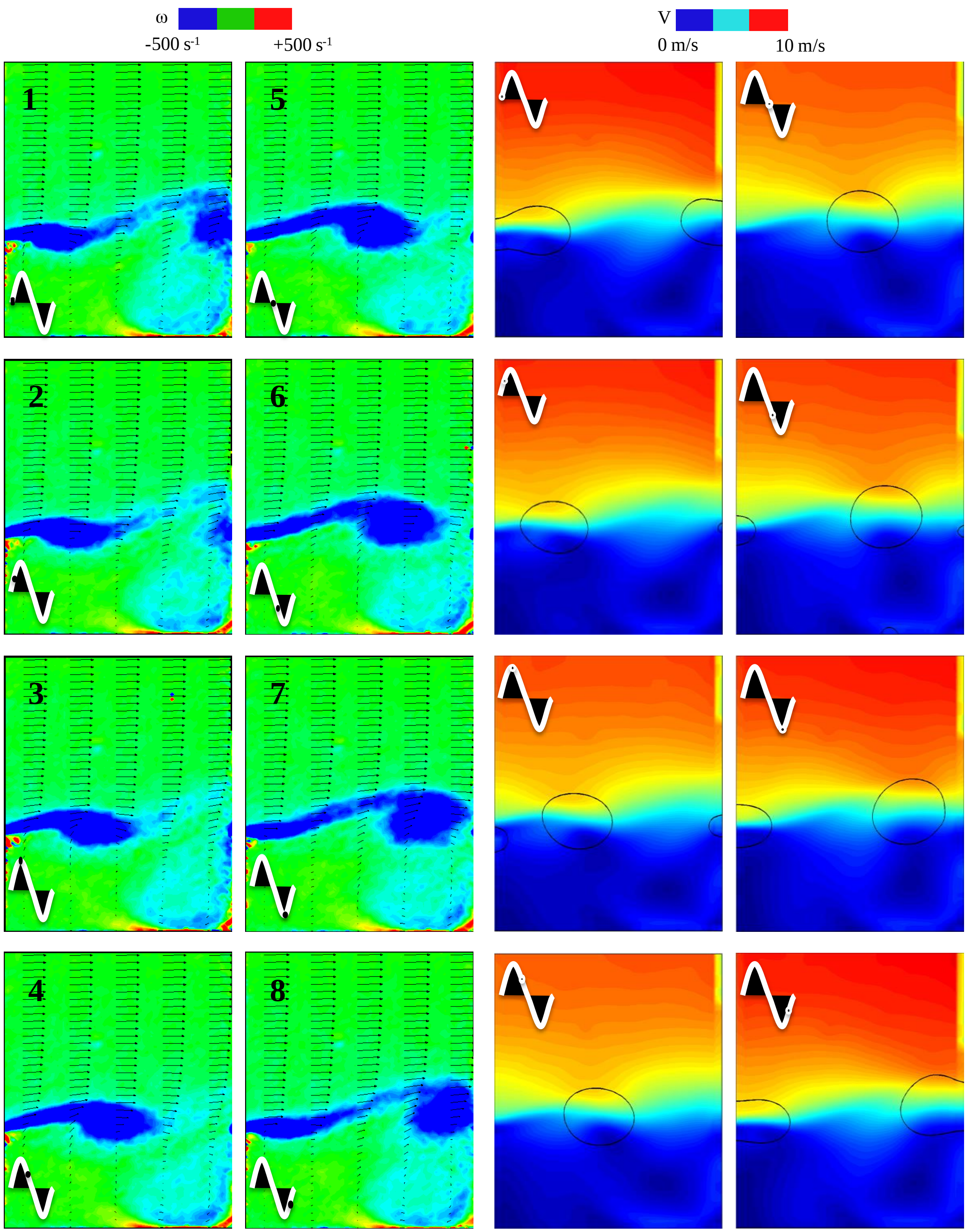

Figure 5.3: Sample of the flow visualization results at the eight instants during the acoustic cycle for the small cavity at the peak whistling condition St = 0.65 and υ/U = 5%. Right column is the velocity field and the left column is the vorticity field. Arrows in vorticity field show the velocity vectors.

5.1.2 Effect of Strouhal Number on the Flow-Structure-Sound Interaction

Figures 5.4 and 5.5 show the spatial distributions of the vorticity field for two cavity sizes at different flow velocities (Strouhal number) but constant acoustic amplitude ratio of 5%. The selected velocities include: (a) the flow velocity matching the peak whistling Strouhal number at the first hydrodynamic mode, i.e.$U = U_{peak1}$ (St =0.65 for the small cavity and 0.8 for the large cavity), for which the time scale of flow oscillation (the hydrodynamic period) matches the acoustic cycle periodic time; (b) higher flow velocities ($U > U_{peak1}$) at which the Strouhal numbers are lower than the peak whistling Strouhal number and therefore the travelling time of the free shear layer disturbance becomes shorter than the peak whistling traveling time; and (c) lower flow velocities ($U < U_{peak1}$), at which the Strouhal numbers are higher than the peak whistling Strouhal number and therefore the travelling time of the free shear layer disturbance is longer than the disturbance traveling time at the peak whistling condition.

For the case of peak resonance condition, $U = U_{peak1}$ (St = 0.65 in figure 5.4 and 0.8 in figure 5.5), the vorticity field at this condition shows a vorticity cloud covering a certain distance along the cavity mouth followed by a concentrated vortex formation which travels along the remaining length of the cavity mouth. For the case of post-resonance condition ($U > U_{peak1}$), the vorticity field at this condition shows a vorticity cloud covering a larger portion of the cavity mouth. The faster travelling vorticity field reaches the downstream corner before the acoustic particle velocity reverses direction, and therefore this flow condition is not conducive to self-excitation of acoustic resonances and acoustic disturbances would be dampened out.

For the case of pre-resonance condition ($U < U_{peak1}$), the vorticity field at this condition shows more than one concentrated vortex traveling along the cavity mouth during the same acoustic cycle which means that the vorticity field travels so slow such that the acoustic field reverses direction again (in comparison to the peak resonance case) before the arrival of the relevant vortex. Here again, the net effect of sound generation is not sufficiently high to sustain acoustic resonances. As the flow velocity becomes close to half the peak resonance condition velocity, the second hydrodynamic mode of the shear layer excites the acoustic resonance at resonance at St =1.3 ($U = U_{peak2}$) for the large cavity as shown in figure 5.5.

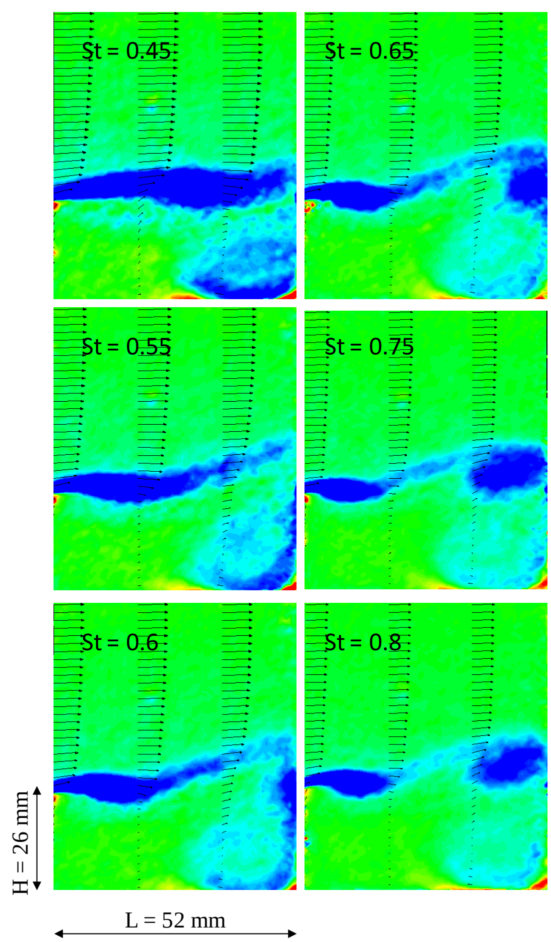

Figure 5.4: The spatial distributions of the vorticity field at different flow velocities (St number) with constant acoustic amplitude ratio of 5% at the same instant in the acoustic cycle. Small cavity size 52 x 26 mm.

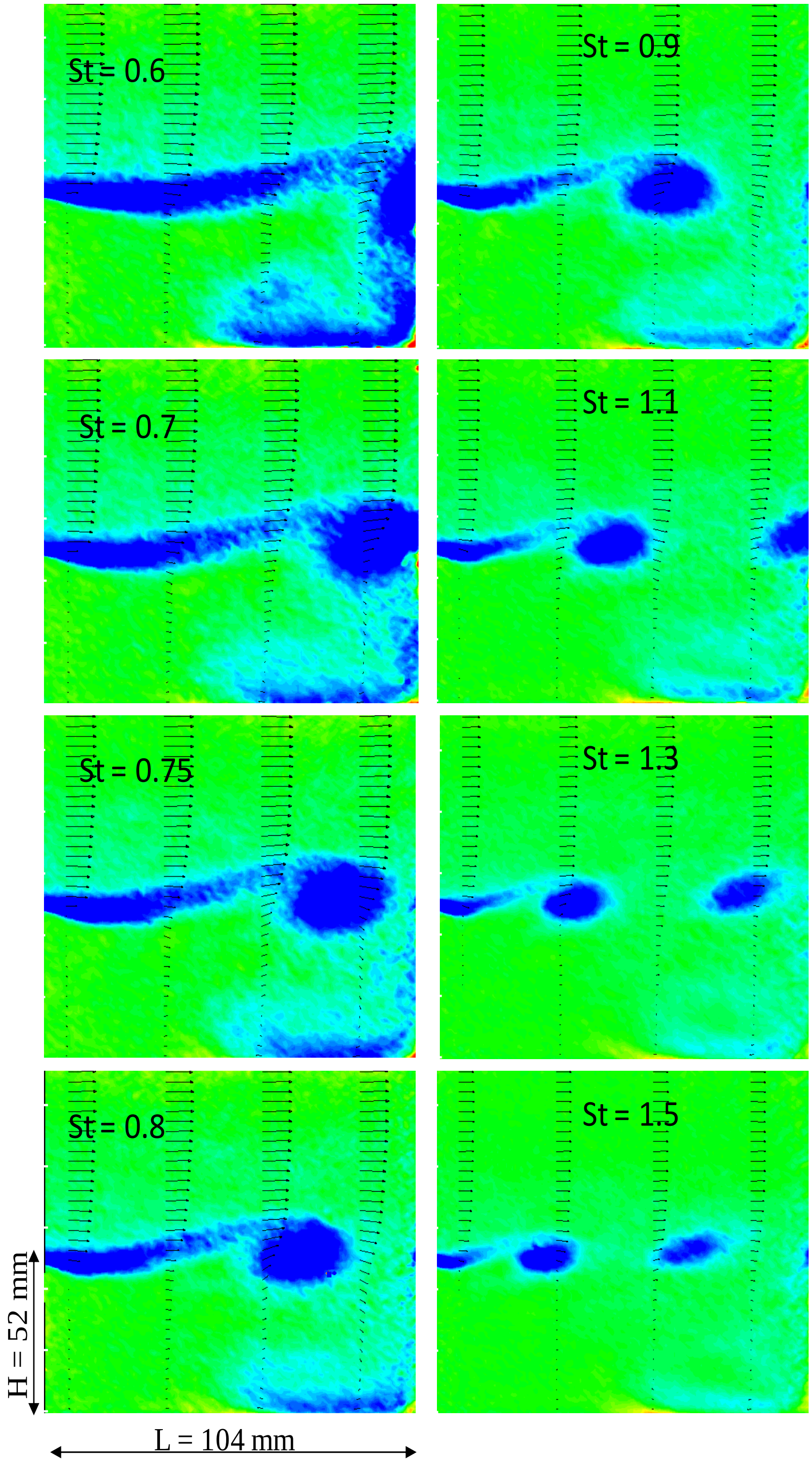

Figure 5.5: The spatial distributions of the vorticity field at different flow velocities (St Number) with constant acoustic amplitude ratio of 5% at the same instant in the acoustic cycle. Large cavity size 104 x 52 mm.

5.1.3 Effect of Acoustic Resonance Amplitudes on Flow-Structure-Sound Interactions

Visualizations of the flow-sound interaction patterns for the cavity flow at the peak-whistling Strouhal number (St = 0.65 for the small cavity and 0.8 for the large one) at different amplitude ratios show that the variation of the amplitude ratio υ/U strongly affects the vorticity field, and hence the aeroacoustic source strength as shown in figures 5.6 and 5.7

One can observe that there are three vorticity field distribution patterns with the variation of the amplitude of resonance υ/U. First, a low level of oscillations in which the vorticity field takes the form of a vorticity cloud along the cavity mouth. Secondly, high levels of oscillation regime (10% and 20%) in which the vorticity field takes the form of well-defined vortices which appear near the cavity leading edge and travel along the cavity mouth. As the resonance amplitude increases in this regime, the released concentrated vortex will always be generated at the leading edge but with a higher circulation rate. Finally, an intermediate level of oscillation regime (as in the case of υ/U = 5%) in which the vorticity field takes the form of a combination of an initial vorticity cloud followed by a well-defined vortex which forms after a certain distance from the cavity leading edge and travels along the remaining part of the cavity mouth. This can be considered as a transition regime between the low and high amplitude patterns. An investigation of the relation between the change in the vorticity field distribution pattern and the aeroacoustic power will be presented in the next section.

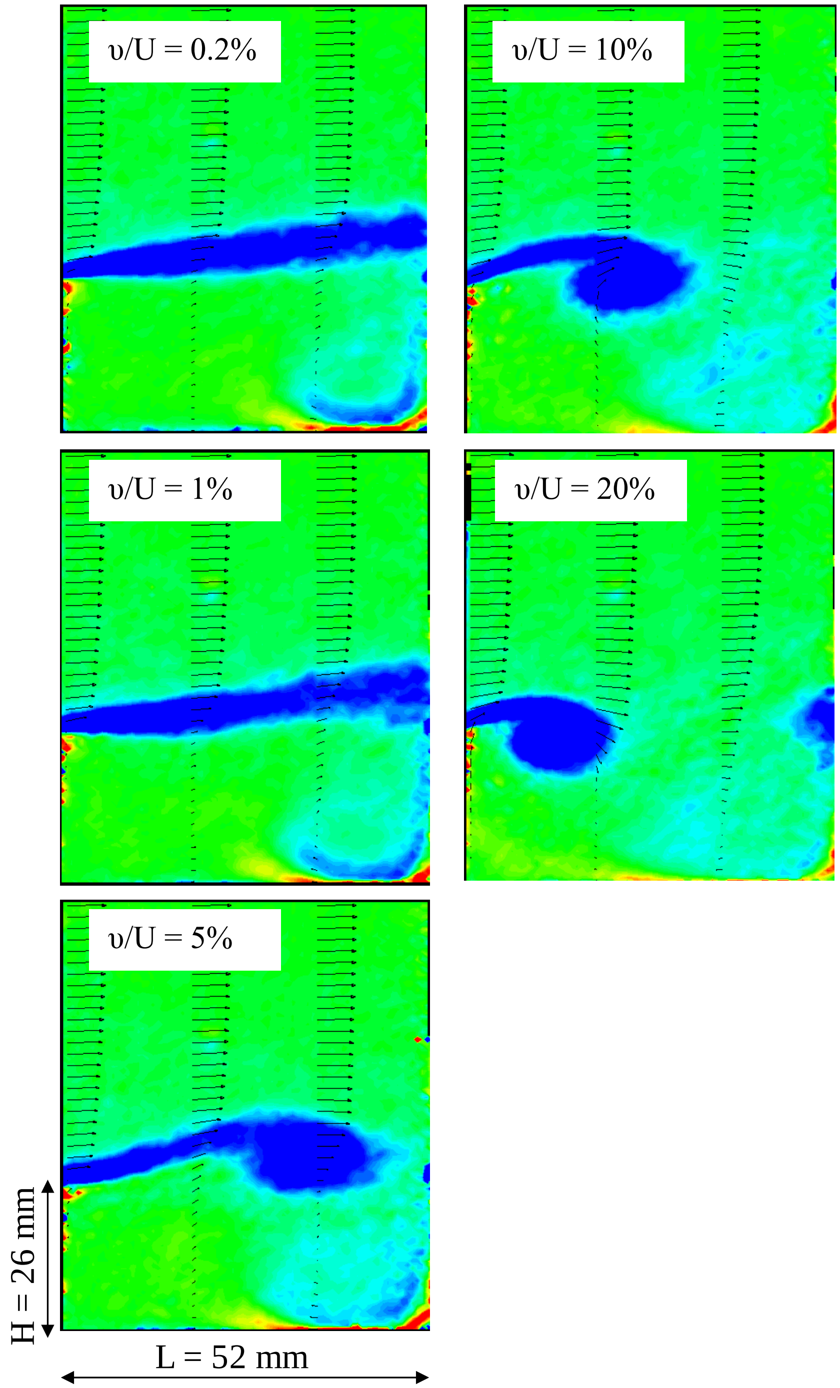

Figure 5.6: Visualization of the flow-sound interaction patterns for the cavity flow at the peak-whistling Strouhal number at the same instant in the acoustic cycle (St = 0.65 for the small cavity)

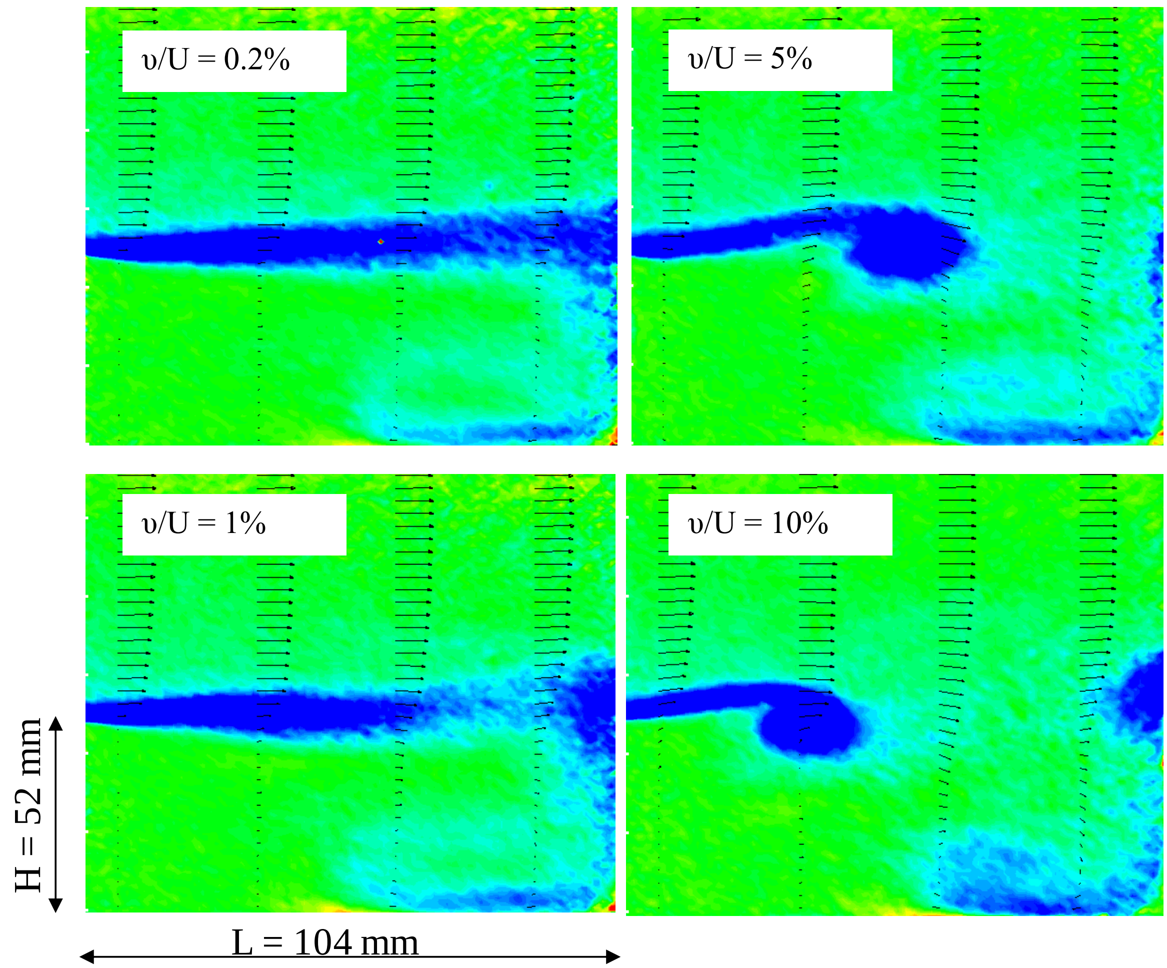

Figure 5.7: Visualization of the flow-sound interaction patterns for the cavity flow at the peak-whistling Strouhal number at the same instant in the acoustic cycle. (St = 0.8 for the large cavity)

5.2 PIV Measurements of Aeroacoustic Sources

In this section, the aeroacoustic sources generated by flow over a shallow cavity in a pipeline are studied in the presence of plane sound waves at various Strouhal numbers and sound intensities. This study is based on the extensive PIV flow measurements which are described in the previous section to characterize the unsteady velocity and vorticity fields at various time instants within the sound cycle. Finite element analysis is used to obtain the particle velocity distribution of the sound field. The results of the PIV flow measurements and those of the finite element simulations are combined into Howe's aeroacoustic integrand (equation 2.18) to compute the spatial and temporal distributions of the aeroacoustic sources resulting from the cavity shear layer interaction with the sound field. Howe states that the instantaneous acoustic energy source is proportional to the triple product of the vorticity ω, flow velocity U, and the acoustic particle velocity υ. The results are compared with the measured aeroacoustic source strength obtained by means of the Sound Wave Method (SWM), which has been addressed in chapter 4.

5.2.1 Simulation of the Acoustic Field

A numerical simulation of the resonant sound field was performed using finite element analysis in ABAQUS 6.1. At resonance, a strong standing sound wave forms longitudinally throughout the length of the pipe housing the cavity. The acoustic pressure field of this standing wave is presented as follows:

$$p(x,y,t) = p(x,y).\ p(t) \qquad (5.1)$$

where p(x,y) is the spatial variation component and p(t) is the time variation component. This time component of the acoustic pressure is a simple harmonic oscillator and can be expressed as:

$$p(t) = p_{max} \sin(\omega t) \qquad (5.2)$$

where $\omega = 2\pi f$ and p_{max} is the maximum amplitude acoustic pressure obtained by the three microphones method. The spatial component p(x,y) was computed by solving the Helmholtz equation for the entire piping system without flow using finite element analysis. The piping system housing the cavity is modeled as shown in figure 5.8. At the inlet and outlet sections of the pipe, the boundary condition for the acoustic mode is set to zero acoustic pressure. The computational grid consisted of three-node linear 2-D acoustic triangular elements with a finer mesh size at the cavity zone. Grid independency tests were performed to ensure the reliability of the results before performing the final computation runs.

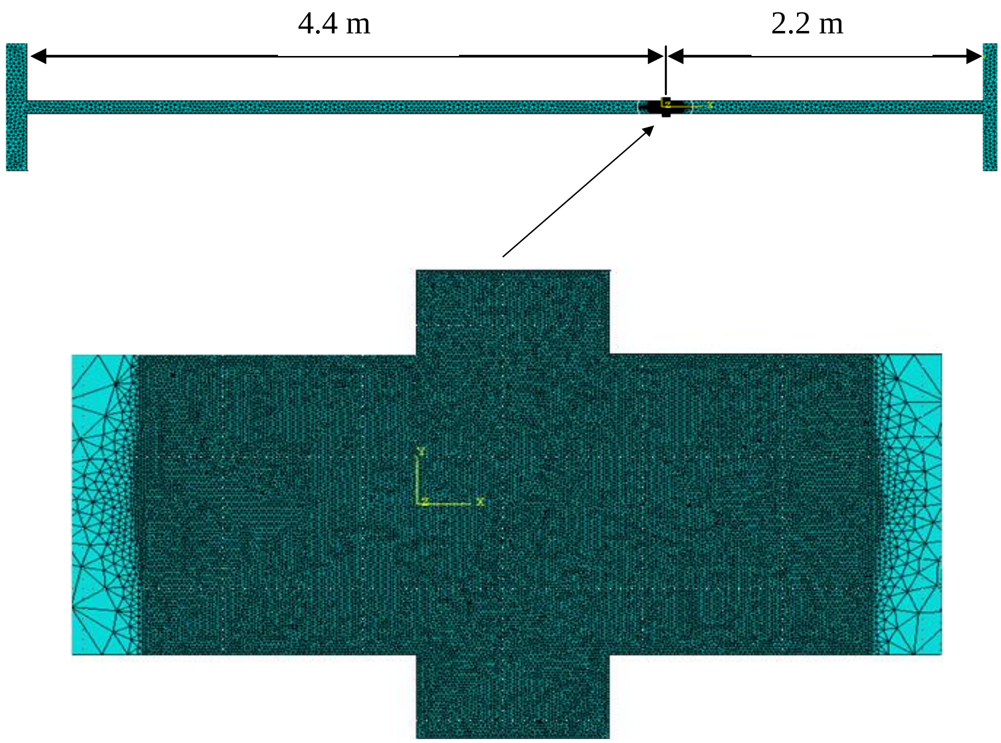

Figure 5.8: Simulation domain and grid

Figure 5.9 shows the spatial component of the acoustic pressure distribution for the first harmonic acoustic mode of a complete wavelength upstream and a half wavelength downstream of the cavity while the cavity is located at a pressure node. This acoustic mode is the same mode used for the PIV measurements in the previous section. Figure 5.10 shows the acoustic pressure at an instant of the acoustic cycle which is the same for the 8 instants used in the PIV measurements except that the time function varies between

1 and -1 over the oscillation cycle. The figure covers a view size similar to that captured by the PIV camera. Figure 5.11 shows acoustic particle velocity streamlines for the same view field at a specified time instant associated with the first acoustic mode of the duct housing the cavity. This particle velocity distribution was determined from the computed acoustic pressure field by means of Euler's equation as follows:

$$\upsilon = - \frac{1}{\rho_o} \int \nabla p(x,y,t)\, dt \tag{5.3}$$

$$\upsilon = - \frac{p_{max}}{\rho_o} \nabla p(x,y) \cos(\omega t) \tag{5.4}$$

From equations 5.2 to 5.4, it can be seen that the acoustic particle velocity leads the acoustic pressure by 90°. From this simulation, the acoustic particle velocity distributions at 8 equivalent instants to the PIV measurements were computed and they can be used as input data to Howe's integrand. Figure 5.12 shows the cross stream component of the acoustic particle velocity υ_y at three instants of these 8 instants. As it will be illustrated in chapter 6, υ_y is a dominant parameter that controls the aeroacoustic power.

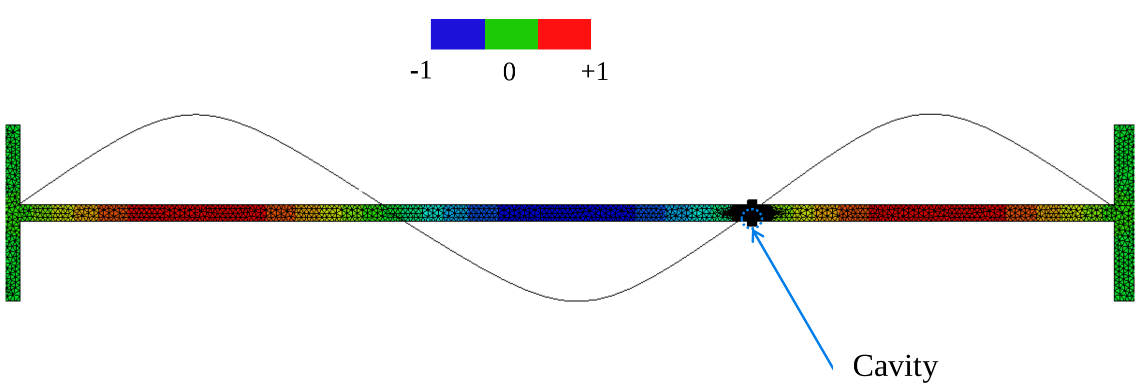

Figure 5.9: Normalized spatial acoustic pressure distribution in the pipeline

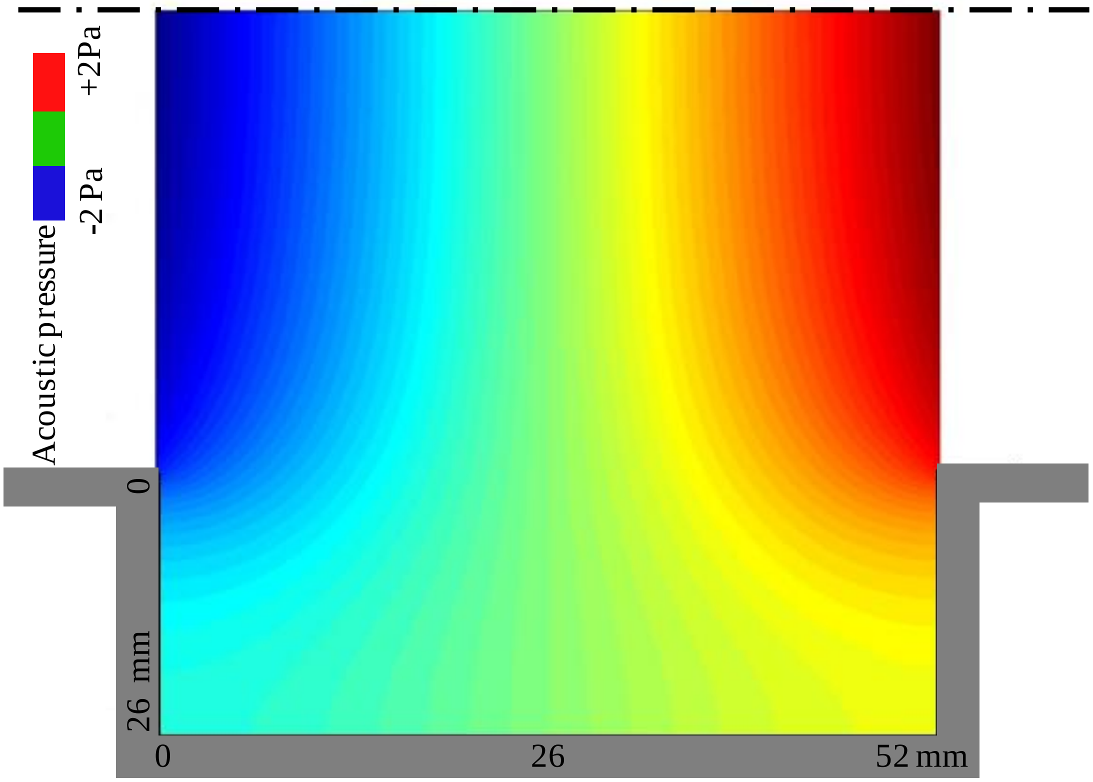

Figure 5.10: Acoustic pressure distribution in the cavity

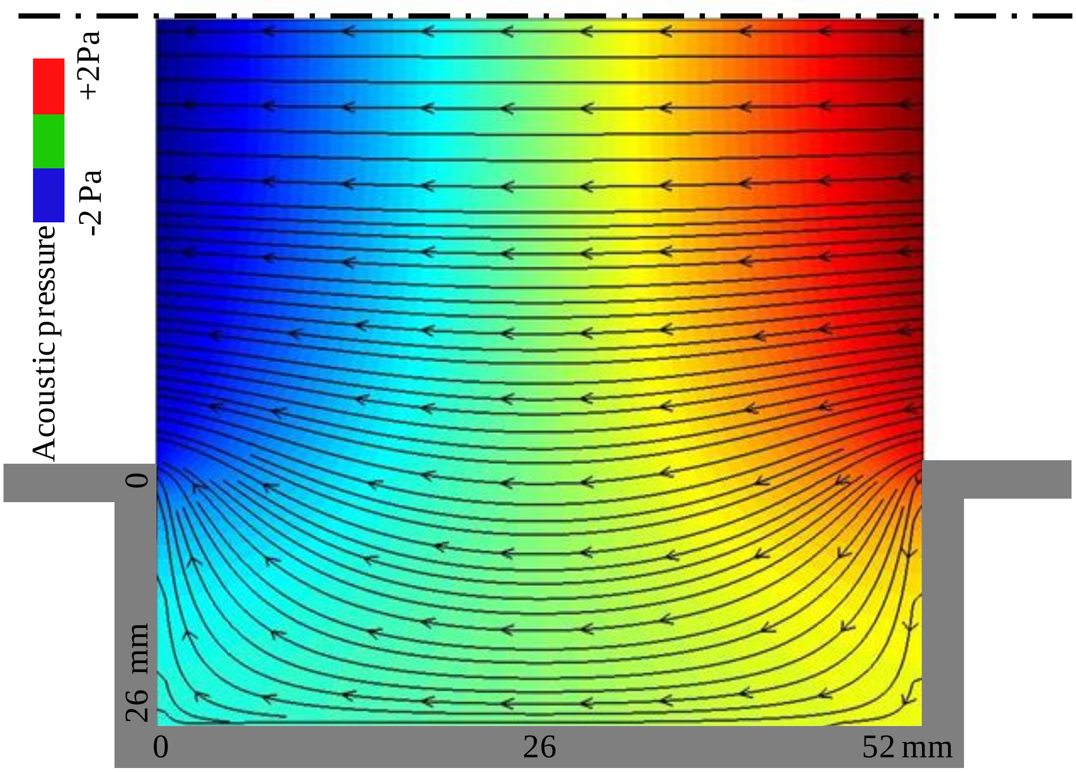

Figure 5.11: Acoustic particle velocity streamlines in the cavity

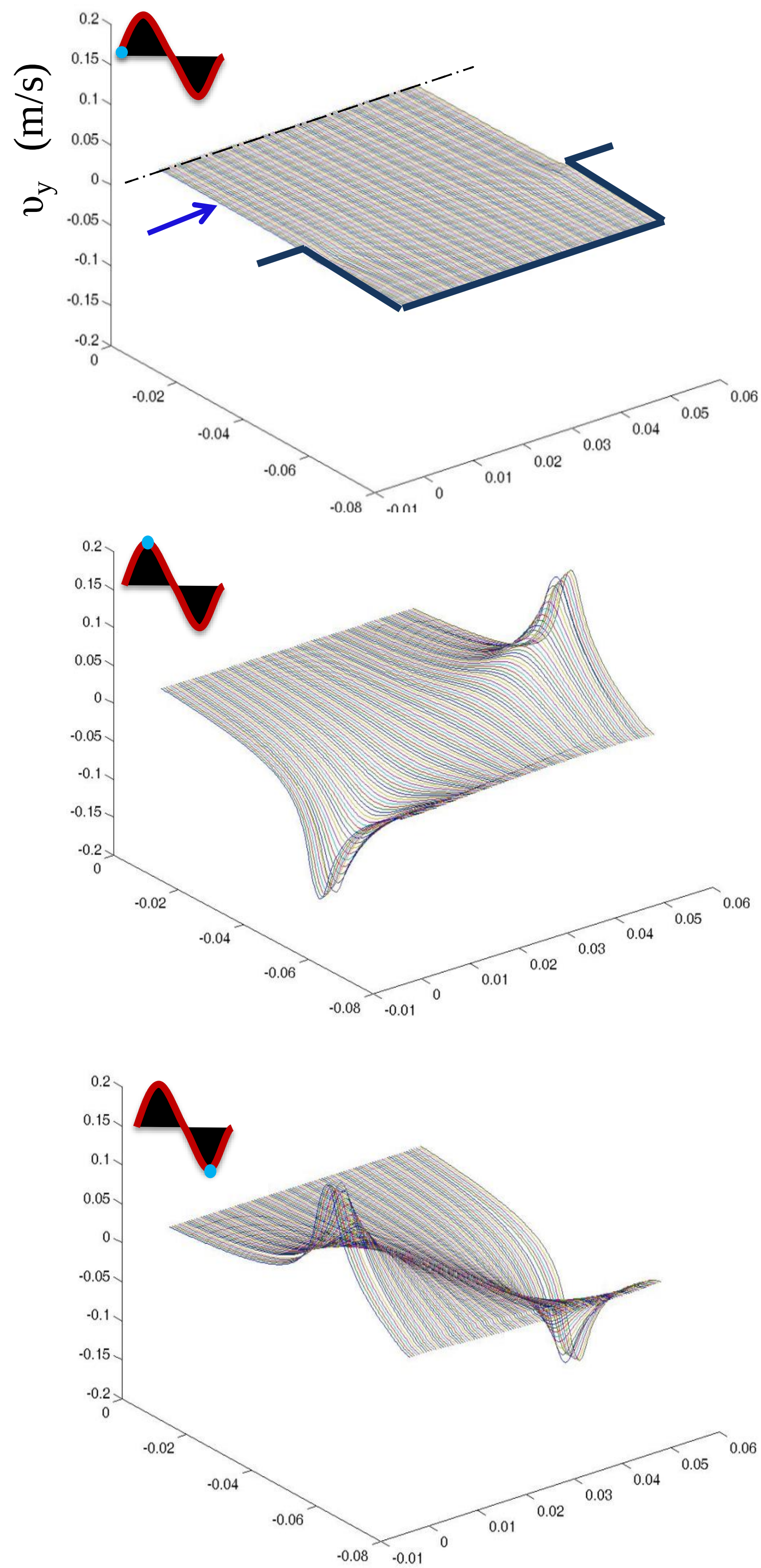

Figure 5.12: Cross-stream component of the acoustic particle velocity in the cavity at three instants of the acoustic cycle

5.2.2 Identification of the Aeroacoustic Source

Howe derived the volume integral of the triple product of the vorticity vector ω, the flow velocity vector U, and the acoustic particle velocity vector υ to calculate the instantaneous aeroacoustic power P as shown by equation 2.18. In this study, the flow field and sound field were obtained separately. The flow field was measured using the PIV system for each specified phase angle over the acoustic cycle, as shown in section 5.1. The aeroacoustic sources or sinks in the flow field were then computed by combining the solution of the acoustic field, which was modeled by the finite element method in section 5.2.1, with the measured flow field. The net acoustic energy is the time integral of the instantaneous acoustic power over a complete acoustic cycle.

Figure 5.13 shows the procedure of the acoustic source computation process using Howe's integrand. The locations within the flow field where the acoustic energy is either absorbed (-) or generated (+) are identified. Spatial volume integration of the net acoustic energy is used to calculate the total acoustic energy at each specified Strouhal number and amplitude ratio. This amount is normalized in the same way used for the acoustic source term **S** (St,υ/U) as shown by equation 3.2. By repeating this procedure for different combinations of Strouhal number and amplitude ratio, the aeroacoustic source was obtained and compared to the measured source term using the sound wave method, SWM. An example of using Howe's integrand, with the procedure shown in figure 5.13, is presented in figure 5.14. In this figure, the instantaneous spatial distributions of the aeroacoustic power per unit volume at 8 instants of the acoustic cycle are shown followed by the aeroacoustic power over a complete acoustic cycle.

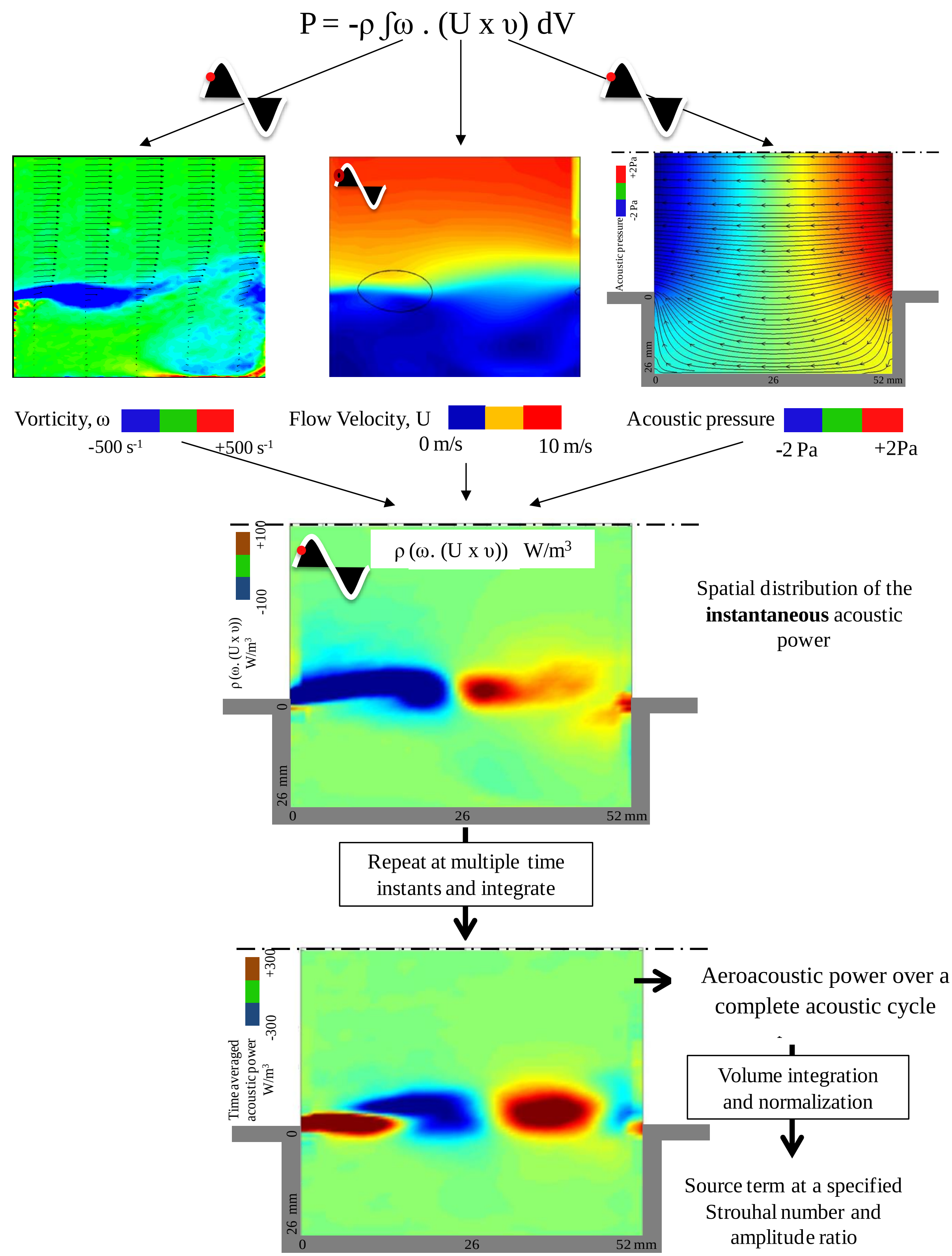

Figure 5.13: The procedure of the acoustic source extraction process using Howe's integrand

These aeroacoustic power distributions, in this example, are calculated at the peak whistling Strouhal number of 0.65 and the oscillations amplitude ratio of 5% for the cavity size of 52 mm long and 26 mm deep. The integrating aeroacoustic power over the cavity volume is normalized to the acoustic source term **S** as shown by equation 3.2 which leads to the dimensionless source term **S** (St =0.65 and υ/U = 5%) = 2.1. By repeating the same procedure for different combinations of Strouhal numbers and acoustic oscillations amplitude ratios, the normalized source term **S** (St, υ/U) is calculated.

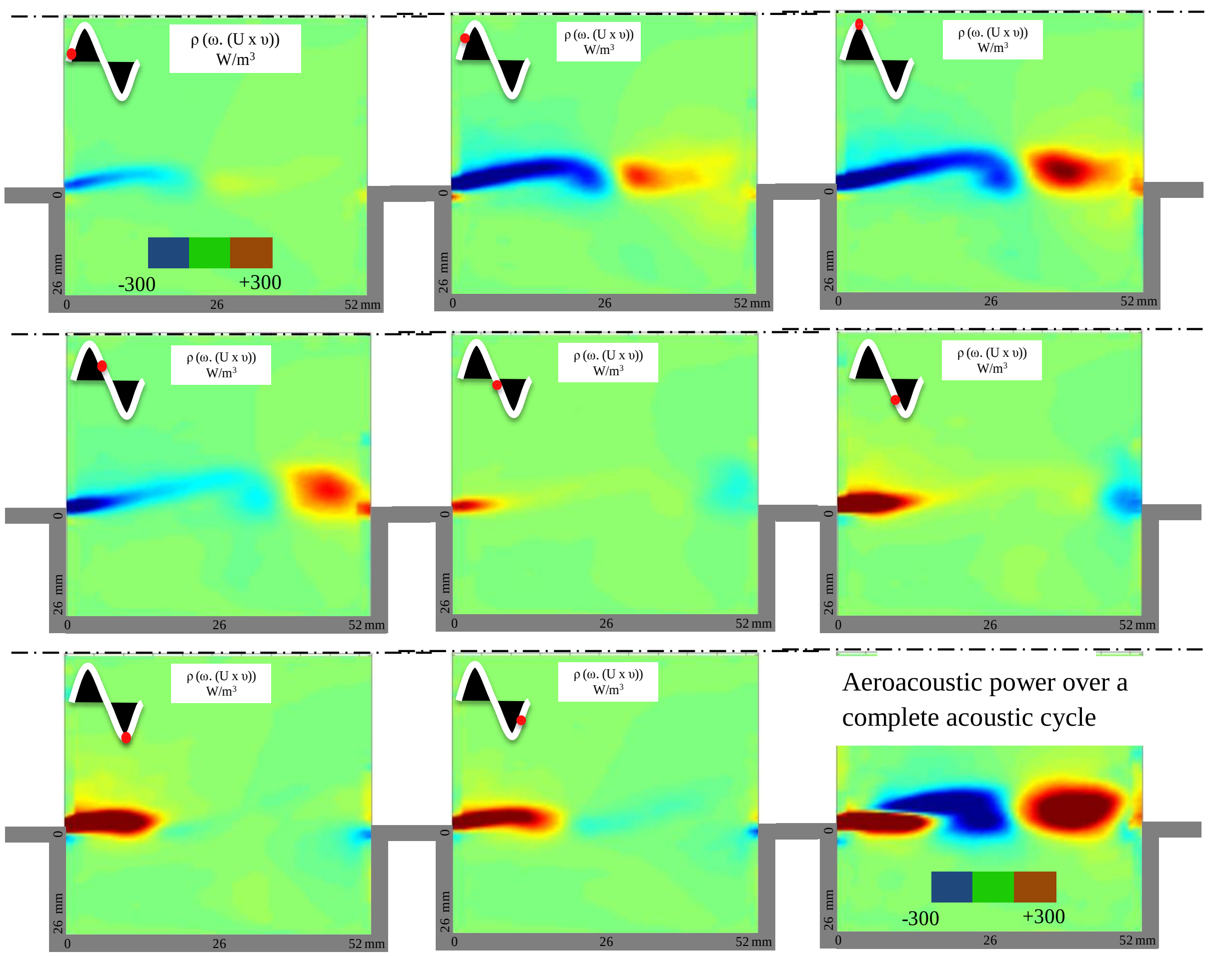

Figure 5.14: Spatial distributions of the aeroacoustic power per unit volume (ρ_o ω. U x υ) at 8 instants of the acoustic cycle followed by the time integral of the instantaneous acoustic power over a complete acoustic cycle. Measurements taken at St = 0.65 and υ/U = 5% for a cavity size of 52 mm long and 26 mm deep.

5.2.3 Results and Discussion

There are two main parameters affecting the aeroacoustic source strength. The first parameter is the matching between the period of the oscillation cycle and the time required by the shear layer disturbance to travel across the cavity length. This matching can be presented by the Strouhal number or the reduced velocity. The second parameter is the dimensionless amplitude of the feedback disturbance which is described by the ratio of acoustic particle velocity to the mean flow velocity υ/U at the peak-whistling Strouhal number. The effects of Strouhal number and υ/U on the spatial distributions of the aeroacoustic power are investigated and presented in the following sections. Thereafter, a comparison between the normalized acoustic source measured by Howe's integrand method and that measured by SWM is presented.

5.2.3.1 Effect of Strouhal Number on the Spatial Distribution of the Aeroacoustic Power

Figures 5.15 and 5.16 show the spatial distributions of the integrated aeroacoustic power over a complete acoustic cycle for two cavity sizes at different flow velocities (Strouhal number) with constant acoustic amplitude ratio of 5%. The selected velocities for the smaller cavity (52 mm x 26 mm) are covering the lock-in range of the first hydrodynamic mode, as shown in figures 5.15 and 5.17, which include:

- The flow velocity matching the peak whistling Strouhal number (St = 0.6) at the first hydrodynamic mode ($U = U_{peak1}$), for which the time scale of flow oscillation (the hydrodynamic period) matches the acoustic cycle periodic time. In this case, identification of the spatial distribution of the acoustic power at resonance condition shows an acoustic power generation source (+) at the first and the last thirds of the cavity length and an acoustic power absorption sink (-) in the middle third. This distribution leads to a maximum net generating power over the cavity volume. The vorticity field at this condition, figure 5.4, shows a vorticity cloud covering a certain distance along the cavity mouth followed by a concentrated vortex formation which travels along the remaining length of the cavity mouth.

- Higher flow velocity ($U > U_{peak1}$) at which the Strouhal numbers (St = 0.5) is lower than the peak whistling Strouhal number. In this case, the travelling time of the free shear layer disturbance is shorter than the peak whistling traveling time. The spatial distribution of the acoustic power over the cavity length shows a source generation (+) at the first half of the cavity mouth and an absorption sink (-) in the second half. The vorticity field at this condition shows a vorticity cloud covering the whole cavity mouth. The faster travelling vorticity field reaches the downstream corner before the acoustic particle velocity reverses direction and therefore acoustic power continues to be absorbed near the trailing edge, instead of being generated as in the peak whistling case. This flow condition is therefore not conducive to self-excitation of acoustic resonances and acoustic disturbances would be dampened out.
- Lower flow velocities ($U < U_{peak1}$), at which the Strouhal numbers (St = 0.7, 0.8, and 0.85) are higher than the peak whistling Strouhal number. In these cases, the travelling time of the free shear layer disturbance is longer than the disturbance traveling time at the peak whistling condition. Identification of the spatial distribution of the acoustic power over the cavity length shows an additional sink (negative spot) at the last quarter of the cavity mouth which did not exist in the

peak resonant case, St =0.6 and 0.65. From figure 5.4, the vorticity field at this condition shows more than one concentrated vortex traveling along the cavity mouth during the same acoustic cycle which means that the vorticity field travels so slow such that the acoustic field reverses direction again (in comparison to the peak resonant case) before the arrival of the relevant vortex and therefore an additional sound absorption region is formed at the cavity downstream corner. Here again, the net (or integrated) effect of sound generation is not sufficiently high to sustain acoustic resonances.

The selected velocities for the large cavity (104 mm x 52 mm) are covering both lock-in ranges of the first hydrodynamic mode (St = 0.6-0.9 with a peak whistling at St =0.75) and the second hydrodynamic mode (St = 1.1-1.5 with a peak whistling at St =1.3) as shown in figures 5.16 and 5.18. From figure 5.16, one can remark that the spatial distributions of the aeroacoustic power in the first hydrodynamic lock-in range (St = 0.6-0.9) are similar to that identified for the small cavity in figure 5.15. This similarity leads to the independency of the spatial distribution of the aeroacoustic power from the cavity volume. In addition to clarifying the effect of cavity volume on the acoustic power distributions, the resonance of the large cavity occurs at higher flow velocities which give us the ability to measure the second hydrodynamic mode (St = 1.1-1.5). As the flow velocity becomes close to half that causing resonance at the first hydrodynamic mode, the second hydrodynamic mode of the shear layer excites the acoustic resonance at St =1.3 ($U = U_{peak2}$) for the large cavity as shown in figure 5.18. For acoustic resonance to occur at the second hydrodynamic mode, the flow velocity must match the peak whistling Strouhal number at the second hydrodynamic mode (St =1.3). In this case, the spatial distribution of the acoustic power at resonance condition shows acoustic power generation sources (+) over around 3/5 of the cavity length and acoustic power absorption sinks (-) over around 2/5 of the cavity length, which leads to an approximate ratio of power generation to absorption of 3/2. But as the flow velocity deviates from (lower or higher) the whistling condition (e.g., St = 1.1 and St =1.5), the generation to absorption ratio is reduced to approximately 2/2 or 3/3, respectively. Here again, the net (or integrated) effect of sound generation is not sufficiently high to sustain acoustic resonances. The normalized net aeroacoustic source terms for both cavities (small and large) are presented in figures 5.17 and 5.18, respectively, by open square data points.

5.2.3.2 Effect of the Acoustic Amplitude Ratio on the Spatial Distribution of the Aeroacoustic Power

The visualization of the flow-sound interaction patterns for the cavity flow at the peak-whistling Strouhal number at different amplitude ratios shows that the variation of the amplitude ratio υ/U strongly affects the vorticity field as shown in figure 5.6, and hence the aeroacoustic source strength. Figure 5.19 shows the effect of the acoustic amplitude ratio (υ/U) on the spatial distributions of the aeroacoustic power at the first hydrodynamic peak whistling condition ($U = U_{peak1}$) when the υ/U ratio varies from 0.2% to 20%. As identified in the previous section, the acoustic power spatial distributions at the first peak resonance condition show an acoustic power generation source (+) at the first and the last thirds of the cavity length and an acoustic power absorption sink (-) in the middle third.

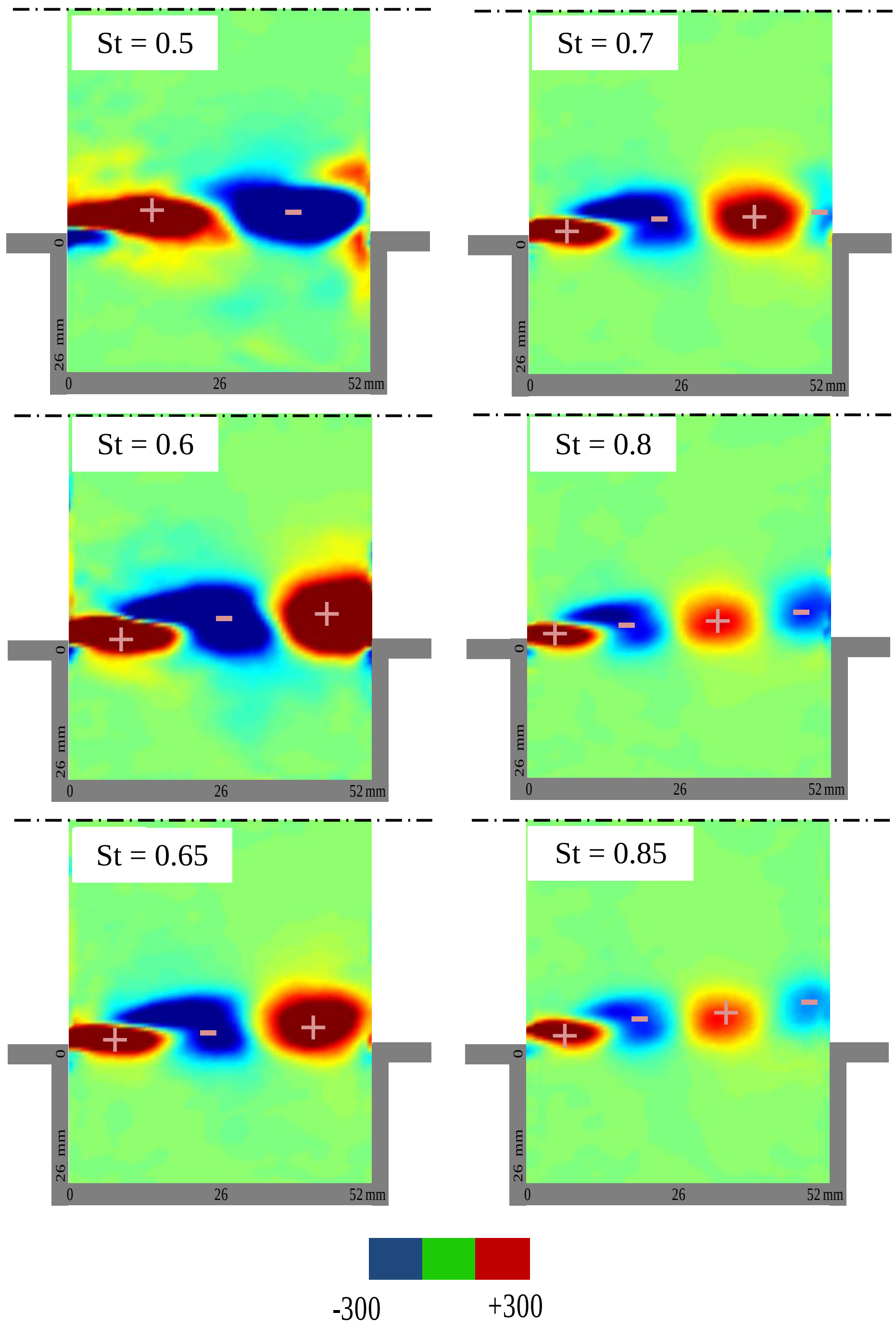

Figure 5.15: Effect of flow velocity (or Strouhal number) on the spatial distributions of the aeroacoustic power per unit volume over a complete acoustic cycle, at υ/U = 5% for a cavity size of 52 mm long and 26 mm deep. The vorticity fields are shown in figure 5.4

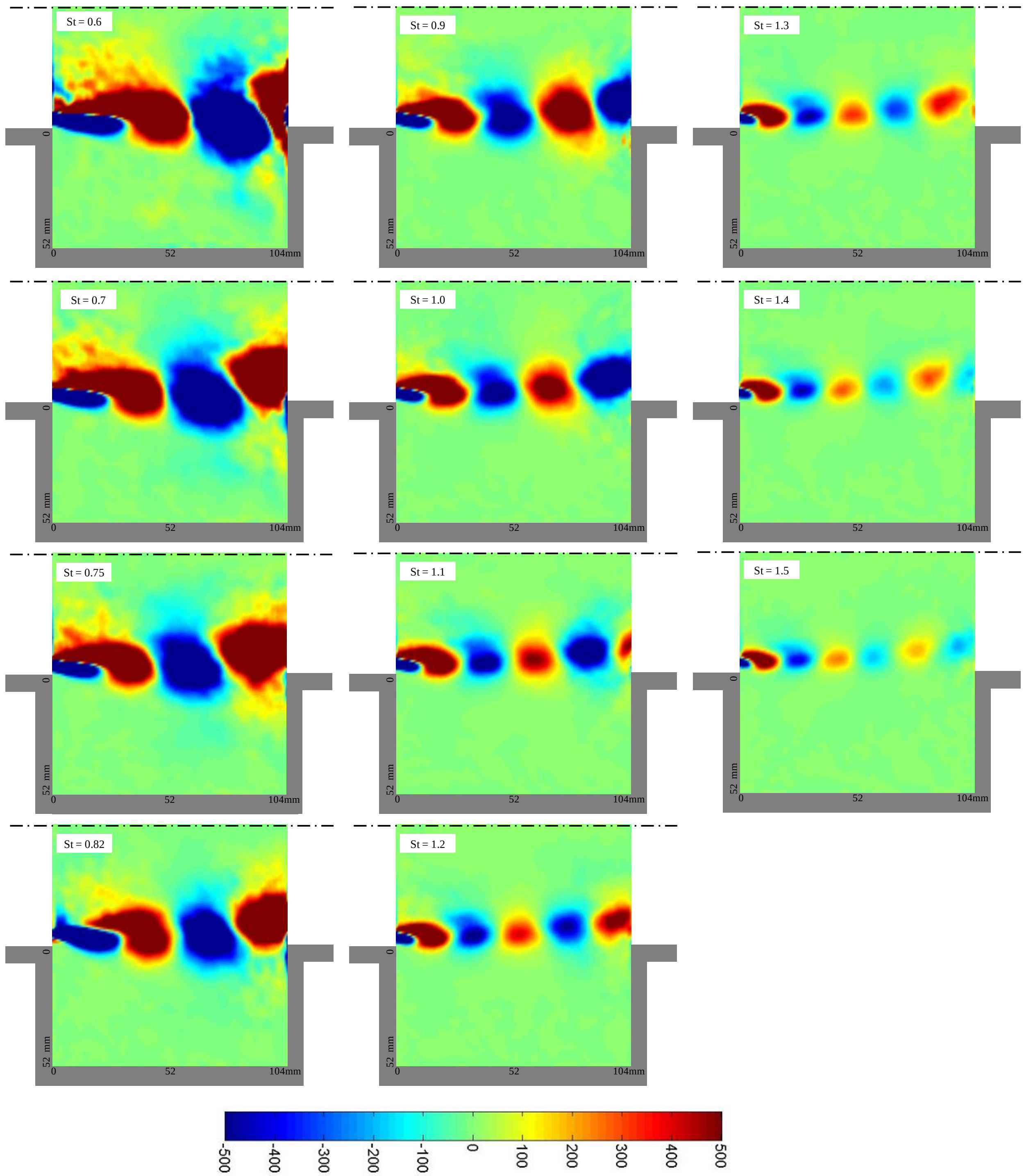

Figure 5.16: Effect of flow velocity (or Strouhal number) on the spatial distributions of the time averaged aeroacoustic power per unit volume over a complete acoustic cycle, at υ/U = 5% for a cavity size of 104 mm long and 52 mm deep. The vorticity fields are shown in figure 5.6

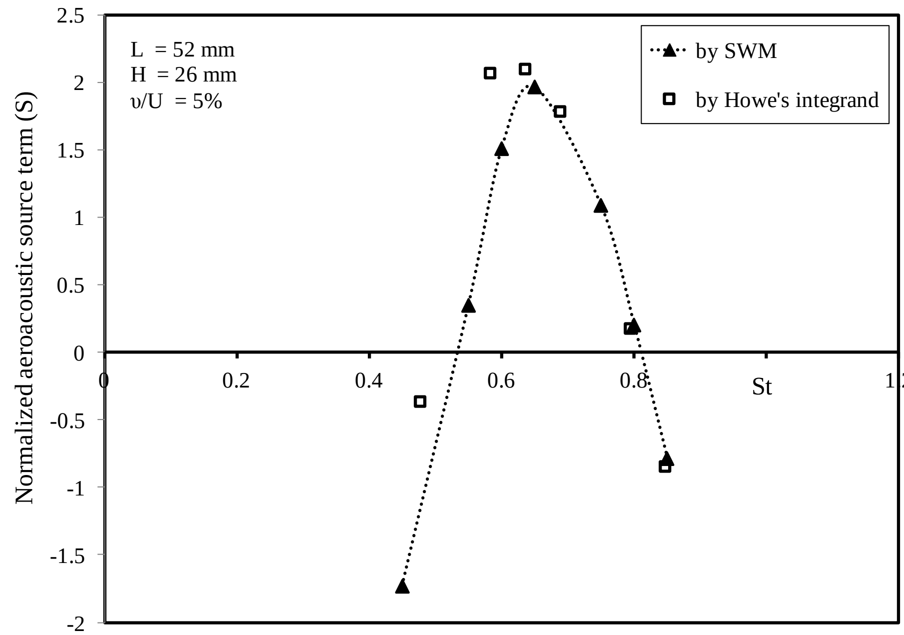

Figure 5.17: Effect of flow velocity (Strouhal number) on the normalized real part of the aeroacoustic source term (**S**) using both the SWM and Howe's integrand for a cavity size of 52 mm long and 26 mm deep and at υ/U = 5%

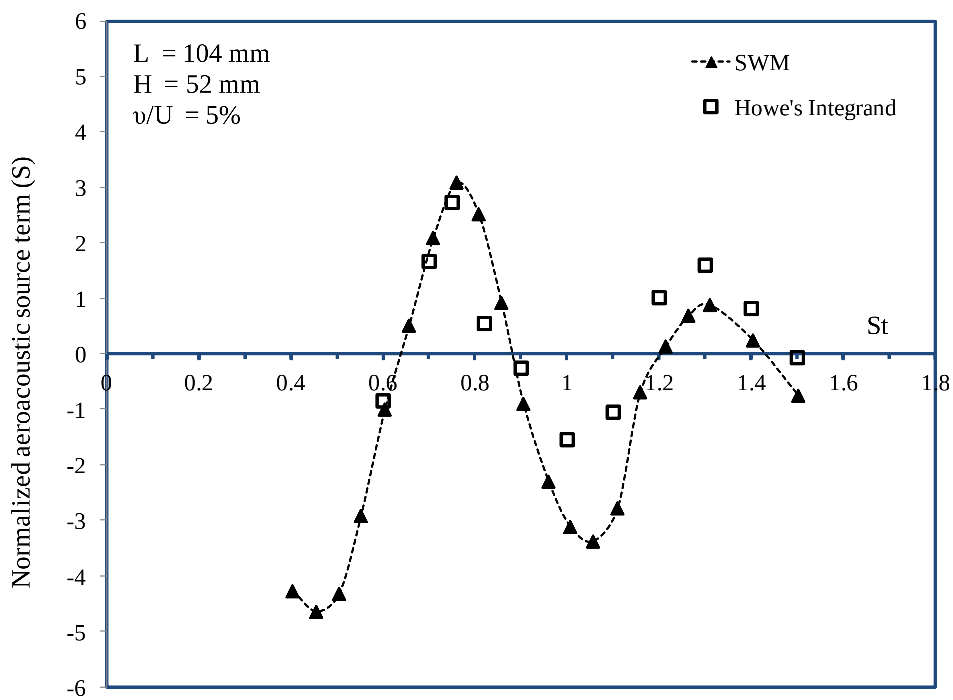

Figure 5.18: Effect of flow velocity (Strouhal number) on the normalized aeroacoustic source term (**S**) using both the SWM and Howe's integrand for a cavity size of 104 mm long and 52 mm deep and at υ/U = 5%

Although the distribution of acoustic sources does not change (e.g. by adding more sources or sinks) as υ/U changes, the strength and the spreading of each source and sink regions increase as the oscillation amplitude ratio increases till they reach saturation as in the cases of υ/U = 10% and 20% in figure 5.19. The net normalized acoustic source term **S** variation with the amplitude ratio is presented in figure 5.20. Also, the effect of the excitation level (υ/U) on the aeroacoustic power in Watts for a constant whistling Strouhal number is shown in figure 5.21.

Referring to figure 5.21, the variation of the aeroacoustic power with the amplitude of resonance υ/U is divided into three ranges. First, a low level of oscillations (as in the Case of υ/U = 0.2% of figure 5.6) in which the vorticity field takes the form of a vorticity cloud along the cavity mouth and the aeroacoustic power increases with υ/U at a relatively small rate of increase, as shown in figure 5.21. Secondly, a high level of oscillation range (as in Cases of υ/U = 10% and 20% of figure 5.6) in which the vorticity field takes the form of well-defined vortices which appear near the cavity leading edge and travels along the cavity mouth. In this range, the aeroacoustic power increases with υ/U at a relatively high rate of increase. Finally, an intermediate level of oscillation range (as in Case υ/U = 5%) in which the vorticity field takes the form of a combination of initial vorticity cloud followed by a well-defined vortex which forms after a certain distance from the cavity leading edge and travels along the remaining part of the cavity mouth. In this region, the aeroacoustic power increases nonlinearly with υ/U as the flow-sound interaction pattern transforms from distributed vorticity cloud over the whole length of the cavity to rapid discrete vortex formation at the cavity upstream corner. This transition is associated with a gradual increase in the proportionality factor (i.e. the slope of the curve in figure 5.21) which relates the source strength to the particle velocity amplitude. These observations explain the nonlinear trend observed in the source strength as the acoustic particle velocity is increased.

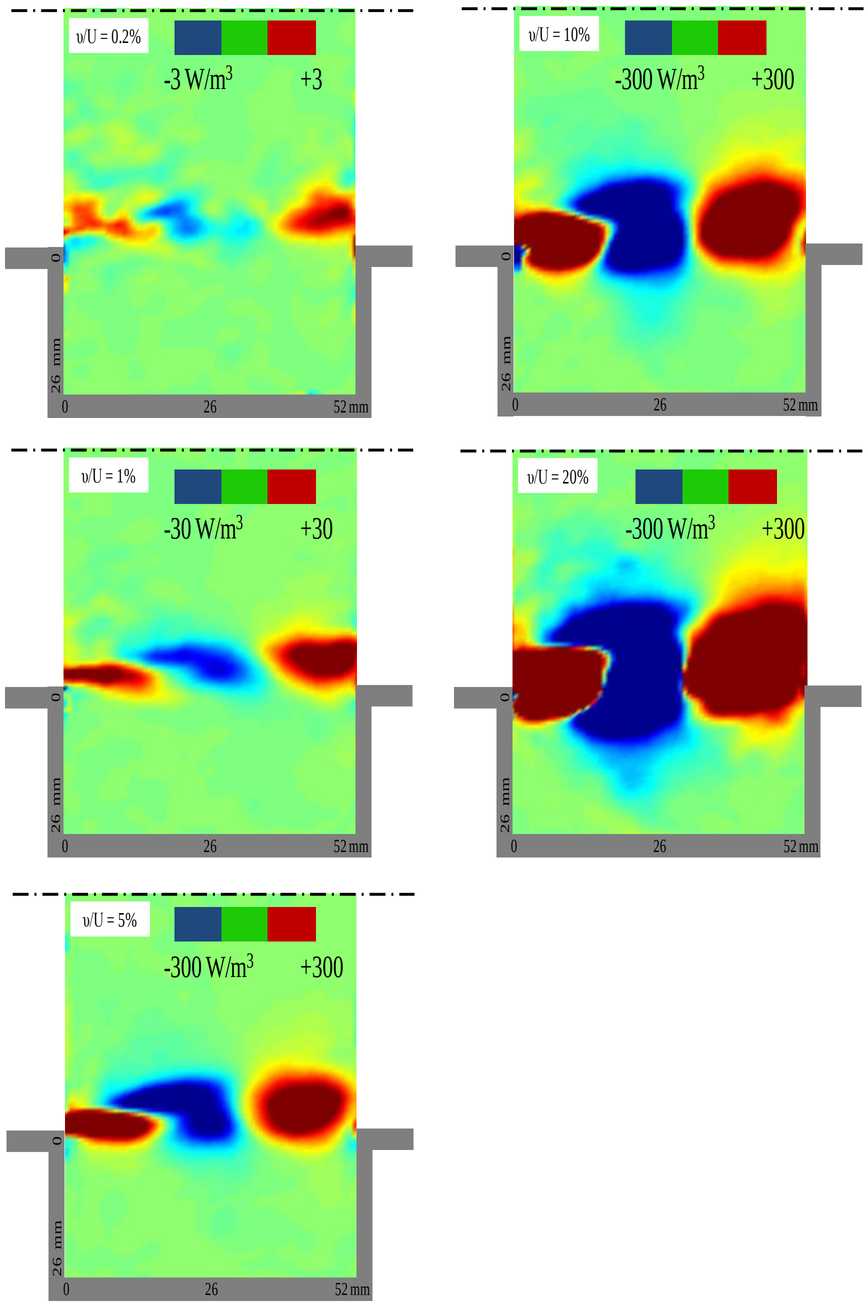

Figure 5.19: Effect of the acoustic amplitude ratio (υ/U) on the spatial distributions of the aeroacoustic power per unit volume over a complete acoustic cycle. Images corresponding to the peak whistling condition for a cavity size of 52 mm long and 26 mm deep. The vorticity fields are shown in figure 5.6

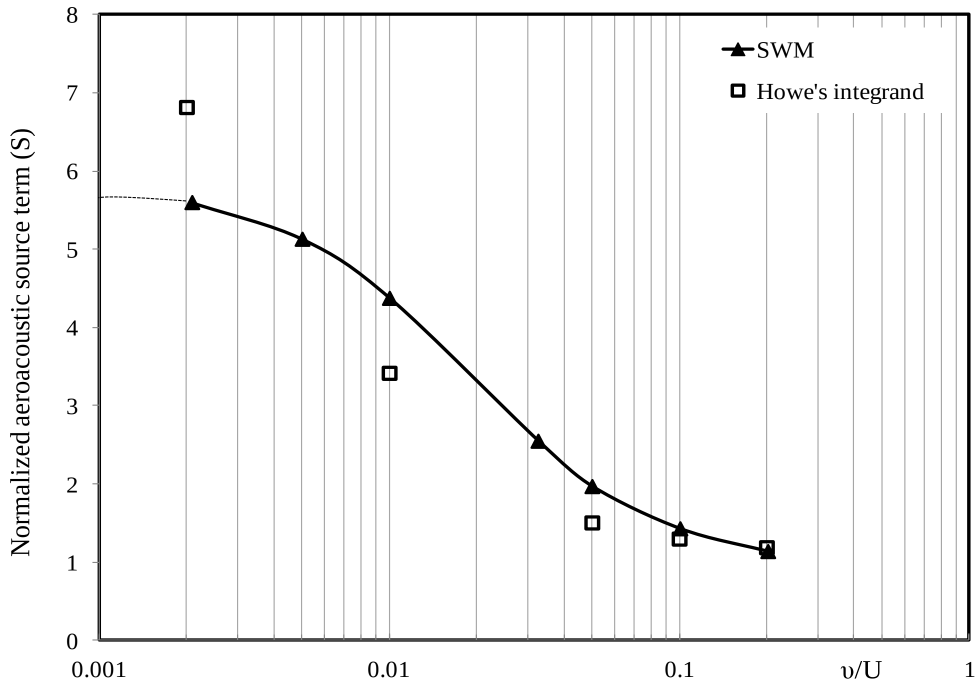

Figure 5.20: Effect of the acoustic amplitude ratio (υ/U) on the normalized aeroacoustic source term (S) using both the SWM and Howe's integrand. St = 0.65; cavity size is 52 mm long and 26 mm deep.

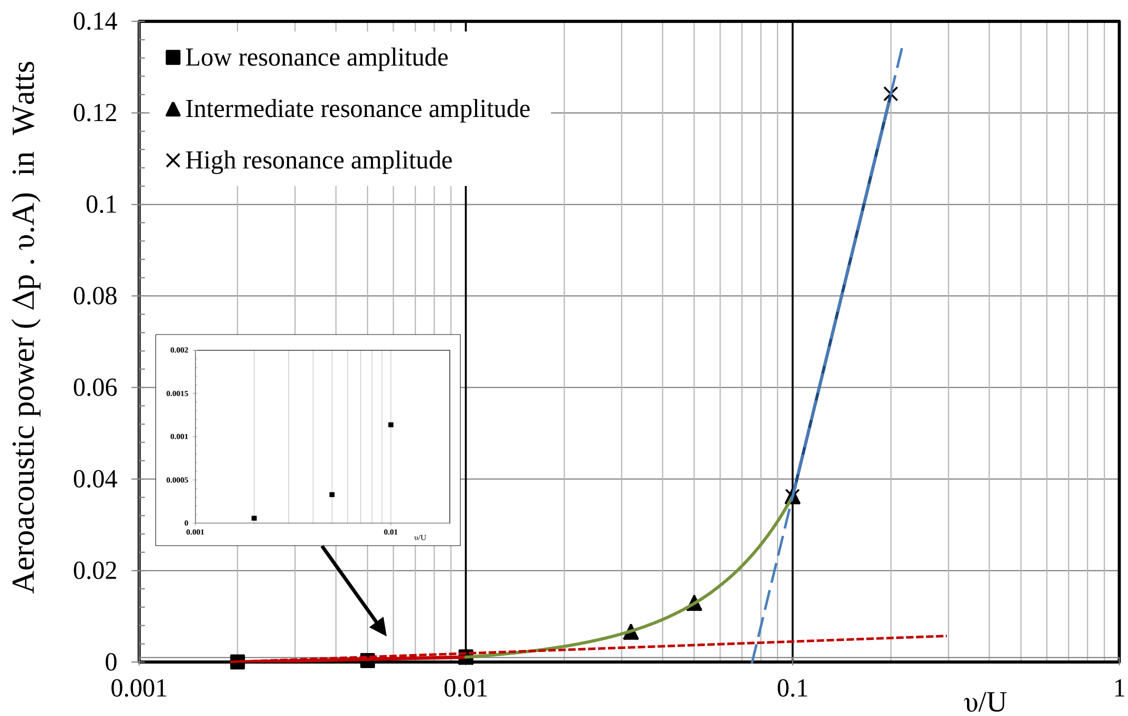

Figure 5.21: Effect of the excitation level (υ/U) on the aeroacoustic power in Watts for a constant whistling Strouhal number of St = 0.65 for cavity 52 x 26 mm.

5.2.3.2 Comparison between Measured Aeroacoustic Source Terms from Both SWM and Howe's Integrand Method

Figures 5.17, 5.18, and 5.20 show the normalized aeroacoustic source terms measured by both SWM and Howe's integrand method. The comparison shows that a good agreement is achieved, especially at high amplitude ratios as shown in figures 5.17 and 5.18. In figure 5.20, there is a difference between the two methods of about 25% at low resonance oscillation amplitudes, but this difference vanishes at high resonance oscillation amplitudes when the signal to noise ratio improves. This difference at low amplitudes is likely caused by the three dimensionality effects of the flow field. At high amplitudes, the unsteady flow is very coherent and can be assumed to be two dimensional. Therefore, as the oscillation amplitude becomes stronger, the results of the PIV method, which assumes the flow to be two dimensional, are expected to become closer to those obtained by the SWM, which accounts for 3-D effects. Thus, the results substantiate the assumption that the flow is predominantly two-dimensional at large amplitude oscillation. However, at small amplitudes, which is relevant to the onset of oscillations, the two dimensional assumption is not accurate to estimate the aeroacoustic source strength.

From the comparison between the two measuring methodologies of the aeroacoustic source, the following conclusions can be made. The most important advantage of the SWM is that it does not deal with the details of the unsteady flow field and the flow-structure-sound interaction mechanism as it considers the object (cavity) as a “black box” and therefore it is more applicable for complex geometries and flows. In addition, Howe's integrand method requires detailed knowledge of the flow and acoustic fields, which requires substantial effort for complex flow geometries. For example, in order to compute the source term at a specified Strouhal number and υ/U ratio, a PIV accompanied by microphones and loudspeaker for flow visualization and finite element simulation of the acoustic field prediction were required. A measurement and analysis time of several days for each source term data point was needed. For the SWM, measurement and analysis time requires only a few minutes for each source term data point.

The great challenge of the SWM is the difficulty to measure the tiny flow-induced pressure difference Δp which is induced by the unsteady flow along the cavity. The spatial distributions of the aeroacoustic power along the cavity mouth, as shown in figures 5.15, 5.16, and 5.19 are the most important advantage of the Howe's integrand method which gives a better understanding of the flow-sound interaction mechanism and the dependence of the aeroacoustic power on the main parameters, such as the Strouhal number, the acoustic feedback disturbance amplitude υ/U, and the cavity volume. Another advantage of the SWM is that it can be used to measure the sound source at small amplitude pulsations, which is most relevant for the initial phase of acoustic resonance. At these conditions, the flow structure is three-dimensional and the PIV methodology assumes the flow to be two-dimensional which is inappropriate.

The above discussion highlights the advantages of the SWM over the PIV method in determining the aeroacoustic source term for various flow geometries, especially for complex flow geometries and small amplitude oscillations. These advantages also stand in comparison to other methods which uses CFD simulations to characterize the instantaneous velocity and vorticity fields of the unsteady flow and then combine these fields with the simulated acoustic field.

In summary, visualization of the flow-sound interaction for cavity flow at different acoustic resonance amplitudes and Strouhal numbers explained the non-linear behaviour of the aeroacoustic source as the acoustic particle velocity level is increased. It also explained the dependence of the flow-sound interaction patterns on the main system parameters, i.e., the Strouhal number and υ/U ratio. Comparison between the measured aeroacoustic sources based on Howe's integrand, which must be supplemented by details of the flow and acoustic fields, with those measured by means of the sound wave method (SWM) highlighted the superior efficiency of the SWM technique. Identification of the spatial distribution of the acoustic power over the cavity length at resonance condition shows sources of sound generation at the first and last thirds of the cavity mouth and an absorption sink in the middle third. This distribution is different from the source distributions for deep cavities and trapped mode acoustic resonance cases (Ziada, 1994; Oshkai & Yan, 2008). Due to these differences in the aeroacoustic source distributions, the effects of cavity geometrical parameters for the present shallow cavity are not necessarily similar to those reported in the literature for deep cavities and trapped mode resonance cases. The non-linear behaviour of the aeroacoustic source strength at moderate sound levels is caused by a gradual transition in the vorticity field oscillation pattern; from a distributed vorticity cloud which dominates the whole cavity length at small excitation amplitudes to a pattern involving rapid formation of (discrete) vortices at the leading edge which becomes dominant at large excitation levels. In the next chapter, the effect of the cavity sizes and rounding-off the edges on the aeroacoustic resonance will be presented.

Chapter 6

Effect of Cavity Geometrical Parameters

6.1 Introduction

Up to this point in the research, the developed methodology of SWM was used with a single sharp edged shallow cavity to measure the aeroacoustic power as a function of Strouhal number and the acoustic amplitude ratio υ/U. Also, the measured source is used in a linear acoustic model to predict the self-excited resonance response (amplitude and frequency). This predicted response was compared with the measured self-excited response for validation. The comparison showed an excellent improvement in predicting the self-excited response than the source models existing in the literature. The next step after developing and validating the methodology is to study the effect of cavity geometrical parameters, including rounding-off the edges, on the aeroacoustic power. This is the objective of this chapter.

6.2 Effect of Cavity Geometry

6.2.1 Motivation

The effect of the cavity size on the self-excited resonant oscillations has always been presented as an effect of the length to depth ratio (L/H) in previous studies. Some examples of these studies are the work by Rockwell et al. (2003) and Nakiboglu at.al (2012). In these studies, the ratio L/H was controlled by changing the cavity depth while the cavity length was kept constant. Rockwell et al., (2003) investigated a fully turbulent inflow past a shallow cavity for the configuration of an axisymmetric cavity mounted in a pipe. This study experimentally tested the self-excited acoustic resonance oscillations for a range of cavity depth, H, for the same cavity length, L, in order to identify the frequencies of the instability (Strouhal) modes for different cavity depths. The tested cavities had a length, L = 2.5 cm and length to depth ratios of L/H = 2, 5, 10, and 20. The results showed that as the cavity gets shallower (smaller H), the whistling Strouhal number of the fluid-resonant oscillations decreases, then remains fixed as the ratio L/H becomes larger than 5. Additionally, the tones were observed to be totally suppressed for cavities with L/H $\geq$ 10.

Nakiboglu at al., (2012) experimentally investigated the self-excited fluid-resonant oscillation conditions (Strouhal number and resonance amplitudes) and numerically identified the aeroacoustic source using Howe's Integrand for an axisymmetric cavity of a fixed length, L = 4 cm, and a range of length to depth ratio, L/H = 0.85- 5.0. The results showed that as the cavity gets shallower, the whistling Strouhal number decreases from 0.74 to 0.55 and the aeroacoustic power remains constant, but then it decreases sharply for L/H >3.

Although the previous studies have achieved substantial progress, open issues still exist. Some of these issues are the effect of cavity size for the same L/H ratio, and also, the effect of changing the cavity length for the same cavity depth. Hence, there is a need of a comprehensive study of the effect of the cavity geometry on the aeroacoustic source and the acoustic resonance intensity of a shallow cavity coupled with acoustic longitudinal modes in a duct conveying a high Reynolds number, fully developed turbulent flow. This study is the focus of the first part of this chapter. The second part will deal with the effect of rounding-off the cavity corners.

6.2.2 Tested Geometries

In this part, the effect of cavity geometry on the aeroacoustic source is investigated by measuring the source term **S** using the Sound Wave Method (SWM) that was presented in section 4.2. In addition, the effects of cavity geometry on the self-excited resonance amplitude and the whistling Strouhal number are also investigated by using the same system and methodology used in section 4.3.1. The geometries of tested cavities for both the aeroacoustic source strength and the self-excited resonance measurements are summarized in table 6.1. As shown in this table, first, the study is performed for three different groups of L/H ratios (L/H = 1, 2 and 3) and for each group of L/H, three different cavity volumes are investigated which leads to 9 cavity sizes in order to study the effect of cavity volume for the same L/H ratio. Second, the effect of cavity length for the same cavity depth is investigated. In this case, three cavity depths (H= 13, 26, and 52 mm) are tested with different cavity lengths. This set of length and depth combinations is shown in table 6.2. Finally, the effect of cavity depth for the same cavity length is investigated. In this case, three cavity lengths of 26, 52, and 78 mm are tested with different cavity depths as shown in table 6.3.

6.2.3 Results

In this section, the complete results of the aeroacoustic sources of the different cavity sizes as a function of Strouhal number and the acoustic oscillation amplitude ratio are presented. Thereafter, the effect of cavity volume for the same L/H ratio, the effect of cavity length for same depth, and the effect of cavity depth for same length on the aeroacoustic source and self-excited resonance response are analyzed.

Cavity Dimensions length (L) x depth (H) (mm)	L/H
26 x 26	1
52 x 52	1
78 x 78	1
26 x 13	2
52 x 26	2
104 x 52	2
39 x 13	3
78 x 26	3
156 x 52	3

Table 6.1: Cavity dimensions to study the effect of volume at the same L/H

Cavity Depth (H) (mm)	Cavity length (L) (mm)	L/H ratio
13	26	2
13	39	3
26	26	1
26	52	2
26	78	3
52	52	1
52	104	2
52	156	3

Table 6.2: Cavity dimensions to study the effect of length at the same depth

6.2.3.1 Aeroacoustic Sources of Different Cavity Sizes

Figures 6.1 to 6.9 are presenting the real component of the source term as a function of Strouhal number with the oscillation level as a parameter for different cavity sizes. These

Cavity length (L) (mm)	**Cavity Depth (H) (mm)**	**L/H ratio**
26	13	2
26	26	1
52	26	2
52	52	1
78	26	3
78	78	1

Table 6.3: Cavity dimensions to study the effect of depth at the same length

results are obtained by means of the SWM. In these figures, two ranges of Strouhal number with generation of acoustic power are apparent. The lower range of Strouhal number resulting in generation of acoustic power can be attributed to the "Single Vortex Mode", where only one discrete vortex is formed over the cavity length, and the higher range of Strouhal number with acoustic power generation is resulting from the "Double Vortex Mode", where two vortices are formed over the cavity length at any instant in the acoustic cycle. For some small cavity volumes, the source corresponding to the double vortex mode is very weak and is expected to generate only weak responses if any at all.

The effect of the excitation level υ/U on the source term shown in these figures indicates a slight decrease of St for the condition of maximum power generation (peak whistling Strouhal number St_{pw1}) as the oscillation level increases. For example, figure 6.4 for cavity 78 mm long by 26 mm deep shows the peak of power generation at St ≈ 0.65 for $\upsilon/U = 0.005$, whereas for $\upsilon/U = 0.1$, the peak of power generation is at St ≈ 0.55. Based on the flow visualization study using the PIV system shown in the previous chapter, this is because the level of oscillation influences the timing and the location of the formation of the discrete vortices and thereby their propagation within the oscillation cycle. At very high oscillation levels, the discrete vortices form earlier, closer to the upstream edge, where the convection velocity is lower. Therefore, their propagation across the cavity span is delayed in comparison to the case of lower υ/U. Consequently, the timing for optimal generation of acoustic power requires higher U at a given frequency and cavity span L, and therefore the corresponding St is somewhat lower. This change in St_{pw1} with the oscillation amplitude ratio is only clear in large cavities, where the measured sources are sufficiently large to distinguish these variations. Although the imaginary component of the source term is equally important in the overall context as it is associated with the reactive acoustic power which effects the system resonance frequency, only the real part of the source term is presented here as it is the term responsible for the exchange of the active acoustic power.

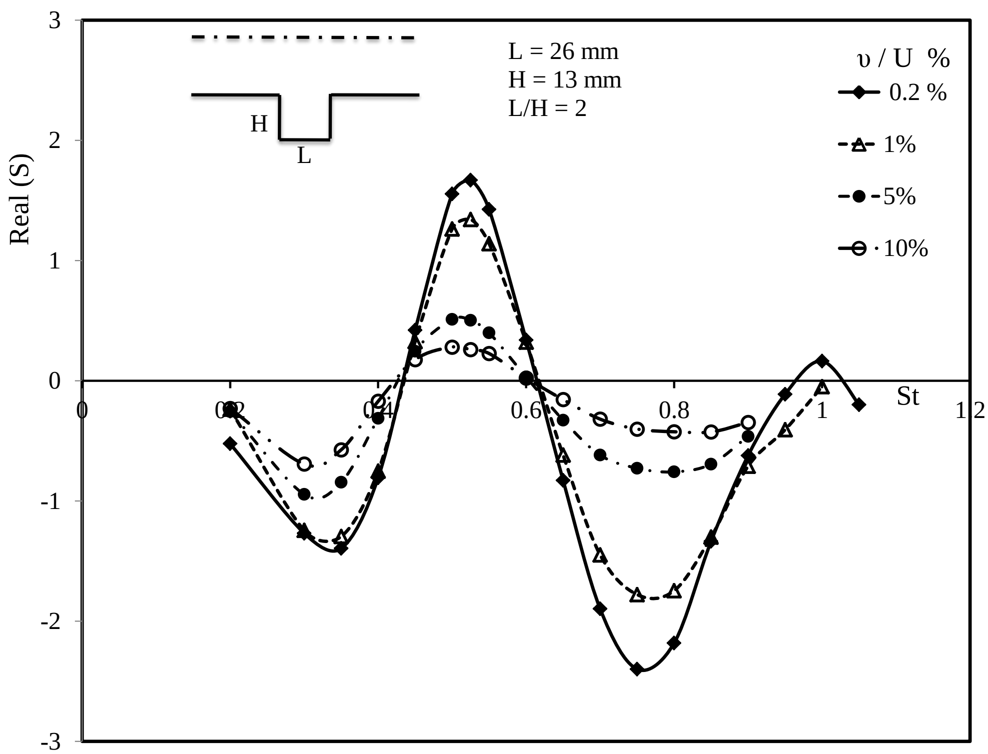

Figure 6.1: Real part of the aeroacoustic source term Real (**S**) as a function of Strouhal number for different values of the acoustic particle velocity υ/U at the cavity center (cavity 26 x 13 mm).

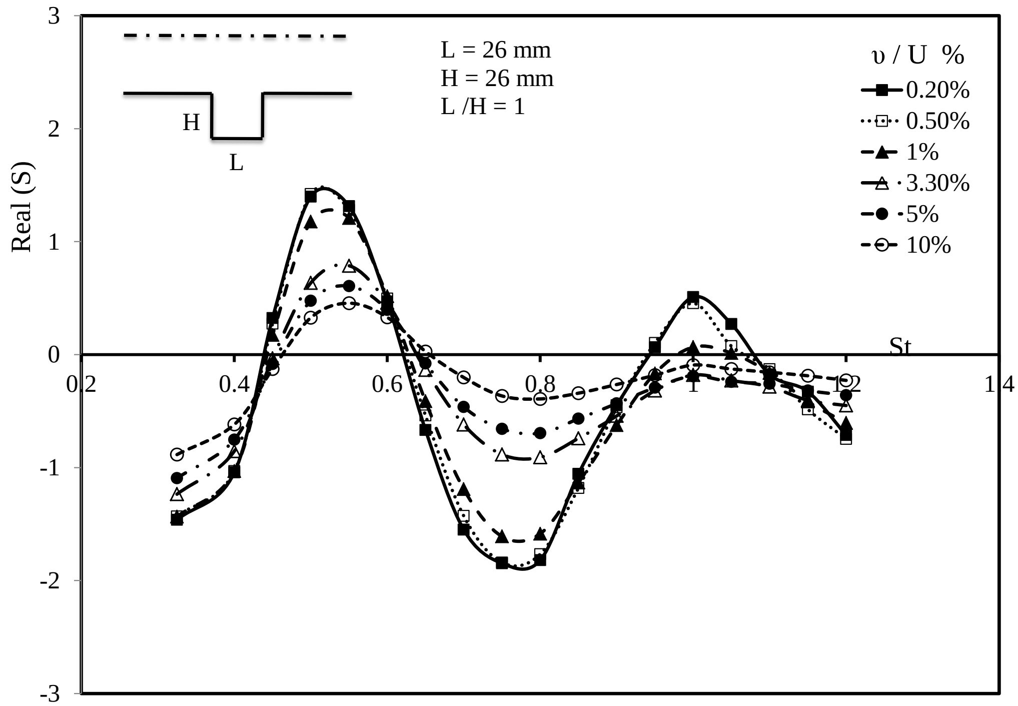

Figure 6.2: Real part of the aeroacoustic source term Real (**S**) as a function of Strouhal number for different values of the acoustic particle velocity υ/U at the cavity center (cavity 26 x 26 mm).

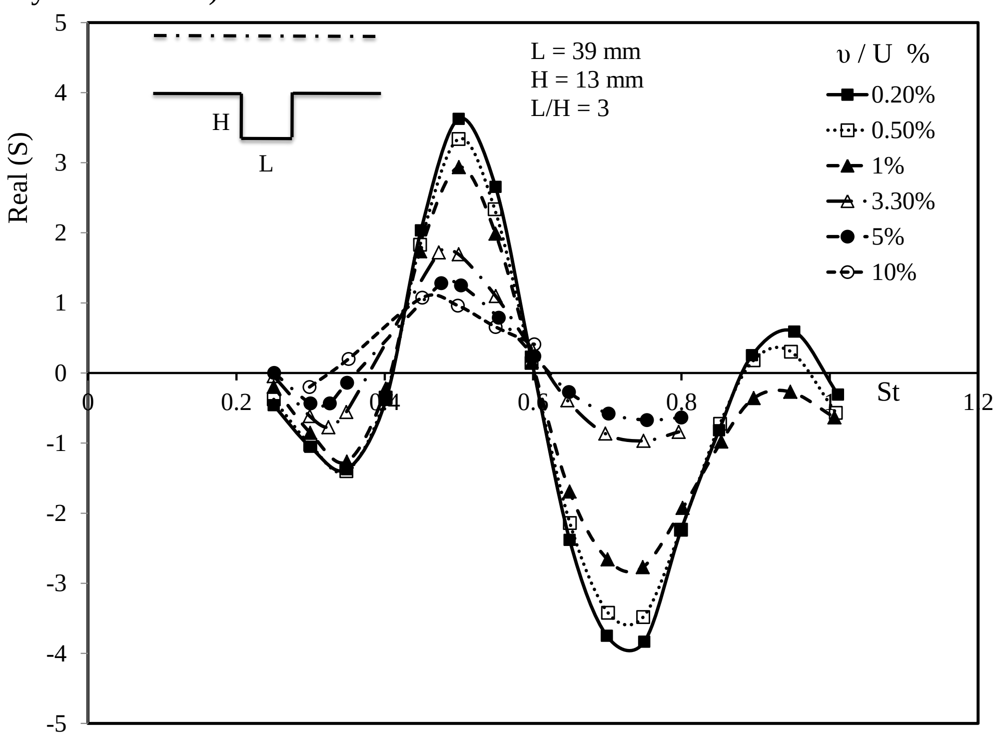

Figure 6.3: Real part of the aeroacoustic source term Real (**S**) as a function of Strouhal number for different values of the acoustic particle velocity υ/U at the cavity center (cavity 39 x 13 mm).

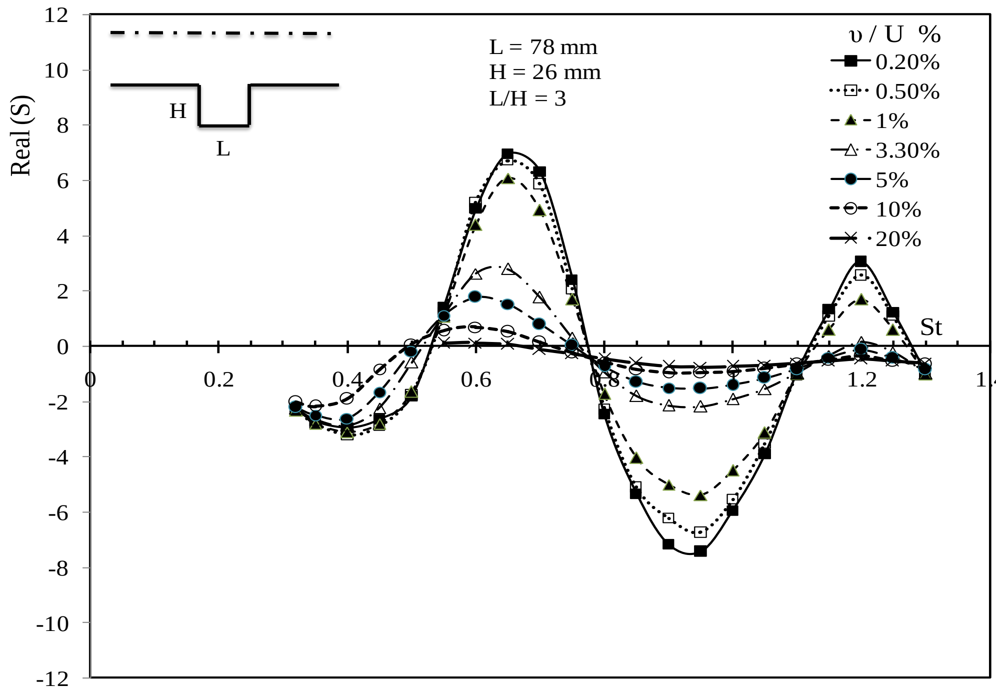

Figure 6.4: Real part of the aeroacoustic source term Real (**S**) as a function of Strouhal number for different values of the acoustic particle velocity υ/U at the cavity center (cavity 78 x 26 mm).

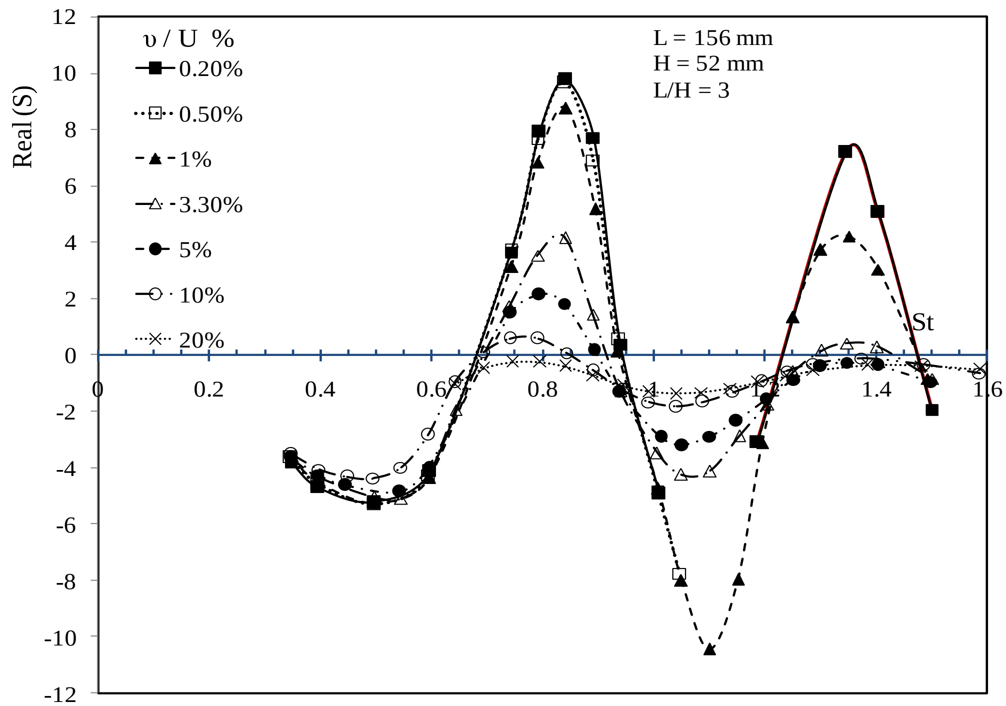

Figure 6.5: Real part of the aeroacoustic source term Real (**S**) as a function of Strouhal number for different values of the acoustic particle velocity υ/U at the cavity center (cavity 156 x 52 mm).

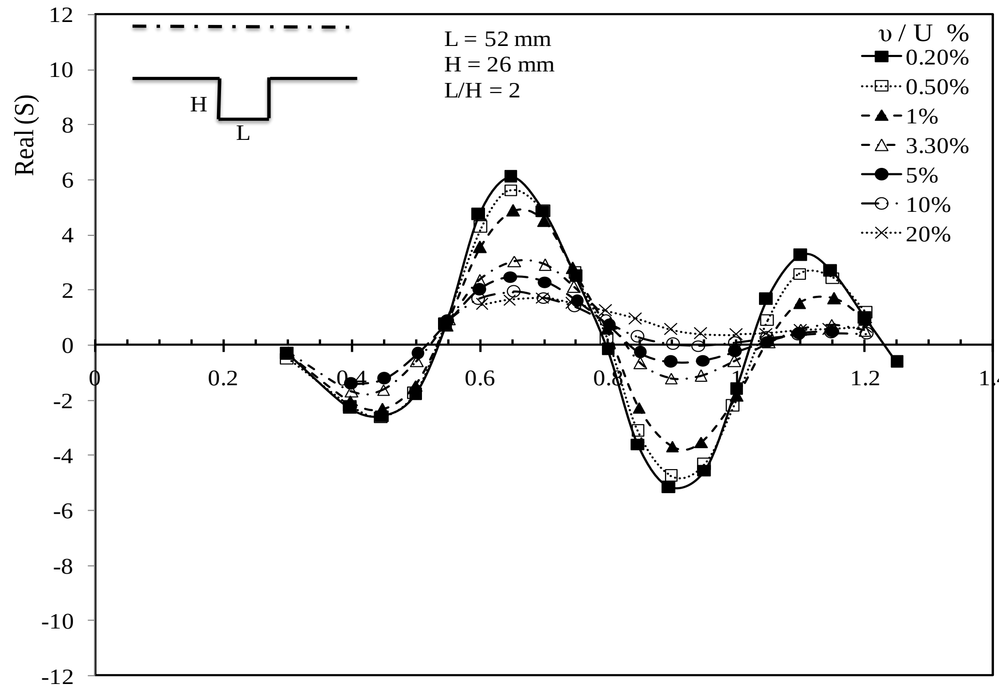

Figure 6.6: Real part of the aeroacoustic source term Real (**S**) as a function of Strouhal number for different values of the acoustic particle velocity υ/U at the cavity center (cavity 52 x 26 mm).

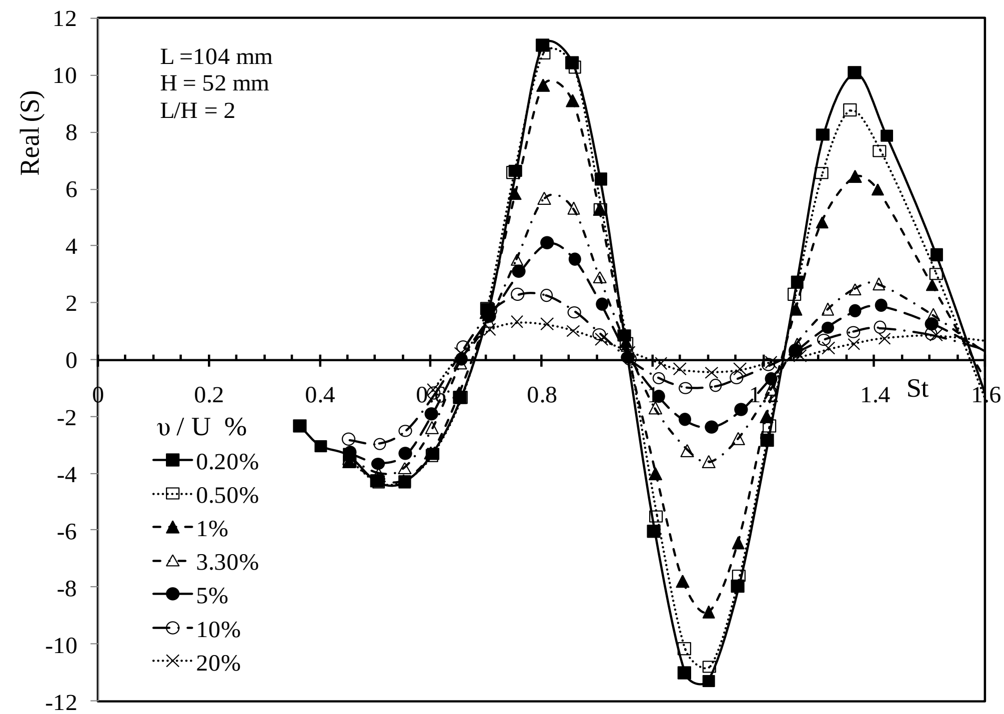

Figure 6.7: Real part of the aeroacoustic source term Real (**S**) as a function of Strouhal number for different values of the acoustic particle velocity υ/U at the cavity center (cavity 104 x 52 mm).

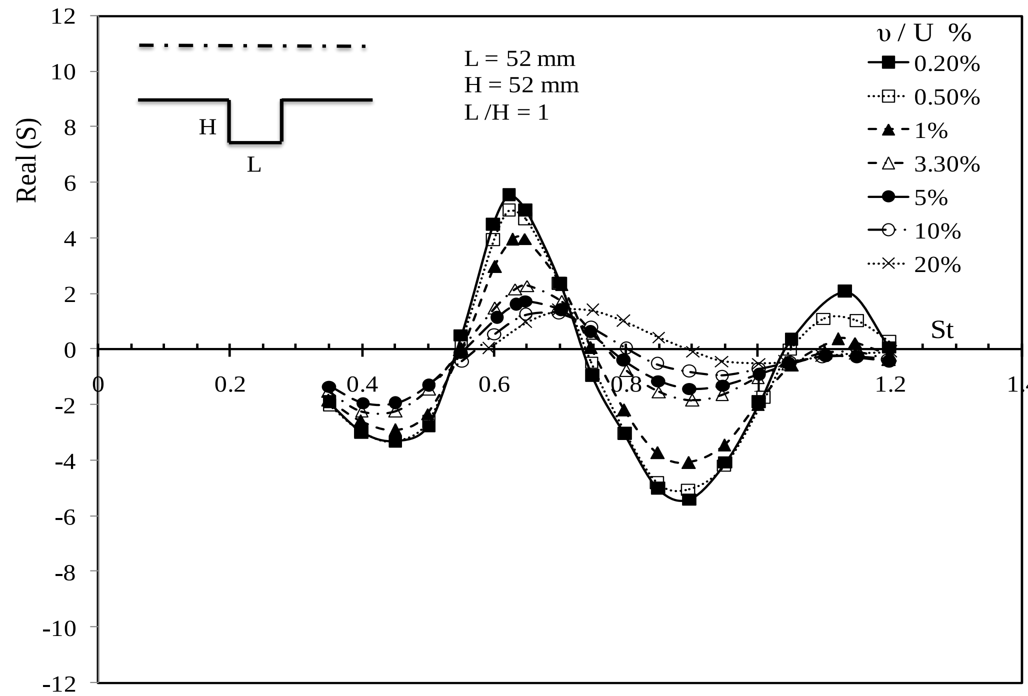

Figure 6.8: Real part of the aeroacoustic source term Real (**S**) as a function of Strouhal number for different values of the acoustic particle velocity υ/U at the cavity center (cavity 52 x 52 mm).

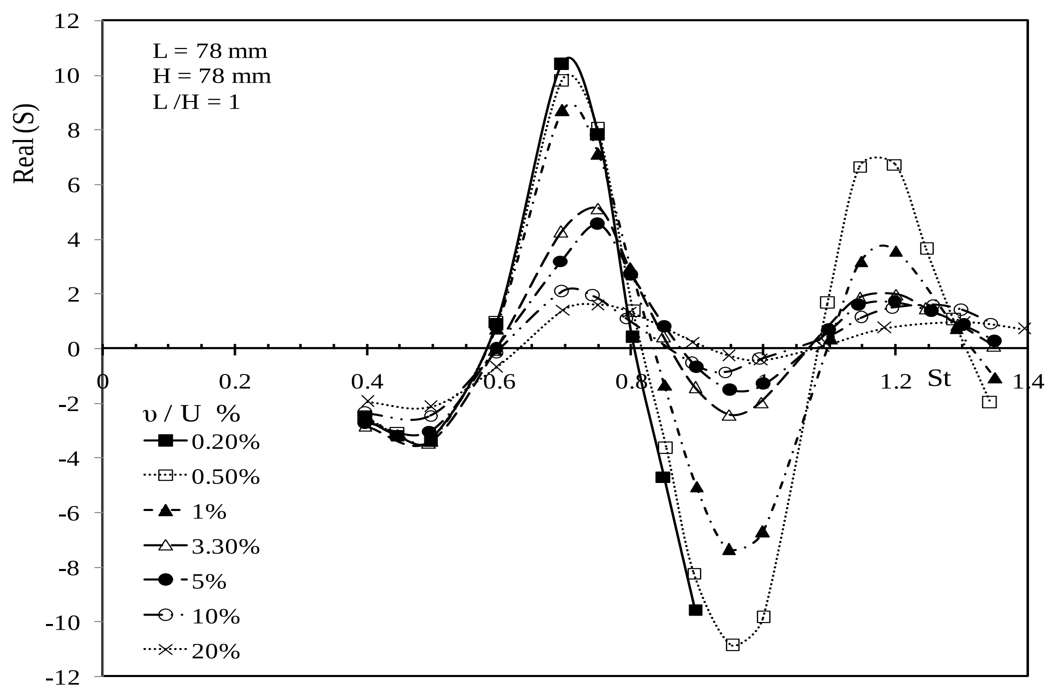

Figure 6.9: Real part of the aeroacoustic source term Real (**S**) as a function of Strouhal number for different values of the acoustic particle velocity υ/U at the cavity center (cavity 78 x 78 mm).

6.2.3.2 Effects of the Cavity Volume for the Same L/H Ratio

The effects of the cavity volume for the same L/H ratio on the aeroacoustic source strength and the self-excited resonance are presented in figures 6.10, 6.11, and 6.14. Figure 6.10 shows the effect of the cavity volume at the same length to depth ratio on the real component of the aeroacoustic source term, Real (**S**), as a function of Strouhal number for three length to depth ratios [(L/H= 1, top inset), (L/H= 2, middle inset), and (L/H= 3, bottom inset)] and different cavity volumes for each L/H ratio. In addition Figure 6.10 shows that the effect of the cavity volume is persistent for various excitation amplitude ratio, as it shows the real component of the aeroacoustic source term, Real (**S**), for two values of the acoustic oscillation amplitude, $\upsilon/U = 0.5\%$ (left column) and $\upsilon/U = 5\%$ (right column). The results of figure 6.10 for the first hydrodynamic mode are summarized in figure 6.14

The results show that as the cavity volume increases at the same L/H ratio, the peak aeroacoustic source strength increases consistently for all values of L/H ratio as shown in figure 6.14 (bottom). In addition, the Strouhal number at the peak amplitude of resonance (St_{pw1}) increases for all L/H ratios as the cavity volume increases, figure 6.14 (top).

Figure 6.11 presents the measurements results of the self-excited acoustic resonance cases at the first hydrodynamic mode, St ≈ 0.5 to 0.9 for three length to depth ratios [(L/H= 1, top inset), (L/H= 2, middle inset), and (L/H= 3, bottom inset)] and different cavity volumes for each L/H ratio. Similar trends can be seen for the effect of the cavity volume on both the aeroacoustic source characteristics and the self-excited response of the acoustic resonance. A discussion of the reasons causing the observed behavior of the aeroacoustic source as the cavity volume change for the same L/H ratio will be presented later in this chapter with the aid of the PIV measurements in section 6.2.4.

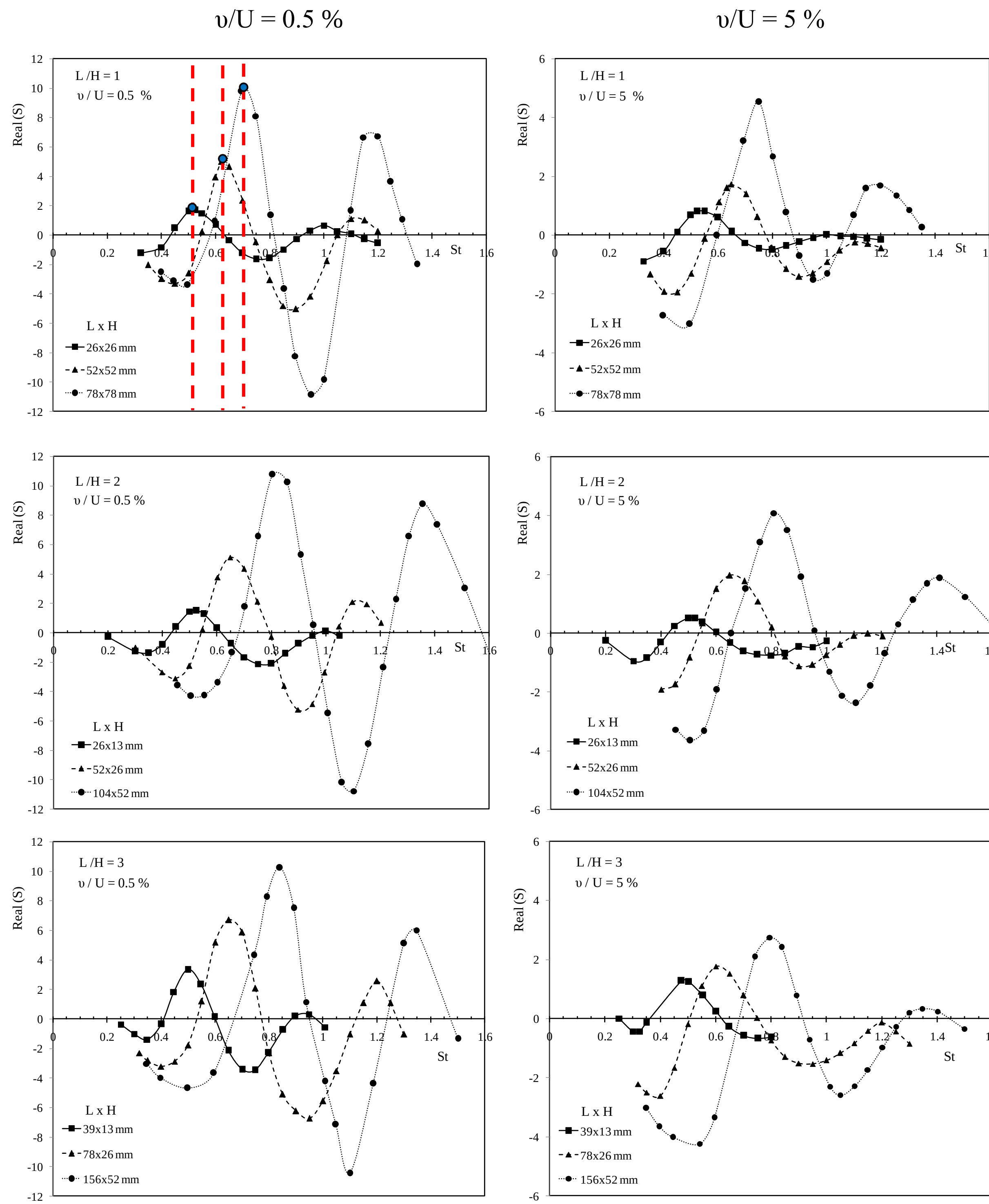

Figure 6.10: Effect of the cavity volume at the same length to depth ratio: Real component of the aeroacoustic source term, **S**, as a function of Strouhal number for three length to depth ratios (L/H= 1, 2 & 3) and different cavity volumes for each L/H ratio.

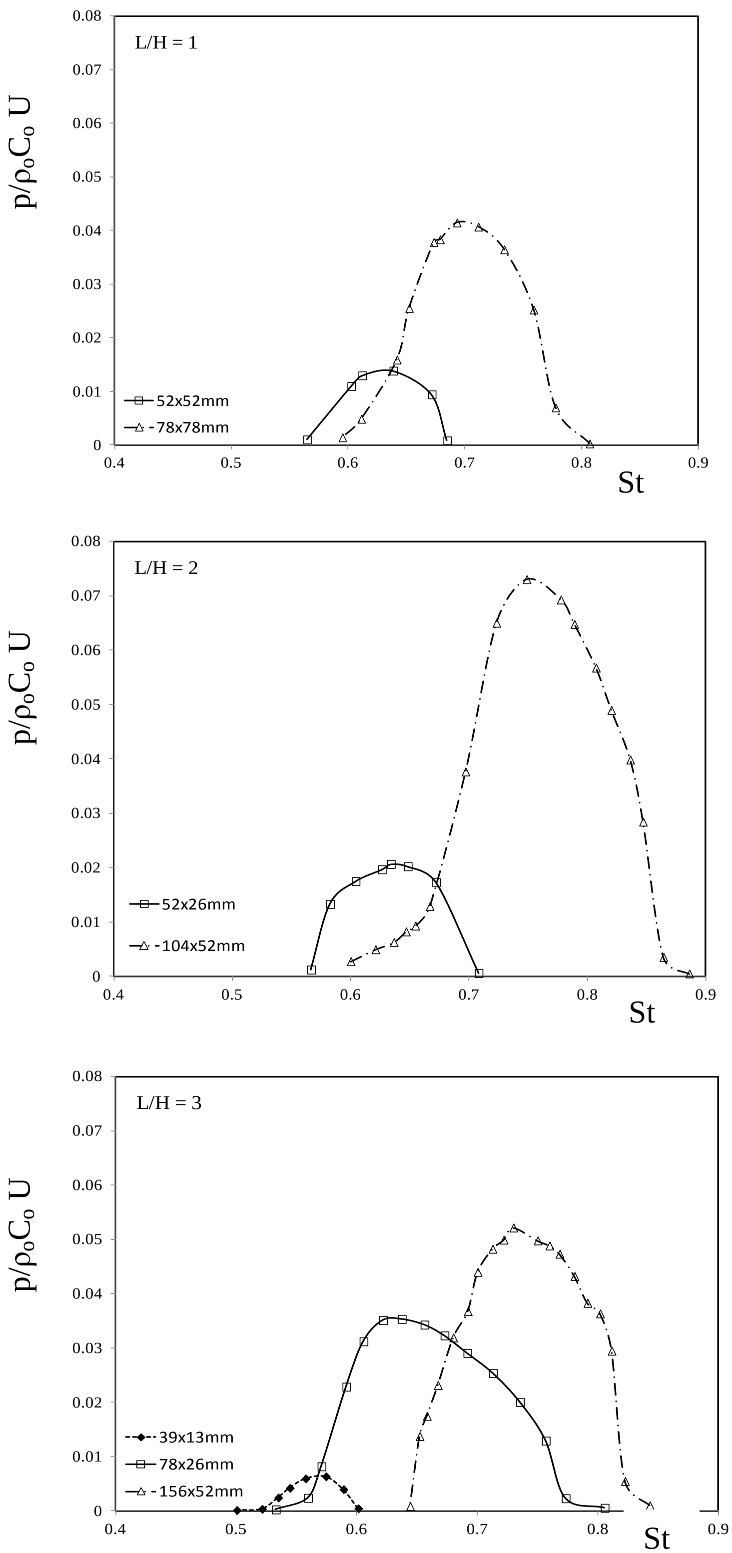

Figure 6.11: Effect of the cavity volume at the same length to depth ratio: Normalized self-excited resonance amplitude (**p**/$\rho_o C_o$U) as a function of Strouhal number for three length to depth ratios (L/H= 1, 2 & 3) and different cavity volumes for each L/H ratio.

6.2.3.3 Effects of the Cavity Length for the Same Depth

The effects of the cavity length for the same cavity depth on the aeroacoustic source strength and the peak whistling Strouhal number (St_{pw1}) are presented in figures 6.12. In this figure, the real component of the aeroacoustic source term, **S**, as a function of Strouhal number for three cavity depths (H= 13, 26 & 52 mm) and different cavity lengths for each depth are presented. Here again, in order to show the independency of the effect of the cavity length on the amplitude ratio, the results for two values of the acoustic oscillation amplitude ratio, υ/U = 0.5% (left column) and υ/U = 5% (right column) are shown in figure 6.12. The results show that increasing the cavity length at constant depth increases both the source strength (figure 6.14 bottom) and the peak Strouhal number (figure 6.14 top). However, as the ratio L/H exceeds the value of 2 (for the present experiments), the source strength and the peak Strouhal number appear to asymptote to constant values as shown by the vertical dot line in figure 6.12. This trend is persistent for several values of cavity depth.

6.2.3.4 Effects of the Cavity Depth for the Same Length

The effects of the cavity depth for the same cavity length on the aeroacoustic source strength and the peak whistling Strouhal number (St_{pw1}) are presented in figures 6.13. In this figure, the real component of the aeroacoustic source term, **S**, as a function of Strouhal number for three cavity lengths (L= 26, 52 & 78 mm) and different cavity depths for each length are presented for two values of the acoustic oscillation amplitude ratio, υ/U = 0.5% and 5%. The results show that as the cavity depth is increased at constant length, both the source strength and the peak whistling Strouhal number appear to remain constant.

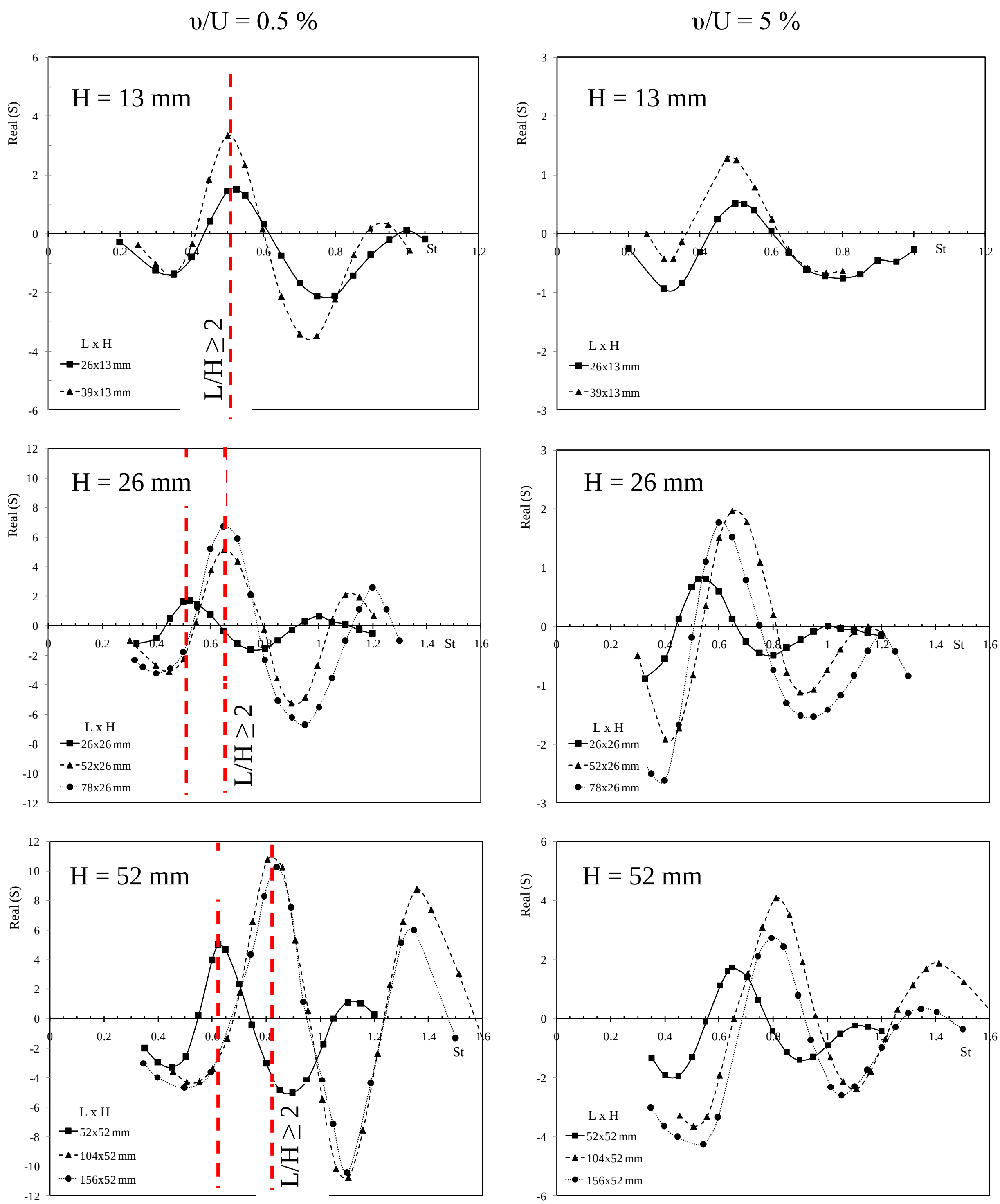

Figure 6.12: Effect of the cavity length at the same depth: Real component of the aeroacoustic source term, **S**, as a function of Strouhal number for three cavity depths (H= 13, 26 & 52 mm) and different cavity lengths for each depth.

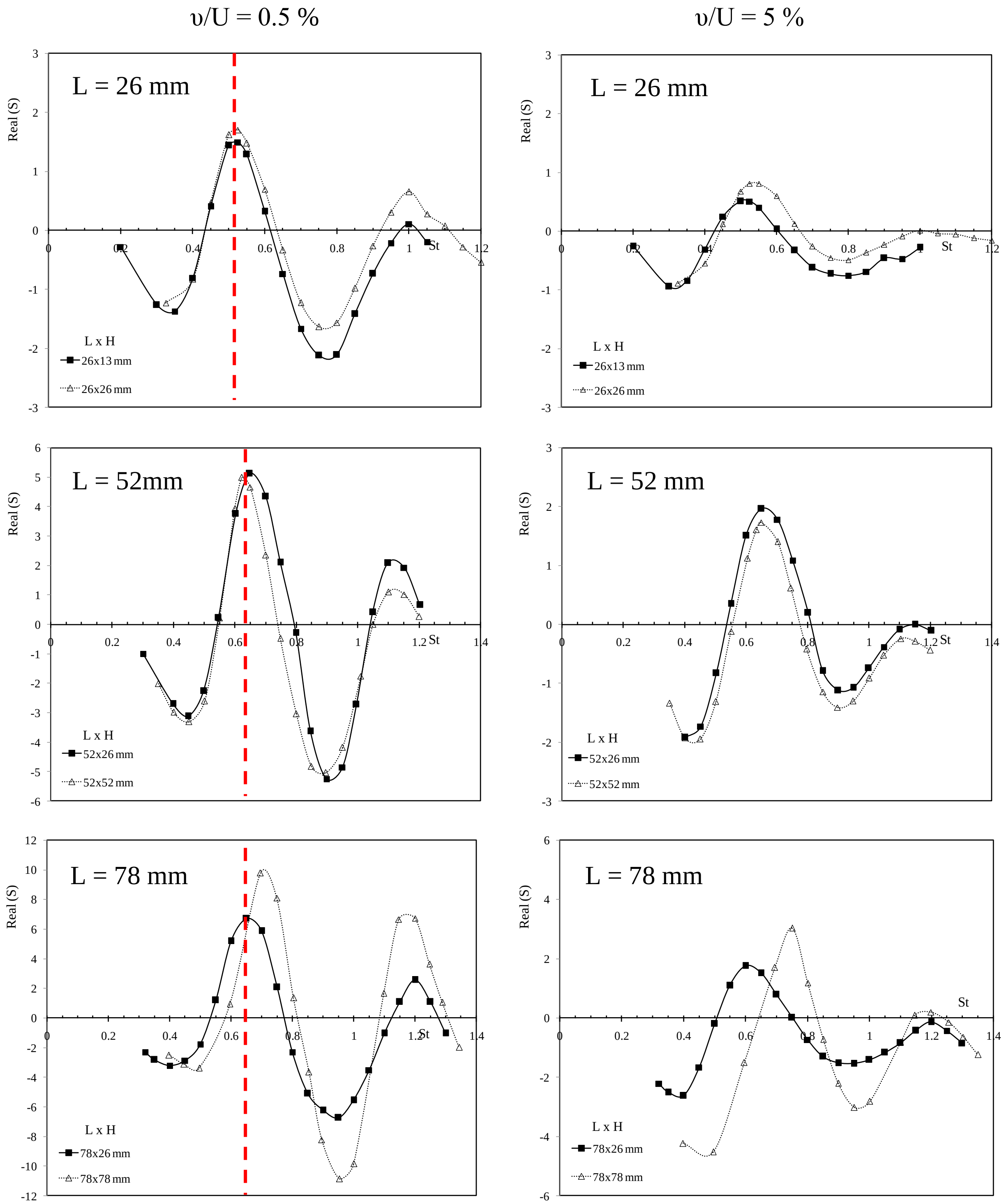

Figure 6.13: Effect of the cavity depth at the same length: Real component of the aeroacoustic source term, **S**, as a function of Strouhal number for three cavity lengths (L= 26, 52 & 78 mm) and different cavity depths for each length.

The results of the aeroacoustic source terms can be correlated with different system parameters to show the effects of varying the ratios L/H and L/D (free shear layer distance to the pipe diameter), as well as the effect of changing the cavity length L at a constant cavity depth H. As shown in figures 6.14 and 6.15, changes in these parameters affect both the peak whistling Strouhal number and the peak aeroacoustic source strength for the first hydrodynamic mode. Figure 6.14 shows the effect of L/H for various values of cavity depth. For small L/H ($L/H < 2$), increasing the cavity length at constant depth (the connected points in figure 6.14) increases both the source strength and the peak Strouhal number. However, as the ratio L/H exceeds the value of 2 (for the present experiments), the source strength and the peak Strouhal number appear to asymptote to a constant value. This trend is persistent for several values of cavity depth (H =13, 26, 52mm). In contrast, increasing the cavity volume at a constant L/H ratio causes the peak source term and Strouhal number to increase continuously without any apparent saturation in their values as the cavity volume is increased (this can be observed from the three vertical lines plotted at constant L/H ratios in figure 6.14) .

The effect of the cavity volume, expressed by increasing L/D at a constant L/H ratio, is further highlighted in figure 6.15 for the three tested L/H ratios (L/H =1, 2, 3). The peak whistling Strouhal number (top in figure 6.15), and the peak aeroacoustic source (bottom in figure 6.15), are both clearly seen to increase continuously with the increase of the cavity volume. It should be noted that the present results and trends are valid for the tested range of $L/H \leq 3$.

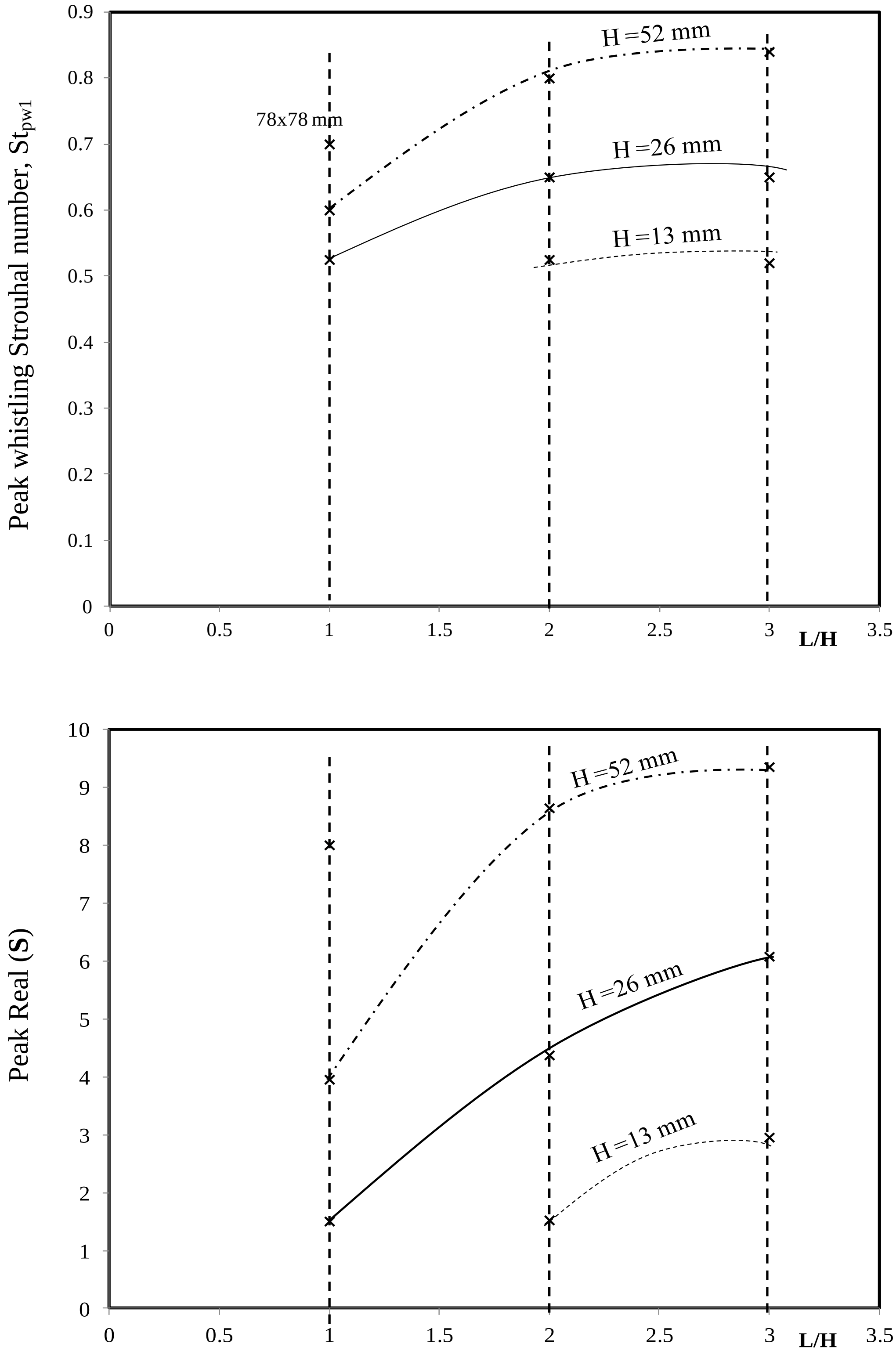

Figure 6.14: Peak whistling Strouhal numbers and peak aeroacoustic real sources at the first hydrodynamic mode for three length to depth ratios (L/H = 1, 2 & 3) and different cavity volumes for each L/H ratio. (υ/U = 1%)

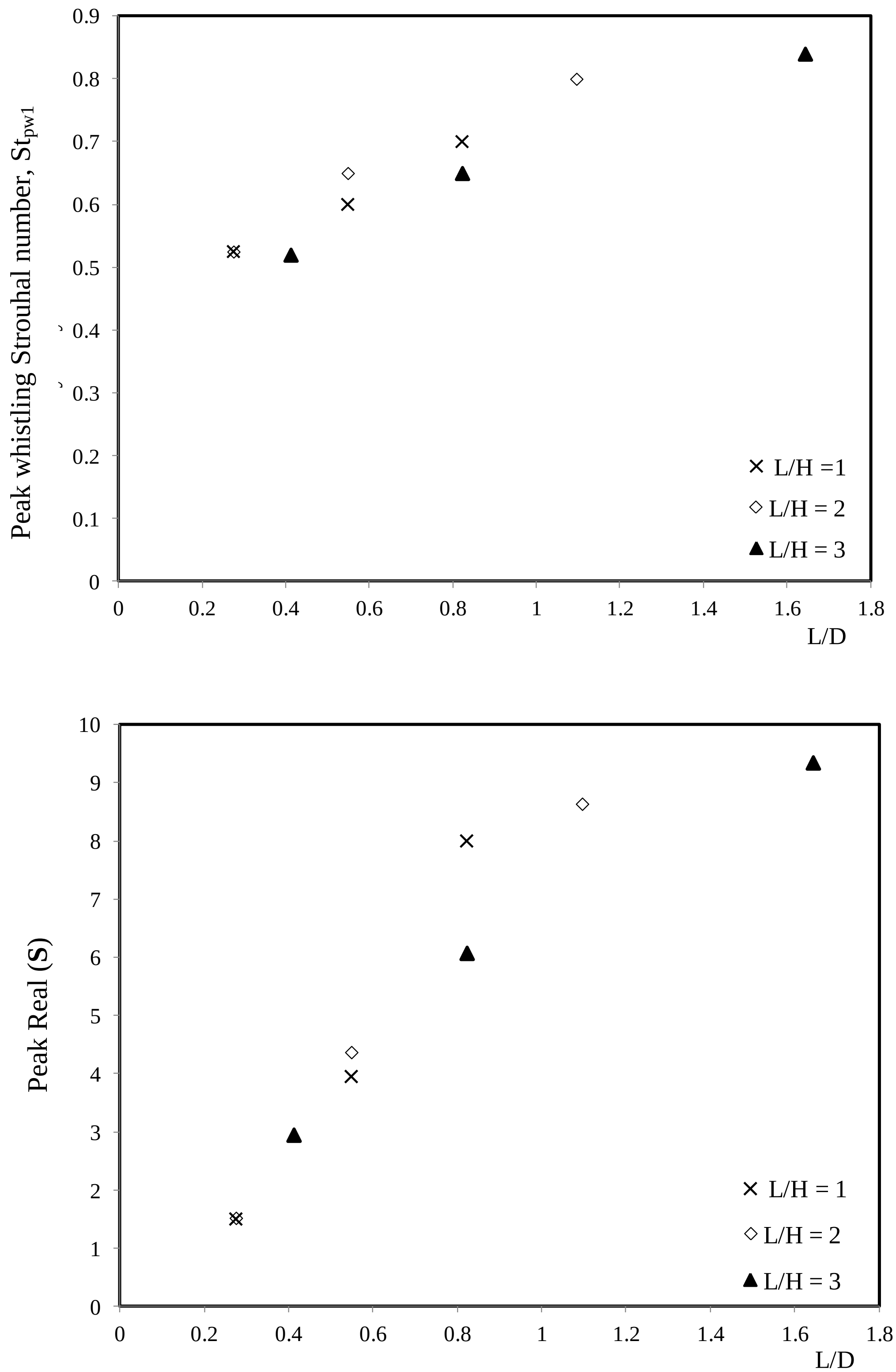

Figure 6.15: Peak whistling Strouhal numbers and peak aeroacoustic real sources at the first hydrodynamic mode for three length to depth ratios (L/H= 1, 2 & 3) as a function of L/D ratio. (υ/U = 1%)

6.2.4 Discussion of Results

Effect of the cavity geometry on the peak-whistling Strouhal number (*$\mathbf{St_{pw1}}$*)

In order to understand the effect of cavity geometrical parameters on the Strouhal number at the peak amplitude of resonance, the Strouhal number relation can be decomposed as follow:

$$\mathrm{St} = \frac{\mathrm{fL}}{\mathrm{U}} = \frac{\mathrm{fL}}{\mathrm{U_c}} \times \frac{\mathrm{U_c}}{\mathrm{U}} \qquad (6.1)$$

where f is the piping system resonance frequency, which is constant as the same system is used in all experiments, U_c is the convection (phase) speed of the shear layer disturbance over the cavity mouth and the ratio (L/U_c) is the travel time of the disturbance along the cavity mouth. At the maximum amplitude of resonance, the disturbance travel time L/U_c must remain virtually constant so that the phasing of events is favorable and acoustic energy is produced. Thus, ($f\ L/U_c$) must remain virtually constant which means that any changes in the resonance Strouhal number at the maximum resonance amplitude must be corresponding to changes in U_c/U ratio, as can be seen from equation 6.1.

The ratio of the convection velocity to the mean flow velocity (U_c/U) depends on the fluid flow pattern over the cavity, which is affected by the mixing process between the cavity stagnant fluid and the main stream flow. This suggests that the cavity geometry must affect the mixing process and the trajectory of the shear layer vortices along the cavity mouth.

In order to explore these effects, we first consider the convection velocity of a cavity with a fixed depth while increasing its length as illustrated schematically in figure 6.16. This figure shows cavities of constant depth H but varying length from L = H to 4H.

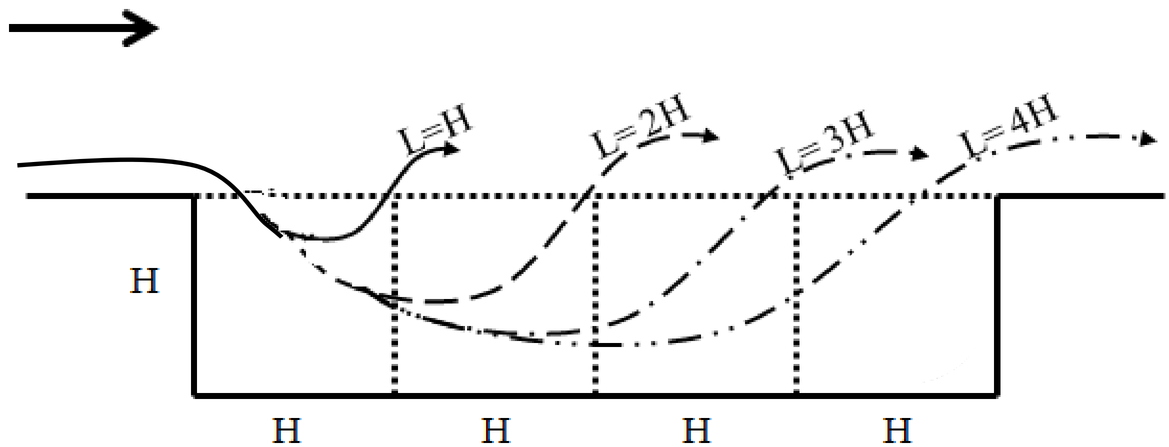

Figure 6.16: Cavity flow patterns as the cavity length increases for the same depth

As the cavity length increases from L=H to L=2H, the main flow is expected to penetrate deeper inside the cavity and more of the stagnant fluid inside the cavity will therefore be entrained with the main flow. This leads to a higher local flow velocity at the cavity mouth and consequently higher convection velocity (higher U_c/U) as well as an increase in peak whistling Strouhal number. However, as the cavity length increases to 3H or 4H, the penetration depth of the main flow will become increasingly limited due to the presence of the cavity floor at a constant depth, leading to an asymptotically constant value of U_c/U or a constant peak whistling Strouhal number as shown in figures 6.12 and 6.14 for the cavities of same depth but different length.

However, as the cavity depth and length increase simultaneously (case of constant L/H with increasing cavity volume, figure 6.10), the proximity effect of the cavity floor on the mixing process weakens, which results in a continuous increase in U_c/U ratio as the volume increases. Therefore, according to equation 6.1, a higher peak whistling Strouhal number occurs as the cavity volume increases for constant L/H ratio as shown in figures 6.10, 6.11, 6.15. For the case of constant length with increasing cavity depth as shown in figure 6.13, the peak whistling Strouhal number remains almost constant because the flow pattern is mainly affected by the cavity length.

In order to assess the above hypotheses, a flow visualization study by means of PIV technique was performed for two cavities of similar L/H =2 but different volumes. The length and depth of the smaller and larger size cavities were 52 x 26 mm and 104 x 52 mm, respectively. The flow conditions and acoustic amplitudes for the visualization study were selected to be at the peak whistling Strouhal number and at the same acoustic amplitude ratio. This corresponds to St = 0.65 and υ/U= 5% for the smaller cavity and St = 0.75 and υ/U= 5% for the larger one. Figures 6.17 and 6.18 present flow visualization images of the instantaneous flow fields at similar instants in the acoustic cycle for both cavity sizes.

The flow fields of both cavities in figures 6.17 and 6.18 show the presence of a vortical structure at a certain location along the cavity mouth at each measured instant in the acoustic cycle. The identification of the vortex structure and its weighted center location is calculated using the velocity discriminate parameter proposed by Vollmers, (2001). The 8 red points in the cavity flow images identify the vortex center locations at 8 instants over a complete acoustic cycle.

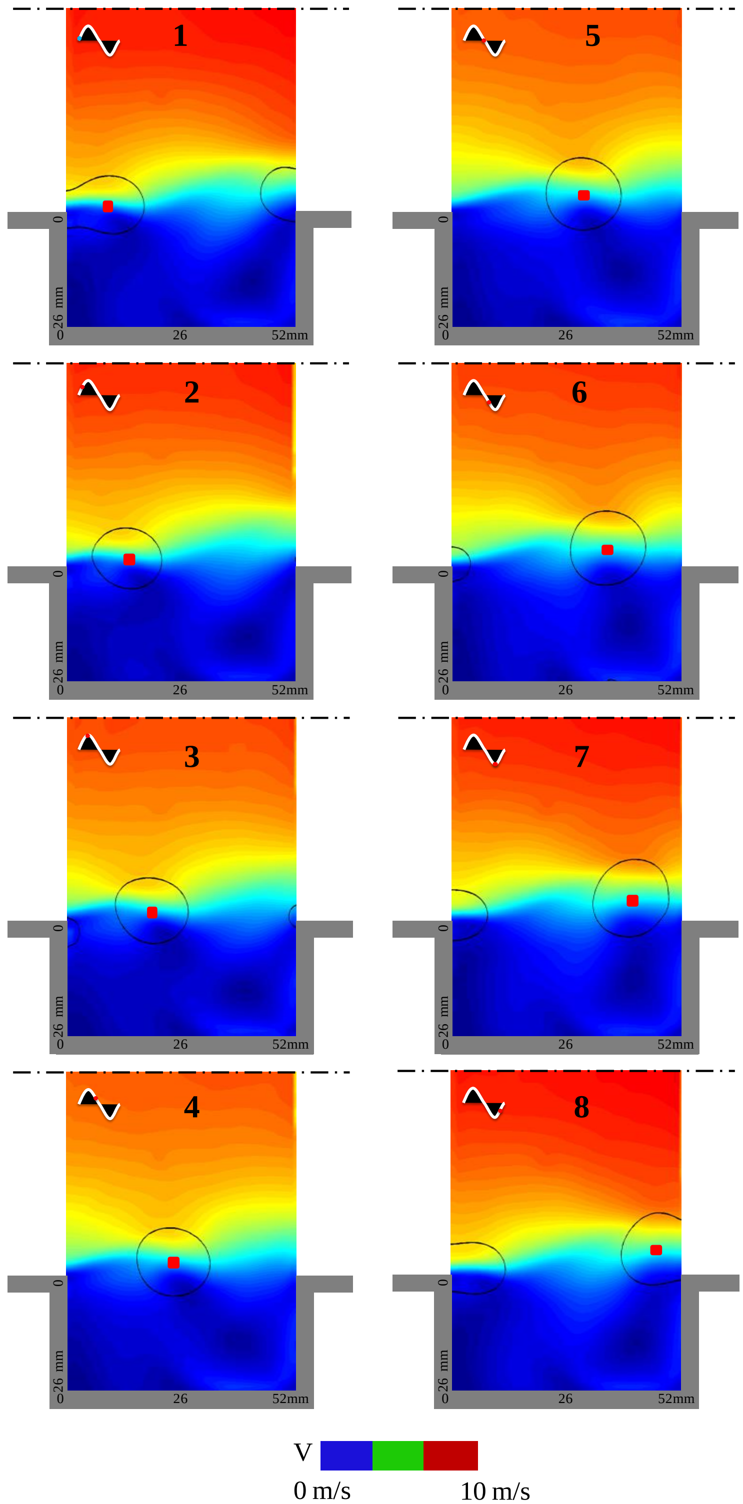

Figure 6.17: Flow fields show the presence of a vortical structure at a certain location along the cavity mouth at 8 measured instants of the acoustic cycle with a constant time interval. The red square point in each instantaneous flow field identifies the vortex center location. Small cavity size of 52 mm long and 26 mm deep.

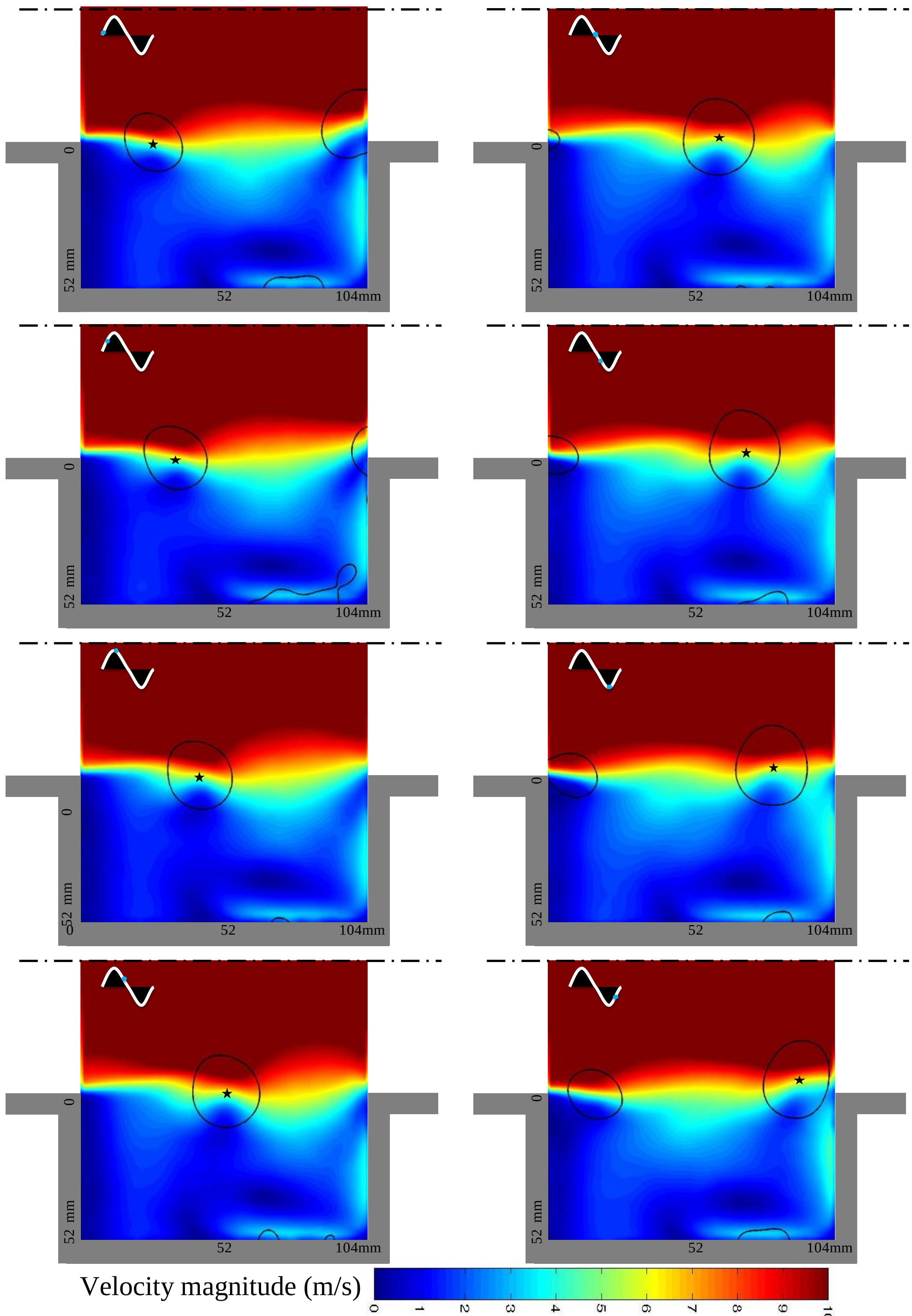

Figure 6.18: Flow fields show the presence of a vortical structure at a certain location along the cavity mouth at 8 measured instants of the acoustic cycle with a constant time interval. The point in each instantaneous flow field identifies the vortex center location. Larger cavity size of 104 mm long and 52 mm deep.

From the flow visualization images, the distributions of the vortex convection velocity (phase speed) along the cavity mouth were calculated for both cavity sizes. The convection velocity is calculated from the ratio of the distance between two consecutive vortex center positions to the time interval between the images. Figure 6.19 presents this convection velocity, normalized by the mean flow velocity, (U_c/U), as a function of the normalized position along the cavity mouth (x/L), where x is the horizontal distance from the cavity leading edge and L is the cavity length. Figure 6.19 shows that for the same L/H ratio, the larger the cavity volume the higher the convection velocity, which leads to a higher whistling Strouhal number according to equation 6.1.

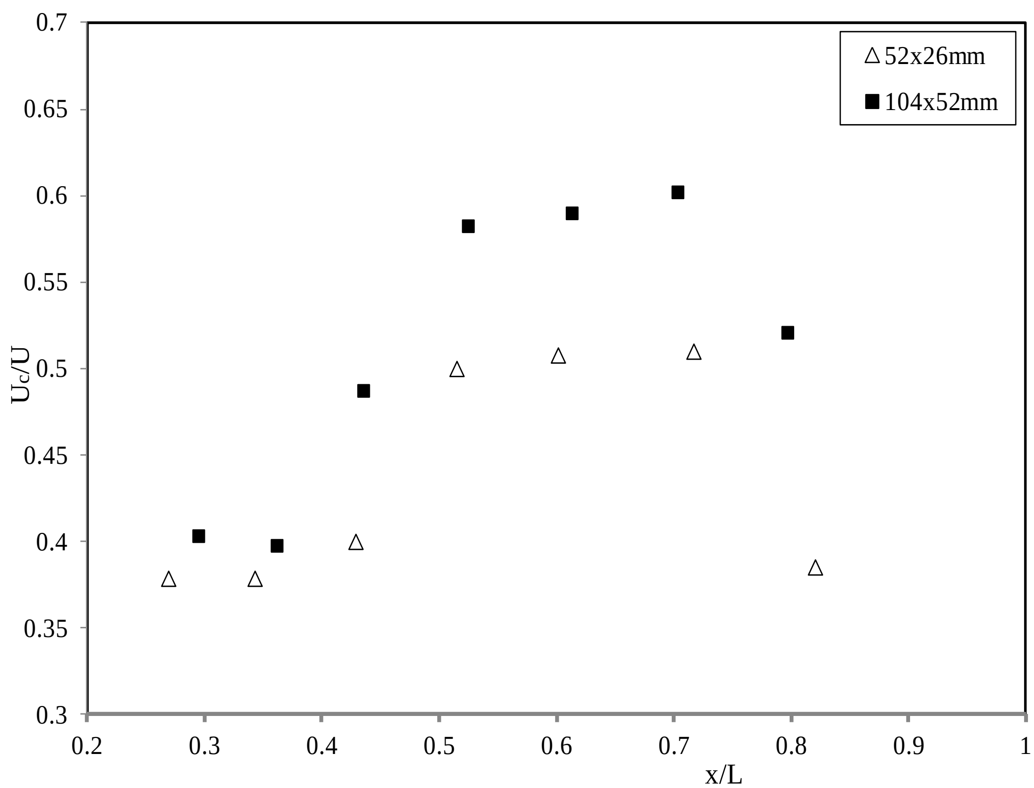

Figure 6.19: Convection velocity U_c/U distributions determined from the PIV measurements for different cavity volumes with the same L/H ratio

Effect of the cavity geometry on the peak value of the source term

Howe (1978) showed that the instantaneous acoustic power P in a non-vanishing vorticity field within a volume V is proportional to the triple product of the vorticity ω, flow velocity U, and acoustic particle velocity υ as presented in equation 2.18. In order to identify the controlling variable of the aeroacoustic power in this type of flow and geometry, the discrete vortex model proposed by Nelson et al. (1983) is applied. This model considers the vorticity in the free shear layer to be concentrated into point vortices travelling with an approximately constant phase speed along the cavity mouth (U_c/U = 1/2). Thus, the vorticity vector ω in Howe's integrand may be replaced by the circulation of the vortex Γ which can be approximately estimated from the flow velocity and the acoustic wave frequency as follow (Howe, 1998):

$$\Gamma = U \times \frac{U}{2} \times \frac{1}{f} \qquad (6.2)$$

The cross product (U x υ) in equation 2.18 can be rearranged for 2-D flow as follows:

$$(U \times \upsilon) = U_x \upsilon_y - U_y \upsilon_x \qquad (6.3)$$

where $U = U_x\, i + U_y\, j$ and $\upsilon = \upsilon_x\, i + \upsilon_y\, j$; x is the flow direction and y is the cross-stream direction. By considering the main flow to be in x-direction or $U_x \gg U_y$, the acoustic power is expected to be strongly affected by the term ($U_x \upsilon_y$). As the relative change in U_x, which is ΔUx/Ux, is very small compared to the relative change in υ_y at the cavity mouth, the parameter with the strongest influence on aeroacoustic power generation appears to be the cross-stream component of the acoustic particle velocity field, υ_y.

In order to scrutinize the cross-stream component of the acoustic particle velocity in the cavity region and how it is affected by the cavity geometrical parameters, the finite element technique using ABAQUS is employed to obtain the acoustic pressure distribution in conjunction with a MATLAB code solving Euler's equation to compute the acoustic particle velocity field and the streamlines for different cavity sizes exposed to the same level of oscillation amplitude. More details on the finite element simulation as well as the mesh size, type, and boundary conditions are available in section 5.2.1.

Figures 6.20 and 6.21 show the cross-stream component of the acoustic particle velocity υ_y at the cavity mouth (y=0) as a function of x/L, where x and y are measured from the cavity leading edge. Figure 6.20 depicts the results of cavities with a constant depth (H= 26 mm) but different lengths (L= 26 to 104 mm), which corresponds to the cavities discussed in figure 6.12. It can be observed that as the cavity length increases at a constant depth, the cross-stream component of the acoustic particle velocity υ_y first increases, but then becomes virtually constant for L/H > 2. However, as the cavity depth and length increase simultaneously (i.e. larger cavity volume with the same L/H ratio), the effect of the cavity floor is largely reduced. That leads to a continuous increase in cross-stream component υ_y as the cavity volume increases, as illustrated in figure 6.21. Note that this increase occurs near the leading and trailing cavity edges where the positive aeroacoustic sources are positioned, but the effect on υ_y is marginal near the cavity center, where the aeroacoustic sink exists. Therefore, a continuous increase in the maximum aeroacoustic source term is observed as the cavity volume is increased at a constant L/H ratio, as illustrated in figure 6.15.

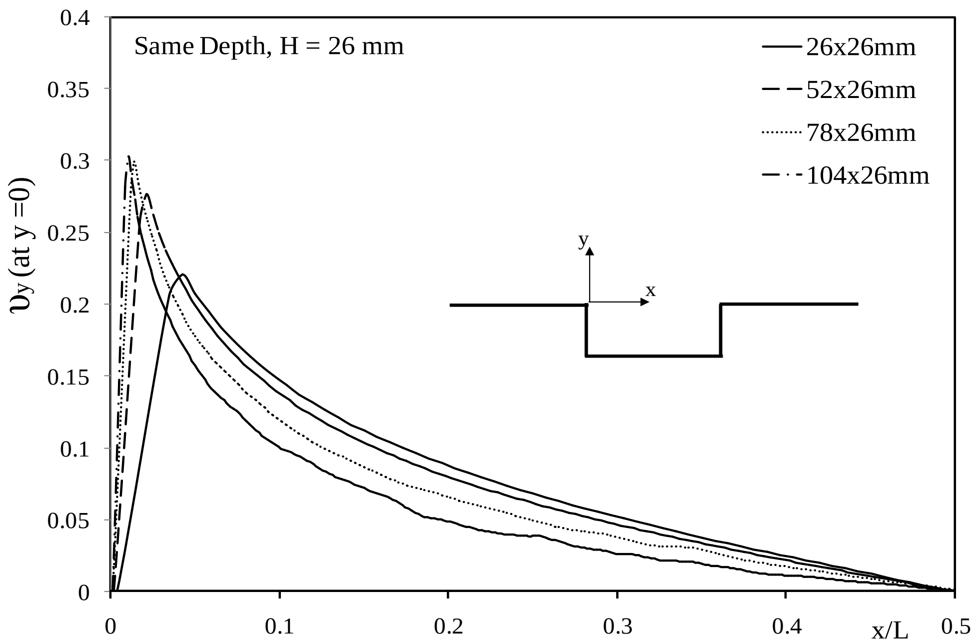

Figure 6.20: Cross stream component of the acoustic particle velocity, υ_y, at the cavity opening, y = 0, at a similar specified instant in the acoustic cycle. Results are shown for a constant cavity depth, H = 26 mm

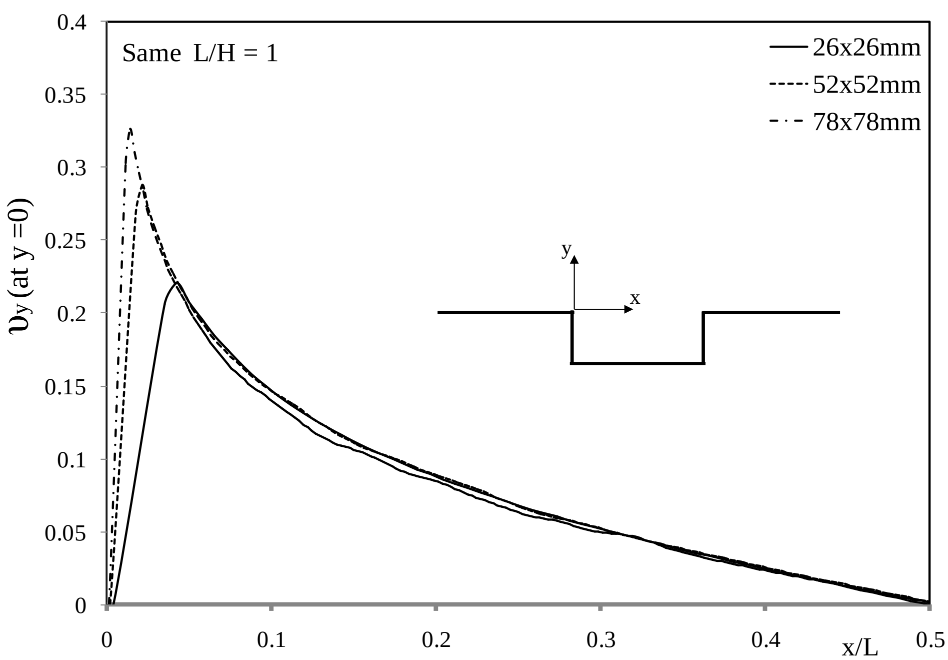

Figure 6.21: Cross stream component of the acoustic particle velocity, υ_y, at the cavity opening, y = 0, at a similar specified instant in the acoustic cycle. Results are shown for the same L/H ratio, L/H = 1

In summary, the effects of the cavity geometrical parameters on the aeroacoustic source strength and acoustic resonance intensity have been experimentally investigated using the SWM and self-excited resonance measurements. The results showed that as the cavity volume increases for the same L/H ratio, the aeroacoustic source strength, the resonance oscillations amplitude and the whistling Strouhal number increase in a consistent manner. The increase in the whistling Strouhal number is caused by the increase in the vortex convection velocity at the cavity mouth as the cavity volume increases for same L/H ratio. This has been confirmed experimentally by means of PIV measurements. The aeroacoustic source strength increases due to the continuous increase in the cross-stream component of the acoustic particle velocity with the increase in the cavity volume for the same L/H ratio. The effect of the cavity volume on the particle velocity distribution has been illustrated by numerical simulation of the acoustic resonant mode.

The present results underline the importance of considering the cavity volume when assessing the aeroacoustic response of shallow cavities in pipelines. In addition, the results show that increasing the cavity length at constant depth increases both the source strength and the peak Strouhal number. However, as the ratio L/H exceeds the value of 2, the source strength and the peak Strouhal number appear to asymptote to a constant value. This trend is persistent for several values of cavity depth. Also, increasing the cavity depth at constant length does not seem to influence the source strength nor the peak Strouhal number. In the next section, the effects of rounding-off the cavity edges on the shallow cavity acoustic resonance response will be investigated.

6.3 Effect of Rounding-off the Cavity Edges

6.3.1 Motivation

In the literature, the effect of the curvature of cavity edges on the flow oscillations is rather ambiguous because these oscillations depend strongly on both the acoustic mode and the cavity type (shallow or deep). Bruggeman et al. (1991) classified the different modes of acoustic pulsations in a deep side-branch into three categories, as shown in figure 6.22. In Case **A**, the acoustic pulsations are trapped between the side-branch and the upstream pipe; and in Case **B**, they are trapped between the side-branch and the downstream pipe (cases **A** and **B** are therefore called Trapped Mode). In Case **C**, the acoustic pulsations are not trapped and oscillate back and forth **longitudinally** between the upstream and the downstream pipe sections. According to Bruggeman classification, curved upstream edge in case **B** will have negligible effect on the acoustic resonance, which is similar to the effect of rounding-off the downstream edge in Case **A**. Conversely, rounding the downstream edge in Case **B** or the upstream edge in Case **A** affects the pulsations amplitude.

Knotts and Selamet (2003) examined the effect of curving both edges on the resonance response for the trapped mode in a side-branch. Figure 6.23 shows a strong reduction in the resonance pulsation amplitude with rounded edges. Bolduc et al. (2014) studied the effect of curving both edges on the resonance response for trapped modes of shallow cavities. Their results show the amplification in the resonance amplitude with the curved edges, as shown in figure 6.24.

The above results are contradictory as they strongly depend on both the acoustic mode pattern and the cavity type (shallow or deep). So the objective in this research section is to investigate the effect of rounding-off the cavity edges on the resonance response of the longitudinal acoustic mode excited by flow over a shallow cavity.

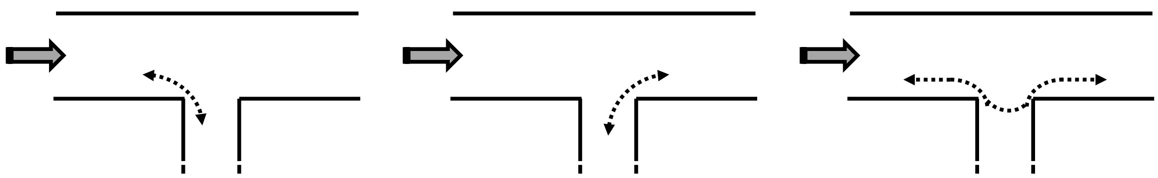

Figure 6.22: Different types of acoustic modes for a side-branch in a pipeline; cases **A** and **B** are trapped modes while case **C** is a longitudinal mode (according to Bruggeman et al., 1991).

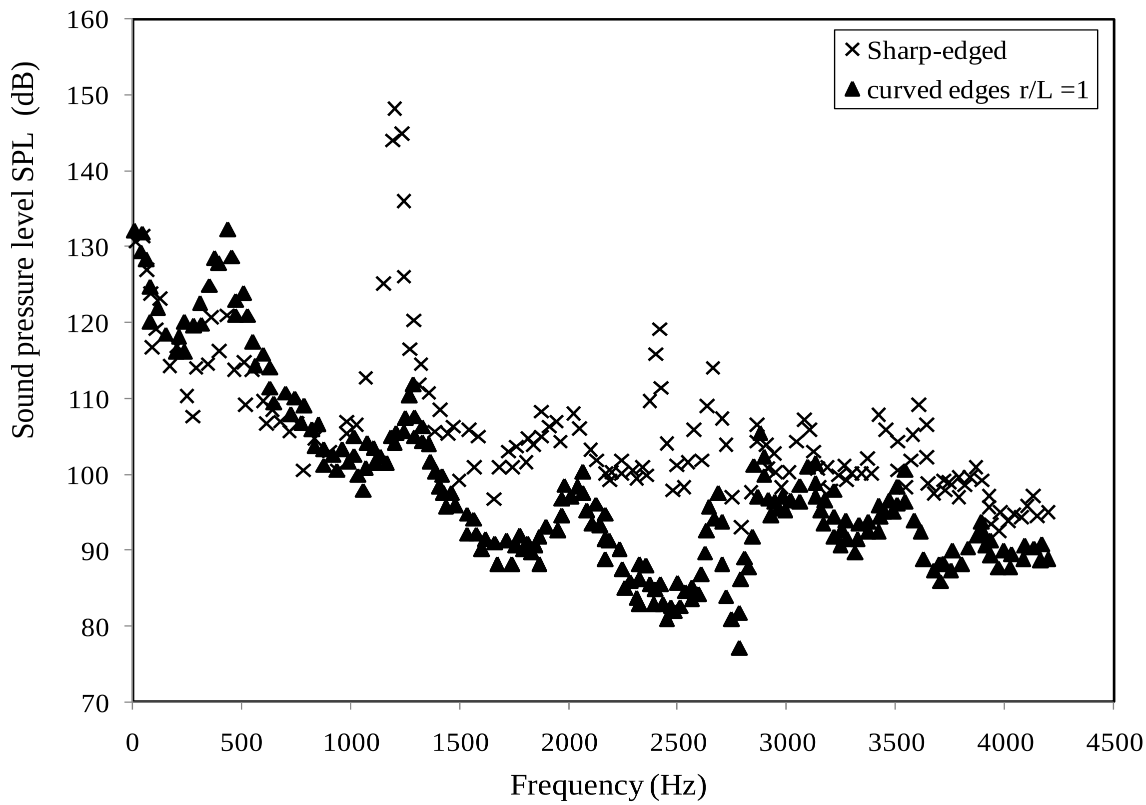

Figure 6.23: Effect of rounding-off edges on the resonance response of the trapped acoustic mode in a side-branch (Knotts & Selamet, 2003).

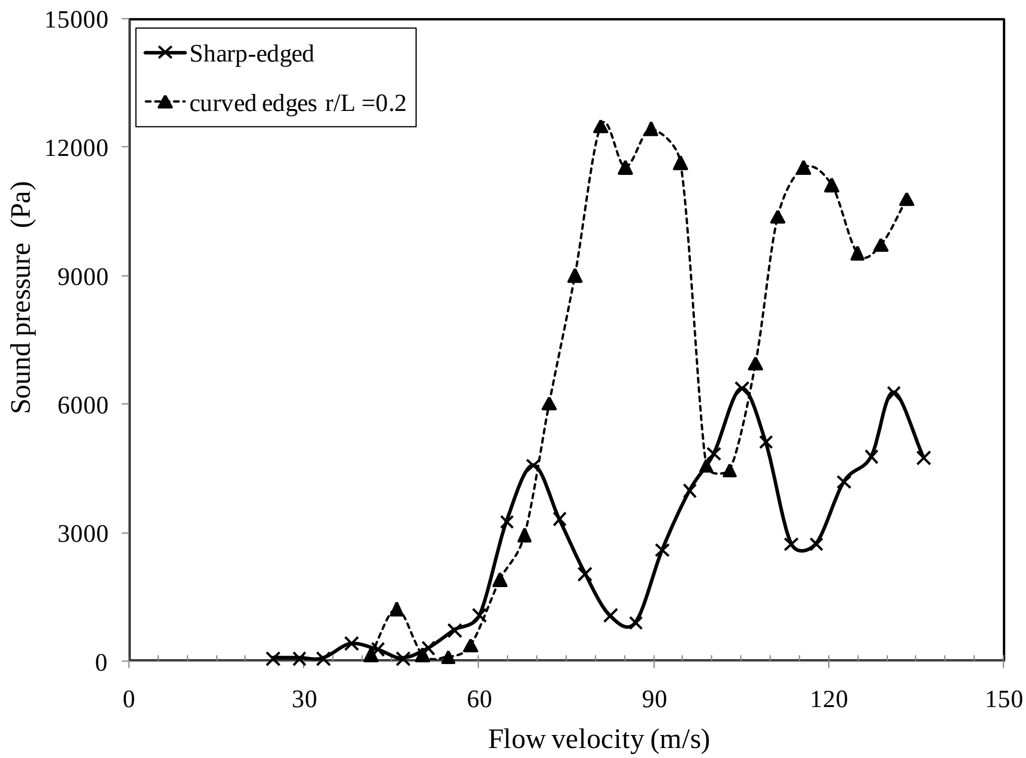

Figure 6.24: Effect of rounding-off edges on the resonance response of the trapped acoustic mode in a shallow cavity (Bolduc et al., 2014).

6.3.2 Methodology and Tested Geometries

One cavity size is selected (78 mm long by 26 mm deep) to be tested with different combinations and sizes of edge curvatures. The self-excited resonance response is investigated by using the same system and methodology described in section 3.2. Table 6.4 and figure 6.25 show the combinations and sizes of edge curvatures that are studied.

Description	Upstream edge curvature r_{up}/H	downstream edge curvature r_{dn}/H
Sharp-Sharp	0	0
Curved-Sharp	20%, 40%, 100%	0
Sharp-Curved	0	20%, 40%, 100%
Curved-Curved	20%, 40%, 100%	20%, 40%, 100%

Table 6.4: Tested cavities with rounded-off edges

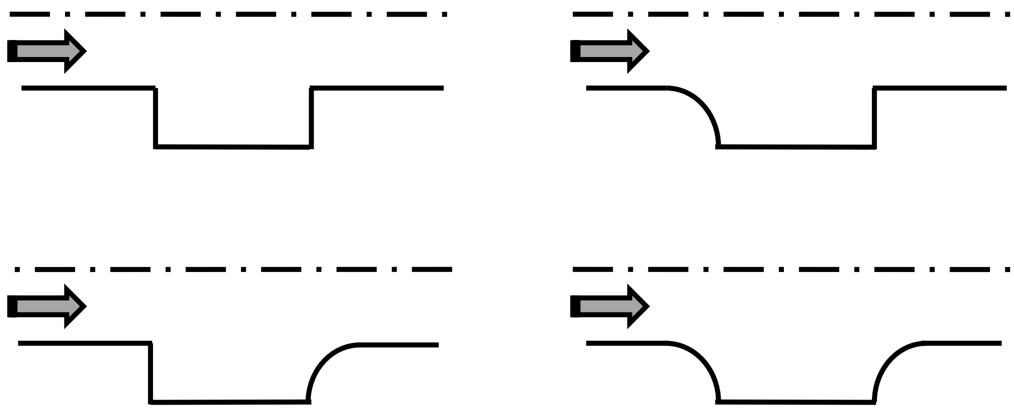

Figure 6.25: Different studied cases of rounded edges

6.3.3 Results

Figures 6.26 and 6.27 present the effect of edge curvature on the self-excited resonance amplitude. In figure 6.26, the effects of the location and curvature size of the curved edge(s) on the normalized self-excited resonance amplitude are illustrated for the four possible cases; sharp-sharp, curved-sharp, sharp-curved, and curved-curved, as well as for three curvature sizes (r/H = 20%, 40%, and 100%) for the cavity size of 78 mm long and 26 mm deep. The following observations can be made:

- Whatever the size of the curvature, the cavity with curved upstream edge and sharp downstream edge has the highest normalized resonance amplitude ratio followed by the sharp-sharp then the sharp-curved cases while the lowest resonance amplitude ratio is for the curved-curved case.
- The reduction in the normalized resonance amplitude from the strongest to the weakest resonance cases is around 15-20% for r/H values of 20 and 40% (top and middle insets of figure 6.26), but for the case of r/H is equal to 100%, the maximum reduction is about 40% (bottom inset of figure 6.26).

- From the top inset of figure 6.27 (all cases with sharp-curved edges), as the downstream edge curvature size increases, the resonance amplitude slightly decreases, and the maximum reduction is about 20%.
- From the middle inset of figure 6.27 (all cases with curved-sharp edges), as the upstream edge curvature size increases, the resonance amplitude slightly increases and then saturates. The maximum increase is about 16%.
- According to the bottom inset of figure 6.27 (all cases with curved-curved edges), as the edges curvature size increases, the resonance amplitude slightly decrease till r/H = 40% and then a maximum reduction of about 30% occurs for the case of r/H = 100%.
- In general, based on the above results, there are no significant effects of the upstream or downstream edge curvature on the normalized acoustic resonance amplitude for the case of shallow cavity coupled with longitudinal acoustic mode except for relatively large radius. This finding is totally different from published results on the effects of edge curvature for the cases of side-branches and shallow cavities coupled with trapped acoustic modes which were investigated in previous works by Knotts and Selamet (2003), Bolduc et al. (2014), and many others. This difference effect is expected as the spatial distribution of the aeroacoustic sources in the present case is found to be different from those observed in previous studied patterns.

6.3.4 Discussion of Results

From the above observations on the effect of cavity edge curvature, there is no significant effect on the resonance amplitude from rounding-off the edges of the cavity, except for relatively large radius. In order to understand these results, the acoustic particle velocity streamlines in the cavity region and how they are affected by the cavity edge curvature are computed.

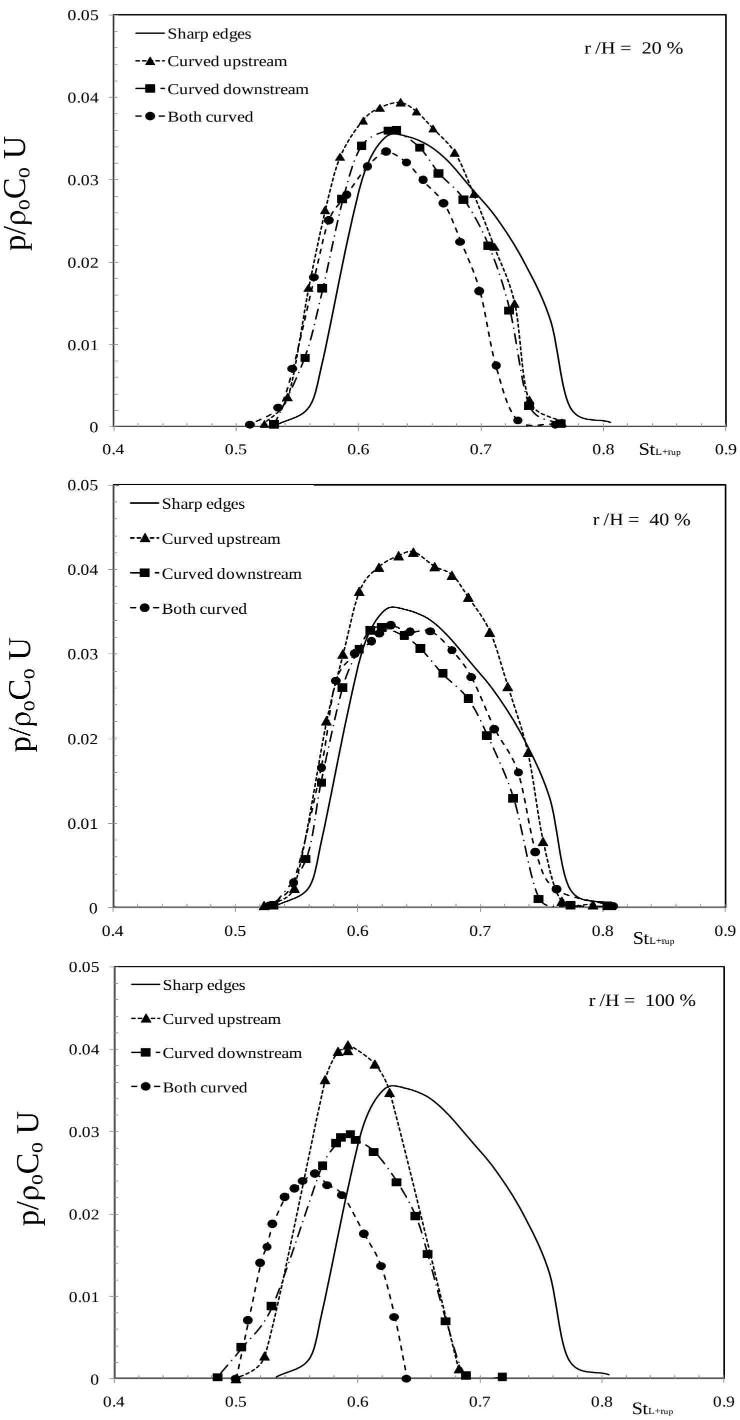

Figure 6.26: Effect of the location of the curved edge(s) on the normalized self-excited resonance amplitude. Three curvature sizes are tested (r/H = 20%, 40%, and 100%) for cavity size of 78 mm long and 26 mm deep.

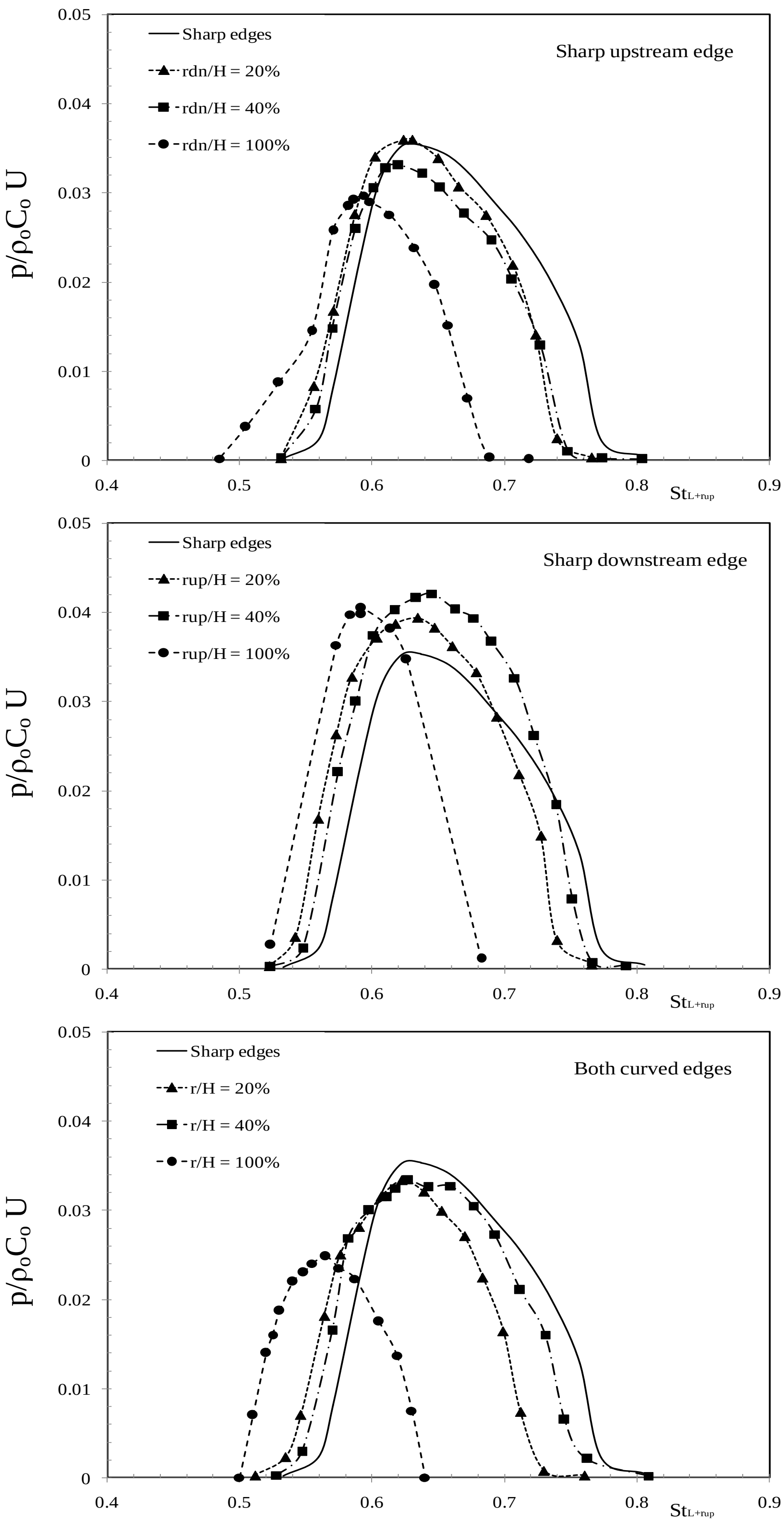

Figure 6.27: Effect of the edge curvature sizes on the normalized self-excited resonance amplitude. Four curvature sizes are tested (r/H = 0%, 20%, 40%, and 100%) for all possible curvature location cases. Cavity size of 78 mm long and 26 mm deep.

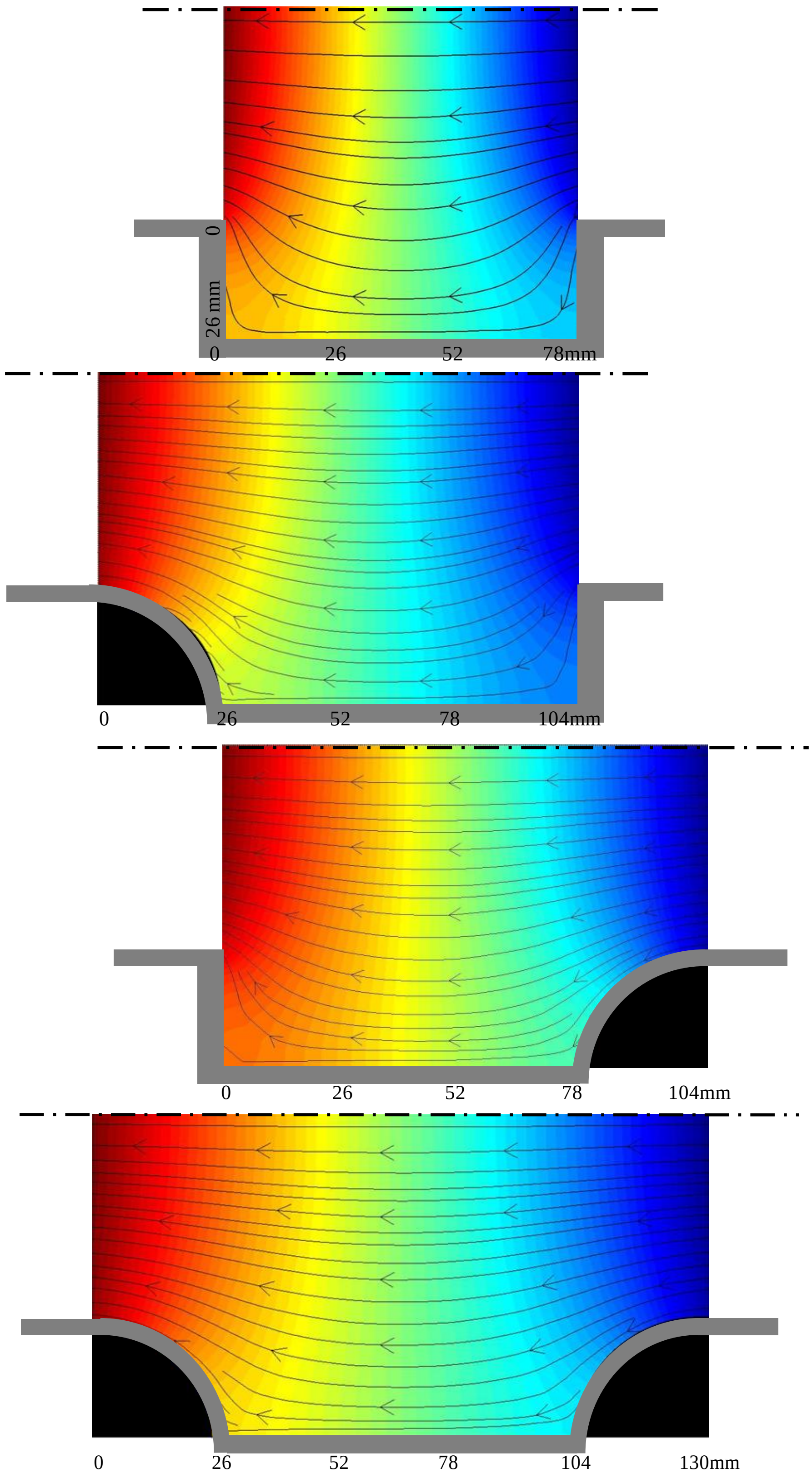

Figure 6.28: Effect of location of the curved edge on the acoustic particle velocity streamlines for cavity of 78 mm x 26 mm

The finite element technique using ABAQUS is employed to obtain the acoustic pressure distribution of the resonance acoustic mode and a MATLAB code solving Euler's equation is used to compute the acoustic particle velocity field and the streamlines for different locations of curved edges. More details on the finite element simulation as well as the mesh size, type, and boundary conditions are available in section 5.2.1.

Figure 6.28 shows the acoustic particle velocity streamlines for different locations of the curved edge. The curved edge seems to reduce the vertical component of the acoustic velocity as the streamlines have more space for gradual change than in the case of sharp edged cavity. On the other hand, the curved edge increases the length over which the source power is integrated. These two opposite effects make the overall influence of the curved edges on the normalized self-excited resonance amplitude insignificant.

In summary, a comprehensive study of the effects of rounding-off the cavity edges is presented. From this study, rounding-off the cavity edges causes a reduction in the vertical component of the acoustic particle velocity that leads to a reduction in the acoustic power. However, increasing the cavity length provides a larger volume over which the acoustic power is integrated which increases the acoustic power. These opposite effects cancel out and therefore the acoustic amplitude is not significantly affected by rounding-off the cavity edges, except for relatively large radius. This finding is different from published results on the effects of edge curvature for other flow-sound interaction patterns. This difference is expected as the spatial distribution of the aeroacoustic power in this flow sound interaction pattern is found to be different than previous studied patterns.

Chapter 7

Summary and General Contributions

7.1 Summary and Conclusions

An experimental investigation of the aeroacoustic source of an axisymmetric cavity in a pipeline is presented in this research. This aeroacoustic source is generated due to the interaction of the cavity shear layer oscillation with the resonant acoustic field in the pipe. The distributed aeroacoustic source is modeled by a lumped acoustic dipole source which is dependent on the Strouhal number and the acoustic particle velocity at the cavity. The source is determined under high Reynolds number, fully developed turbulent pipe flow. The experimental technique (Sound Wave Method, SWM) employs six microphones distributed upstream and downstream of the cavity to evaluate the fluctuating pressure difference generated by the oscillating cavity shear layer in the presence of externally imposed sound waves. The amplitude and phase of this pressure difference is used to determine the dimensionless aeroacoustic source of the cavity shear layer. The results are in good agreement with the concepts of free shear layer instability and the fluid-resonant oscillation behavior.

As the acoustic pressure difference induced by the vortical flow in the cavity is rather small, many accuracy checks of the method are performed including checks of the microphones' residuals and validation of the conservation of acoustic volume velocity at the cavity center. In addition, the overall accuracy of the SWM is examined by measuring the induced acoustic pressure for two cases generating negligible aeroacoustic sources (no flow with cavity and flow without cavity) and comparing them to that measured for the actual case of cavity flow.

A validation study is performed in order to validate the measurement technique and the measured source term from the Sound Wave Method. The validation methodology consisted of comparing the self-excited resonance response (resonance amplitude and frequency) obtained from self-excitation measurements with that estimated from an acoustic model supplemented with the measured source term using the SWM. The comparison depicts a very good agreement for the resonance frequency, lock-in ranges, and the resonance amplitude.

Extensive PIV flow measurements are performed to characterize the unsteady velocity and vorticity fields at various time instants within the sound cycle. The visualization of the flow-sound interaction for cavity flow is also performed at different acoustic resonance amplitudes and Strouhal numbers in order to clarify the non-linear behavior of the aeroacoustic source at high levels of the acoustic particle velocity and clarifies the dependence of the flow-sound interaction patterns on the main system parameters, i.e., the Strouhal number and υ/U ratio. In addition, finite element analysis is used to obtain the particle velocity distribution from the sound field. The results of the PIV flow measurements and those of the finite element simulations are combined into Howe's aeroacoustic integrand to compute the spatial and temporal distributions of the aeroacoustic sources. The results are compared with the measured aeroacoustic source strength obtained by means of the Sound Wave Method (SWM) in order to identify the advantages and disadvantages of both techniques. The comparison between the measured aeroacoustic sources based on Howe's integrand, which must be supplemented by details of the flow and acoustic fields, with those measured by means of the sound wave method (SWM) highlighted the superior efficiency of the SWM technique.

Identification of the aeroacoustic source distributions as function of the acoustic excitation levels showed that the non-linear behaviour of the source strength which occurs at moderate sound levels is caused by a gradual transition in the vorticity field oscillation pattern; from a distributed vorticity cloud over the whole cavity length at small excitation amplitudes to a pattern involving rapid formation of (discrete) vortices at the leading edge which becomes dominant at large excitation levels.

Identification of the spatial distribution of the acoustic power over the cavity length at resonance condition shows sources of sound generation at the first and last thirds of the cavity mouth and an absorption sink in the middle third. This distribution is different from the source distributions for deep cavities and trapped modes of shallow cavities. Due to these differences in the aeroacoustic source distributions, the effects of cavity geometrical parameters for the present shallow cavity are not necessarily similar to those reported in the literature for deep cavities and trapped mode resonance cases.

Although the previous studies have achieved substantial progress on the effect of the cavity depth with the same length, the effect of cavity volume for the same L/H ratio, and also, the effect of changing the cavity length for the same cavity depth needed additional research. Hence, this research introduces a comprehensive study of the effect of cavity geometrical parameters (including rounding-off the cavity edges) on the aeroacoustic source generated by fully developed pipe flow through an axisymmetric shallow cavity. Nine cavity sizes are studied in three different groups of length to depth ratios (L/H = 1, 2 and 3) with three different cavity volumes for each group of L/H. The Sound Wave Method (SWM) is used to measure the aeroacoustic sources as function of the Strouhal number. The aeroacoustic source strength and the Strouhal number corresponding to its maximum value are found to increase in a systematic manner as the cavity volume is increased for the same L/H ratio. These results indicate that the aeroacoustic sources of shallow cavities are affected not only by the ratio L/H, but also by the cavity volume.

The increase in the whistling Strouhal number is caused by the increase in the vortex convection velocity at the cavity mouth as the cavity volume increases for same L/H ratio. This has been confirmed experimentally by means of PIV measurements for two cavities of same L/H ratio but differ in volume. The aeroacoustic source strength increases due to the continuous increase in the cross-stream component of the acoustic particle velocity with the increase in the cavity volume for the same L/H ratio. The effect of the cavity volume on the particle velocity distribution has been illustrated by numerical simulations of the acoustic resonant mode. The present results underline the importance of considering the cavity volume when assessing the aeroacoustic response of shallow cavities in pipelines.

The results of previous works on the effect of rounding-off the cavity edges on the resonance response are found to be contradictory. Therefore, another objective of this research is to investigate the effect of rounding-off the cavity edges on the resonance response in a shallow cavity flow coupled with a longitudinal acoustic mode. The effect of cavity edge curvatures on the resonance response is experimentally investigated by testing different sizes of curvatures at different locations (upstream, downstream or both edges). The results show that rounding-off the cavity edges causes a reduction in the vertical component of the acoustic particle velocity but also an increase in the cavity length. These two consequences have opposite effects on acoustic power generation and therefore, rounding-off the edges has no significant effect on the resonance amplitude, except for relatively large radius.

7.2 Research Contributions

This research introduces a new application of the three microphones method which was originally developed to analyse standing waves, to measure the aeroacoustic power of a duct housing a shallow cavity coupled with a longitudinal acoustic mode. In addition, this work provides, for the first time, the spatial distribution of the acoustic power over the cavity region for this type of flow-sound-structure interaction pattern. Moreover, this research introduces a comprehensive study of the effect of cavity geometrical parameters on the characteristics of the cavity aeroacoustic source. The main contributions of this work are:

- This research developed a methodology to measure the aeroacoustic source for shallow cavities. This method can be used for three dimensional flows and complex geometries because it deals with the cavity (object) as a black box.
- For the first time in the case of shallow cavity subjected to a longitudinal acoustic mode, the aeroacoustic source can be measured without requiring the complex details of the unsteady flow in the cavity region

- The measured aeroacoustic source provides substantially better predictions of the self-excited resonance amplitude and lock-in range in comparable to previous works.

- This work provides, for the first time, a comprehensive study of the effect of cavity geometrical parameters on the resonance Strouhal number and source strength at the peak whistling conditions.

- This research identifies, for the first time, the importance of considering the cavity volume when assessing the aeroacoustic response of shallow cavities in pipelines. The aeroacoustic source of shallow cavities is shown to be affected not only by the ratio L/H, but also by the cavity volume.

- The effect of rounding-off the cavity edges on the self-excited resonance amplitude is clarified. It is demonstrated that the effect of edge geometry on the flow-sound interaction is not unique for various patterns of flows, acoustic modes, and geometries.

- This work improves the fundamental understanding of the variation of the aeroacoustic power with the resonance sound level for this pattern of flow-sound interaction. It clarified that the non-linear behaviour of the aeroacoustic source strength at moderate sound levels is caused by a gradual transition in the vorticity field oscillation pattern.

- This research reveals the spatial distribution of the aeroacoustic sources over the cavity length for shallow cavity in the presence of longitudinal acoustic resonance mode. This distribution is different from the source distributions for deep cavities and trapped mode resonances which exist in the literature.

7.3 Recommendations for Future Work

The present research improved the fundamental understanding of the flow-sound interaction mechanisms for a single shallow cavity with fluid-resonance oscillations in a pipeline. It also provides a proper and efficient methodology to measure the aeroacoustic sources generated by complex geometries and flows. It is suggested to extend this work to investigate acoustic resonances in corrugated pipes. Therefore, future extended steps for this research may include:

- As the SWM is applied to a single cavity and it provided validated results, it is recommended to apply and validate the sound-wave method to the case of multiple cavities. In order to study the effect of increasing the number of cavities on the aeroacoustic power, it is suggested to test different number of cavities and identify the effect of each added cavity on the total aeroacoustic source.
- This research provided a comprehensive study to the effect of cavity geometrical parameters on the aeroacoustic source (including cavity length, depth, volume at same L/H, and rounding-off the edges). For the case of multiple cavities, the pitch between cavities is an important geometrical parameter. Thus, it is recommended to study the effect of the pitch length on the aeroacoustic sources of the corrugated section.
- This work used the tool of PIV measurements to identify the flow and vorticity fields in a single cavity. This flow visualization helps in the better understanding of the non-linear behaviour of the aeroacoustic source. The visualization results are

also used as input data to Howe' integrand to identify the spatial distribution of the aeroacoustic sources in a single shallow cavity. It is recommended to expand this work to multiple cavities in order to investigate the hydrodynamic coupling between the different cavities in the corrugation section and to identify the contribution of each cavity in the total aeroacoustic source of the whole set of cavities. In addition, it is recommended to use the PIV measurements to illustrate the effect of the cavity pitch length on the hydrodynamic coupling and on the overall aeroacoustic power.

- As the SWM is developed and validated for a single cavity, it is recommended to apply the method for complex geometries and flows. Some examples are measuring the aeroacoustic sources in real valves, orifices and other complex pipe fittings.

7.4 Supporting Papers

1- Mohamed, S., Graf, H. R., & Ziada, S. (2011, January). Aeroacoustic Source of a Shallow Cavity in a Pipeline. In *ASME 2011 Pressure Vessels and Piping Conference* (pp. 269-276). American Society of Mechanical Engineers.

2- Mohamed, S., & Ziada, S. (2014, July). PIV Measurements of Aeroacoustic Sources of a Shallow Cavity in a Pipeline. In *ASME 2014 Pressure Vessels and Piping Conference* (pp. V004T04A054-V004T04A054). American Society of Mechanical Engineers.

3- Salt, E., Mohamed, S., Arthurs, D., & Ziada, S. (2014). Aeroacoustic Sources Generated by Flow–Sound Interaction in a T-Junction. *Journal of Fluids and Structures*, *51*, pp. 116-131.

4- Mohamed, S. and Ziada, S. (2015, July). Effect of Cavity Volume on the Flow-Excited Acoustic Resonance of a Shallow Cavity in a Pipe-Line. In *ASME 2015 Pressure Vessels and Piping Conference*. American Society of Mechanical Engineers.

5- Salt, E., Mohamed, S., Arthurs, D., & Ziada, S. (2014, July). Identification of Aeroacoustic Sources in a T-Junction. In *ASME 2014 Pressure Vessels and Piping Conference* (pp. V004T04A005-V004T04A005). American Society of Mechanical Engineers.

BIBLIOGRAPHY

Åbom, M., Karlsson, M., & Kierkegaard, A. (2009). On the use of linear aeroacoustic methods to predict whistling, Noise and Vibration: Emerging Methods. Oxford, United Kingdom.

Akula, B., Roy, P., Razi, P., Anderson, S., & Girimaji, S. (2015). Partially-Averaged Navier-Stokes (PANS) Simulations of Lid-Driven Cavity Flow—Part 1: Comparison with URANS and LES. *In Progress in Hybrid RANS-LES Modelling*, 359-369.

Aly, K. (2008). Aerodynamic excitation of the diametral modes of an internal axisymmetric cavity. (*Doctoral dissertation*). McMaster, Hamilton, Canada.

Aly, K., & Ziada, S. (2010). Flow-excited resonance of trapped modes of ducted shallow cavities. *Journal of Fluids and Structures*, *26*(1), 92-120.

Aly, K., & Ziada, S. (2012). Effect of mean flow on the trapped modes of internal cavities. *Journal of Fluids and Structures*, *33*, 70-84.

Bruggeman, J. C. (1987). Flow induced pulsations in pipe systems. (*Doctoral dissertation*). Technische Universiteit Eindhoven, Eindhoven, Netherlands.

Bruggeman, J. C., Hirschberg, A., Van Dongen, M. E. H., Wijnands, A. P. J., & Gorter, J. (1991). Self-sustained aero-acoustic pulsations in gas transport systems: experimental study of the influence of closed side-branches. *Journal of Sound and Vibration*, *150*(3), 371-393.

Blevins, R. D. (1985). The effect of sound on vortex shedding from cylinders. *Journal of Fluid Mechanics*, *161*, 217-237.

Bolduc, M., Elsayed, M., & Ziada, S. (2014). Passive control of trapped mode resonance of ducted cavities. *Journal of Pressure Vessel Technology*, *136*(5), 051311.

Coltman, J. W. (1968). Sounding mechanism of the flute and organ pipe. *The Journal of the Acoustical Society of America*, *44*(4), 983-992.

Cramer, O. (1993). The variation of the specific heat ratio and the speed of sound in air with temperature, pressure, humidity, and CO2 concentration. *The Journal of the Acoustical Society of America*, *93*(5), 2510-2516.

Davies, P. O. A. L. (1981). Flow-acoustic coupling in ducts. *Journal of Sound and Vibration*, *77*(2), 191-209.

Davies, P. O. A. L. (1987). Plane wave reflection at flow intakes. *Journal of sound and vibration*, *115*(3), 560-564.

Davies, P. O. A. L. (1988). Practical flow duct acoustics. *Journal of Sound and Vibration*, *124*(1), 91-115.

Davies, P. O. A. L., Bhattacharya, M., & Bento Coelho, J. L. (1980). Measurement of plane wave acoustic fields in flow ducts. *Journal of Sound and Vibration*, *72*(4), 539-542.

Debut, V., Antunes, J., & Moreira, M. (2007). A phenomenological model for sound generation in corrugated pipe. In *Proceedings of the International Symposium on Musical Acoustics (ISMA),* Barcelona, Spain.

Dequand, S., Willems, J. F. H., Leroux, M., Vullings, R., Van Weert, M., Thieulot, C., & Hirschberg, A. (2003). Simplified models of flue instruments: Influence of mouth geometry on the sound source. *The Journal of the Acoustical Society of America*, *113*(3), 1724-1735.

Doherty, J., Ngan, P., Monty, J., & Chong, M. (2007). The development of turbulent pipe flow. In *16th Australasian Fluid Mechanics Conference (AFMC),* Australia.

Durgin, W. W., & Graf, H. R. (1992). Flow-excited acoustic resonance in a deep cavity: An analytical model. In *Proceedings of the Third International Symposium on Flow-Induced Vibrations and Noise.* Anaheim, California, United States.

Elder, S. A. (1978). Self-excited depth-mode resonance for a wall-mounted cavity in turbulent flow. *The Journal of the Acoustical Society of America*, *64*(3), 877-890.

Elder, S. A. (1980). Forced oscillations of a separated shear layer with application to cavity flow-tone effects. *The Journal of the Acoustical Society of America*, *67*(3), 774-781.

Elsayed, M. F. M. (2013). Effect of upstream edge geometry on the trapped mode resonance of ducted cavities. (*Master Thesis*), McMaster, Hamilton, Canada.

Eriksson, L. J. (1980). Higher order mode effects in circular ducts and expansion chambers. *The Journal of the Acoustical Society of America*, *68*(2), 545-550.

Finnegan, S. L., Meskell, C., & Ziada, S. (2009). Experimental investigation of the aeroacoustic sources in a tandem cylinder configuration. In *ASME 2010 ICNMM2010.* Montreal, Quebec, Canada.

Finnegan, S. L., Meskell, C., & Ziada, S. (2010). Experimental investigation of the acoustic power around two tandem cylinders. *Journal of Pressure Vessel Technology*, *132*(4), 041306.

Finnegan, S., Oshkai, P., & Meskell, C. (2010). Experimental methodology for aeroacoustic source localization in ducted flows with complex geometry. In *Proceedings of the 16th AIAA/CEAS Aeroacoustic Conference*. Stockholm, Sweden.

Föller, S., Polifke, W., & Tonon, D. (2010). Aeroacoustic characterization of t-junctions based on large eddy simulation and system identification. In *16th AIAA/CEAS Aeroacoustics Conference*. Stockholm, Sweden.

Freymuth, P. (1966). On transition in a separated laminar boundary layer. *Journal of*

Fluid Mechanics, *25*(04), 683-704.

Geveci, M., Oshkai, P., Rockwell, D., Lin, J. C., & Pollack, M. (2003). Imaging of the self-excited oscillation of flow past a cavity during generation of a flow tone. *Journal of Fluids and Structures*, *18*(6), 665-694.

Graf, H. R., & Ziada, S. (1992). Flow-induced acoustic resonance in closed side-branches: an experimental determination of the excitation source. *International Symposium on Flow-Induced Vibration and Noise*. Anaheim, California, United States.

Graf, H. R., & Ziada, S. (2010). Excitation source of a side-branch shear layer. *Journal of Sound and Vibration*, *329*(14), 2825-2842.

Hirschberg, A., & Rienstra, S.W. (1994). Elements of aero-acoustics. *VKI Lecture Series notes*. Brussels, Belgium.

Hofmans, G. C. J. (1998). Vortex sound in confined flows. (*Doctoral dissertation*). Technische Universiteit Eindhoven, Eindhoven, Netherlands.

Hourigan, K., Welsh, M. C., Thompson, M. C., & Stokes, A. N. (1990). Aerodynamic sources of acoustic resonance in a duct with baffles. *Journal of Fluids and Structures*, *4*(4), 345-370.

Howe, M. S. (1975). Contributions to the theory of aerodynamic sound, with application to excess jet noise and the theory of the flute. *Journal of Fluid Mechanics*, *71*(04), 625-673.

Howe, M. S. (1980). The dissipation of sound at an edge. *Journal of Sound and Vibration*, *70*(3), 407-411.

Howe, M. S. (1998). *Acoustics of fluid-structure interactions*. Cambridge University Press.

Huang, X. Y., & Weaver, D. S. (1994). Control of flow-induced fin vibration by anti-sound. *Journal of sound and vibration*, *169*(3), 428-432.

Karal, F. C. (1953). The analogous acoustical impedance for discontinuities and constrictions of circular cross section. *The Journal of the Acoustical Society of America*, *25*(2), 327-334.

Karamcheti, K. (1955). Acoustic radiation from two-dimensional rectangular cutouts in aerodynamic surfaces. *NACA Report No. TN*, *3487*.

Karlsson, M., & Åbom, M. (2010). Aeroacoustics of T-junctions: An experimental investigation. *Journal of Sound and Vibration*, *329*(10), 1793-1808.

Karlsson, M., & Åbom, M. (2011). On the use of linear acoustic multiports to predict whistling in confined flows. *Acta Acustica united with Acustica*, *97*(1), 24-33.

Keller, J. J., & Escudier, M. P. (1983). Flow-excited resonances in covered cavities. *Journal of Sound and Vibration*, *86*(2), 199-226.

Kergomard, J., & Garcia, A. (1987). Simple discontinuities in acoustic waveguides at low frequencies: critical analysis and formulae. *Journal of Sound and Vibration*, *114*(3), 465-479.

Kirchhoff, G. (1868). On the influence of heat conduction in a gas on sound propagation. *Annual Review of Physical Chemistry*, *134*, 177-193.

Knotts, B. D., & Selamet, A. (2003). Suppression of flow–acoustic coupling in side-branch ducts by interface modification. *Journal of Sound and Vibration*, *265*(5), 1025-1045.

Kook, H., & Mongeau, L. (2002). Analysis of the periodic pressure fluctuations induced by flow over a cavity. *Journal of Sound and Vibration*, *251*(5), 823-846.

Kriesels, P. C., Peters, M. C. A. M., Hirschberg, A., Wijnands, A. P. J., Iafrati, A., Riccardi, G., ... & Bruggeman, J. C. (1995). High amplitude vortex-induced pulsations in a gas transport system. *Journal of Sound and Vibration*, *184*(2), 343-368.

Laufer, J. (1954). The structure of turbulence in fully developed pipe flow (NACA report, 1174). *National committee for aeronautics*.

Lucas, M. J., Noreen, R. A., Sutherland, L. C., Cole III, J. E., & Junger, M. C. (1997). Handbook of the acoustics characteristics of turbomachinery cavities. *ASME Press*.

Luo, K., & Xiao, Z. (2015). Improved Delayed Detached-Eddy Simulation of Transonic and Supersonic Cavity Flows. *In Progress in Hybrid RANS-LES Modelling*, 163-174.

Martinez-Lera, P., Schram, C., Föller, S., Kaess, R., & Polifke, W. (2009). Identification of the aeroacoustic response of a low Mach number flow through a T-joint. *The Journal of the Acoustical Society of America*, *126*(2), 582-586.

Michalke, A. (1964). On the inviscid instability of the hyperbolic tangent velocity profile. *Journal of Fluid Mechanics*, *19*(04), 543-556.

Michalke, A. (1965). On spatially growing disturbances in an inviscid shear layer. *Journal of Fluid Mechanics*, *23*(3), 521-544.

Miksad, R. W. (1972). Experiments on the nonlinear stages of free shear layer transition. *Journal of Fluid Mechanics*, *56*(04), 695-719.

Mohamed, S., & Ziada, S. (2014). PIV measurements of aeroacoustic sources of a shallow cavity in a pipeline. In *ASME PVP2014 Pressure Vessels and Piping Conference.* Anaheim, California, United States.

Mohamed, S., Graf, H. R., & Ziada, S. (2011). Aeroacoustic source of a shallow cavity in a pipeline. In *ASME PVP2011 Pressure Vessels and Piping Conference*. Baltimore, Maryland, United States.

Mohany, A., & Ziada, S. (2009). Numerical simulation of the flow-sound interaction mechanisms of a single and two-tandem cylinders in cross-flow. *Journal of Pressure Vessel Technology*, *131*(3), 031306.

Monkewitz, P. A., & Huerre, P. (1982). Influence of the velocity ratio on the spatial instability of mixing layers. *Physics of Fluids (1958-1988)*, *25*(7), 1137-1143.

Munjal, M. L. (1987). *Acoustics of ducts and mufflers with application to exhaust and ventilation system design*. John Wiley & Sons.

Munjal, M. L., & Doige, A. G. (1990). The two-microphone method incorporating the effects of mean flow and acoustic damping. *Journal of Sound and Vibration*, *137*(1), 135-138.

Nakiboğlu, G., & Hirschberg, A. (2010). A numerical study of the aeroacoustic interaction of a cavity with a confined flow: effect of edge geometry in corrugated pipes. In *ASME 2010 ICNMM2010.* Montreal, Quebec, Canada.

Nakiboğlu, G., Belfroid, S. P. C., Golliard, J., & Hirschberg, A. (2011). On the whistling of corrugated pipes: effect of pipe length and flow profile. *Journal of Fluid Mechanics*, *672*, 78-108.

Nakiboğlu, G., Manders, H. B. M., & Hirschberg, A. (2012). Aeroacoustic power generated by a compact axisymmetric cavity: prediction of self-sustained oscillation and influence of the depth. *Journal of Fluid Mechanics*, *703*, 163-191.

Naudascher, E., & Rockwell, D. (1994). *Flow-induced vibrations: An engineering guide*, AA Balkema, Rotterdam.

Nelson, P. A., Halliwell, N. A., & Doak, P. E. (1981). Fluid dynamics of a flow-excited resonance, part I: experiment. *Journal of Sound and Vibration*, *78*(1), 15-38.

Nelson, P. A., Halliwell, N. A., & Doak, P. E. (1983). Fluid dynamics of a flow excited resonance, Part II: Flow-acoustic interaction. *Journal of Sound and Vibration*, *91*(3), 375-402.

Oshkai, P., & Yan, T. (2008). Experimental investigation of coaxial side-branch resonators. *Journal of Fluids and Structures*, *24*(4), 589-603.

Peters, M. C. A. M. (1993). Aeroacoustic sources in internal flows. (*Doctoral dissertation*). Technische Universiteit Eindhoven, Eindhoven, Netherlands.

Radavich, P. M., Selamet, A., & Novak, J. M. (2001). A computational approach for flow-acoustic coupling in closed side-branches. *The Journal of the Acoustical Society of America*, *109*(4), 1343-1353.

Raffel, M., Willert, C., Wereley, S., & Kompenhans, J. (2007). *Particle image velocimetry: a practical guide*. Springer.

Rayleigh, L. (1879). On the stability, or instability, of certain fluid motions. *Proceedings of the London Mathematical Society*, *1*(1), 57-72.

Rockwell, D. (1977). Prediction of oscillation frequencies for unstable flow past cavities. *Journal of Fluids Engineering*, *99*(2), 294-299.

Rockwell, D. (1983). Oscillations of impinging shear layers. *AIAA journal*, *21*(5), 645-664.

Rockwell, D., & Knisely, C. (1979). The organized nature of flow impingement upon a corner. *Journal of Fluid Mechanics*, *93*(03), 413-432.

Rockwell, D., & Naudascher, E. (1978). Review: self-sustaining oscillations of flow past cavities. *Journal of Fluids Engineering*, *100*(2), 152-165.

Rockwell, D., & Naudascher, E. (1979). Self-sustained oscillations of impinging free shear layers. *Annual Review of Fluid Mechanics*, *11*(1), 67-94.

Rockwell, D., & Schachenmann, A. (1982a). Self-generation of organized waves in an impinging turbulent jet at low Mach number. *Journal of Fluid Mechanics*, *117*, 425-441.

Rockwell, D., & Schachenmann, A. (1982b). The organized shear layer due to oscillations of a turbulent jet through an axisymmetric cavity. *Journal of Sound and Vibration*, *85*(3), 371-382.

Rockwell, D., Lin, J. C., Oshkai, P., Reiss, M., & Pollack, M. (2003). Shallow cavity flow tone experiments: onset of locked-on states. *Journal of Fluids and Structures, 17*(3), 381-414.

Ronneberger, D. (1972). The acoustical impedance of holes in the wall of flow ducts. *Journal of Sound and Vibration*, *24*(1), 133-150.

Ronneberger, D. (1980). The dynamics of shearing flow over a cavity: a visual study related to the acoustic impedance of small orifices. *Journal of Sound and Vibration*, *71*(4), 565-581.

Sarohia, V. (1977). Experimental investigation of oscillations in flows over shallow cavities. *AIAA Journal*, *15*(7), 984-991.

Scarano, F., & Riethmuller, M. (2000). Advances in iterative multigrid PIV image processing. *Experiments in Fluids, 29*, 51–60.

Schlichting, H., Gersten, K., & Gersten, K. (2000). *Boundary-layer theory*. Springer.

Stoneman, S. A. T., Hourigan, K., Stokes, A. N., & Welsh, M. C. (1988). Resonant sound caused by flow past two plates in tandem in a duct. *Journal of Fluid Mechanics*, *192*, 455-484.

Tam, C. K., & Block, P. J. (1978). On the tones and pressure oscillations induced by flow over rectangular cavities. *Journal of Fluid Mechanics*, *89*(2), 373-399.

Thompson, M. C., Hourigan, K., Welsh, M. C., & Brocher, E. (1992). Acoustic sources in a tripped flow past a resonator tube. *AIAA journal*, *30*(6), 1484-1491.

Thompson, M. C., Hourigan, K., Welsh, M. C., & Soh, W. K. (1988). Prediction of vortex shedding from bluff bodies in the presence of a sound field. *Fluid Dynamics Research*, *3*(1-4), 349.

Tonon, D., Hirschberg, A., Golliard, J., and Ziada, S. (2011). Aeroacoustics of pipe systems with closed branches. *Noise Notes, 10*(3), 27-88.

Tropea, C., Yarin, A. L., & Foss, J. F. (Eds.). (2007). *Handbook of Experimental Fluid Mechanics*. Springer Science & Business Media.

United States Nuclear Regularity Commission (2002). U.S.NRC information notice. *2002-26.*

Vollmers, H. (2001). Detection of vortices and quantitative evaluation of their main parameters from experimental velocity data. *Measurement Science and Technology*, *12*(8), 1199.

White, F. M., & Corfield, I. (1991). *Viscous fluid flow* (Vol. 3). New York: McGraw-Hill.

Ziada, S. (1994). A flow visualization study of flow-acoustic coupling at the mouth of a resonant side-branch. *Journal of Fluids and Structures*, *8*(4), 391-416.

Ziada, S. (1995). Feedback control of globally unstable flows: impinging shear flows. *Journal of Fluids and Structures*, *9*(8), 907-923.

Ziada, S. (2001). Interaction of a jet-slot oscillator with a deep cavity resonator and its control. *Journal of Fluids and Structures 15*(6), 831–843.

Ziada, S. (2002). Active stabilization of a planar jet impinging on a flexible wedge. *Journal of fluids and structures*, *16*(5), 613-626.

Ziada, S. (2010). Flow-excited acoustic resonance in industry. *Journal of Pressure Vessel Technology*, *132*(1), 015001.

Ziada, S., & Bühlmann, E. T. (1991). Flow-induced vibrations in long corrugated pipes. In *Proceedings of International Conference on Flow-Induced Vibrations, Inst. of Mech. Eng.*, England, 417-426.

Ziada, S., & Buehlmann, E. T. (1992). Self-excited resonances of two side-branches in close proximity. *Journal of Fluids and Structures*, *6*(5), 583-601.

Ziada, S., Buehlmann, E. T., & Bolleter, U. (1989). Flow impingement as an excitation source in control valves. *Journal of Fluids and structures*, *3*(5), 529-549.

Ziada, S., & Lafon, P. (2014). Flow-excited acoustic resonance excitation mechanism, design guidelines, and counter measures. *Applied Mechanics Reviews*, *66*(1), 010802.

Ziada, S., Ng, H., & Blake, C. E. (2003). Flow-excited resonance of a confined shallow cavity in low Mach number flow and its control. *Journal of Fluids and Structures*, *18*(1), 79-92.

Ziada, S., & Rockwell, D. (1982). Oscillations of an unstable mixing layer impinging upon an edge. *Journal of Fluid Mechanics*, *124*, 307-334.

Ziada, S., & Shine, S. (1999). Strouhal numbers of flow-excited acoustic resonance of closed side-branches. *Journal of fluids and structures*, *13*(1), 127-142.

Appendix A

Results of Different Cavity Sizes

Introduction

This appendix shows the complete experimental results of the aeroacoustic sources as a function of Strouhal number (flow velocity), and the acoustic amplitude ratio υ/U. The results are presented for 9 cavities with different values of cavity's length and depth as shown in table A.1.

Cavity Dimensions length (L) x Depth (H) (mm)	**L/H**
26 x 26	1
52 x 52	1
78 x 78	1
26 x 13	2
52 x 26	2
104 x 52	2
39 x 13	3
78 x 26	3
156 x 52	3

Table A.1: Tested cavity sizes

Cavity 26 mm x 26 mm

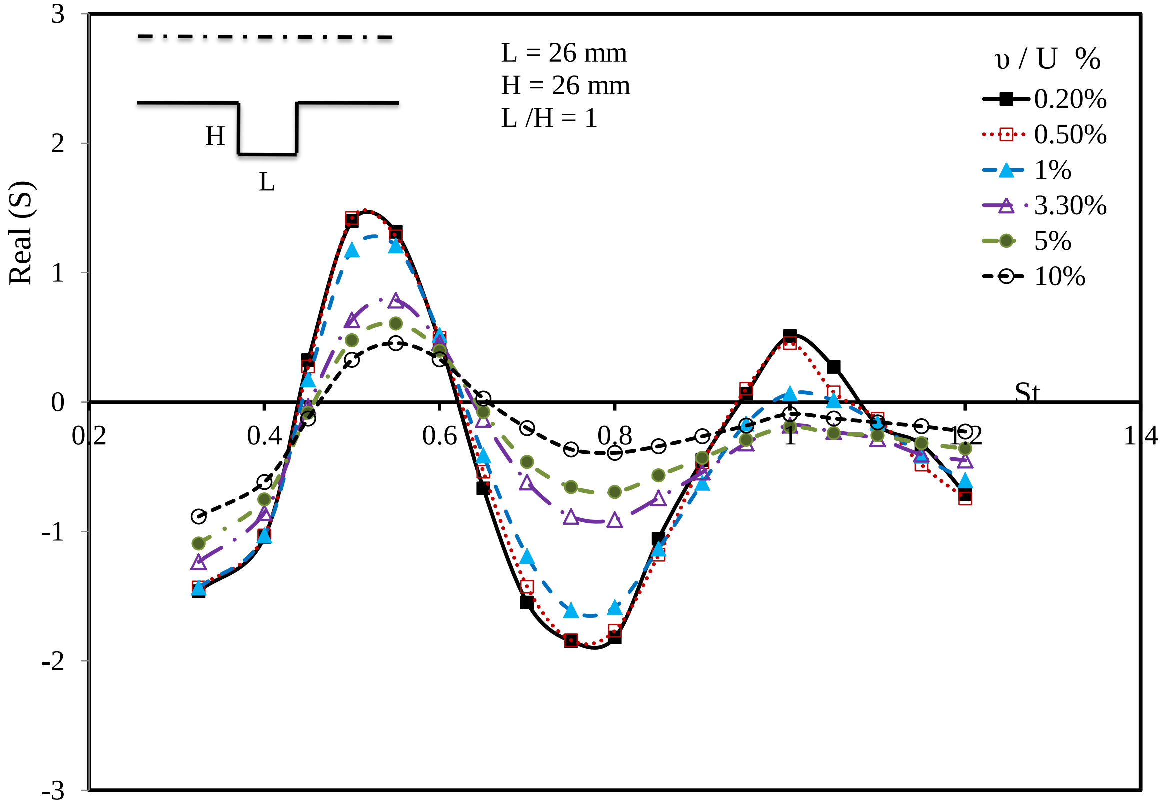

Figure A.1: Real part of the aeroacoustic source term R(S) as a function of St number for different values of the acoustic particle velocity υ/U at the cavity center (cavity 26 x 26 mm).

Cavity 52 mm x 52 mm

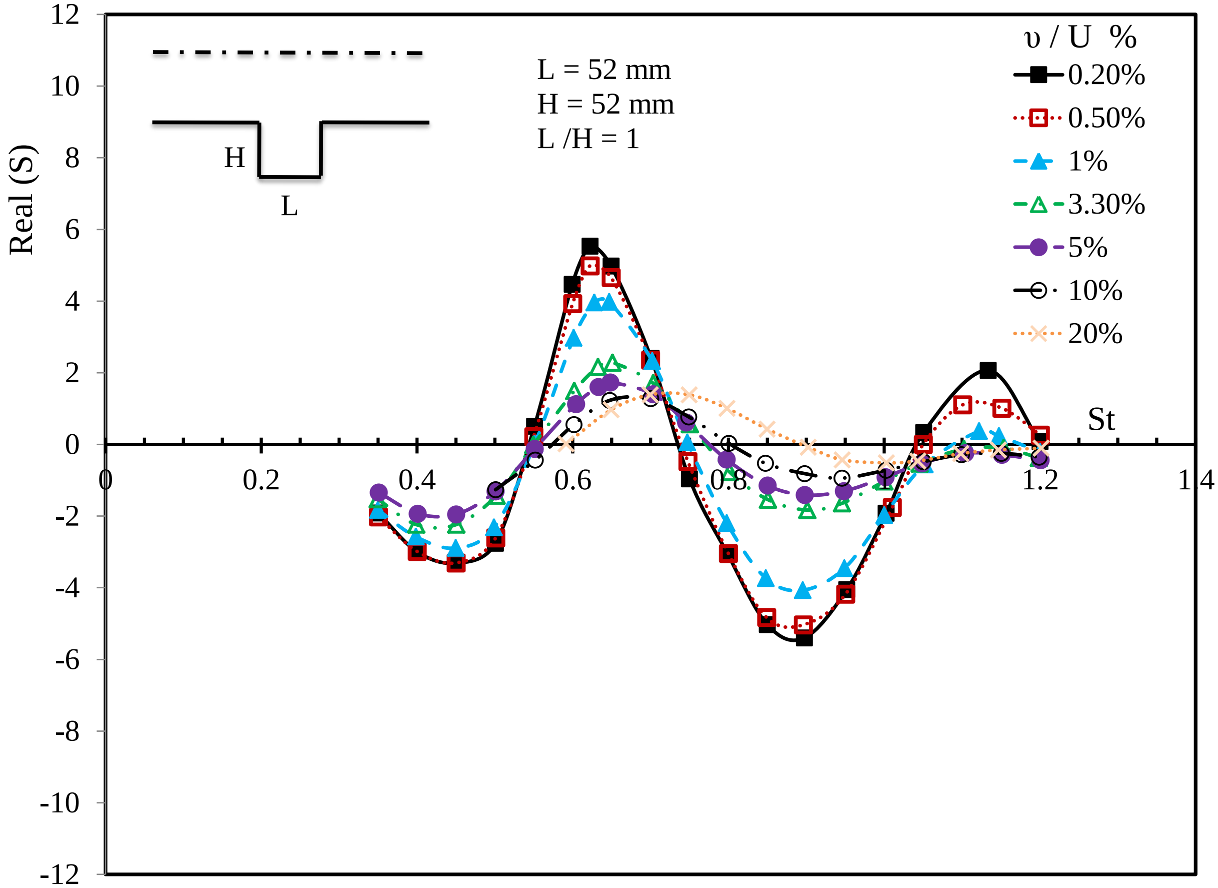

Figure A.2: Real part of the aeroacoustic source term R(S) as a function of St number for different values of the acoustic particle velocity υ/U at the cavity center (cavity 52 x 52 mm).

Cavity 78 mm x 78 mm

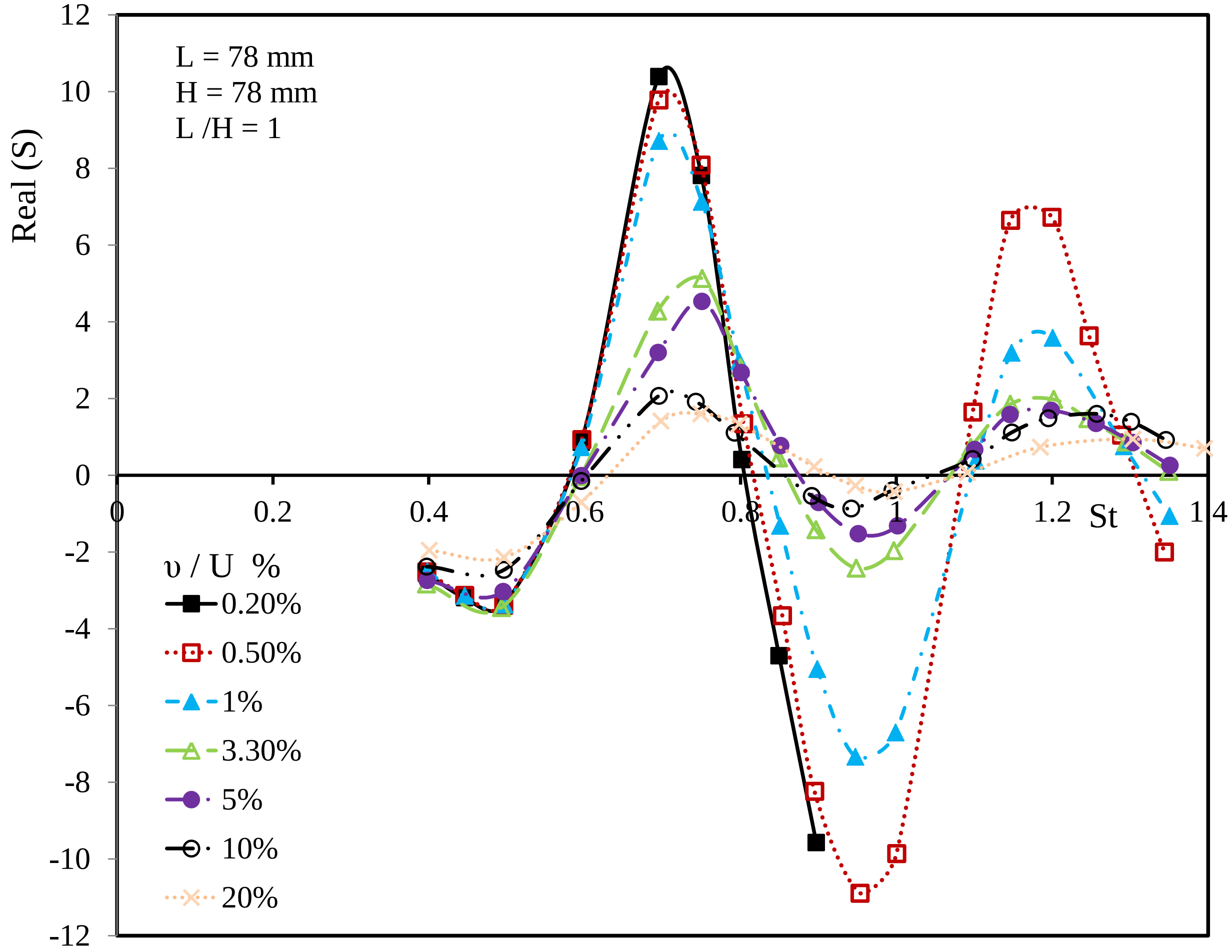

Figure A.3: Real part of the aeroacoustic source term R(S) as a function of St number for different values of the acoustic particle velocity υ/U at the cavity center (cavity 78 x 78 mm).

Cavity 26 mm x 13 mm

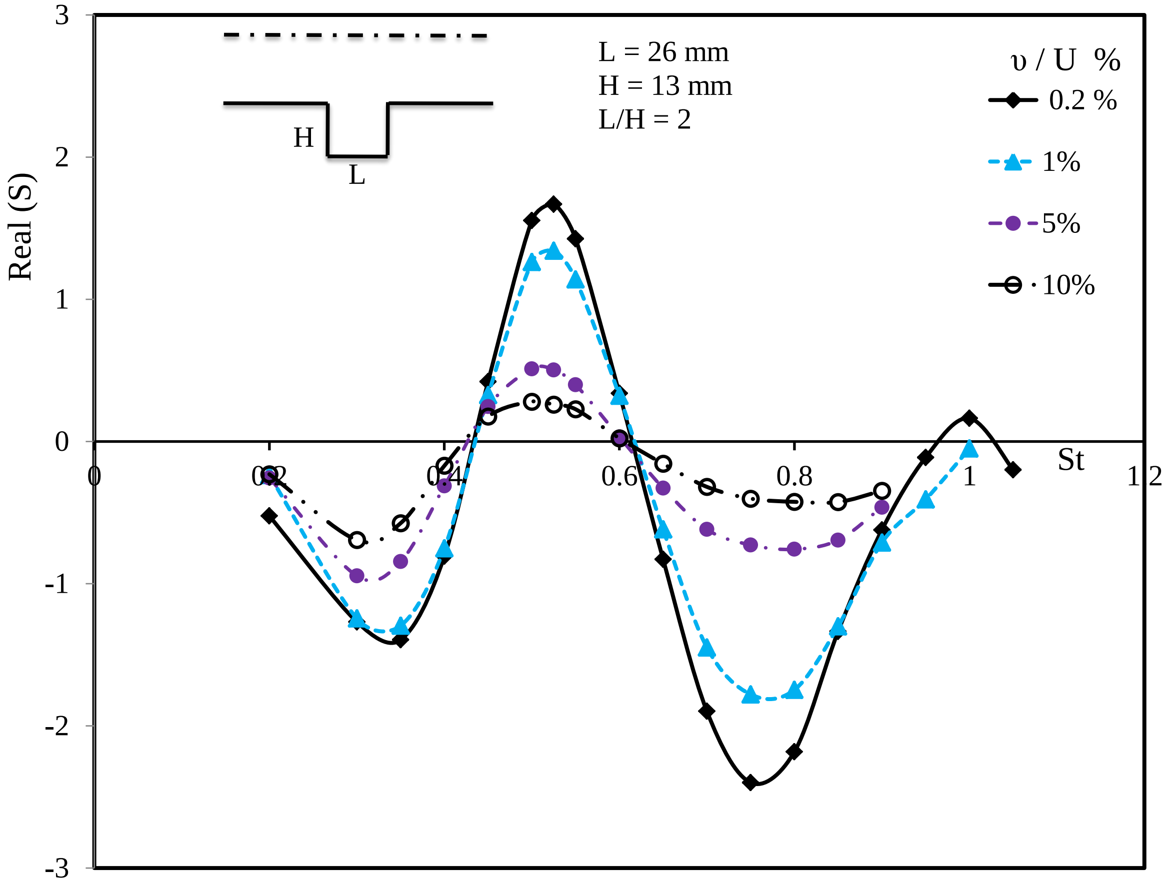

Figure A.4: Real part of the aeroacoustic source term R(S) as a function of St number for different values of the acoustic particle velocity υ/U at the cavity center (cavity 26 x 13 mm).

Cavity 52 mm x 26mm

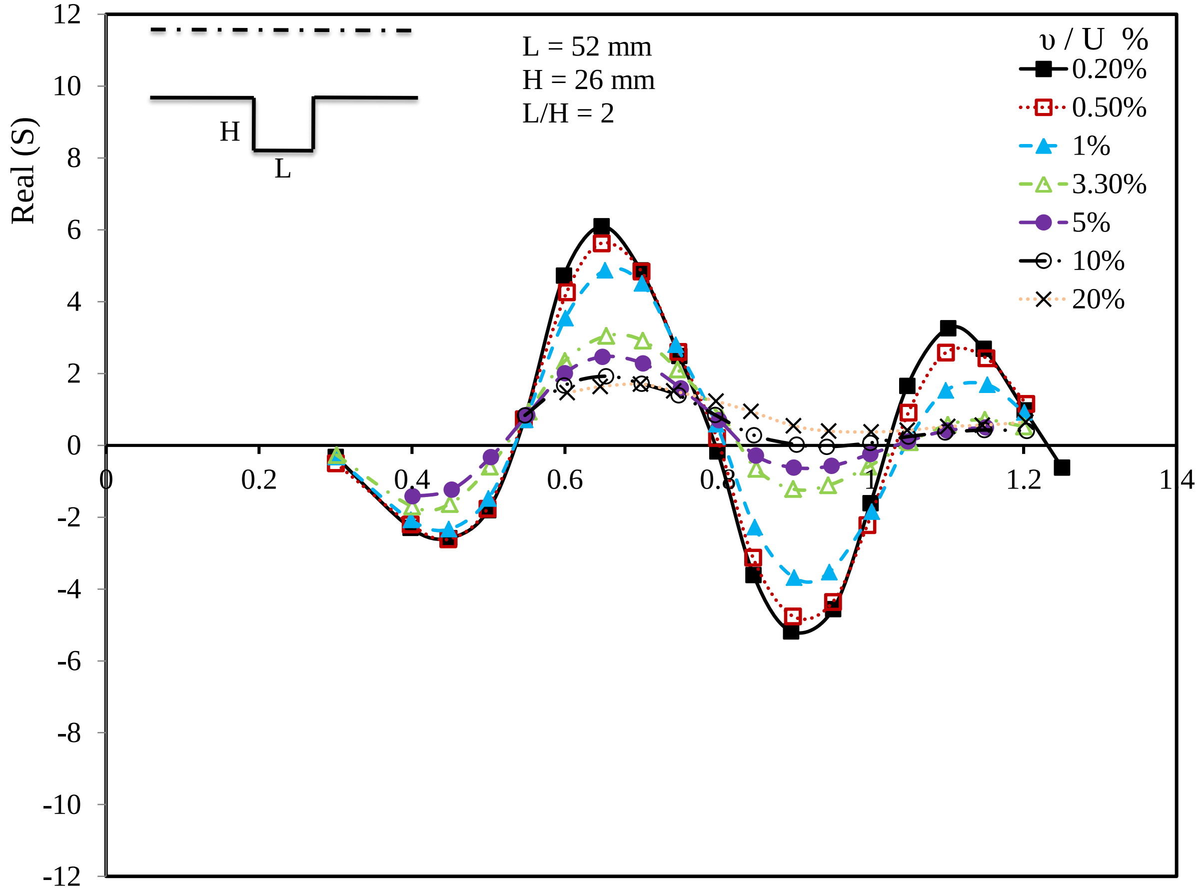

Figure A.5: Real part of the aeroacoustic source term R(S) as a function of St number for different values of the acoustic particle velocity υ/U at the cavity center (cavity 52 x 26 mm).

Cavity 104 mm x 52 mm

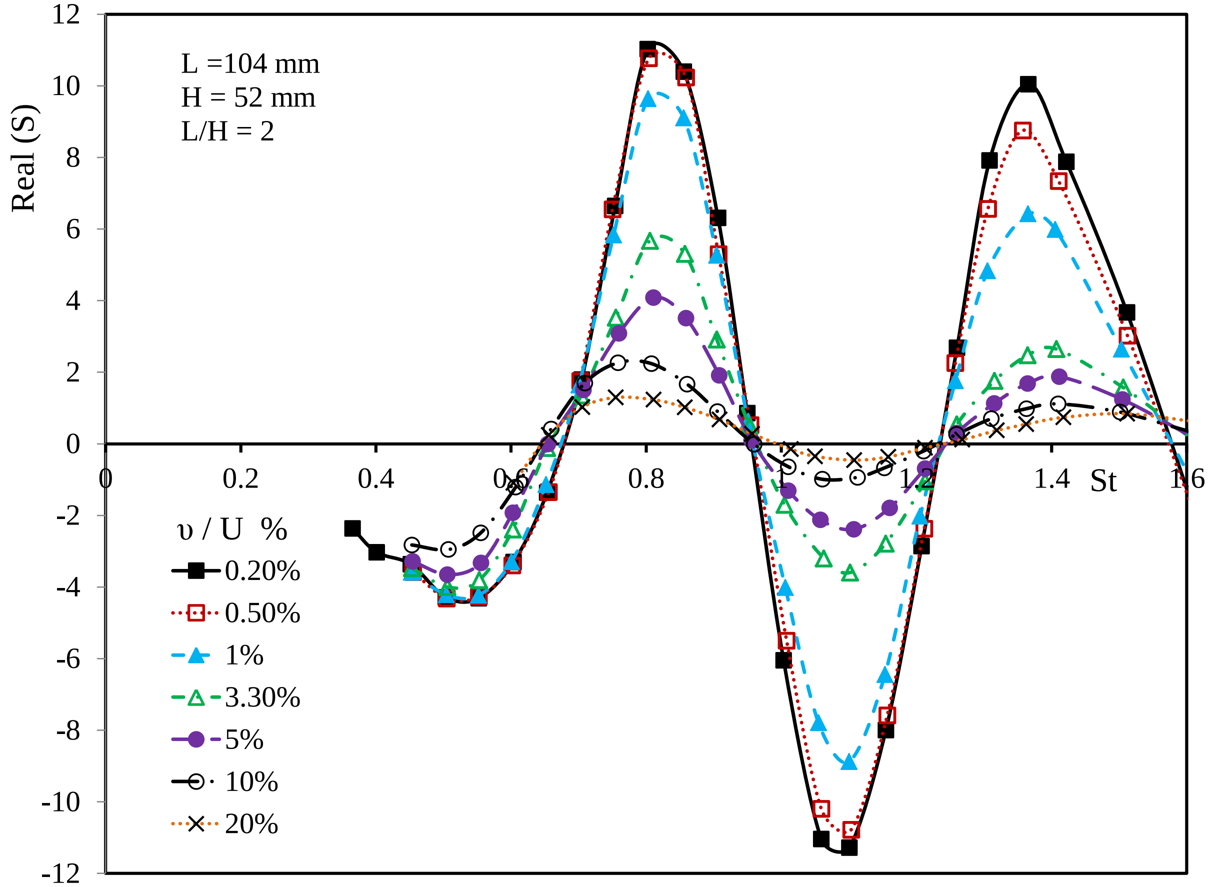

Figure A.6: Real part of the aeroacoustic source term R(S) as a function of St number for different values of the acoustic particle velocity υ/U at the cavity center (cavity 104 x 52 mm).

Cavity 39 mm x 13 mm

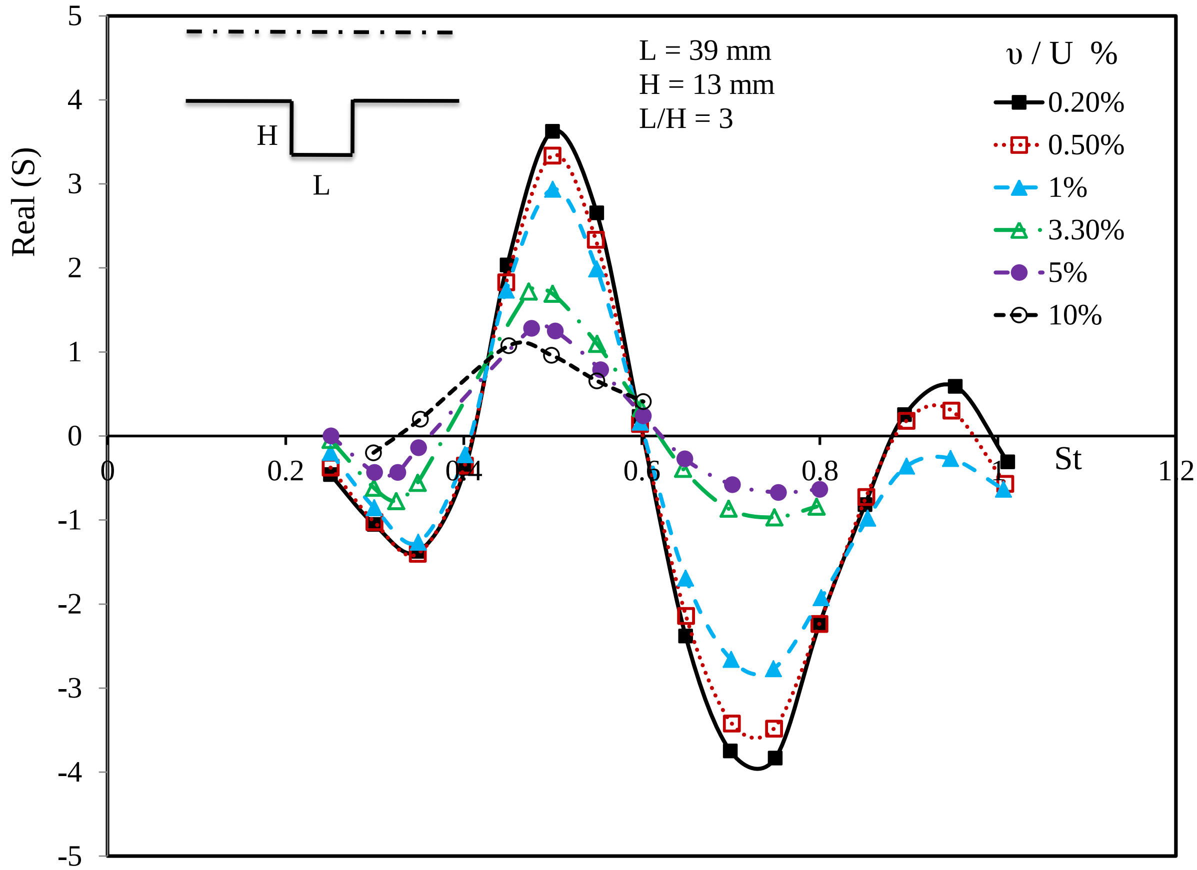

Figure A.7: Real part of the aeroacoustic source term R(S) as a function of St number for different values of the acoustic particle velocity υ/U at the cavity center (cavity 39 x 13 mm).

Cavity 78 mm x 26 mm

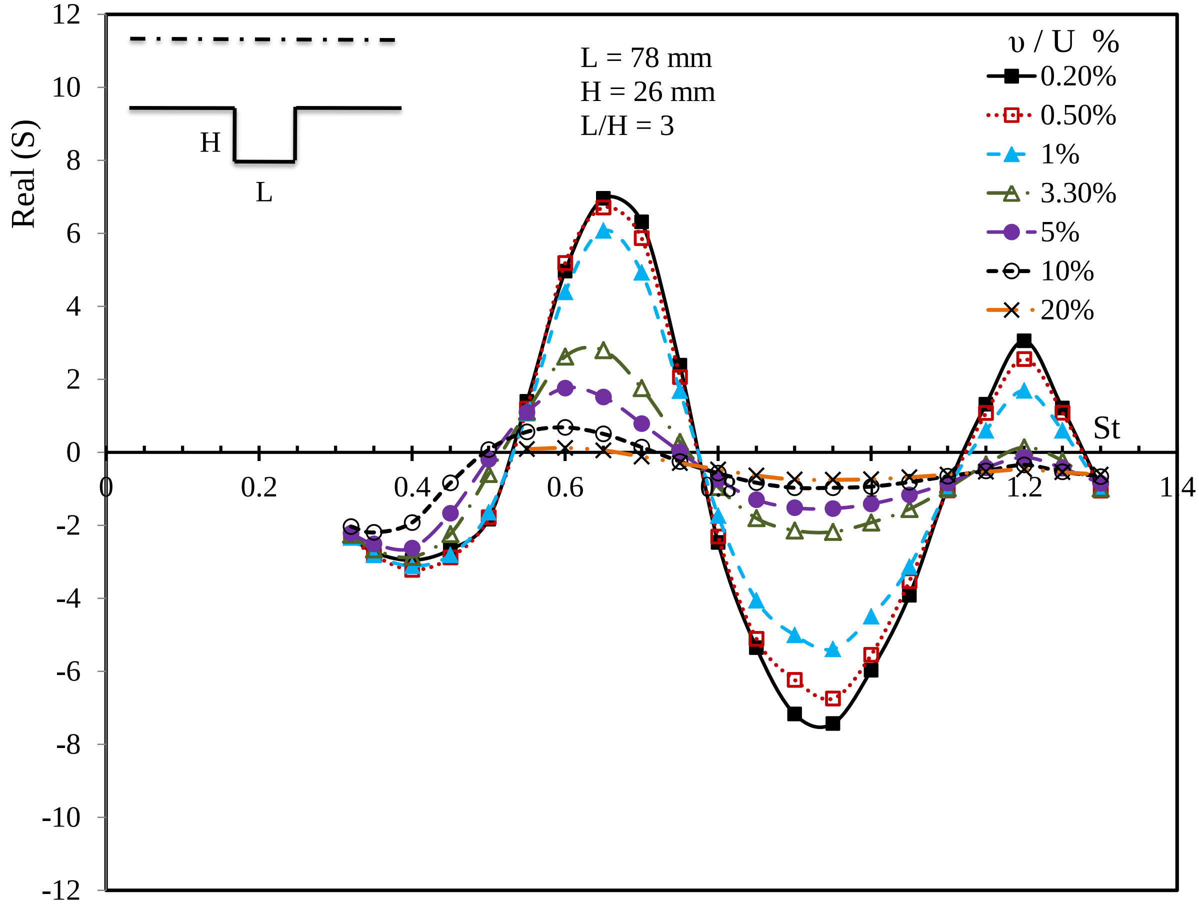

Figure A.8: Real part of the aeroacoustic source term R(S) as a function of St number for different values of the acoustic particle velocity υ/U at the cavity center (cavity 78 x 26 mm).

Cavity 156 mm x 52 mm

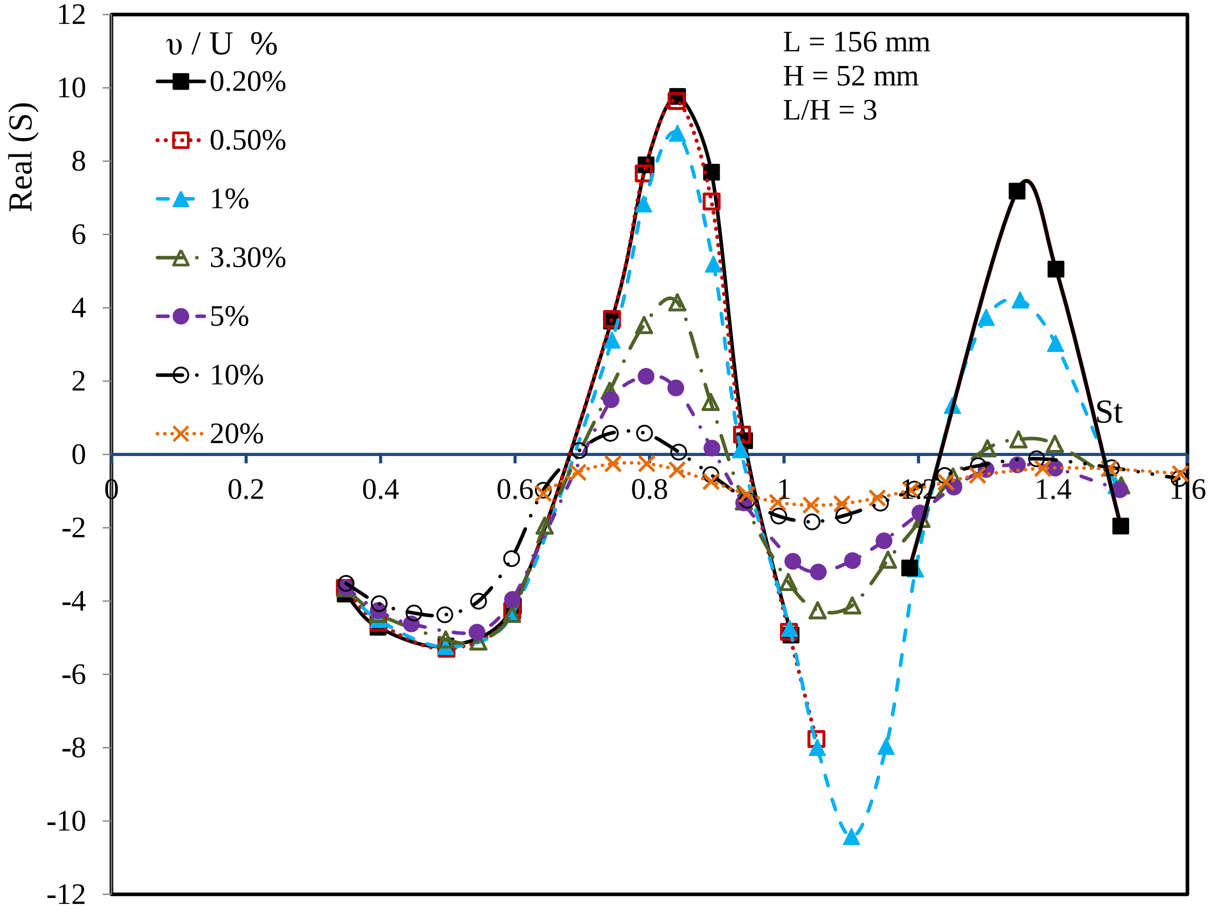

Figure A.9: Real part of the aeroacoustic source term R(S) as a function of St number for different values of the acoustic particle velocity υ/U at the cavity center (cavity 156 x 52 mm).

Cavities of L/H = 1 (26 mm x 26 mm, 52 mm x 52 mm, and 78 mm x 78 mm)

At υ /U = 0.5% & 1%

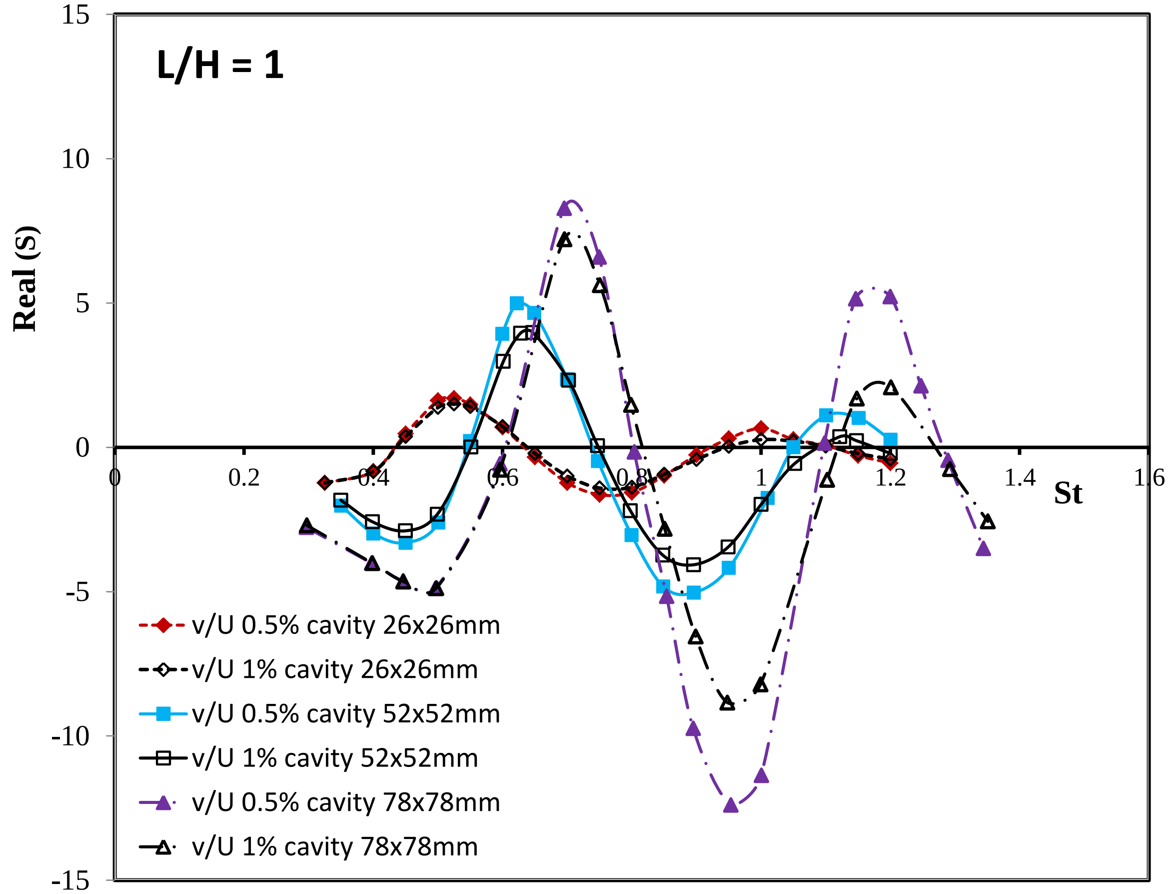

Figure A.10: Real part of the aeroacoustic source term R(S) as a function of St number for different cavity volumes with the same L/H ratio of 1 for values of the acoustic particle velocity ratio υ/U = 0.5% and 1%.

Cavities of L/H = 1 (26 mm x 26 mm, 52 mm x 52 mm, and 78 mm x 78 mm)

At υ /U = 5%

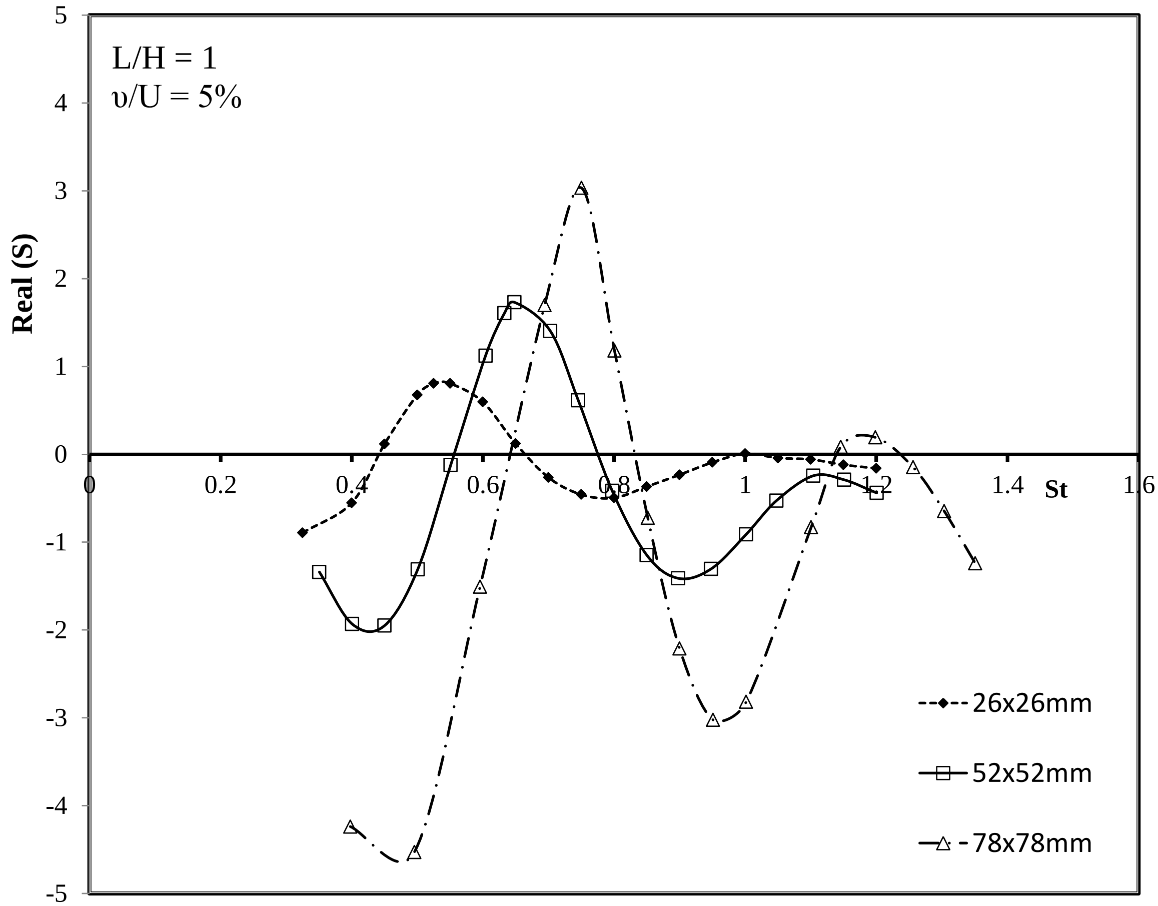

Figure A.11: Real part of the aeroacoustic source term R(S) as a function of St number for different cavity volumes with the same L/H ratio of 1 for values of the acoustic particle velocity ratio υ/U = 5%.

Cavities of L/H = 2 (26 mm x 13 mm, 52 mm x 26 mm, and 104 mm x 52 mm)

At υ /U = 0.5% & 1%

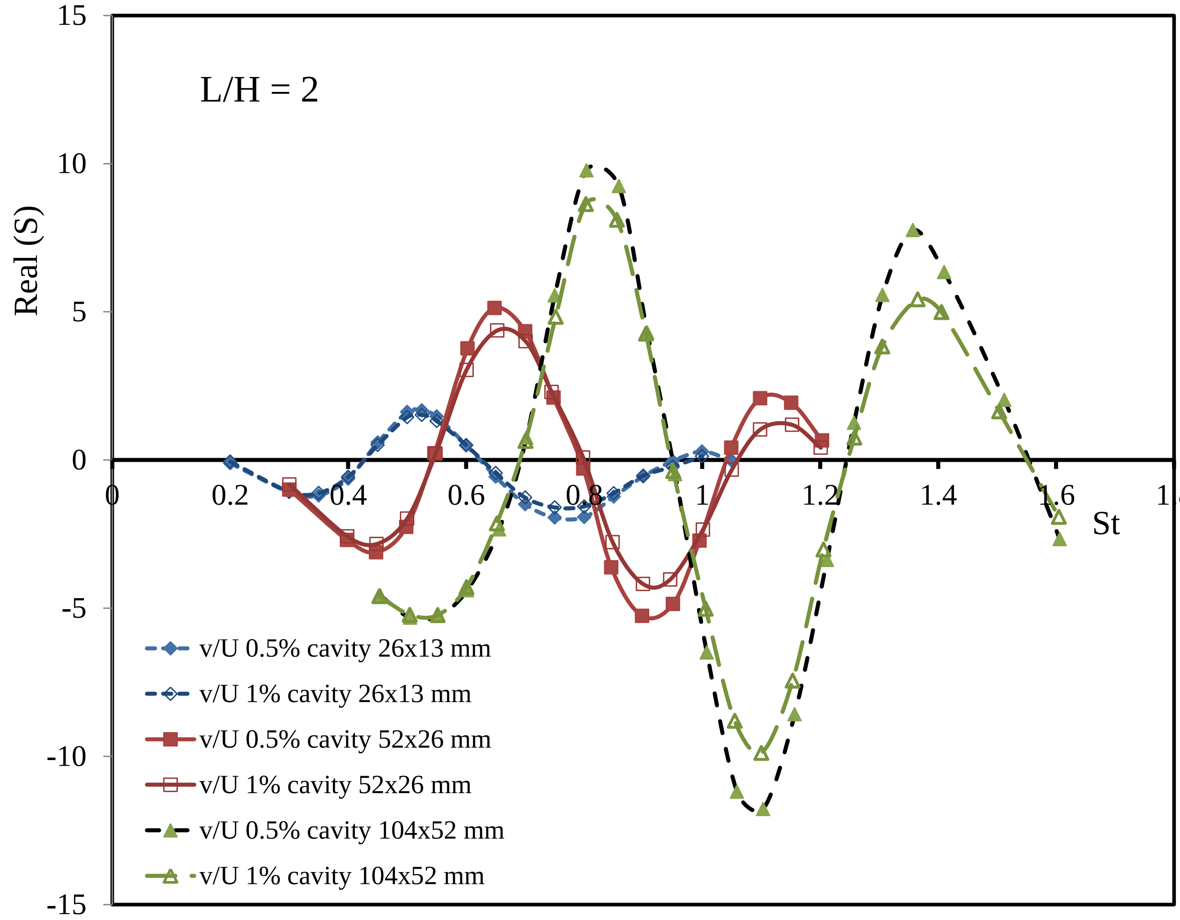

Figure A.12: Real part of the aeroacoustic source term R(S) as a function of St number for different cavity volumes with the same L/H ratio of 2 for values of the acoustic particle velocity ratio υ/U = 0.5% and 1%.

Cavities of L/H = 2 (26 mm x 13 mm, 52 mm x 26 mm, and 104 mm x 52 mm)

At υ /U = 5%

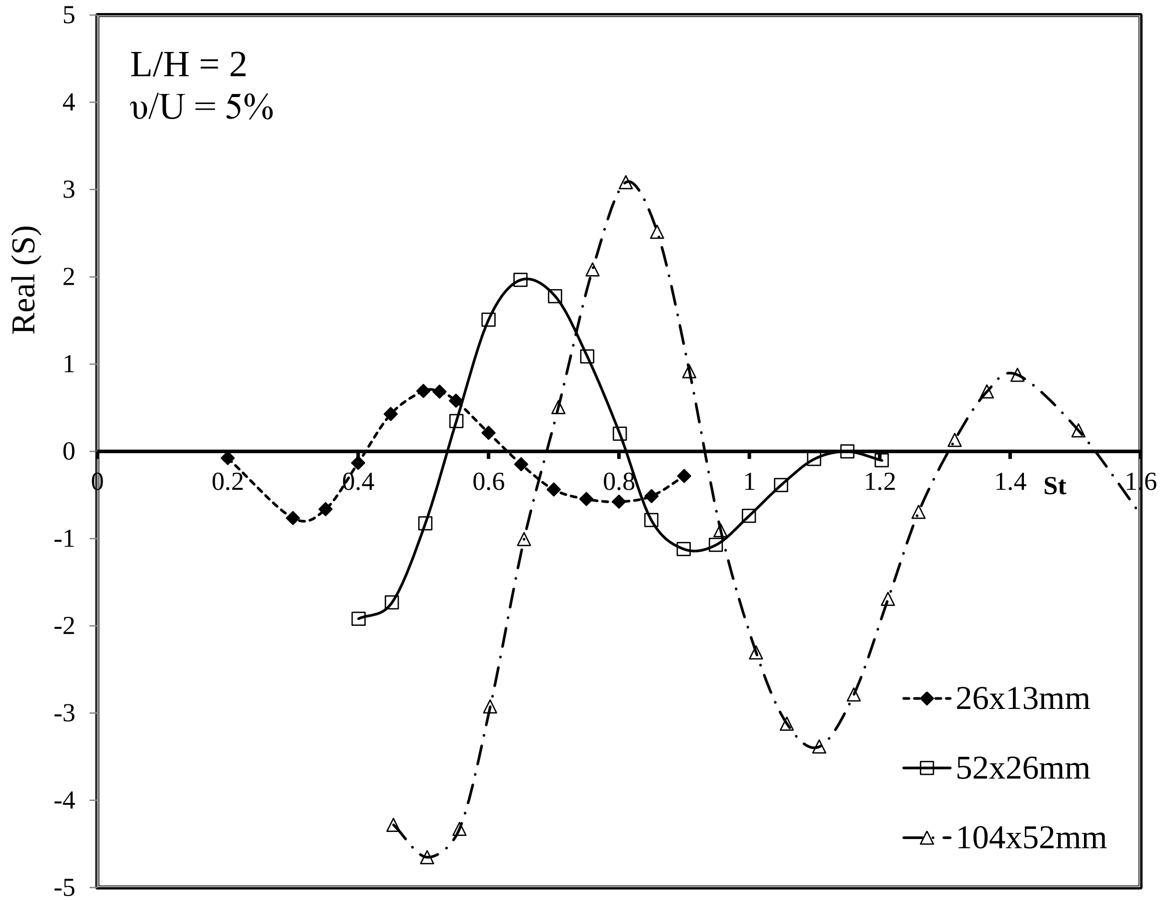

Figure A.13: Real part of the aeroacoustic source term R(S) as a function of St number for different cavity volumes with the same L/H ratio of 2 for values of the acoustic particle velocity ratio υ/U = 5%.

Cavities of L/H = 3 (39mm x 13 mm, 78 mm x 26 mm, and 156 mm x 52 mm)

At υ /U = 0.5% & 1%

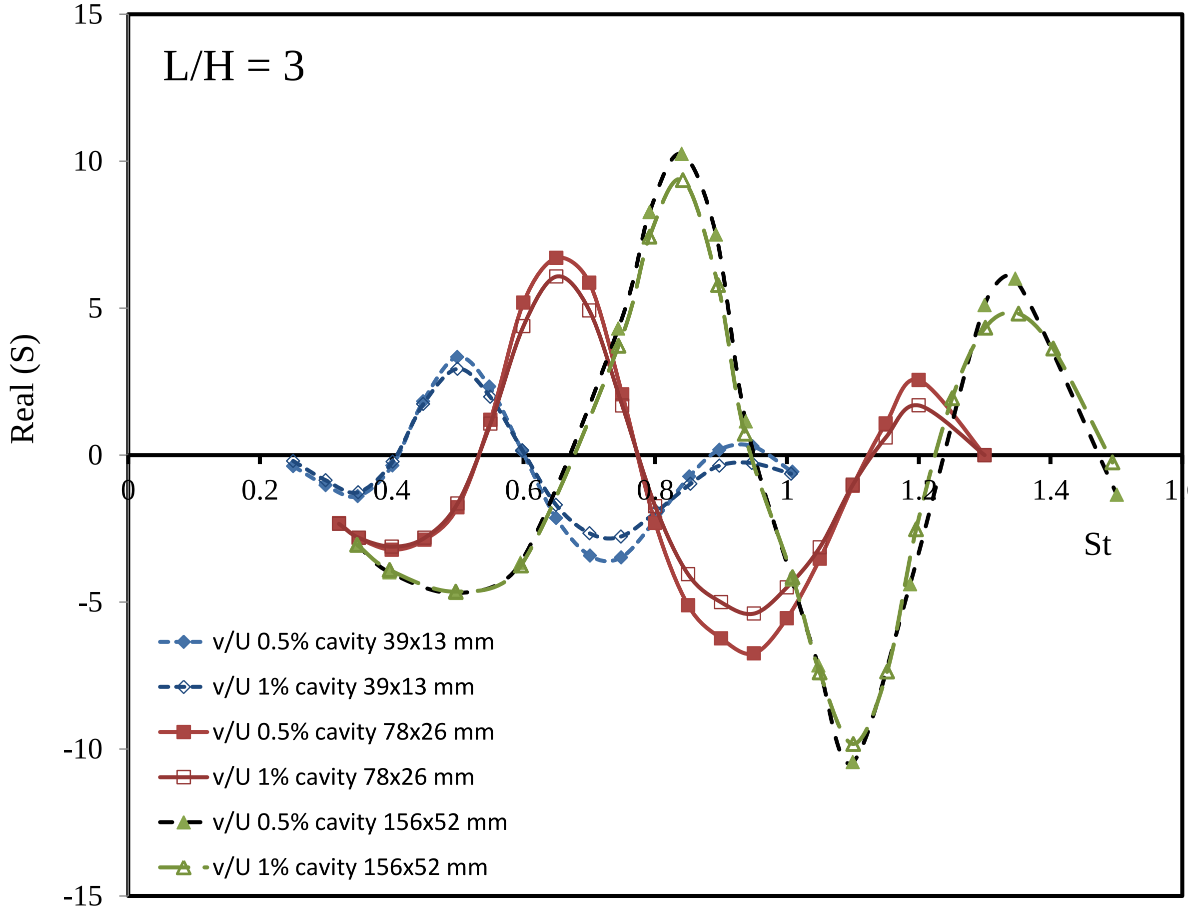

Figure A.14: Real part of the aeroacoustic source term R(S) as a function of St number for different cavity volumes with the same L/H ratio of 3 for values of the acoustic particle velocity ratio υ/U = 0.5% and 1%.

Cavities of L/H = 3 (39 mm x 13 mm, 78 mm x 26 mm, and 156 mm x 52 mm)

At υ /U = 5%

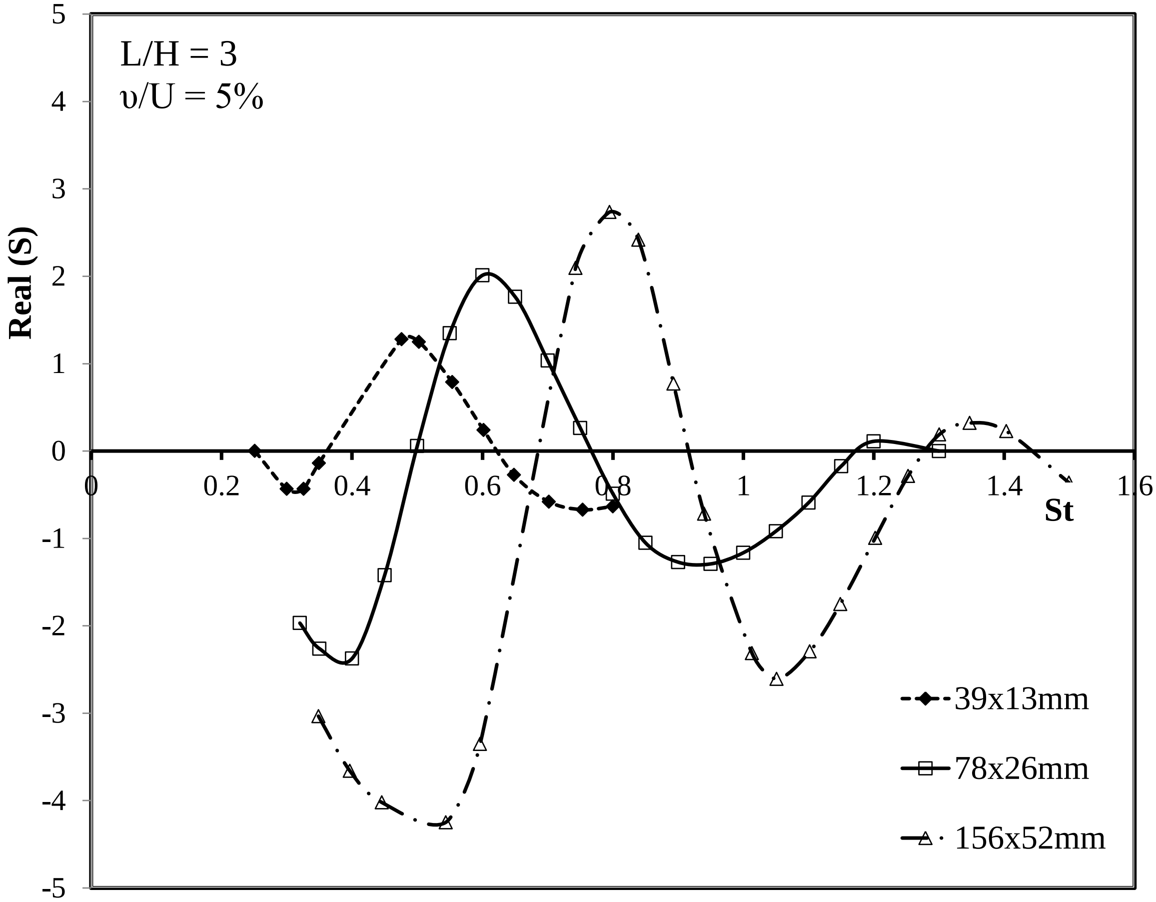

Figure A.15: Real part of the aeroacoustic source term R(S) as a function of St number for different cavity volumes with the same L/H ratio of 3 for values of the acoustic particle velocity ratio υ/U = 5%.

Cavities of L/H = 1 (26 mm x 26 mm, 52 mm x 52 mm, and 78 mm x 78 mm)

At whistling Strouhal number

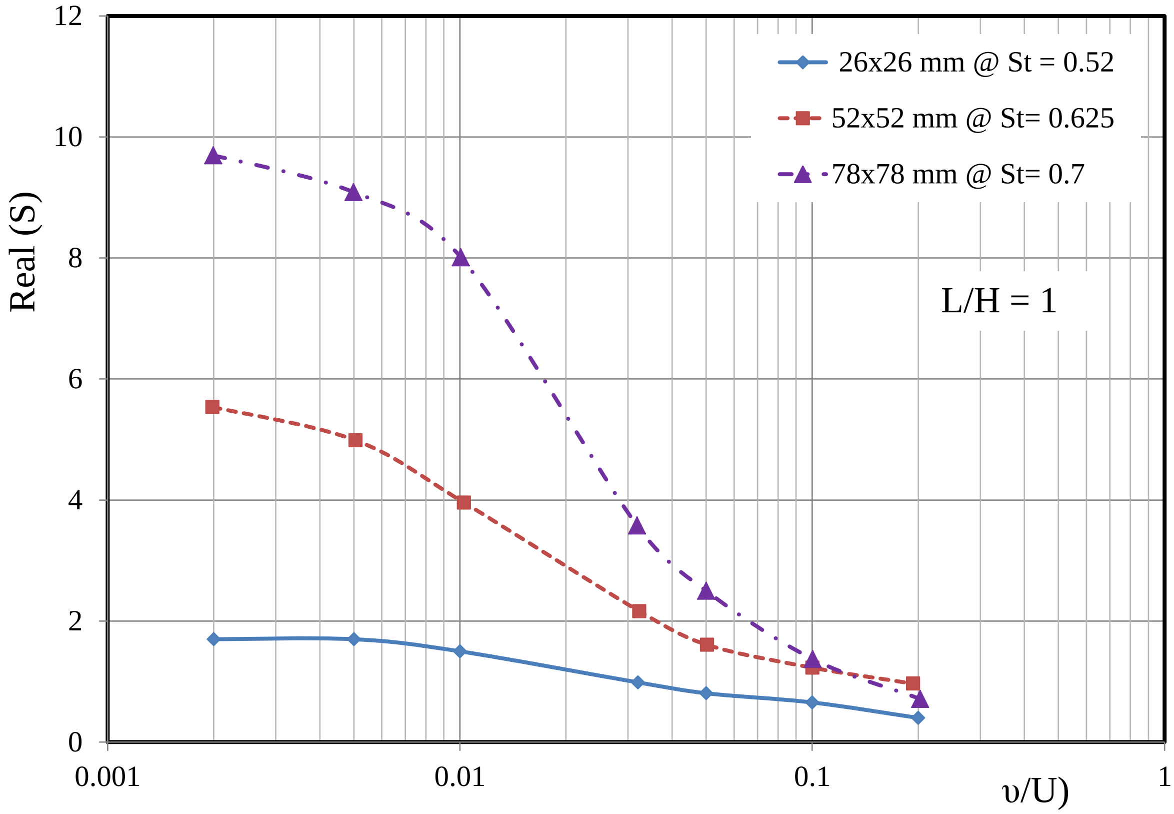

Figure A.16: Variation of the aeroacoustic source term with the amplitude ratio at the peak whistling Strouhal number for the first hydrodynamic mode for L / H = 1

Cavities of L/H = 3 (39 mm x 13 mm, 78 mm x 26 mm, and 156 mm x 52 mm)

At whistling Strouhal number

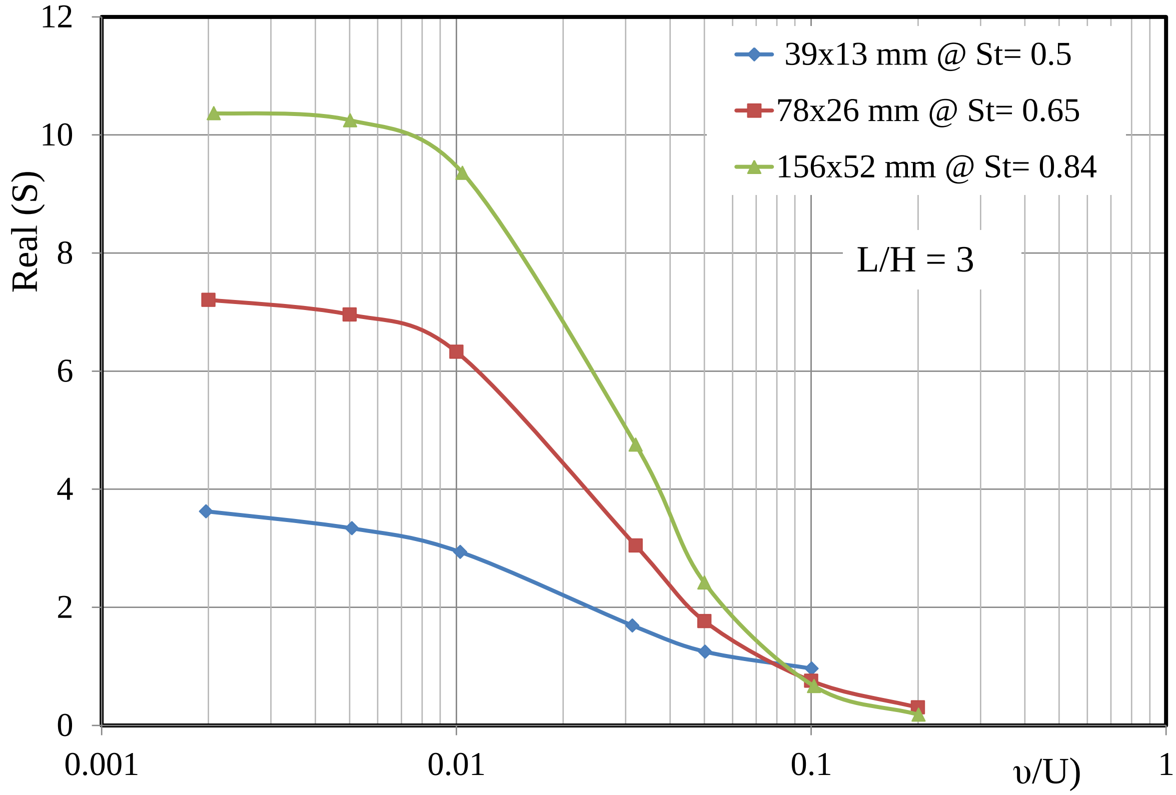

Figure A.17: Variation of the aeroacoustic source term with the amplitude ratio at the peak whistling Strouhal number for the first hydrodynamic mode for L / H = 3

Appendix B

Uncertainty Analysis

This appendix presents the uncertainty associated with the different measured and calculated quantities. Kline and McClintock method or the error propagation equation is used to calculate the uncertainty of each dependent variable from its independent variables as follows:

$$Y = f\,(X_1, X_2, X_3, \ldots\ldots.., X_n) \qquad \text{(B.1)}$$

Where Y is the dependent variable and X_i are the independent variables. Therefore, the error propagation equation for Variable Y will be:

$$dY = \sqrt{\sum_{i=1}^{n} \left(\frac{\partial Y}{\partial X_i} dX_i\right)^2} \qquad \text{(B.2)}$$

where dY is the uncertainty of the dependent variable Y, and dX_i is the known uncertainty of the independent variable X_i.

The next section shows the uncertainty analysis of the measured quantities such as the acoustic pressure **p**, the mean flow velocity U, and the speed of sound C_o followed by the uncertainty analysis of the calculated quantities such as the ideal acoustic impedance Y_o, the acoustic particle velocity **υ**, the acoustic amplitude ratio **υ**/U, Strouhal number St, and the source term **S**.

The flow velocity at the centerline of the pipe was measured by means of a pitot tube which was connected to a Validyne differential pressure transducer of model number DP15-42 which has an accuracy of ± 0.25% of the full scale. Most of the measurements are used a full scale of the differential pressure of 860 Pascal. Hence, the uncertainty of the differential pressure d(dP) = ± 0.25% x 860 = ± 2.15 Pa. From equation 3.1, the mean flow velocity is function of the square root of the differential pressure. Therefore, the relative uncertainty of the mean flow velocity dU/U can be expressed as:

$$\frac{dU}{U} = \frac{1}{U}\sqrt{\left(\frac{\partial U}{\partial (dP)}\ d(dP)\right)^2} \qquad \text{(B.3)}$$

So, the relative uncertainty of the mean flow velocity dU/U is ± 0.125%.

The acoustic (fluctuating) pressure inside the pipeline is measured by means of 1/4" GRAS 40BP condenser microphones with uncertainty of 0.25 Pascal in the measurement frequency range. The measured dynamic pressure is about 200 Pascal as shown in figure 4.3. Hence, the relative uncertainty of the acoustic pressure d**p**/**p** is about ± 0.125%.

The speed of sound is dependent on the square root of the ambient temperature which is measured by an accurate thermometer of uncertainty of dT/T = 0.05%. Therefore, the relative uncertainty of the speed of sound dC/C_o is about ± 0.025%.

For the uncertainty analysis of the calculated quantities, the ideal acoustic impedance Y_o is used in the calculation of the acoustic particle velocity from the measured acoustic pressure. By considering a constant ambient density, the relative uncertainty of the acoustic impedance dY/Y_o is the same as the relative uncertainty of the speed of sound dC/C_o which is about ± 0.025%.

As the acoustic particle velocity is the ratio between the acoustic pressure and the acoustic impedance, the relative uncertainty of the acoustic particle velocity dυ/υ can be calculated as follows:

$$\frac{d\boldsymbol{\upsilon}}{\boldsymbol{\upsilon}} = \frac{1}{\boldsymbol{\upsilon}}\sqrt{\left(\frac{\partial \boldsymbol{\upsilon}}{\partial(\mathbf{p})}\, d(\mathbf{p})\right)^{2} + \left(\frac{\partial \boldsymbol{\upsilon}}{\partial(Y)}\, d(Y)\right)^{2}} \tag{B.4}$$

From equation B.4, the relative uncertainty of the acoustic particle velocity d**υ**/**υ** is about 0.127 %.

The amplitude ratio is the ratio of the acoustic particle velocity to the mean flow velocity, so the relative uncertainty of the amplitude ratio d(**υ**/U)/(**υ**/U) is about 0.18 %. The uncertainty of the Strouhal number (St=fL/U) depends on the uncertainty of the frequency, f (df/f = 0.1%, from microphone's manual); the cavity length, L (tolerance in the cavity length is 1%.); and the mean flow velocity, U (dU/U = 0.125%). The Strouhal number relative uncertainty is calculated as follow:

$$\frac{dSt}{St} = \sqrt{\left(\frac{df}{f}\right)^{2} + \left(\frac{dL}{L}\right)^{2} + \left(\frac{dU}{U}\right)^{2}} \tag{B.5}$$

Therefore, the Strouhal number relative uncertainty is about 1%.

The uncertainty of the dimensionless source term **S** from SWM measurements, **S** (**p**,U,**υ**/U), depends on the uncertainty of the acoustic pressure (d**p**/**p** = 0.125%); the flow velocity (dU/U = 0.125%); and the amplitude ratio (d (**υ**/U) /(**υ**/U) = 0.18%). The source term relative uncertainty is calculated as follow:

$$\frac{d\mathbf{S}}{\mathbf{S}} = \sqrt{\left(\frac{d\mathbf{p}}{\mathbf{p}}\right)^{2} + \left(\frac{d(\boldsymbol{\upsilon}/U)}{(\boldsymbol{\upsilon}/U)}\right)^{2} + \left(\frac{dU}{U}\right)^{2}} \tag{B.6}$$

Therefore, the source term relative uncertainty is about 0.25%.

More analysis of the experimental error of the SWM were presented in Section 4.2.3

PIV error analysis

Seeding particles tracking and vector validation: The quantity of seeding material, the camera focal position and zooming are adjusted and tested such that each image contains vector validation rates (ratio of number of good vectors to the total number of vectors) in excess of 99%. The Stokes number of seeding particles, which indicates how seeding particles follow the fluid flow particles, for all PIV cases based on the seed droplet properties and the maximum test flow velocity, is much smaller than 0.1 which results in tracking error of less than 1%. (Tropea, et al., 2007).

Error analysis of the flow field from PIV measurements: Uncertainty in flow field measurements using PIV have been presented by Scarano & Riethmuller (2000) who provided PIV displacement uncertainty data for known particle displacement gradients. Raffel et al. (2007) outlined the corresponding uncertainty in the vorticity field.

From the measured velocity field at the maximum flow velocity, maximum displacement gradient $(\partial u/\partial y)_{max}$ = 0.054 pixel/pixel located at the entrance plane to the cavity region, and $(\partial v/\partial x)_{max}$ = 0.01 pixel/pixel. According to Scarano & Riethmuller (2000), the uncertainty in particle displacement ε_u = 0.02 pixel and ε_v = 0.005 pixel in both components. Therefore, the relative uncertainty of particle displacement $\varepsilon_u/\delta u$ = 0.5 % and $\varepsilon_v/\delta v$ = 0.8 %. So d/U/U = 0.95%

According to Raffel et al. (2007), the uncertainty in vorticity $\varepsilon_{(\partial u/\partial y)} = 0.7\varepsilon_u/\Delta X$ = 0.0035 pixels/pixel, and $\varepsilon_{(\partial v/\partial x)} = 0.7\varepsilon_v/\Delta Y$ = 0.000875 pixels/pixel, where $\Delta X = \Delta Y$= 4 pixels from the PIV measuring grid. Therefore, the relative uncertainty of vorticity $\varepsilon_{(\partial u/\partial y)}/(\partial u/\partial y)_{max} = 6.5\ \%$ and $\varepsilon_{(\partial v/\partial x)}/(\partial v/\partial x)_{max} = 8.75\ \%$. So $d\omega/\omega = 10.9\%$

Error analysis of the acoustic particle velocity from finite element analysis:

The acoustic particle velocity from the finite element analysis are calculated based on Eqn. 5.4, from which υ is function of (p_{max}, $\nabla p(x,y)$, and f). As mentioned above the uncertainty of acoustic pressure d**p**/**p** is about ± 0.125%. The maximum residual error in $\nabla p(x,y)$ is 0.01% from FE solver, and the error in frequency is df/f = 0.1%, from microphone's manual.Therefore, the relative uncertainty of the acoustic particle velocity $d\upsilon/\upsilon$ from FE simulations can be calculated from equation B.7 as follow:

$$\frac{d\upsilon}{\upsilon} = \sqrt{\left(\frac{d\boldsymbol{p}}{p}\right)^2 + \left(\frac{d\nabla p}{\nabla p}\right)^2 + \left(\frac{df}{f}\right)^2} \qquad \text{(B.7)}$$

From equation B.7, the relative uncertainty of the acoustic particle velocity $d\upsilon/\upsilon$ is about 0.16 %.

Uncertainty in the aeroacoustic power, P, from Howe's integrant method

(**P** is a function of (vorticity, flow velocity, acoustic particle velocity) as follow:

$$\frac{d\mathbf{P}}{\mathbf{P}} = \sqrt{\left(\frac{d\omega}{\omega}\right)^2 + \left(\frac{d(\boldsymbol{\upsilon})}{(\boldsymbol{\upsilon})}\right)^2 + \left(\frac{dU}{U}\right)^2} \qquad \text{(B.8)}$$

So, dP/P is about 10.95%. And the uncertainty in the normalized source term S calculated from the aeroacoustic power P will be about 11%. Figure B.1 shows the error bars for the aeroacoustic source term from both methods SWM and Howe's Integrand one. The error in the source term determined by the SWM is very small to be indicated in figure B.1.

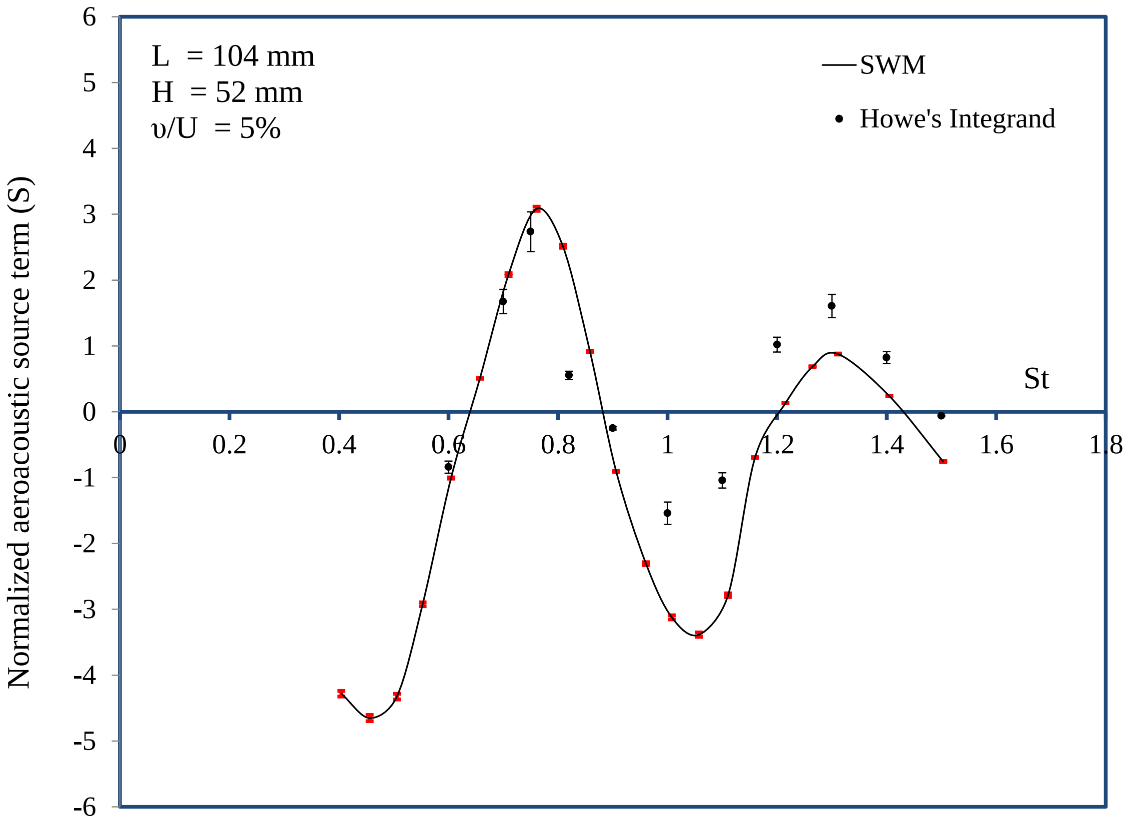

Figure B.1: Error bars for the aeroacoustic source term from both methods; SWM (red bars) and Howe's Integrand Method.